

PERFORMANCE CHARACTERIZATION AND MODELLING OF A
LITHIUM-ION CELL USING ELECTROCHEMICAL IMPEDANCE
SPECTROSCOPY

Performance Characterization and Modelling of a Lithium-Ion Cell using Electrochemical Impedance Spectroscopy

by

Abdel Rahman Tawakol, B.Eng.Mgt.

A Thesis

Submitted to the Department of Mechanical Engineering
and the School of Graduate Studies
of McMaster University
in Partial Fulfilment of the Requirements
for the Degree of
Master of Applied Science

© Copyright by Abdel Rahman Tawakol, May 2020
All Rights Reserved

Master of Applied Science (2020)
Department of Mechanical Engineering

McMaster University
Hamilton, Ontario, Canada

TITLE: Performance Characterization and Modelling
of a Lithium-Ion Cell using Electrochemical
Impedance Spectroscopy

AUTHOR: Abdel Rahman Tawakol
B.Eng.Mgt. (Mechatronics Engineering &
Management)
McMaster University, Hamilton, Canada

SUPERVISOR: Dr. Saeid R. Habibi, Ph.D., P.Eng., FCSME,
FASME
Professor and Senior NSERC Industrial Research
Chair
Director, Centre for Mechatronics and Hybrid
Technologies
McMaster University, Hamilton, Canada

NUMBER OF PAGES: [xix, 198](#)

Abstract

The electrification of transportation is gradually becoming more prominent as it is more efficient and sustainable than conventional transportation alternatives found today. At the centre of this growth is battery testing and research, as they are the primary energy storage devices used to power electric vehicles. With the growing complexity of battery systems, testing and monitoring their performance relies on highly specialized and precise equipment. Furthermore, the use of battery models helps researchers improve their research while reducing the time and costs involved in testing. As such, accurate battery modelling is a critical component in predicting how a battery will behave in specific applications and under various conditions.

In this research, a lithium-ion cell is tested extensively, and its performance is characterized across a wide range of operating conditions including temperature, current rates and [state of charge \(SOC\)](#) values. An equivalent circuit model for impedance modelling is proposed, which utilizes constant phase elements represented in the time domain to improve fitting accuracy. This is done concurrently with the development of a state of the art, fully automated battery test system which is showcased throughout the course of the research. In addition to this, an analysis is conducted on the low frequency impedance data used

during research, as well as its effect on model accuracy. To provide significance behind the results and relevance to real-world applications, all of the impedance modelling is experimentally validated using temporal drive cycle data. This research was able to demonstrate that the use of a ZARC element can improve the mid-frequency fitting of impedance data relative to a conventionally used modelling approach. It also showcases how the use of low frequency [electrochemical impedance spectroscopy \(EIS\)](#) data can negatively impact the accuracy of impedance modelling.

To the loving memory of my dear grandmother Ragaa Ibrahim Tawakol.

Acknowledgments

All praise is due to Allah, the most Beneficent, the most Merciful. I thank Allah for His endless blessings and for giving me health, patience and knowledge to complete this work to the best of my ability.

First and foremost, I would like to thank my supervisor, Dr. Saeid Habibi, for his support and guidance during the course of my graduate studies. Joining the Centre for Mechatronics and Hybrid Technologies (CMHT) was an enriching experience which allowed me to work on industry driven projects that are helping shape the future of transportation electrification. Thank you to all of the CMHT team members for being great mentors and for making this journey as enjoyable as possible.

I would also like to convey my appreciation to Mr. Cam Fisher for sharing his ample expertise and technical knowledge throughout my research. Mr. Fisher manages various aspects of the facilities and resources used to complete this thesis, and his efforts allowed me to complete my research in collaboration with industry professionals; without his help, I would not have been able to complete this work.

I owe an enormous deal of gratitude to Dr. Phillip Kollmeyer, who was instrumental in the completion of my research and this thesis. Dr. Kollmeyer never hesitated to share his wealth of knowledge and provide advice whenever possible, even when it was not his responsibility to do so. Whether it was explaining simple lab procedures or providing detailed research help, Dr. Kollmeyer always went above and beyond to help myself and many other students. His knowledge, passion for success, genuine kindness and willingness to help are an invaluable asset for the entire research team at the McMaster Automotive Resource

Centre (MARC). The McMaster community is lucky to have someone like Dr. Kollmeyer and I feel extremely fortunate and honoured to have worked with him throughout my studies.

I would like to thank D&V Electronics for giving me the opportunity to gain valuable work experience and collaborate with some of the brightest minds in the automotive industry. This opportunity provided a bridge between industrial applications and key research concepts and I am grateful to have worked with the D&V team who made me feel at home from day one. Financial support by D&V is also acknowledged and greatly appreciated.

Additionally, I would like to acknowledge financial support from the following: the Natural Sciences and Engineering Research Council of Canada (NSERC), the Ontario Research Fund (ORF), the McMaster University School of Graduate Studies as well as the Department of Mechanical Engineering at McMaster University. Your generous contributions have allowed me to pursue higher education and focus solely on my research without any financial burdens.

I would have not been able to complete my academic journey without the help of my friends, both at McMaster and back home, whom I thank for their support and for all of the memories we've shared thus far. McMaster University has been my home for the past seven years, and I am lucky to have shared my time here with many phenomenal people; thank you for helping me get through this chapter of my life.

Last, but certainly not least, I am incredibly grateful for the unwavering support of my family and for all that they have done to get me to where I am today. Thank you to my siblings for being a source of inspiration that I can look up to and for always helping me strive to become better. Thank you to my parents, Hashem and Suhair, who are the biggest blessing in my life and without whom I could have never enjoyed so many opportunities. They made countless sacrifices many years ago, leaving everything they had and starting somewhere completely new, to give myself and my siblings the privileged life we live today. I am forever indebted to them for their unconditional love, encouragement, prayers and support; saying "thank you" will simply never be enough. I hope to always make you proud.

Table of Contents

Abstract	iii
Acknowledgments	vi
List of Figures	xi
List of Tables	xvi
Abbreviations	xviii
1 Introduction	1
1.1 Project Description	5
1.2 Thesis Objectives	6
1.3 Thesis Outline	7
2 Energy Storage in Electrified Vehicles	9
2.1 Background on Electric Vehicles	10
2.1.1 History of Transportation Electrification	10
2.1.2 Energy Storage Alternatives	14
2.1.2.1 Lithium-Ion Batteries	15
2.2 Overview of Terminology and Definitions	18
2.3 Electrochemical Impedance Spectroscopy (EIS)	26

2.4	Battery Modelling	31
2.4.1	Mathematical Models	34
2.4.2	Electrochemical Models	35
2.4.3	Equivalent Circuit Models	36
2.4.4	Comparison	38
2.5	Battery Testing and Characterization Methods	39
2.5.1	Preconditioning/Break-In	39
2.5.2	Capacity Test	41
2.5.3	OCV-SOC Test	41
2.5.4	Hybrid Pulse Power Characterization (HPPC) Test	42
2.5.5	Drive Cycle Profiles	47
2.6	Summary	49
3	D&V Battery Testing System	50
3.1	Industry Cell Testers	51
3.2	Hardware Components	54
3.2.1	High Frequency Signal Module	54
3.2.2	Cycler Module (High Power)	56
3.2.3	Coulombic Efficiency Module (High Precision)	56
3.2.4	Advantages of Hardware Integration	57
3.3	Tester Software	58
3.4	Testing Sequence	62
3.5	Experimental Setup	67
3.5.1	Description of Apparatus	67
3.5.2	Cell Fixture and Connections	73
3.5.3	Remote Testing	77
3.6	Summary	81

4	Battery Testing and Characterization Using D&V Battery Testing System	83
4.1	Break-in Cycles	85
4.2	OCV - SOC Test	89
4.3	HPPC Test	95
4.4	EIS Test	106
4.5	Summary	116
5	Impedance Modelling	117
5.1	Battery Model Structure	119
5.2	Model Parameterization	124
5.3	Impedance Spectra Fitting Results	127
5.4	Experimental Validation	144
5.4.1	Drive Cycle Simulation Results	150
5.5	Analysis of Low Frequency Impedance Data	158
5.6	Summary	164
6	Conclusions and Future Work	169
6.1	Future Work	172
	References	175
	APPENDICES	186
A	Sample Test Script	187
B	$L - R - RC - RC - Z_{wb}$ Model Parameters	188
C	$L - R - ZARC - Z_{wb}$ Model Parameters	192
D	Drive Cycles for Model Validation	198

List of Figures

1.1	Greenhouse gas emissions by economic sector, Canada, 1990 to 2016 [5] . . .	3
1.2	Significant thinning at Alaska’s Muir Glacier, 63 years apart [8]	4
2.1	Gustave Trouvé’s tricycle in 1881 [10]	11
2.2	Power and energy density comparison for various energy storage devices [15]	16
2.3	General overview of the electrochemical processes involved in charging (a) and discharging (b) a battery [16]	17
2.4	Battery state of charge depicted as a gauge reading	19
2.5	The effect on cell capacity as a result of discharging at various C-rates [23]	21
2.6	An example curve demonstrating the relationship between open-circuit voltage and state of charge	23
2.7	Change in depth of discharge with increased cycling for a nickel-iron battery [27]	25
2.8	Nyquist plot with impedance vector [28]	29
2.9	Sample impedance plot for a lithium-ion battery [30]	30
2.10	Change in impedance spectrum at different SOC levels; $T = 25\text{ }^\circ\text{C}$ [33] . . .	32
2.11	Impedance plot comparing a fresh cell to an aged cell [32]	33
2.12	First-order RC equivalent circuit model diagram [49]	37
2.13	Discharging capacity of a Lithium Iron Phosphate/Graphite battery during break-in cycles [53]	40
2.14	OCV-SOC characteristic of a Lithium Iron Phosphate/Graphite battery observed at $25\text{ }^\circ\text{C}$ [53]	43

2.15	An example pulse current profile used in an HPPC test [69]	45
2.16	Sample current pulse and voltage response used for dynamic characterization of a battery [33]	46
2.17	Urban Dynamometer Driving Schedule (UDDS) profile [72]	48
3.1	D&V Electronics' BCT-150 battery cell tester [77]	55
3.2	The main screen of the BCT test application	59
3.3	The BCT test application provides a list of available devices and test scripts to the user	60
3.4	During a test, the BCT test application provides realtime measurements and information regarding test progress	61
3.5	An example battery specification profile used during testing	63
3.6	The custom script editor used as part of the BCT software	65
3.7	The BCT application used to view results	66
3.8	An overview of the test environment and the appropriate connections between each component	68
3.9	Samsung INR21700-50E Lithium-Ion Cell	69
3.10	Envirotronics SH16 Temperature/Humidity System	71
3.11	Cell fixture used during testing	74
3.12	An example of a cell label with identifying information, used for traceability in the test environment	75
3.13	Installation of cell fixture and cabling inside environmental chamber	76
4.1	An overview of the tests used to characterize a lithium ion cell	84
4.2	Applied current and measured voltage of the cell during a single break-in cycle	86
4.3	Applied current profile for break-in cycles	87
4.4	Measured voltage during break-in cycles ($T = 25\text{ }^{\circ}\text{C}$)	87
4.5	Charging and discharging capacity of the cell during the course of break-in cycling ($T = 25\text{ }^{\circ}\text{C}$)	88

4.6	Applied current and measured voltage during a C/20 discharge ($T = 25\text{ }^{\circ}\text{C}$)	91
4.7	Applied current and measured voltage during a C/20 charge ($T = 25\text{ }^{\circ}\text{C}$)	91
4.8	Hysteresis effect observed between charge and discharge curves during an OCV-SOC test ($T = 25\text{ }^{\circ}\text{C}$)	92
4.9	Resampled discharge and charge OCV-SOC curve with averaged curve ($T = 25\text{ }^{\circ}\text{C}$)	93
4.10	OCV-SOC relationship across a range of temperatures	94
4.11	Pulse profile applied to cell during HPPC test	97
4.12	Applied current during entire duration of HPPC test ($T = 25\text{ }^{\circ}\text{C}$)	99
4.13	Measured voltage response of the cell during entire duration of HPPC test ($T = 25\text{ }^{\circ}\text{C}$)	99
4.14	Applied current pulses and measured voltage response of the cell ($T = 25\text{ }^{\circ}\text{C}$, 90% SOC)	100
4.15	Internal resistance of the cell at different SOC values (measured for 0.5C discharging current)	101
4.16	Internal resistance of the cell across all SOC values and temperatures (measured for 0.5C discharging current)	102
4.17	Normalized resistance versus temperature (measured for 0.5C discharging current)	103
4.18	Internal resistance of the cell at different pulse current values (20% SOC)	104
4.19	Normalized resistance versus pulse current between 80% and 70% SOC	105
4.20	Results of simple EIS measurement sweep to determine appropriate current amplitude ($T = 25\text{ }^{\circ}\text{C}$)	108
4.21	Impedance spectrum of cell ($T = 25\text{ }^{\circ}\text{C}$, 95% SOC)	110
4.22	Dependence of cell's impedance spectra on operating temperature (measured at 60% SOC)	111
4.23	A magnified view of impedance spectra across a range of temperatures (measured at 60% SOC)	112
4.24	Impedance spectra at various SOC levels ($T = 25\text{ }^{\circ}\text{C}$)	113
4.25	Impedance spectra at various SOC levels ($T = -10\text{ }^{\circ}\text{C}$)	114

4.26	A magnified view of impedance spectra at various SOC levels ($T = -10^{\circ}\text{C}$)	115
5.1	An overview of the battery modelling approach used in this research	118
5.2	Example equivalent circuit model used for EIS fitting [83]	120
5.3	Representation of Warburg element using a series of RC-circuit pairs	120
5.4	Example model fit to EIS measurement at -10°C and 80 % SOC [83]	121
5.5	Time domain representation of ZARC element	123
5.6	Proposed equivalent circuit model for EIS fitting, utilizing a constant phase element	124
5.7	Optimized R_{wb} values for $L - R - RC - RC - Z_{wb}$ model at 25°C	128
5.8	Fitting of $L - R - RC - RC - Z_{wb}$ model to impedance data measured at 15 % SOC ($T = 25^{\circ}\text{C}$)	129
5.9	Fitting of $L - R - RC - RC - Z_{wb}$ model to impedance data measured at 95 % SOC ($T = 10^{\circ}\text{C}$)	130
5.10	Optimized R_{wb} values for $L - R - ZARC - Z_{wb}$ model at 40°C	131
5.11	Fitting of $L - R - ZARC - Z_{wb}$ model to impedance data measured at 10 % SOC ($T = 40^{\circ}\text{C}$)	132
5.12	Fitting of $L - R - ZARC - Z_{wb}$ model to impedance data measured at 25 % SOC ($T = 25^{\circ}\text{C}$)	133
5.13	Fitting of $L - R - ZARC - Z_{wb}$ model to impedance data measured at 50 % SOC ($T = -10^{\circ}\text{C}$)	134
5.14	Fitting of $L - R - ZARC - Z_{wb}$ model to impedance data measured at 80 % SOC ($T = 0^{\circ}\text{C}$)	135
5.15	Fitting of example and proposed models to impedance data measured at 100 % SOC ($T = -10^{\circ}\text{C}$)	136
5.16	Comparing fit of example and proposed models to impedance data measured at 100 % SOC ($T = 10^{\circ}\text{C}$)	138
5.17	Comparing fit of example and proposed models to impedance data measured at 95 % SOC ($T = 25^{\circ}\text{C}$)	139
5.18	Real and imaginary impedance RMSE for example ($2RC$) and proposed ($ZARC$) models	141

5.19	US06 drive cycle profile data	145
5.20	Example of adjustment applied to US06 current profile to avoid peak currents that are above the safety specifications of the cell	146
5.21	Example of procedure used to determine drive cycle stopping condition ($T = 25^\circ\text{C}$)	148
5.22	Measured voltage during HWFET drive cycle current profile ($T = 25^\circ\text{C}$)	149
5.23	Experimental validation of UDDS drive cycle with $L - R - RC - RC - Z_{wb}$ model ($T = 10^\circ\text{C}$)	152
5.24	Experimental validation of UDDS drive cycle with $L - R - ZARC - Z_{wb}$ model ($T = 40^\circ\text{C}$)	153
5.25	Experimental validation of HWFET drive cycle with $L - R - RC - RC - Z_{wb}$ model ($T = 25^\circ\text{C}$)	154
5.26	Experimental validation of US06 drive cycle with $L - R - ZARC - Z_{wb}$ model ($T = 25^\circ\text{C}$)	155
5.27	Voltage RMSE between model predicted and experimentally measured voltage for all drive cycles	156
5.28	Real and imaginary impedance RMSE for ZARC model at different stopping frequencies ($T = 25^\circ\text{C}$)	159
5.29	Modelling impedance data with $L - R - ZARC - Z_{wb}$ model using different frequency ranges ($T = 25^\circ\text{C}$, 80 % SOC)	160
5.30	Comparing error values from model validation using different stopping frequencies ($T = 25^\circ\text{C}$)	163
5.31	Experimental validation of HWFET drive cycle with $L - R - ZARC - Z_{wb}$ model after fitting down to 1 mHz ($T = 25^\circ\text{C}$)	165
5.32	Experimental validation of HWFET drive cycle with $L - R - ZARC - Z_{wb}$ model after fitting down to 25 mHz ($T = 25^\circ\text{C}$)	166
D.1	HWFET drive cycle profile data	199
D.2	LA92 drive cycle profile data	200
D.3	UDDS drive cycle profile data	201

List of Tables

2.1	Comparison of the various approaches that can be used to model the behaviour of a lithium-ion battery	38
3.1	A comparison of the specifications of existing battery testing solutions currently available in industry	52
3.2	A summary of the specifications for each module used in the BCT-150 battery test system	57
3.3	Samsung INR21700-50E Lithium-Ion Cell Specifications	70
3.4	Envirotronics SH16 Temperature/Humidity System Specifications	72
3.5	A list of relevant serial commands that can be used to communicate between the BCT and environmental chamber	79
4.1	Hardware protection limits used during characterization tests	84
4.2	Summary of parameters used for HPPC test	95
4.3	Summary of parameters used for EIS test	106
5.1	Summary of optimization algorithm options used to parametrize model in MATLAB	127
5.2	Average percentage change in RMSE between example (<i>2RC</i>) and proposed (<i>ZARC</i>) models	142
5.3	Total computation time required to parameterize original (<i>2RC</i>) and proposed (<i>ZARC</i>) models	143
5.4	Characteristics summary of drive cycles used for experimental validation [72]	144
5.5	Discharge capacity used for drive cycle profiles at each temperature	149

5.6	Time constant values for Warburg element when modelling with different stopping frequencies	161
5.7	Average Warburg element time constant values across all SOC levels for different stopping frequencies ($T = 25\text{ }^{\circ}\text{C}$)	162
B.1	Solution values for $L - R - RC - RC - Z_{wb}$ model at $-10\text{ }^{\circ}\text{C}$	189
B.2	Solution values for $L - R - RC - RC - Z_{wb}$ model at $0\text{ }^{\circ}\text{C}$	189
B.3	Solution values for $L - R - RC - RC - Z_{wb}$ model at $10\text{ }^{\circ}\text{C}$	190
B.4	Solution values for $L - R - RC - RC - Z_{wb}$ model at $25\text{ }^{\circ}\text{C}$	190
B.5	Solution values for $L - R - RC - RC - Z_{wb}$ model at $40\text{ }^{\circ}\text{C}$	191
C.1	Solution values for $L - R - ZARC - Z_{wb}$ model at $-10\text{ }^{\circ}\text{C}$	193
C.2	Solution values for $L - R - ZARC - Z_{wb}$ model at $0\text{ }^{\circ}\text{C}$	194
C.3	Solution values for $L - R - ZARC - Z_{wb}$ model at $10\text{ }^{\circ}\text{C}$	195
C.4	Solution values for $L - R - ZARC - Z_{wb}$ model at $25\text{ }^{\circ}\text{C}$	196
C.5	Solution values for $L - R - ZARC - Z_{wb}$ model at $40\text{ }^{\circ}\text{C}$	197

Abbreviations

BMS	battery management system 26, 36, 157, 168
CC	constant current 83, 85, 90, 95, 96, 109, 147
CPE	constant phase element 119, 122, 164
CV	constant voltage 83, 85, 89, 90, 95, 109, 147
DOD	depth of discharge 24, 70
DUT	device under test 59, 60, 62–64, 77, 78
EIS	electrochemical impedance spectroscopy iv, 9, 27, 30, 38, 49, 51, 53, 54, 57, 58, 81, 106, 107, 109, 117, 119, 124, 127, 158, 162, 167, 171, 172
EPA	Environmental Protection Agency 144
EV	electric vehicle 5, 10, 12–15, 18, 26, 36, 47, 49, 71, 157, 170
GHG	greenhouse gas 2
HEV	hybrid electric vehicle 5, 13, 170
HPPC	hybrid pulse power characterization 44, 53, 56, 95, 98, 106, 111
ICE	internal combustion engine 1, 2, 11–15
OCV	open-circuit voltage 22, 24, 41, 42, 47, 89, 90, 92, 94, 116, 150, 171

PC personal computer 54, 67, 77, 78
PDE partial differential equation 36

RMSE root mean square error 137, 140–143, 150, 151, 156–
159, 162, 164, 167, 168, 171, 172
ROM reduced order model 36

SOC state of charge iii, 18–20, 22, 24, 26, 31, 34, 37, 39, 41,
42, 44, 80, 89, 90, 92, 94–96, 98, 106, 107, 109, 111,
113, 114, 116, 128–133, 140, 142, 147, 150, 159, 162,
167, 171, 173, 188, 192
SOH state of health 6

TMU temperature monitoring unit 62, 67, 77, 170

Chapter 1

Introduction

For over 100 years, combustion and the use of fossil fuels have been the driving force behind many essential facets of everyday life all around the world. Among the many different applications of this kind, the [internal combustion engine \(ICE\)](#) has been prevalent because of its prominence in transporting people and goods to every corner of the globe. ICEs are dominant in private transportation, public transit and aviation due to their relatively low cost and the high energy density of fuel. However, the by-products of ICEs and their negative impact on the environment have become a large catalyst in the search for more sustainable energy sources and the need to electrify transportation.

To date, ICEs have been the preferred mechanism in transportation because of the advantages they provide over battery-electric alternatives: their performance, lower cost and convenience. The forms of energy they use, such as gasoline and diesel, are more practical because they provide a much higher energy density by weight and volume. For example, diesel has a specific energy density (measured in watt-hours per kilogram) that is approximately 100 times greater than that of a lithium-ion battery [1]. Furthermore, these

energy sources can be made available more quickly and accessed more conveniently. It typically takes only a few minutes to completely fill a tank of gas in a conventional vehicle, whereas it can take anywhere between one to 12 hours to charge a Tesla depending on the type of charging station used and the size of the battery [2]. In addition, the infrastructure needed to charge electric vehicles is costly and less widespread than what is needed to fuel a vehicle powered by an ICE. These factors make conventional vehicles more attractive to consumers because they are more affordable and can provide better range than the electric alternatives currently available. All of these challenges facing the electrification of transportation are compounded as size, cost and weight increase (i.e. in public transit, transport trucks and airplanes).

However, despite all of the advantages provided by ICEs, the burning of fossil fuels is accompanied by hazardous consequences, primarily air pollution that is emitted during the operation of a vehicle as well as during the production of fuel. One of the main emissions produced by ICEs is carbon dioxide (CO_2), a [greenhouse gas \(GHG\)](#) that traps heat inside the Earth's atmosphere and directly contributes to climate change [3]. Nitrogen oxides (NO_x) are other by-products of combustion, which contribute to acid rain and smog [4]. The transportation and oil and gas sectors have historically been the largest contributors of GHGs in Canada as depicted in Figure 1.1, accounting for over 50% of all CO_2 emissions in 2016 [5]. Furthermore, global CO_2 emissions have increased by approximately 90% since 1970, with fossil fuel combustion and industrial processes contributing roughly 78% of this increase between 1970 and 2011 [6]. These emissions have contributed significantly to the rise of the Earth's average surface temperature by 0.9°C , mostly over the past 35 years [7], and scientists have predicted that a 2°C increase could cause irreversible damage to the

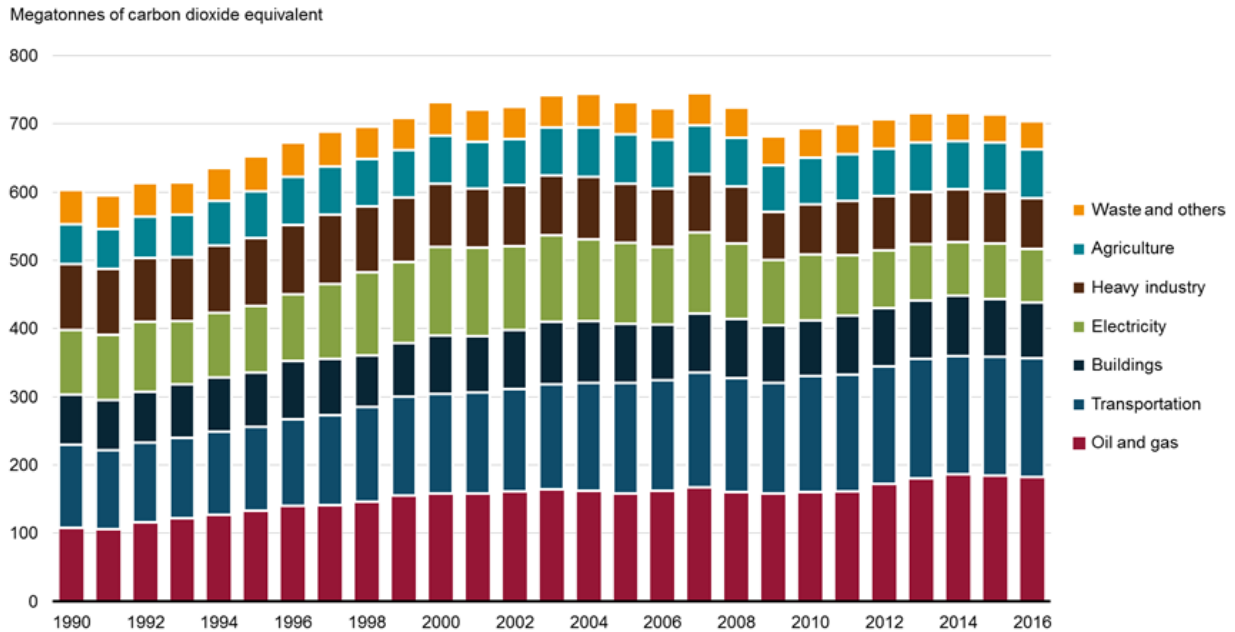


Figure 1.1: Greenhouse gas emissions by economic sector, Canada, 1990 to 2016 [5]

planet [8]. This global temperature rise is gradually leading to more catastrophic climate change including shrinking ice sheets, rising sea levels and more extreme weather events [7]. All of these effects will result in economic, social and physical changes that threaten the future of all life on Earth.

Consequently, these negative effects are driving the need for electrified transportation more than ever before. While this is slowly becoming more feasible in urban private transportation with electric and hybrid electric vehicles, there are other important applications that can also contribute to this shift including public transportation, freight trucks and airplanes. An integral component of electrifying transportation is using batteries to store energy and improving their performance and range to match the technology that is already available today. To achieve this, there are many important considerations and challenges

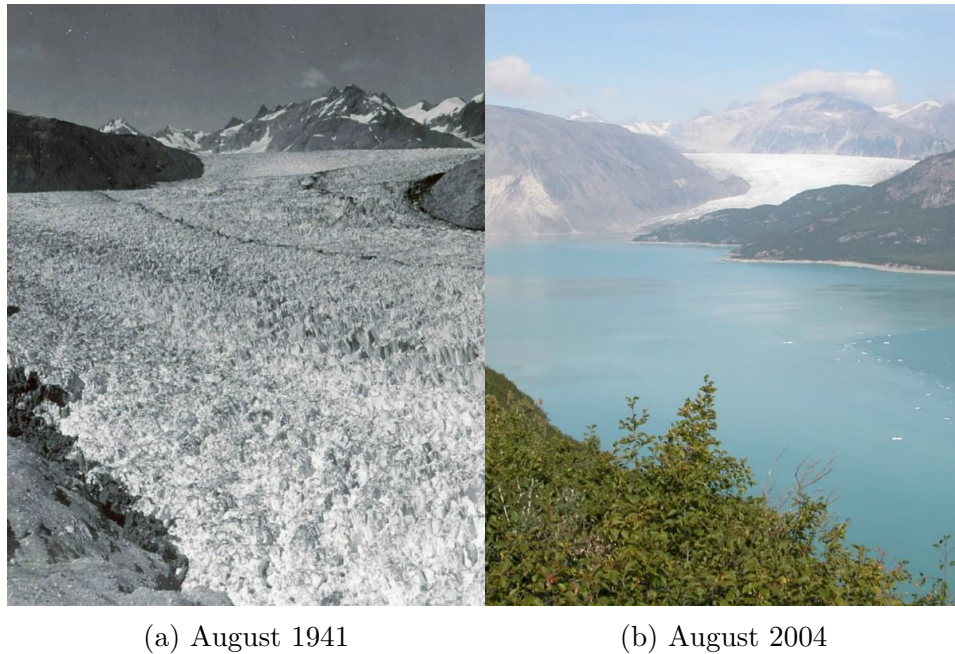


Figure 1.2: Significant thinning at Alaska's Muir Glacier, 63 years apart [8]

such as cost, weight, size and the useful life of a battery.

This research will investigate various factors that influence the performance of batteries, through extensive use and under different operating conditions. Studying these areas will help reveal important information regarding a battery's health and how it can be used to predict performance in numerous applications. It will also help by looking into key areas that can make it easier to predict the health of a battery. Clean transportation is a fundamental challenge in today's world, and it presents an excellent opportunity to move towards a more sustainable future by reducing emissions and relying on renewable energy sources. The motivation behind this research is to help advance the study of battery technology, in hopes of furthering the electrification of transportation.

1.1 Project Description

A major focus of battery research is testing and characterizing different systems, which can entail precise and highly specialized equipment. In some cases, testing procedures can be very time consuming and involve intricate planning to be able to obtain the best results possible. Due to the growing complexity of battery systems that are used in transportation, these tests require more resources and higher costs as they become more involved. As such, battery testing is an important consideration for major automobile manufacturers.

This research project is comprised of two concurrent segments: improving the functionality of an integrated battery cell testing unit through software development, while collecting data that can be used to analyze and characterize the impedance of a cell. The battery cell tester is being developed by a team of power electronics designers, software developers and research engineers at D&V Electronics Ltd. in Woodbridge, Ontario, Canada. D&V Electronics is a worldwide leader in the design and manufacturing of testing systems that are used globally in the automotive industry. As the electrified transportation market continues to grow, D&V Electronics has expanded its lineup of technologies and applications geared towards [electric vehicles \(EVs\)](#) and [hybrid electric vehicles \(HEVs\)](#), including solutions to test electric motors, inverters and batteries.

Among the different battery testing solutions that D&V offers is an integrated, cutting edge battery cell tester that is designed to provide precise measurements and more reliable battery health estimates. This test system also aims to alleviate the challenges faced by manufacturers during battery testing by helping them reduce costs, time and resources. A portion of this thesis will be dedicated to giving an overview of the D&V tester's design

and operation. Through the continued software and functional development of the tester, extensive testing will be conducted to gather data. This data will be used to demonstrate the capabilities of the tester, and to present a study on the impedance characterization of a cell.

1.2 Thesis Objectives

The objective of this thesis is to provide a comprehensive study of battery performance under various operating conditions through the analysis of impedance characterization. To achieve this, data will be collected and fitted to an impedance model that can be used to predict a battery's [state of health \(SOH\)](#) and behaviour in future applications. Furthermore, the objective of this thesis is to continue the development of a unique battery cell tester by validating its capabilities and refining its functionality. The outcomes of this research are as follows:

- To validate the operational features and safety protections of the battery cell tester
- To run extensive tests that mimic industry practices in order to characterize a cell
- To correlate cell data to an impedance model using measurements collected at various operating conditions
- To generate an understanding of how changes in impedance affect the performance of a battery in different environments

1.3 Thesis Outline

This thesis is organized as follows:

- **Chapter One:** The motivation behind the research and its importance is introduced, as well as the main objectives and expected outcomes. A brief project description is provided and the structure of the thesis is laid out.
- **Chapter Two:** A thorough review of the concepts and background knowledge that are necessary to make the research work easier to comprehend is provided. This will include topics such as electric vehicle energy storage systems, general terminology related to battery testing, various battery performance indicators as well as battery modelling techniques. This chapter will also review test strategies and procedures that are commonly used, both in industry and academia.
- **Chapter Three:** An overview of the battery cell tester under development is shown, including the general operation and design objectives. A comparison is made with existing testing solutions to showcase the significance of the tester. The experimental setup is described, highlighting the safety mechanisms and remote testing capabilities that make testing more reliable and efficient.
- **Chapter Four:** An outline of the tests relevant to the research, as well as their specific procedures, is given. A number of standard characterization tests are performed and the results are analyzed for a range of operating conditions.
- **Chapter Five:** An impedance model is chosen to fit the experimental spectral data, and the model parameters are optimized. The performance of the model is examined

and a comparison is carried out to demonstrate how the performance differs under various operating conditions. The accuracy of the model is validated experimentally using temporal drive cycle data.

- **Chapter Six:** A summary of the research and results is given, including obstacles and setbacks. Recommendations for future research work and areas of improvement are made.

Chapter 2

Energy Storage in Electrified Vehicles

As the electrification of transportation continues to advance, and the market for portable electronics continues to grow, there is an increasing demand for inexpensive, dependable and environmentally sustainable energy sources. There are certain criteria which are particularly important in the automotive industry and are heavily considered when examining various energy storage alternatives. These include energy density, weight, cost and safe operation. There are also different procedures and approaches that are used to test and characterize batteries for specific applications.

This chapter will provide an overview of the concepts and background information that are required to make the research work easier to understand. It will first provide a look at the history of electrification in transportation, as well as the current position of electric vehicles in the context of energy storage alternatives. Furthermore, basic battery terminology and definitions used throughout the thesis will be explained. An introduction to [electrochemical impedance spectroscopy \(EIS\)](#) testing, which is used in the research to analyze and characterize the impedance of a battery, is presented. Additionally, this

chapter will discuss and compare various battery modelling techniques. Lastly, different battery testing methods used in industry and replicated in the research are discussed.

2.1 Background on Electric Vehicles

As mentioned in Chapter 1, the vast majority of urban and private transportation currently relies heavily on the use of fossil fuels. This dependence on non-renewable energy sources is gradually leading to severe economic, social and environmental changes that could have catastrophic results for life on Earth. Furthermore, natural resources are being consumed at a rate higher than they are produced, which is unsustainable. Therefore, a shift towards renewable energy sources is desperately needed. Not only are these energy sources applicable to the transportation industry (automotive, aerospace, military, etc.), but they are widely used in everyday consumer goods including portable electronics and home appliances. This section will provide a historical review of electrified transportation as well as a summary of different energy storage devices that are being considered for use in EVs today.

2.1.1 History of Transportation Electrification

The concept of electrified transportation can be traced back hundreds of years to the early beginnings of the battery itself. There are many researchers who made crucial discoveries that would eventually lead to the development of electric motors and generators, both of which are essential components in electric vehicles. Primary examples include Alessandro

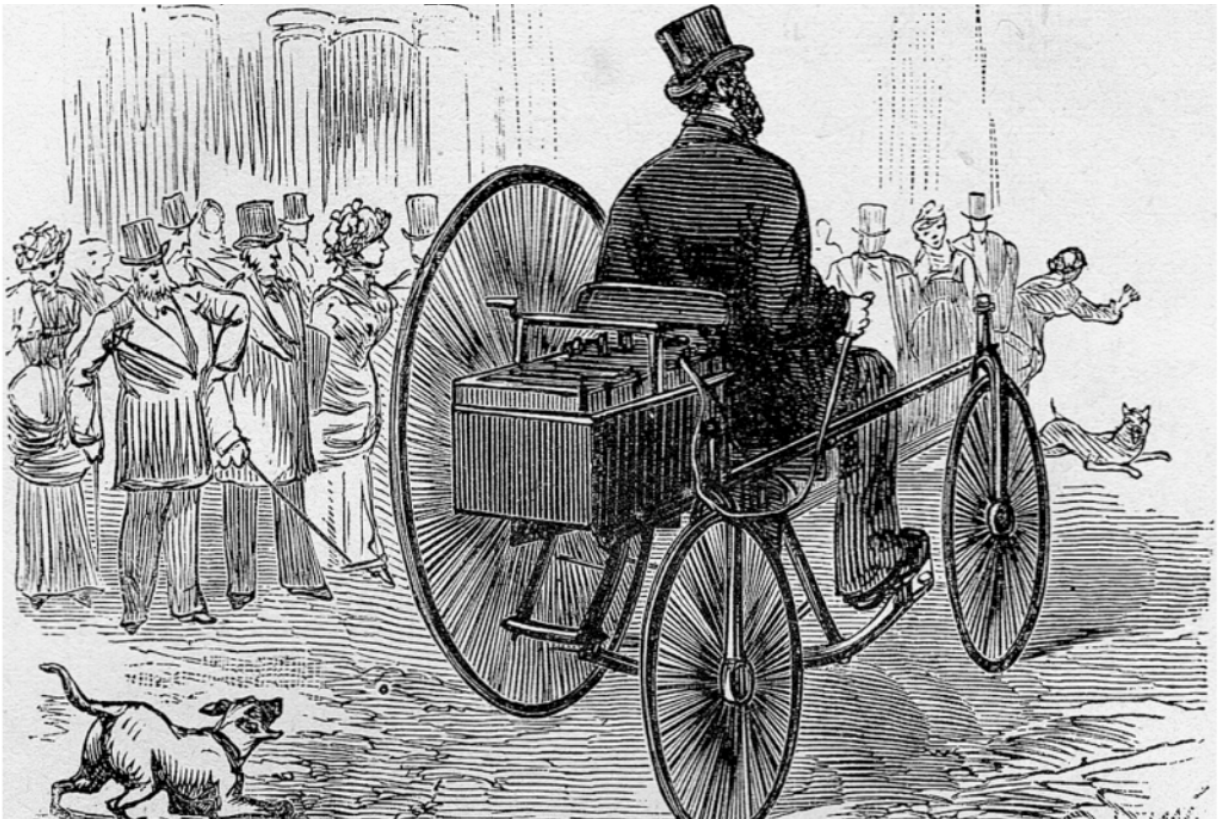


Figure 2.1: Gustave Trouvé's tricycle in 1881 [10]

Volta who demonstrated in 1800 that electrical energy could be stored chemically [9]. Later on in 1821, Michael Faraday showcased key results pertaining to electric motors and electromagnetic induction [9]. In 1859, Gaston Planté helped catalyze the development of lead-acid batteries, which are still used today in conventional ICE vehicles as well electric vehicles. This led the way for the further development of different battery chemistries.

The earliest example of an electric vehicle was a tricycle developed by Gustave Trouvé in 1881, which utilized the lead batteries developed by Planté [10]. A ground breaking advancement was discovered by Thomas Edison in 1901 with the development of a nickel-

iron battery, which was able to store 40 % more energy per weight than a lead acid battery. However, the cost of production for this battery was too high, which limited its adoption.

The period between 1880 and the early 1920s produced the most advancement for electrified transportation as a result of numerous breakthroughs. A network of coin-operated mechanisms was setup in New York around 1900 to allow users to charge their vehicles and obtain more range for city driving [9]. By 1903, EVs made up 20 % of the 4,000 registered vehicles in New York, and between 1899-1909 EVs outsold steam-powered and gasoline ICE vehicles in the United States [9]. Furthermore, the concept of regenerative braking was introduced around 1887, allowing users to increase range up to 40 % [9]. Another important development was the introduction of an electric-gasoline hybrid vehicle by Ferdinand Porsche, which provided noiseless and efficient driving to users in city areas without limiting the range of the vehicle. At the time, this concept proved too costly and was not considered again until the early 1970s [11].

The start of World War I saw an increase in the popularity of EVs for a few reasons. Most gasoline vehicles were deployed as part of the war effort, leaving few alternatives for civilian use. There was also a shortage of gasoline during war time. Furthermore, there was extensive development of electric power stations around the world, making this resource readily available for industrial use as well as transportation. This led to more widespread use of EVs, such as for street cleaning and garbage collection, as well as retail and goods deliveries. Although the potential for large-scale use was there, it did not take off, and production was stopped until World War II. However, when gasoline became an abundant commodity around 1952, automobile manufacturers focused more heavily on developing and producing ICE vehicles.

At the start of the 1960s, discussions began to take place regarding environmental pollution and sustainability, and ICEs were one of the major concerns that forced major automobile manufacturers to start considering EVs. A prototype built by the British Ford Motor Company in 1967, the Commuta, lacked any impressive performance figures and did not show enough potential for commercialization [9]. This was the first setback in a period of time that proved how difficult it was to develop an EV with adequate range, performance and at a low enough cost to be sold to the public. Several other historical events forced an increased focus on the need for alternative and renewable energy sources, namely the oil embargo imposed by major oil producers in the mid-1970s [9].

In the 1990s there were several national and international regulatory acts introduced to control global emission levels, such as the Kyoto Protocol. However, there were still setbacks faced by manufacturers to achieve performance goals, with some choosing to focus on further developing ICE vehicles in an effort to make them more efficient. This period later saw the introduction of the first commercially successful HEV in 1997, the Toyota Prius, which was followed by the Honda Insight in 2003 and the Ford Escape Hybrid in 2004 [9]. To date, there have been many more models and EV configurations produced by major manufacturers.

While EVs have arguably become more widespread, there are still many questions surrounding their environmental impact as well as their economic feasibility. One such question is the source of electricity used to power them; if it comes from ordinary sources such as fossil fuels then the environmental gains of EVs are diminished. Furthermore, environmental conditions such as extremely cold weather greatly impact the performance of EVs, making them less practical in certain geographical regions. Their limited range

and the time associated with recharging also make them impractical in specific cases where a high driving mileage is involved. Lastly, the upfront cost for EVs makes them much less appealing for consumers. For example, the base price for a 2019 Nissan Leaf in Canada is \$42,298 versus \$17,890 for a Honda Civic that is comparable in size [12, 13]. Therefore, the development of a low cost energy source that provides comparable performance and range to an ICE vehicle, as well as quick recharging times, is of paramount importance to the automotive industry.

2.1.2 Energy Storage Alternatives

There are various energy candidates under study that can be considered for automotive applications. These devices must be able to provide enough peak power to operate a vehicle and a high energy density to maximize range. A summary of some of these devices is provided below [9, 14, 15]:

- Lead-Acid batteries: This battery chemistry is one of the oldest but most widely used options today, both in conventional and electric vehicles. It is used as a starter for ICEs and as a power source for EVs. It is highly reliable with a relatively low cost. However, it does not have a high energy density or long cycle life relative to other battery chemistries which makes it impractical for automotive energy storage applications.
- Ultra-Capacitors: These devices contain a very high power density but a much lower energy density when compared to batteries. There is increasing research focusing on creating a hybrid energy storage device that utilizes batteries with ultra-capacitors.

- Fuel Cells: Contrary to ultra-capacitors, fuel cells contain a high energy density, but require a long time to be charged and are very expensive.
- Lithium-Ion batteries: Lithium-Ion batteries provide an energy density, power density and cycle life that make them more advantageous over other battery chemistries. Today, they are widely used in EVs as well as consumer electronics.

Figure 2.2 provides a visual representation of the performance characteristics of some of the aforementioned energy storage devices. The sloped lines indicate how much time is required to add or remove energy from each device [15]. It can be seen from this comparison that ICEs still provide a higher energy and power density relative to batteries and fuel cells. Presently, lithium-ion batteries are the most feasible alternative because they provide a good compromise between energy and power density. As such, there is a great amount of research and investment focused on their development and improving their performance, safety and reliability, especially for automotive applications. For this reason, the research carried out in this thesis will be using a lithium-ion battery. A brief overview of the general operation of lithium-ion batteries is provided in the next section.

2.1.2.1 Lithium-Ion Batteries

The fundamental objective of a battery is converting stored chemical energy into electrical energy (under load) and vice versa (when recharging). A lithium-ion battery is generally comprised of three key components: a positive electrode, a negative electrode and a material that acts as a separator [16]. The two electrodes, an anode and a cathode,

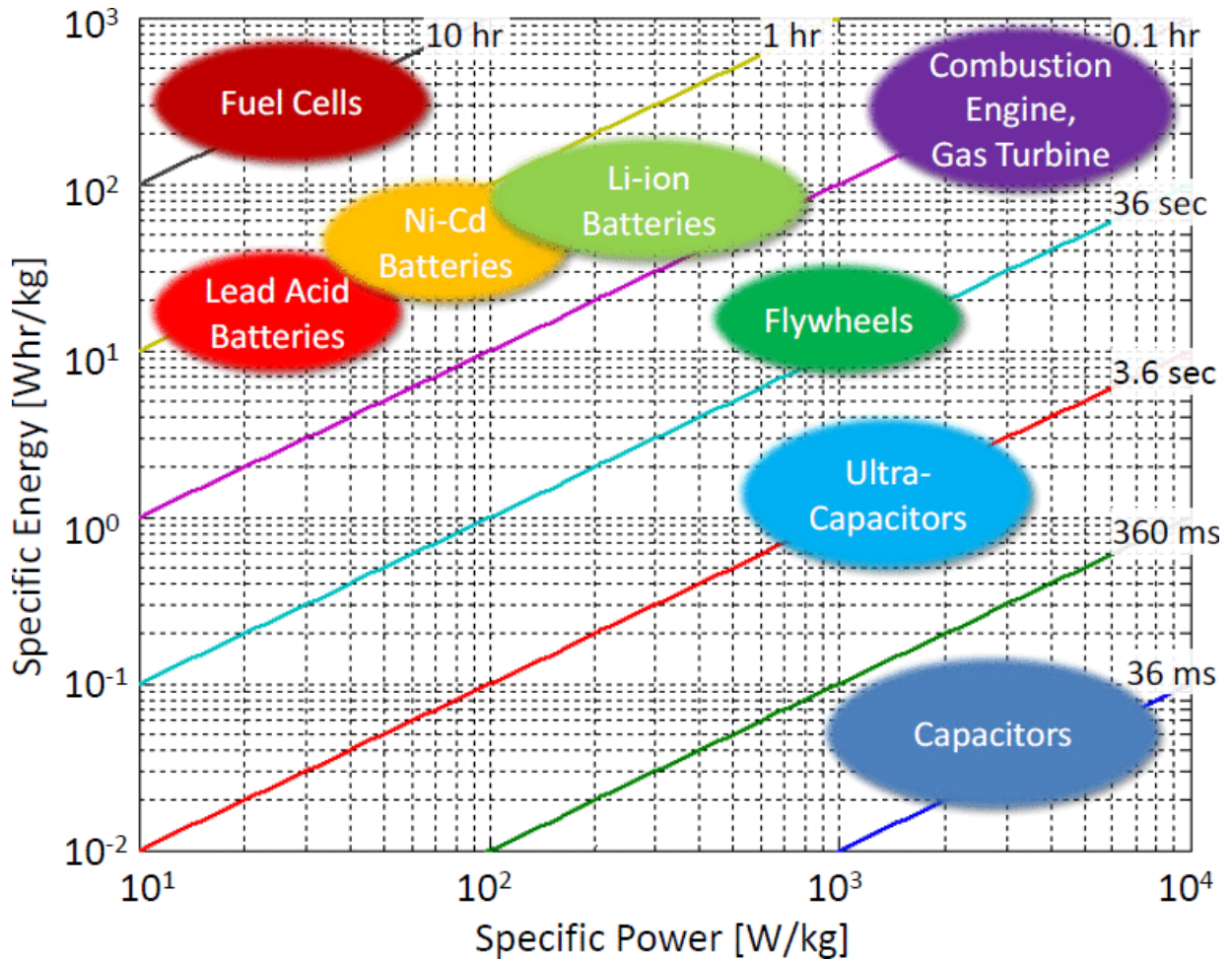


Figure 2.2: Power and energy density comparison for various energy storage devices [15]

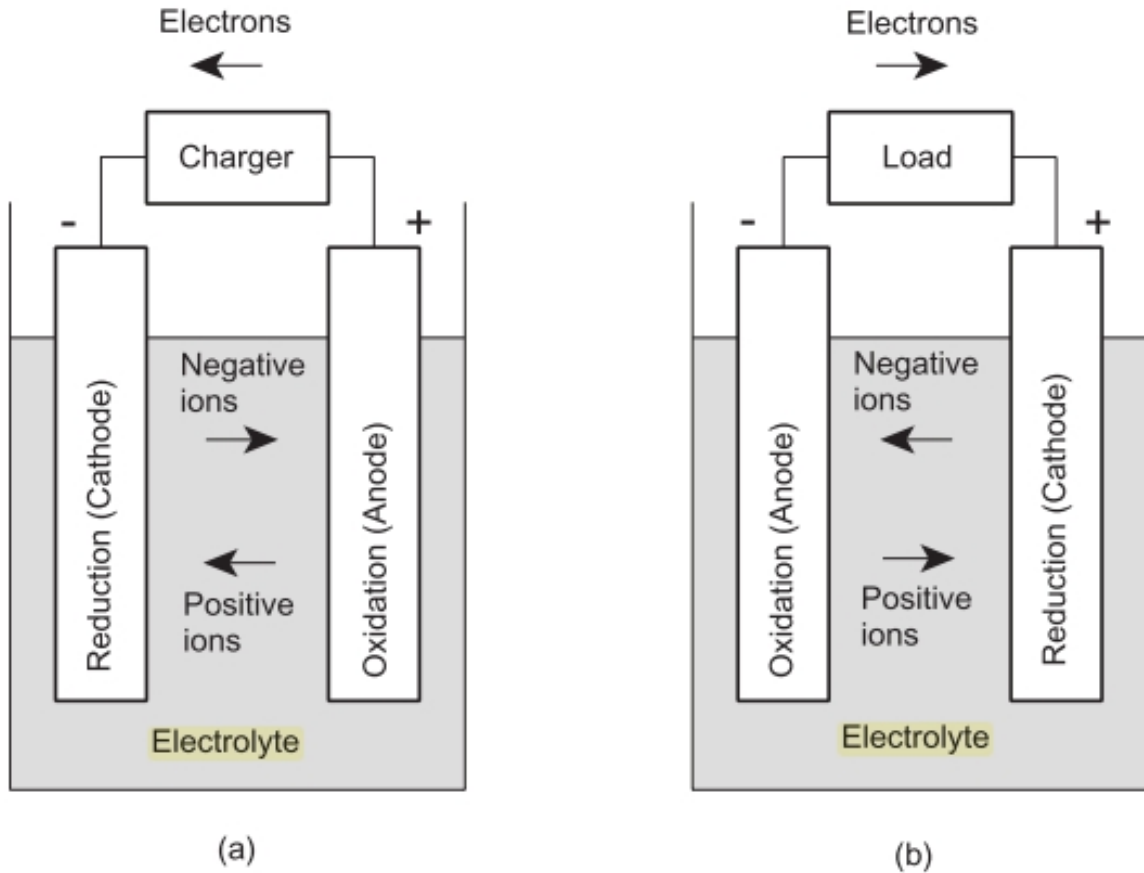


Figure 2.3: General overview of the electrochemical processes involved in charging (a) and discharging (b) a battery [16]

are connected to an external load using current collecting plates which enable the flow of electrons for charging and discharging.

All three components are immersed in an electrolyte solution which facilitates the transfer of ions. A visual representation of the general operating principle of a battery is shown in Figure 2.3. The separating material plays an important role in the process because it acts as a barrier between the electrodes and prevents the battery from short-circuiting [14].

One of the current limitations of batteries is that this process becomes less efficient with extended use and aging, due to material degradation and irreversible side reactions, which diminishes the capacity of the battery and its power capabilities [14].

2.2 Overview of Terminology and Definitions

This section provides definitions for terminology used to describe battery parameters and characteristics, as well as terms that apply to the scope of the research.

State of Charge: A battery's *state of charge (SOC)* is an indication of its remaining capacity relative to its maximum capacity, expressed as a percentage [17]. This can be thought of as analogous to a fuel gauge in a conventional vehicle. The SOC level of a battery, from fully charged, can be calculated as follows:

$$\text{SOC Level (\%)} = \left(1 - \frac{\text{Accumulated Discharge (A h)}}{\text{Rated Capacity (A h)}}\right) \times 100 \quad (2.1)$$

For example, using Equation (2.1), discharging 2.45 A h from a fully charged 4.9 A h battery would result in an SOC level of 50%. SOC is a critical component that is used to operate the battery safely and reliably in EVs, as well as to determine the driving range available for the user operating the vehicle. In a conventional vehicle, remaining fuel levels can be measured directly using a fuel gauge. However, due to the nature of batteries, measuring SOC is challenging because it is affected by many conditions including temperature, aging, current rates and measurement error [18]. Therefore, SOC levels cannot be measured

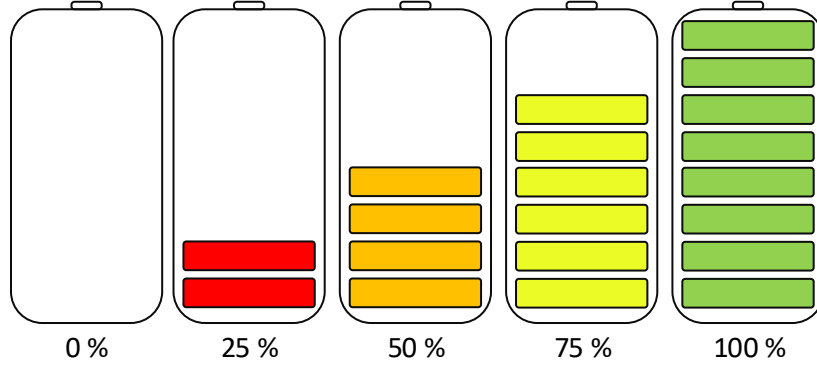


Figure 2.4: Battery state of charge depicted as a gauge reading

directly, and must be estimated using specific techniques and/or algorithms.

A commonly used method for estimating SOC is coulomb counting, which is also known as current integration. Using this technique, the discharging current of a battery is measured and integrated over time, to give an estimate of SOC [19]. If an initial SOC value is known to the user, then coulomb counting can be applied using Equation (2.2) [14]:

$$SOC = SOC_0 - \frac{1}{C_n} \int_{t_0}^t I dt \quad (2.2)$$

where:

I = discharge current

SOC_0 = initial SOC value

C_n = cell capacity

While coulomb counting is a straightforward and reliable technique, there are practical issues that limit its accuracy [20]:

1. There are potential sensor offsets and measurement inaccuracies.
2. The integral operation will magnify any measurement errors present.
3. The total capacity of the battery will change with time and the charging/discharging efficiency will also change. Thus, these cannot be treated as constant for measuring all SOC levels.

These issues can be mitigated if current measurements are accurate and the battery's capacity can constantly be updated, although this can be challenging and costly [14]. There are several approaches discussed in literature which address these concerns, including adding recalibration points and defining a correction factor to account for current losses [21].

Charge Rate (C-rate): The term C-rate refers to the rate at which a battery is charged or discharged relative to its maximum capacity [22]. The C-rate can also be thought of as a numerical representation of the rated ampere-hour capacity of a battery. For example, discharging a battery at a rate of 1C means that the current will discharge the battery completely in one hour. Therefore, a battery with a capacity of 100 A h would have a 1C rate of 100 A. The same battery would have a 5C rate of 500 A ($100 \text{ A} \times 5$) and a C/2 rate of 50 A ($100 \text{ A} \div 2$). The number of hours required to charge or discharge a battery completely is relative to the C-rate:

$$\text{Discharge/Charge Time (h)} = \frac{1}{\text{C-rate}} \quad (2.3)$$

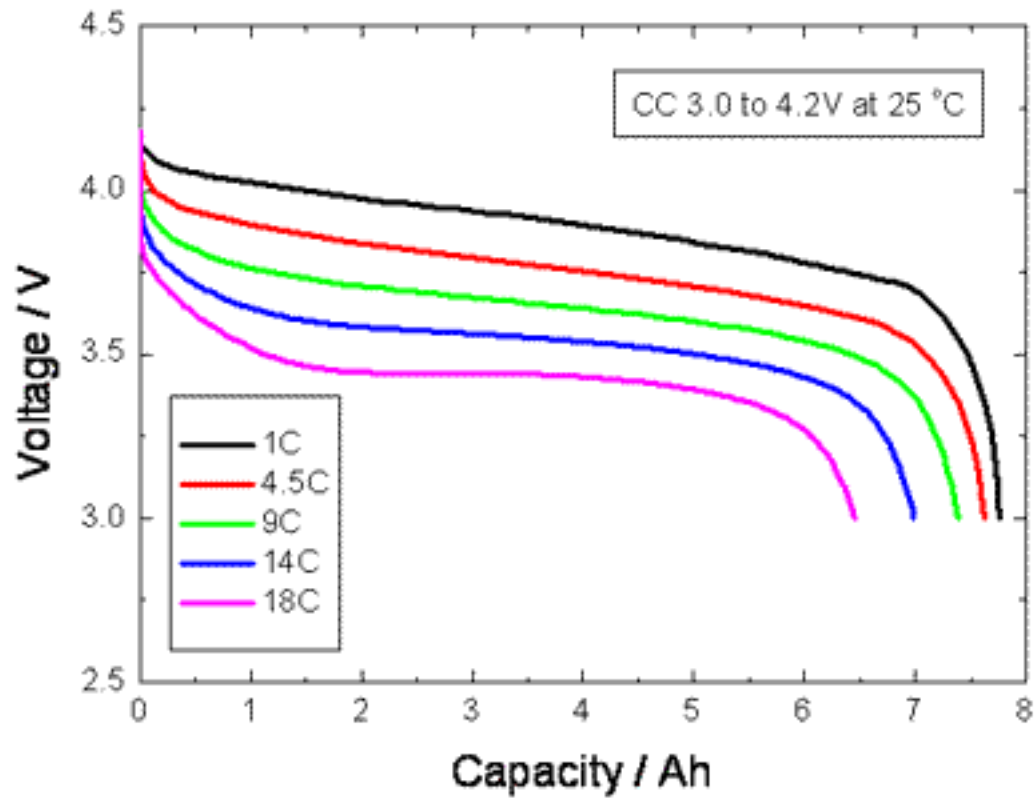


Figure 2.5: The effect on cell capacity as a result of discharging at various C-rates [23]

Using Equation (2.3), discharging/charging a cell at $5C$ and $C/2$ would take 0.2 and 2 hours, respectively.

Nominal Capacity: When discharging a battery at a specific C-rate from 100% SOC to the battery's cut-off voltage, the total Ah available is known as the nominal capacity of the battery [14]. The nominal capacity of a cell is reduced at higher C-rates, as demonstrated

in Figure 2.5, and is calculated as follows:

$$\text{Nominal Capacity (A h)} = \text{Discharge Current (A)} \times \text{Discharge Time (h)} \quad (2.4)$$

Terminal Voltage: The terminal voltage of a battery is the voltage between terminals with a load applied [24]. This value varies at different SOC levels and discharge/charge currents.

Open-Circuit Voltage: The [open-circuit voltage \(OCV\)](#) of a battery is the voltage between terminals without a load applied, which increases with SOC [24]. It has been shown in literature that an OCV-SOC relationship can be observed by measuring this value at different SOC levels [25]. For example, in Figure 2.6, at 50% SOC the open-circuit voltage is roughly 3.3 V.

To obtain this measurement, the battery must be allowed to rest at each SOC level for a period known as the relaxation time [25]. This allows the battery to gradually reach an equilibrium state, after which a new point on the OCV-SOC curve can be measured. Due to the nature of the OCV-SOC relationship, it is not widely used because it is a time consuming process, and therefore not practical for dynamic SOC estimation. Furthermore, as the battery ages, the OCV will change and thus the relationship does not remain consistent.

Cycle Life: A battery's cycle life refers to the number of times it can be charged and discharged (cycles) while still being able to meet minimum performance criteria, which is

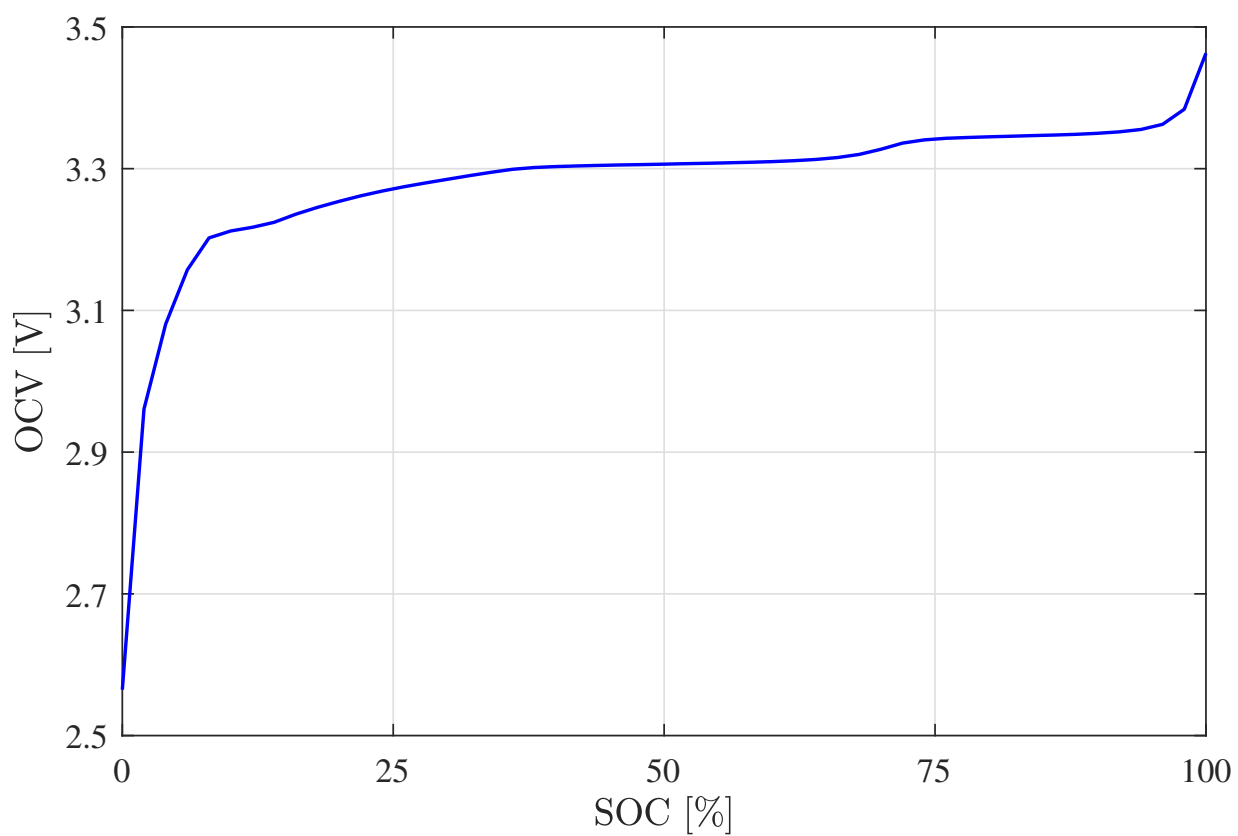


Figure 2.6: An example curve demonstrating the relationship between open-circuit voltage and state of charge

typically 80% of its initial capacity [23]. In general, cycle life is influenced by operating temperatures, different C-rates and the depth of discharge.

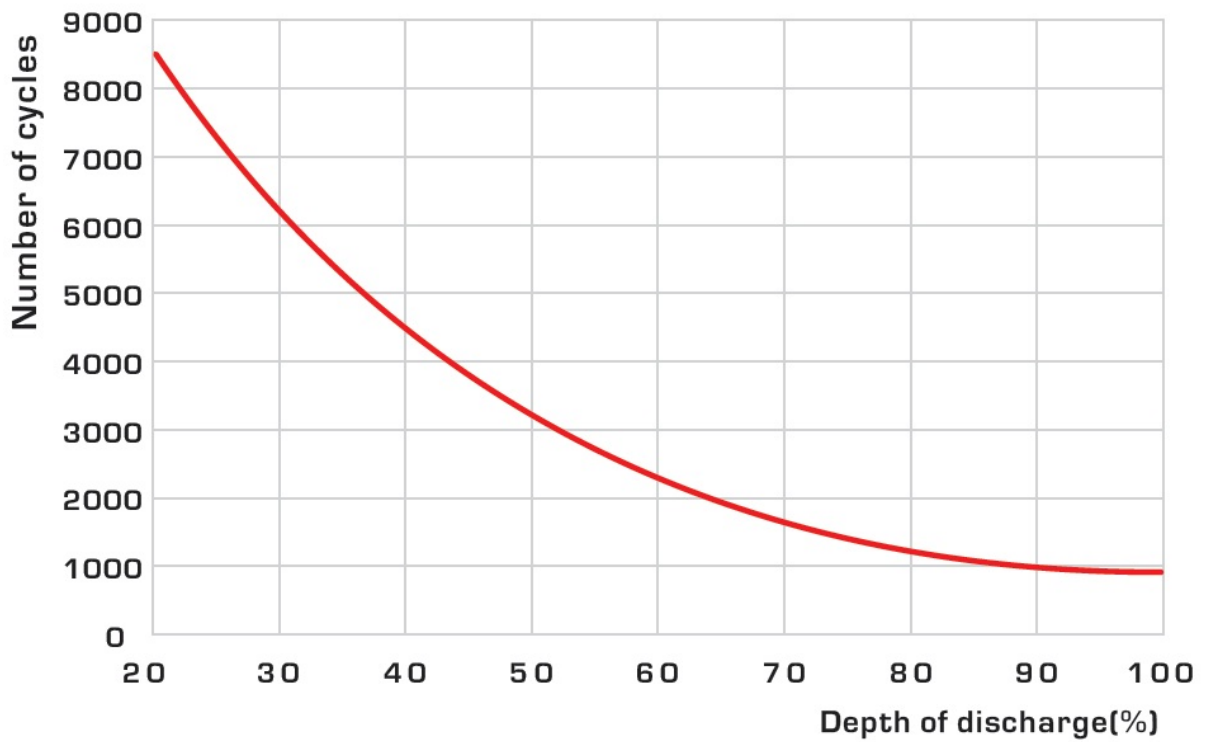
Depth of Discharge: The **depth of discharge (DOD)** refers to the percentage of a battery's maximum capacity that has been discharged [26]. This value can also be seen as an alternative way of expressing the battery's SOC level, as follows:

$$\text{Depth of Discharge (\%)} = 100 - \text{State of Charge (\%)} \quad (2.5)$$

The DOD of a battery is indicative of its health and is directly affected by the number of charge and discharge cycles performed. As a battery ages due to use or storage conditions, and as it is cycled more often, the amount of energy that can be cycled in and out of the battery decreases. Thus, a higher DOD indicates a newer battery with less cycles and vice versa, as demonstrated in Figure 2.7.

Internal Resistance: This value indicates the resistance within a battery, which is generally dependant on SOC as well as charging and discharging conditions. As the internal resistance rises, the efficiency of the battery is lowered [24].

Cut-off Voltage: This value refers to the minimum allowable voltage of a battery [24]. It is the voltage value specified at 0% SOC. In the OCV-SOC curve shown in Figure 2.6, the cut-off voltage is roughly 2.6 V.



Typical cycle life versus DOD(20°C)

Figure 2.7: Change in depth of discharge with increased cycling for a nickel-iron battery [27]

Battery Management Systems: A [battery management system \(BMS\)](#) is used on-board portable electronics and EVs to communicate important information between the battery pack and the device [14]. Typically, a BMS is responsible for critical tasks such as protecting the battery pack and making sure it is operating safely, thermal management, and SOC estimation.

2.3 Electrochemical Impedance Spectroscopy (EIS)

Electrical resistance, as defined by Ohm's law, represents the ability of a circuit element to resist current flow as defined in Equation (2.6):

$$R = \frac{V}{I} \quad (2.6)$$

where:

R = resistance

V = voltage

I = current

This relationship applies to an ideal resistor which is governed by the following assumptions [28]:

- Ohm's law is obeyed at all current and voltage levels
- Resistance is independent of frequency

- AC current and voltage through a resistor are in phase

However, impedance is more practical in real-world applications that exhibit more complex properties. While impedance is also a measure of the ability to resist current flow, similar to resistance, it is not limited to the aforementioned assumptions.

Electrochemical impedance spectroscopy (EIS) is a technique that is used to examine dynamic characteristics of a battery, which can reveal important information about its health. It can highlight information regarding the chemical processes that occur inside the battery and help identify where battery degradation is occurring, as well as how aging affects performance. EIS is measured by applying a small AC current or voltage excitation signal at a fixed frequency and analyzing the response of the battery [28]. There are two types of EIS tests that can be used:

1. Galvanostatic: A current signal is applied, and the voltage response is measured.
2. Potentiostatic: A voltage signal is applied, and the current response is measured.

The impedance is then calculated as follows [29]:

$$Z = \frac{v(t)}{i(t)} = \frac{V \cdot \sin(\omega t)}{I \cdot \cos(\omega t - \phi)} = |Z| \cdot \frac{\sin(\omega t)}{\cos(\omega t - \phi)} \quad (2.7)$$

where:

V = amplitude of voltage signal

I = amplitude of current signal

ω = angular frequency

ϕ = phase shift

$|Z|$ = absolute value of impedance

The impedance can be separated into real and imaginary components [29]:

$$\begin{aligned} Z_{real} &= |Z| \cdot \cos(\phi) \\ Z_{imaginary} &= |Z| \cdot \sin(\phi) \end{aligned} \tag{2.8}$$

It can be noted that in Equation (2.7), a phase shift of 0° resembles an ideal resistor as shown in Equation (2.6). This process is repeated for a range of frequencies (e.g. 10 kHz to 100 mHz) in order to generate an impedance plot. It is important to note that the amplitude of the excitation signal should be kept small in order to obtain a linear response from the battery [28].

A visual representation of measured impedance is shown in Figure 2.8. In this plot, each point on the impedance spectrum represents the impedance at a specific frequency, with higher frequencies on the left side and lower frequencies on the right side. The impedance can be represented as a vector $|Z|$ where the phase shift ϕ is the angle between this vector and the X-axis. Typically, the Y-axis in an impedance plot is negative. Although Nyquist plots are generally the first choice to present impedance data, they do not provide information on the frequency used to obtain the measured impedance points. This shortcoming can be overcome by representing the data with a Bode plot [29].

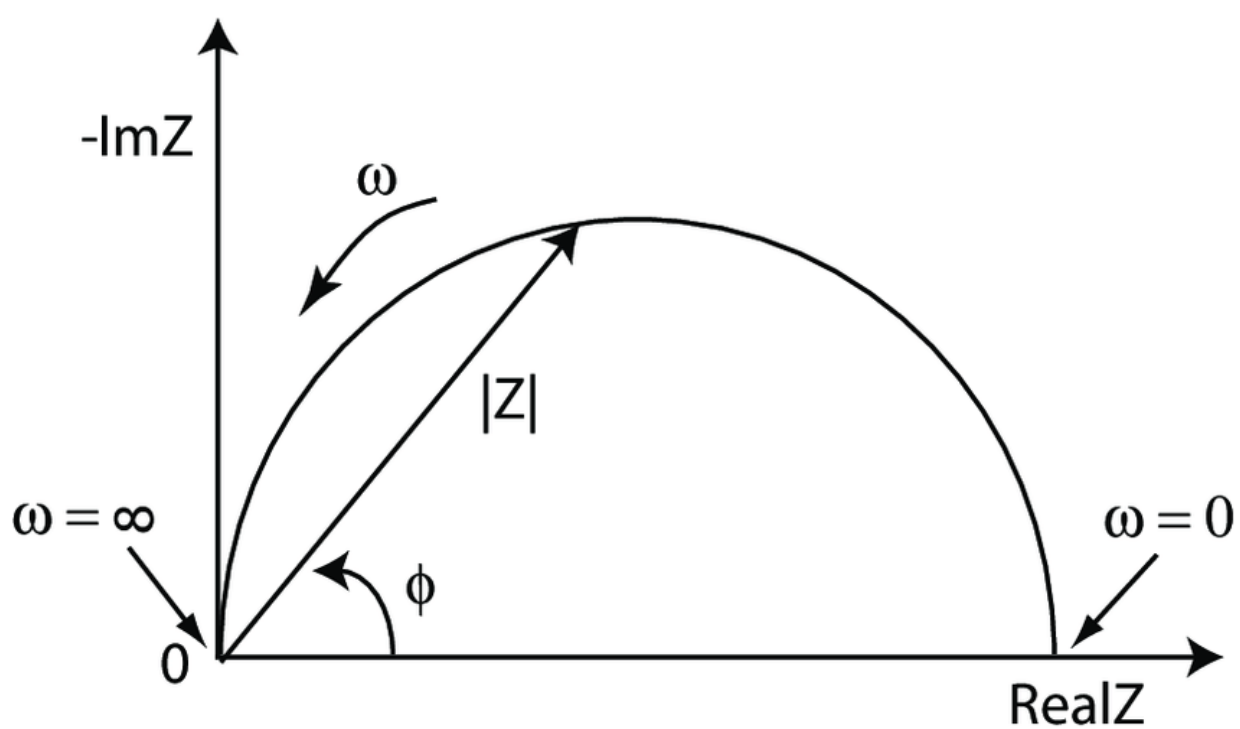


Figure 2.8: Nyquist plot with impedance vector [28]

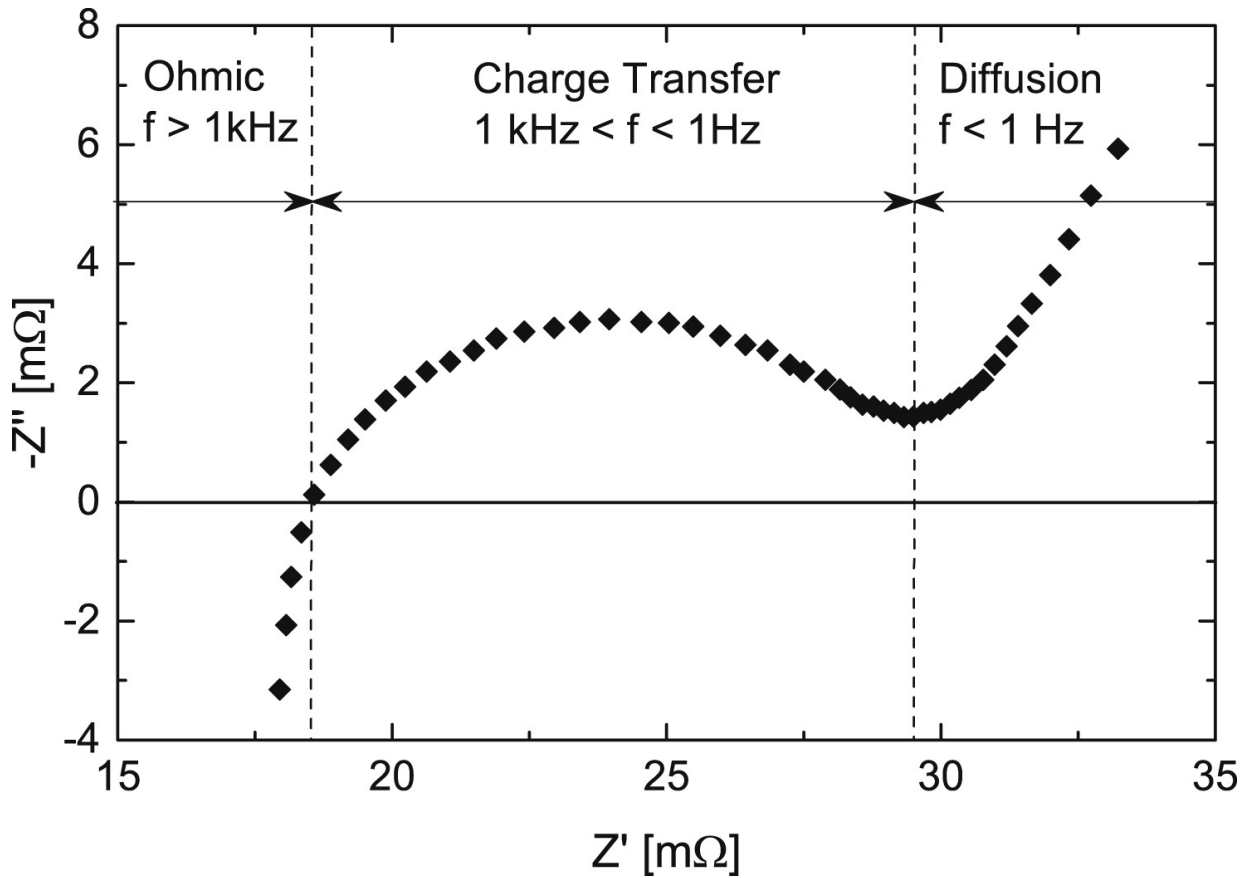


Figure 2.9: Sample impedance plot for a lithium-ion battery [30]

An EIS plot can help identify information on key processes that occur inside a battery. Some of these physical and chemical processes are highlighted in Figure 2.9 [30–32]:

- The high frequency behaviour (below the X-axis) represents the inductive behaviour of the battery.
- The intersection of the plot with the X-axis represents the ohmic resistance of the battery (i.e. pure resistance, without a phase shift).

- The semicircle in the mid-frequency region represents the charge transfer resistance of the battery. This impedance is mainly a result of kinetic reactions inside the battery in response to an imposed signal.
- The tail in the low-frequency region, also known as the Warburg impedance, represents the impedance as a result of diffusion of ions that occurs inside the battery.

These characteristics are altered under different operating conditions, such as SOC and temperature, as well as due to aging of a battery. For example, at higher SOC levels, there is a decrease in the semicircle representing charge transfer resistance, as observed in Figure 2.10. An example of the effect of battery aging on impedance is demonstrated in Figure 2.11. The aged battery is subjected to over 80,000 shallow cycles (roughly 1% Δ SOC swings) at 50 °C. In this plot, a few changes are observed [32]:

- A small increase in the ohmic resistance, as a result of side reactions consuming lithium from the electrolyte.
- A large growth in the charge transfer resistance as the battery's efficiency is lowered with age.
- A shift in the Warburg impedance tail as a result of the increased resistance.

2.4 Battery Modelling

As lithium-ion batteries become a more prevalent choice for portable energy in different applications, it is important to gather information about their performance and be able

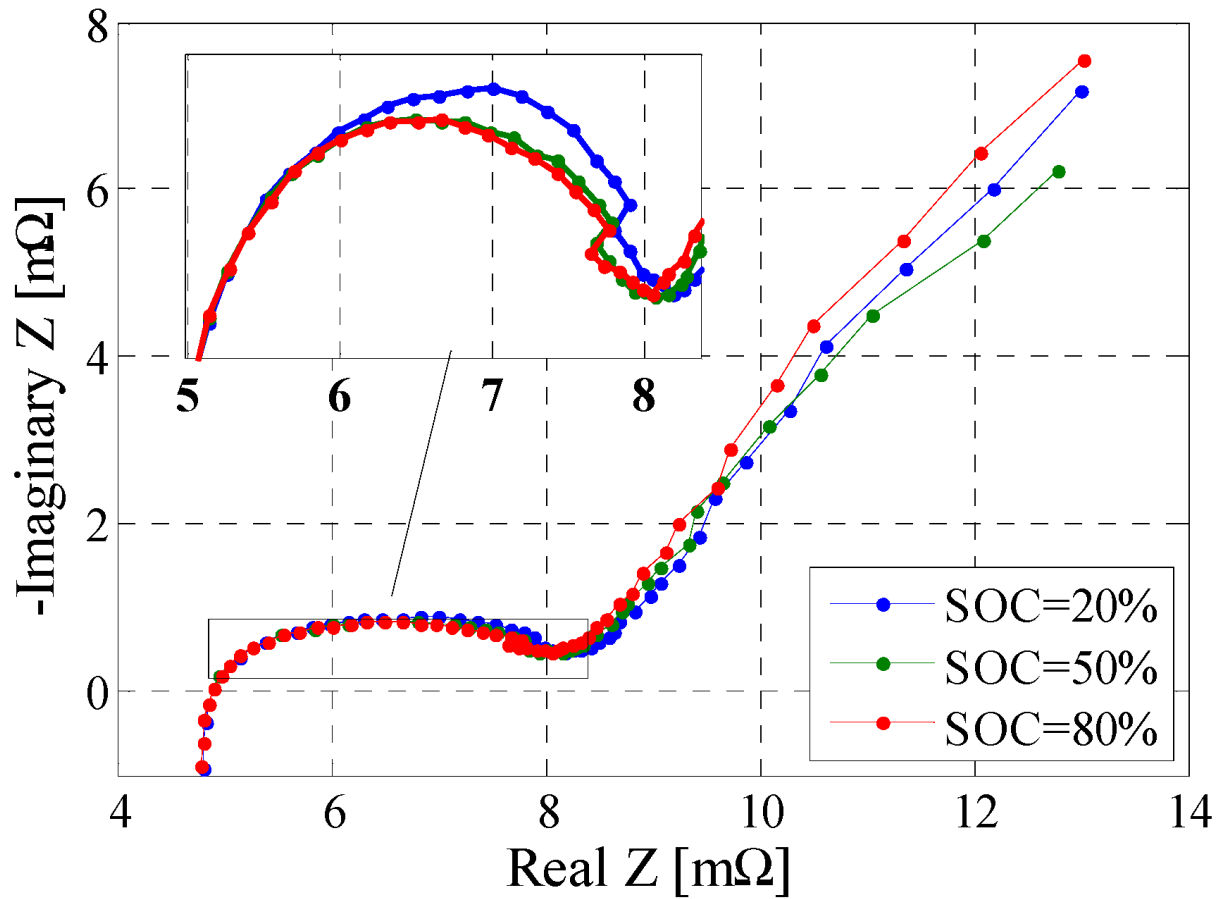


Figure 2.10: Change in impedance spectrum at different SOC levels; $T = 25\text{ }^{\circ}\text{C}$ [33]

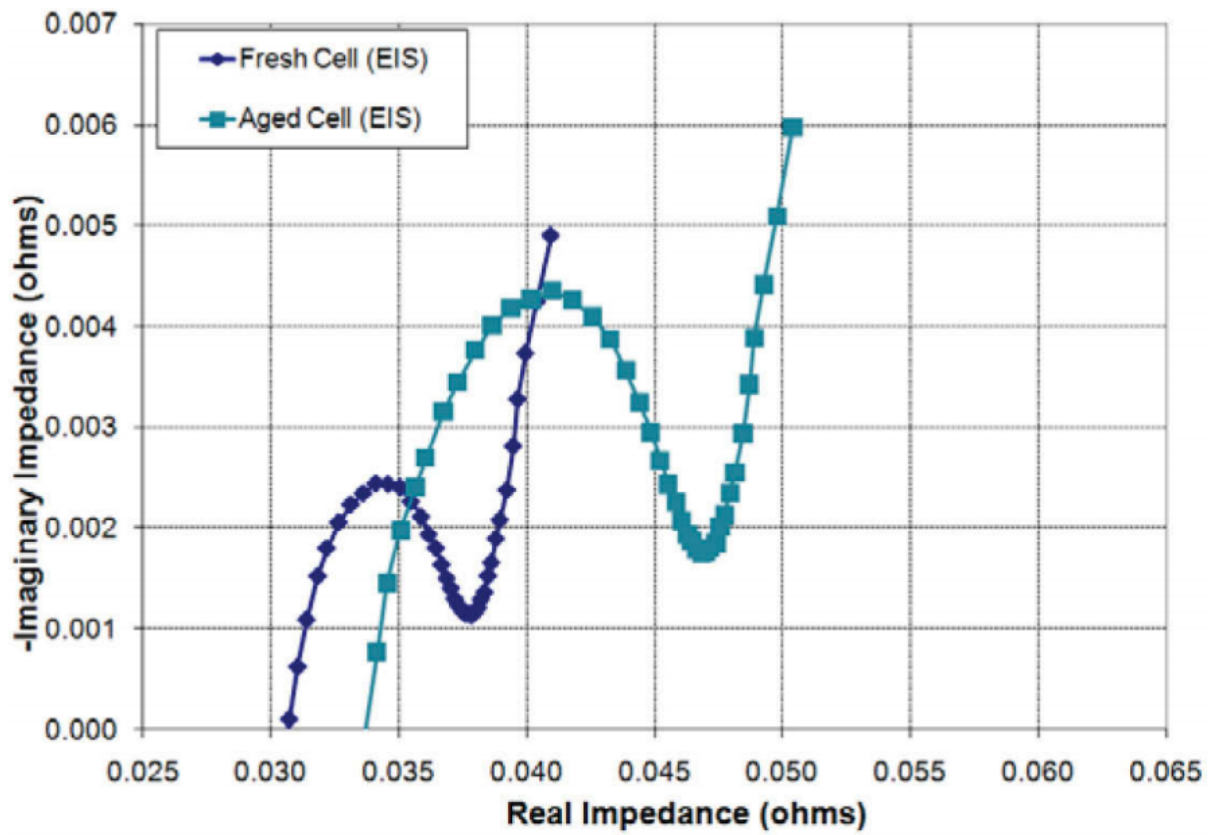


Figure 2.11: Impedance plot comparing a fresh cell to an aged cell [32]

to model said performance across a wide range of conditions. By utilizing precise models researchers can simulate a battery's behaviour and improve its design as well as optimize its performance [34]. Ultimately, this approach can give critical insight about the battery while reducing the cost and time involved in running experiments to achieve the same outcome. Therefore, it is necessary for a battery model to be able to accurately simulate performance parameters at various operating conditions including SOC, temperature and current loads.

There are a variety of battery modelling types and techniques that are proposed in literature, which differ depending on what the research purpose is [35–37]. Three of the most commonly used model types are mathematical models, electrochemical models and equivalent circuit models. Each of these model types varies in complexity and holds advantages and disadvantages compared to the others. This section will briefly discuss these model types and introduce the main differences between each one.

2.4.1 Mathematical Models

Mathematical models, which are also referred to as behavioural models, typically rely on empirical equations to simulate various battery parameters including terminal voltage [38]. As such, these models do not take into account the physical or electrochemical changes of a battery and depend instead on measured data [14]. Many of these models are derived from a theory introduced by Shepherd as follows [39]:

$$V_{bat} = E_0 - K\left(\frac{Q}{Q - it}\right)i - R_i \quad (2.9)$$

where:

V_{bat} = battery voltage

E_0 = open-circuit voltage of battery at full charge

K = cell capacity

Q = instantaneous stored charge

R = internal resistance

i = cell current

it = $\int i \cdot dt$

There are several modifications to this theory that have been introduced in literature which consider factors such as temperature and varying capacity values during charging and discharging [40–42]. While mathematical models have a relatively low computational complexity and their parametrization can be achieved through the datasheet of a battery alone, they do not provide adequate knowledge on the physical and chemical changes of a battery and their accuracy is very limited [34].

2.4.2 Electrochemical Models

Electrochemical models are used to demonstrate underlying physical and chemical changes in a battery, and can help identify processes and reactions that reduce the efficiency of a battery [43]. There are several electrochemical models proposed in literature that focus on different aspects involved in the operation of a battery. One such model in the work of Doyle *et al.* is centred on mass transport in the electrolyte and has demonstrated a high degree of accuracy [44, 45]. Another model, presented by Randall *et al.*, considers

the growth of the solid electrolyte interface [46]. Electrochemical models are advantageous because of their strong ability to model battery performance characteristics (such as voltage) as well as the underlying chemical properties (such as concentration gradients) [47]. However, this high degree of accuracy is compromised by the complexity of these models and the expensive computational resources needed to utilize them.

Due to their scope and nature, electrochemical models rely on **partial differential equations (PDEs)** which are complex and contain many parameters. This makes their parameterization a difficult process that often requires specialized equipment and high computational power [43]. Therefore, they are not a practical choice for real-time applications such as those in a BMS. There are many examples in literature of attempts to develop **reduced order models (ROMs)** that lessen the complexity of the calculations needed for an electrochemical model [48]. Although their adjustments are suitable for certain applications, they are not favourable candidates to model high charging and discharging input currents that are commonly encountered in EV applications.

2.4.3 Equivalent Circuit Models

Equivalent circuit models utilize electrical elements, such as resistors and capacitors, to simulate the behaviour of a battery [34]. Unlike electrochemical models which involve a large number of parameters, equivalent circuit models are simpler and easier to implement [37]. Therefore, equivalent circuit models are more favourable for real time applications, such as onboard a BMS.

Parameterization for equivalent circuit models is achieved using test data collected for

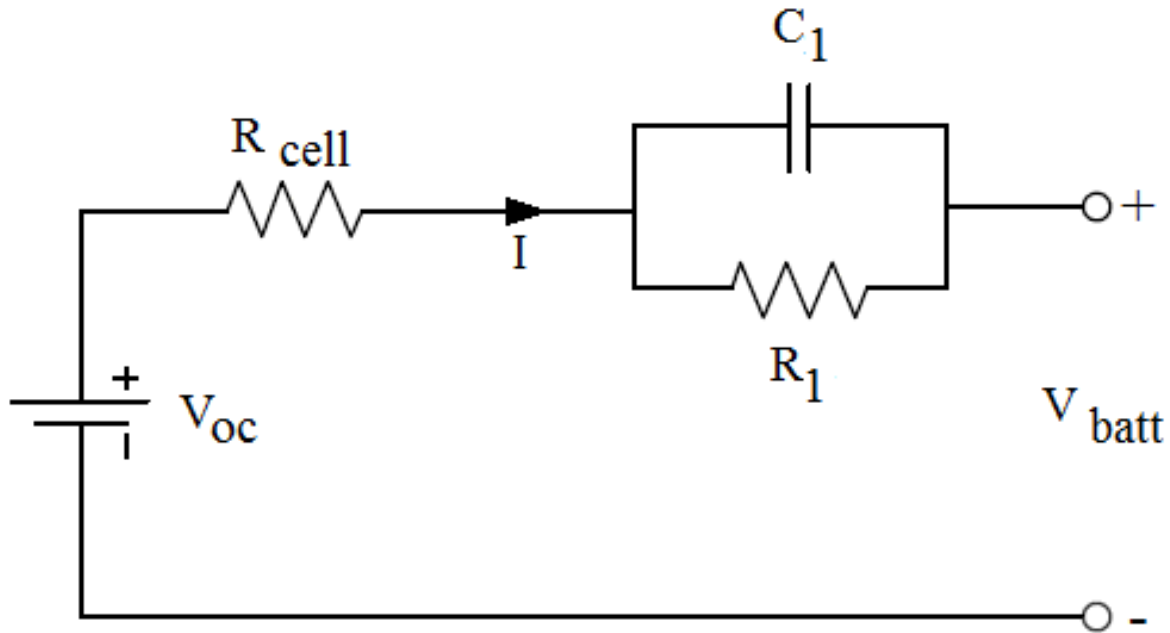


Figure 2.12: First-order RC equivalent circuit model diagram [49]

the battery being modelled. A simple example of an equivalent circuit model is presented in Figure 2.12. In this case, the model parameters are a function of SOC and temperature. Increasing the number of RC pairs (higher order models) can more accurately capture the dynamic behaviour of the battery, but adds more parameters that need to be identified. Some variations to equivalent circuit models have been presented in literature that consider physical and chemical changes in a battery, including the charge redistribution effect [50–52].

Table 2.1: Comparison of the various approaches that can be used to model the behaviour of a lithium-ion battery

Model Type	Accuracy	Computational Complexity	Physical Interpretability	Suitable Applications
Empirical	Reduced	Low	Low	Life time and efficiency prediction
Electrochemical	High	High	High	Battery design and performance optimization
Equivalent Circuit	Relatively high	Medium	Acceptable	Real-time monitoring and diagnosis

2.4.4 Comparison

Table 2.1 provides a summary of the important characteristics of each modelling type discussed in this section [53, 54]. Although electrochemical models relate more to the reactions within the battery, their parametrization is difficult and requires extensive laboratory testing using specialized equipment. Conversely, empirical models are not as complex but their accuracy is limited and they do not provide a good interpretation of the chemical and physical changes that occur inside a battery. Ultimately, equivalent circuit models are a sensible alternative because they provide a reasonable trade-off for each modelling criteria. They present a relatively high accuracy without being overly complex or difficult to parameterize. Therefore, this research will utilize an equivalent circuit modelling approach, along with EIS data, to model the performance of a lithium-ion battery.

2.5 Battery Testing and Characterization Methods

In order to identify the technological and economical feasibility of a battery for a specific application, it is necessary to collect data on how it performs and behaves under certain conditions. The performance of lithium-ion batteries depends heavily on various operating conditions including temperature, SOC and current load [55]. Therefore, it is important to carry out tests that cover a wide range of scenarios in order to develop a model that can accurately simulate the battery's behaviour. This section will discuss a series of tests that are used in industry and academic research, which will be replicated in this thesis to characterize and model the performance of a lithium-ion battery.

2.5.1 Preconditioning/Break-In

The period of time between the manufacturing of a lithium-ion battery and the start of initial testing can result in the battery being subjected to passivation. This phenomenon occurs due to reactions between metal and liquid electrolytes while the battery is being built and results in a high resistance coating forming on the lithium anode [56]. The passivation coating is what allows lithium batteries to have a long shelf life and a low self discharge [56]. However, the high resistance of this coating results in a voltage delay when a load is applied.

It has been shown in literature that subjecting the battery to consecutive charge and discharge cycles is useful in removing the passivation that the battery is subjected to [33]. Furthermore, these break-in cycles are necessary because they are able to stabilize the

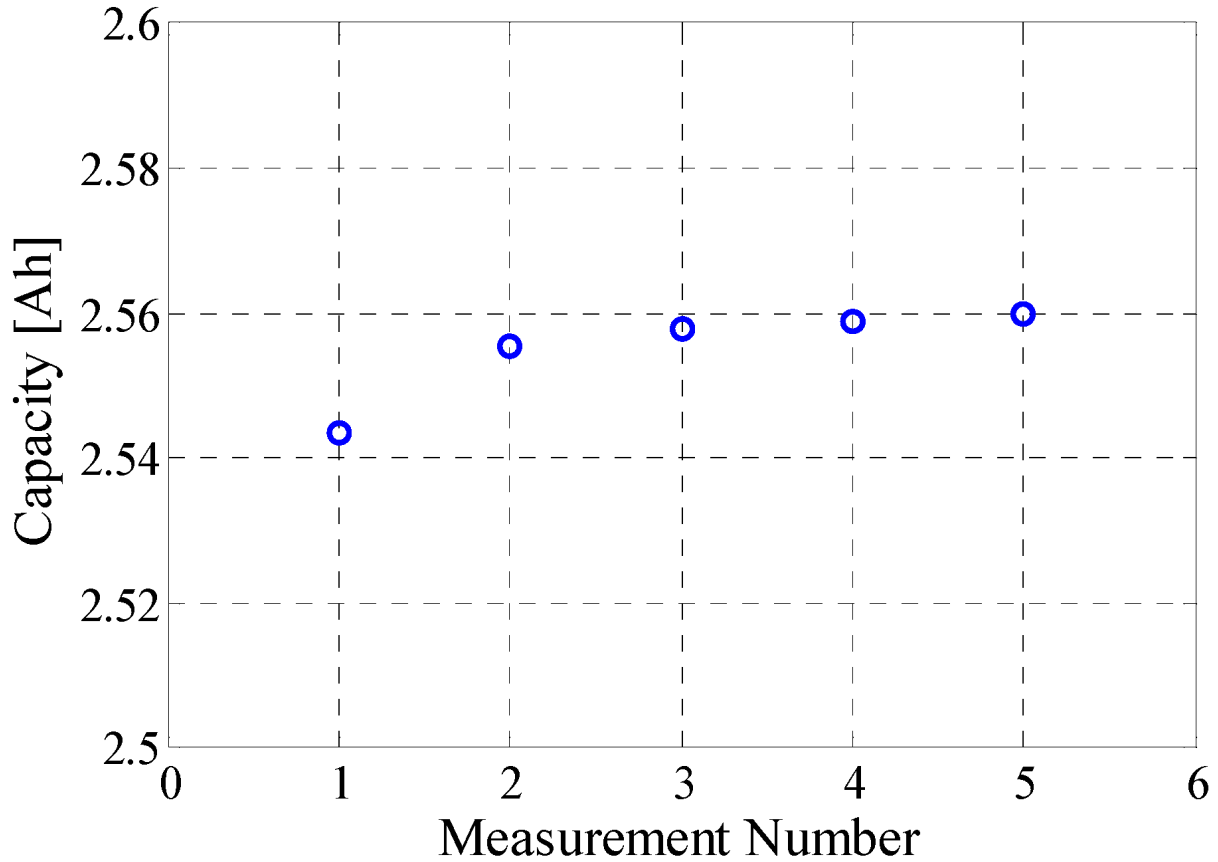


Figure 2.13: Discharging capacity of a Lithium Iron Phosphate/Graphite battery during break-in cycles [53]

electrolyte interface properties of the battery [33]. This results in the capacity of the battery gradually reaching a stable value as demonstrated in Figure 2.13. Therefore, before carrying out tests to characterize a battery, it is generally advisable to include break-in cycles at the start. The number of cycles varies for different batteries, and literature demonstrates that as few as five cycles can provide adequate results [53]. Also, the C-rate for the cycles is dependant on values found in the datasheet for a particular battery. The cycles in Figure 2.13 are performed with a 1C current at 25 °C.

2.5.2 Capacity Test

The capacity of a lithium-ion battery is affected by different operating temperatures and current loads [57]. Furthermore, literature presented by numerous researchers has shown that the capacity diminishes with time [58,59]. Therefore, when collecting data to characterize the performance of a battery, it is important to capture the dependence of capacity on different parameters. This ensures that the data available can account for a wide range of operating conditions and make it easier to develop a more robust model.

To achieve this, a capacity test is used to measure how much energy can be cycled in and out of the battery under specific predetermined conditions. Depending on what the user is aiming to achieve, this can include different C-rates, temperatures and SOC levels [33]. The parameters of the test (such as current rates, relaxation times and stop conditions) rely on the specific characteristics of the battery being tested [53]. As demonstrated in the work of various researchers, the capacity of a battery and how it is influenced by various operating conditions varies by battery chemistry [60].

2.5.3 OCV-SOC Test

As discussed in section 2.2, it is possible to establish a OCV-SOC relationship for a battery. This relationship is also dependant on operating conditions (such as temperature and aging) and does not remain constant throughout the life of a battery [33]. Thus, it is important to observe this relationship under a range of conditions to characterize the performance of a battery thoroughly. There are various methods mentioned in literature that can be used to characterize this relationship, including low-current tests and incremental pulse current

tests [61].

During an incremental OCV test, the battery is discharged using negative pulse currents at 10% SOC intervals, with a relaxation period between each pulse [62]. This is followed by a similar sequence using positive pulse currents to charge the battery. By averaging the results of each test and interpolating the data, an OCV-SOC curve can be obtained [62]. An alternative method to determine an OCV-SOC relationship is discharging and charging the cell at very low rates, typically C/20 or C/25. In such cases, the terminal voltage of the battery can be considered an approximation of the OCV [63].

The long test times involved for each of these methods makes measuring the OCV for online applications very difficult, and as such the measurement is done as an offline test [64]. When measuring the OCV at different SOC values during charging and discharging, a hysteresis effect is observed similar to what is demonstrated in Figure 2.14 [65]. The hysteresis phenomenon is primarily impacted by the history of the battery and how it has been previously handled (charge/discharge cycles, various C-rates, etc.) [66]. To address this, the charge and discharge curves are averaged and the product is taken to be the true OCV-SOC relationship [61].

2.5.4 Hybrid Pulse Power Characterization (HPPC) Test

Impedance modelling is a useful tool because this property represents the dynamic behaviour of a lithium-ion battery. Similar to the other parameters and characteristics of a battery discussed in this section, the impedance is dependent on many factors including C-rates, SOC and temperature [67]. Research presented in literature has also demon-

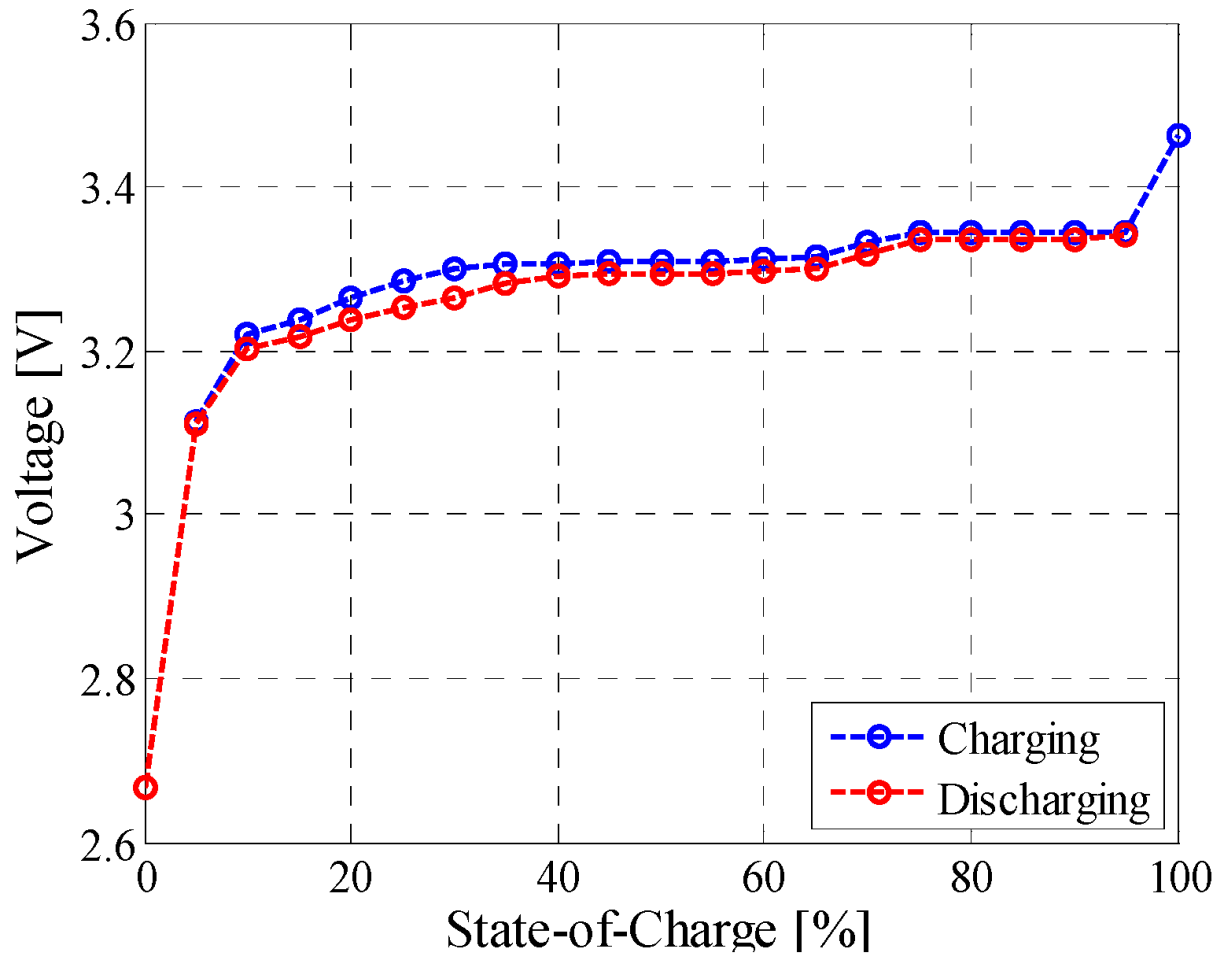


Figure 2.14: OCV-SOC characteristic of a Lithium Iron Phosphate/Graphite battery observed at 25 °C [53]

strated that the impedance changes as the battery ages and becomes less efficient [68]. Therefore, when characterizing the performance of a battery for impedance modelling, it is necessary to take into account all of these dependencies and collect data on the dynamic behaviour of the battery. One method that is used to accomplish this is a [hybrid pulse power characterization \(HPPC\)](#) test.

An HPPC test is used to apply discharge or charge pulses to a battery in order to characterize the voltage response, which helps identify information regarding the dynamics of the battery [69]. This is done at multiple temperatures and SOC levels so that model parameters can be found for a wide range of operating conditions. Figure 2.15 presents an example of a pulse current profile used in an HPPC test. In this case, a relaxation period of one hour is added between each pulse. The magnitude of the current pulses does not necessarily need to be the same, and should be chosen based on the specifications of the battery being tested. Also, the pulses can be discharge, charge or a combination of both.

The dynamic behaviour of the battery can be found using the current pulse and voltage response [70]. Figure 2.16 provides a visual representation of the parameters that are used during this process. Based on this information, the response can be calculated using Equation (2.10) [33]:

$$R_i = \frac{\Delta V}{\Delta I} = \frac{V_1 - V_0}{I_1} \quad (2.10)$$

where:

R_i = battery resistance

ΔV = voltage response due to applied current pulse

I_1 = pulse current amplitude

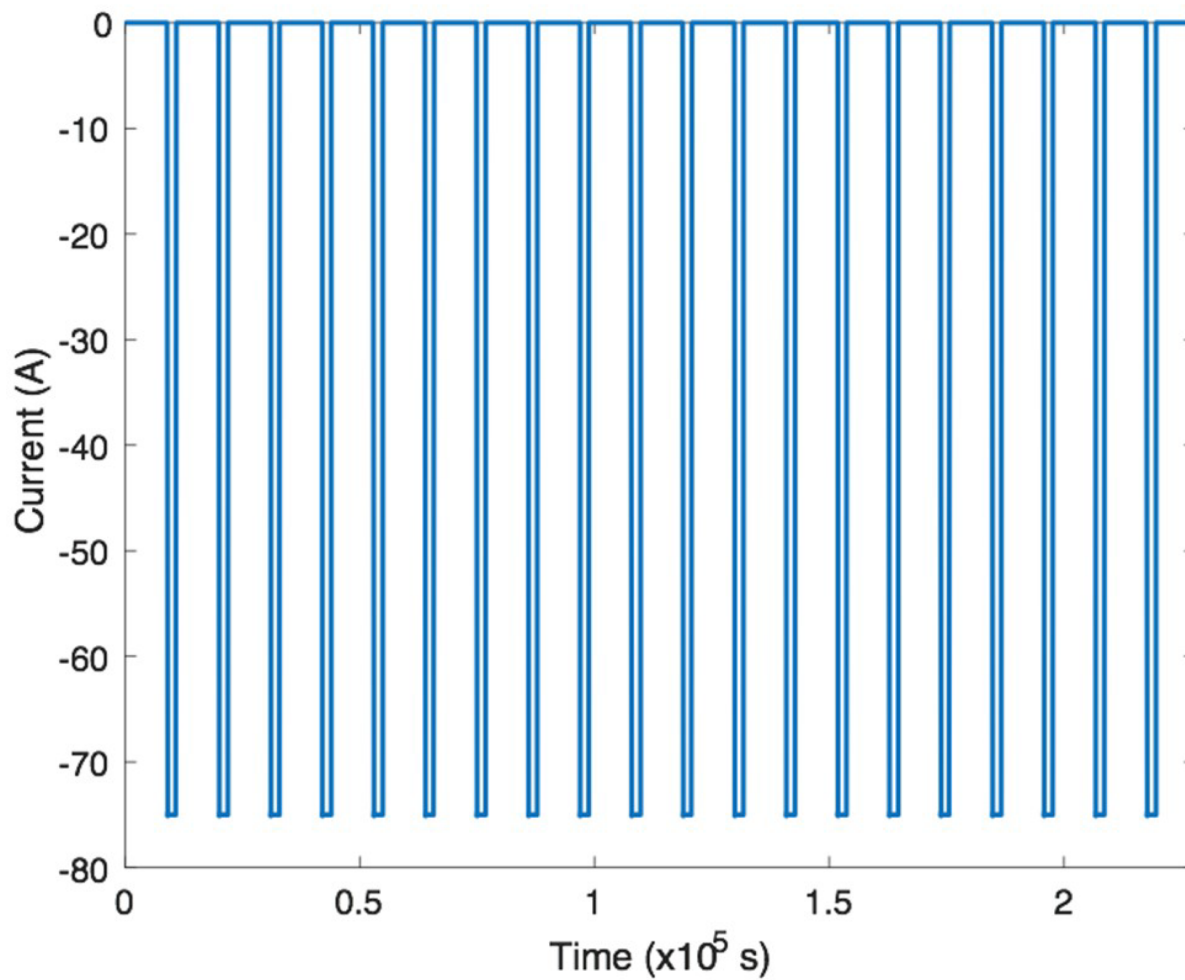


Figure 2.15: An example pulse current profile used in an HPPC test [69]

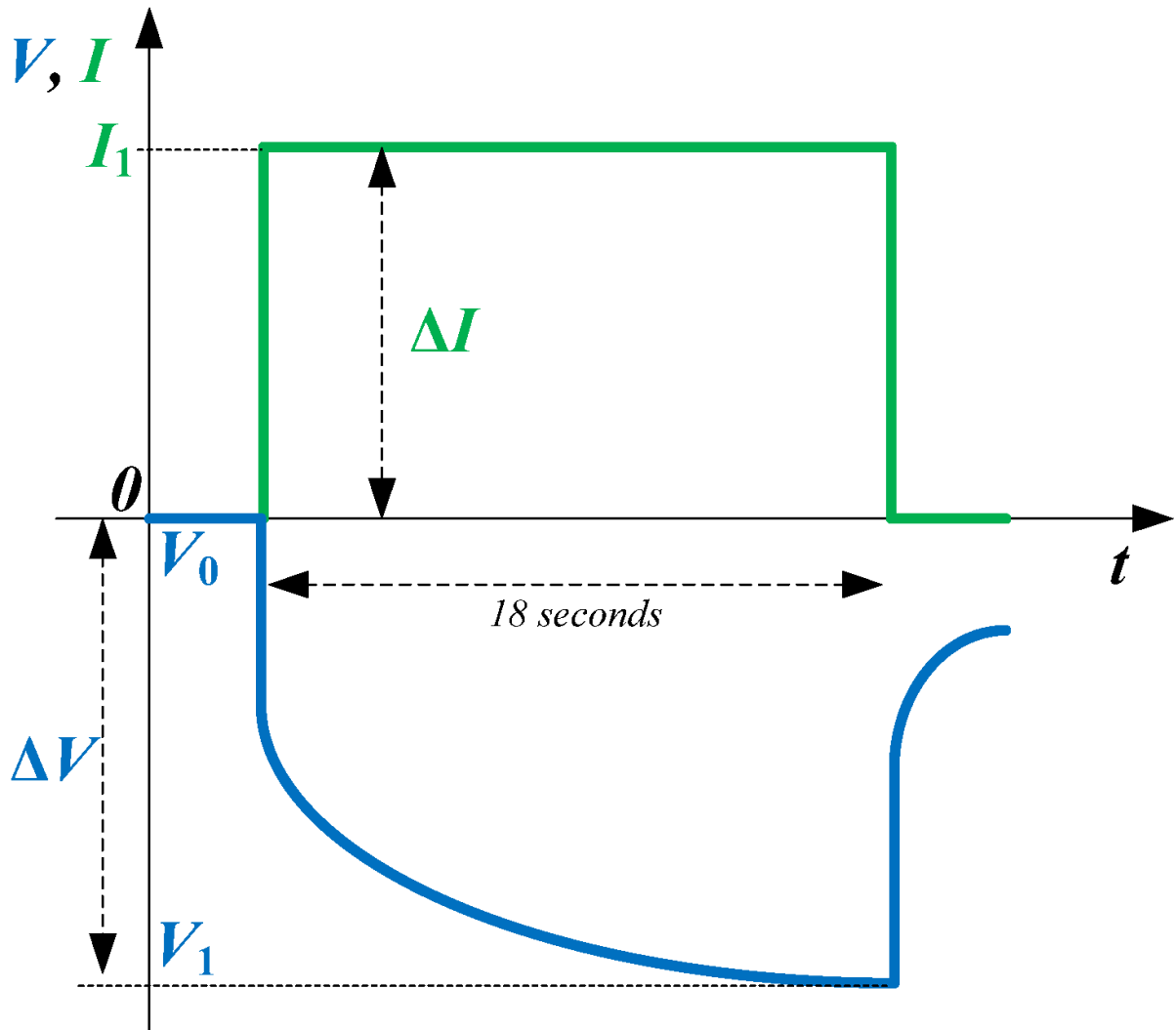


Figure 2.16: Sample current pulse and voltage response used for dynamic characterization of a battery [33]

As seen in Figure 2.16, V_0 and V_1 represent the voltage of the battery at the start and end of the current pulse, respectively. Additional parameters can be extracted from this response as demonstrated in literature, including the resistance at specific stages in the pulse current, time constants and OCV values [71].

2.5.5 Drive Cycle Profiles

When working with an equivalent circuit battery model, it is crucial to validate the performance of the model by comparing its output to experimental data. This is usually done by applying different load current profiles and measuring the output terminal voltage. A common group of load current profiles that are used, especially when testing a battery for EV applications, is drive cycle data. Therefore, drive cycle profiles are a practical tool to have when characterizing the performance of a battery, and will be used in this thesis to validate the equivalent circuit model being studied.

Drive cycles are also used for vehicle emission and fuel economy testing. This data is typically used with a dynamometer and presented as a vehicle speed vs. time profile as demonstrated in Figure 2.17. When applying this profile to a battery, the appropriate current profile must be developed using a vehicle model and should be based on the specifications of the battery being tested. This current profile is then applied to the battery experimentally, and simulated using the equivalent circuit model. The terminal voltage output of each scenario is compared to assess how well the model can simulate the real performance of the battery.

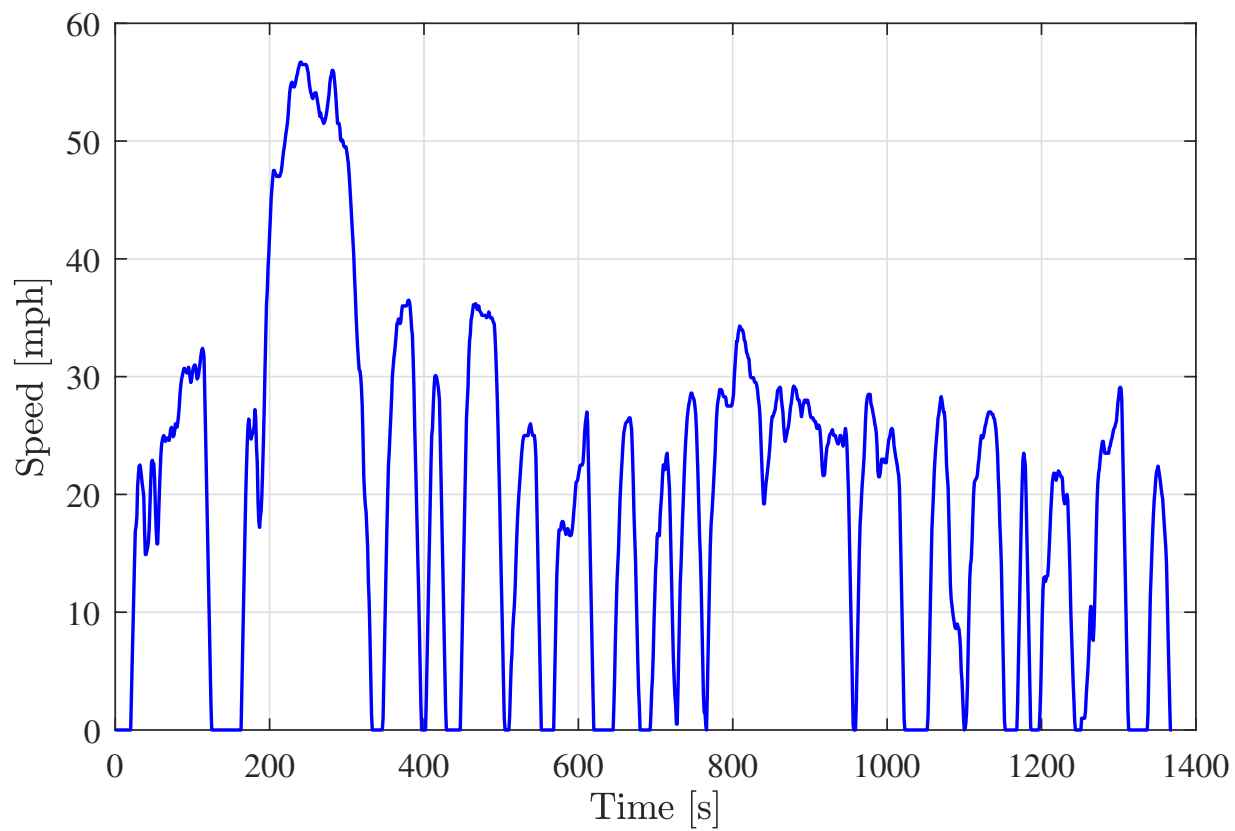


Figure 2.17: Urban Dynamometer Driving Schedule (UDDS) profile [72]

2.6 Summary

The literature review provided a general overview on the history of transportation electrification, as well as energy storage candidates that could be considered for future EV applications. It was shown that a lithium-ion battery is the ideal choice for this research because of its trade-off between high energy and high power density, relative to the other candidates. Furthermore, a summary of the terms and definitions relevant to the research was presented. An introduction to EIS testing was provided, as it will be the basis of the lithium-ion battery impedance characterization that this research will undertake. A review of various battery performance modelling approaches was presented to showcase that equivalent circuit models are the most suitable for this research and its applications. Finally, a number of industry standard characterization tests were introduced, which will be utilized in this research to further develop and validate the battery performance model.

Chapter 3

D&V Battery Testing System

As the field of battery research continues to advance, there is an increasing need for particular equipment that can perform specific tests, depending on the desired applications. These tests are often long, potentially spanning a few hours to weeks or even months, and can involve the combined use of different types of specialized hardware. Therefore, a test solution that can offer users a choice between multiple testing methodologies would help increase the efficiency of testing and reduce the time and costs involved. This chapter is dedicated to discussing the BCT-150, an integrated battery test system under development at D&V Electronics Ltd. It will cover the experimental setup, including the apparatus used and the safety considerations associated with them. Furthermore, it will discuss the remote setup of the test equipment that allows for extended and more thorough tests to be performed. Throughout the remainder of this thesis, the BCT-150 will be referred to simply as *the BCT*.

The BCT is used during the research phase to collect data and characterize the performance of a cell. This chapter will first look at existing industry testers and their offerings,

and identify shortcomings that can be addressed to provide users with a more complete testing solution. It will then provide a detailed overview of the BCT and highlight features that aim to alleviate the concerns surrounding extensive battery performance and endurance testing. The following topics pertaining to the BCT will be discussed:

- The different hardware modules that the BCT is comprised of and how their integration streamlines testing.
- The software components that are used when operating the BCT.
- The main sequence involved in using the BCT to test and characterize a cell.

3.1 Industry Cell Testers

Battery testing equipment is currently produced by numerous manufacturers that cater to specific markets or research areas. For example, Cadex Electronics Ltd. offers a line of products that are geared towards maintaining a fleet of batteries, by focusing on aspects such as remaining capacity, optimized charging cycles and extending battery life. Another example is Gamry Instruments, which produces potentiostat and galvanostat equipment that is primarily used for battery, capacitor, or fuel cell development using EIS testing. Therefore, due to the equipment being highly specialized, researchers are required to consider the type of testing they need before opting for a specific unit.

Table 3.1 presents a comparison of the specifications of various test hardware that is currently available from prominent manufacturers in the battery testing and development industry.

Table 3.1: A comparison of the specifications of existing battery testing solutions currently available in industry

Manufacturer	Model Number	Voltage Range	Current Range	EIS Testing	Maximum Sampling Rate
Cadex	C8000	0 - 45 V	30 mA - 10 A	Unavailable	2 kHz
Gamry	Reference 3000	± 32 V	± 3 A	10 μ Hz - 1 MHz Max. Amplitude: 3 V/3 A	300 kHz
Digatron	MCT-ME	0 - 6 V	0.1 - 100 A	<i>Additional Hardware Required</i> 1 mHz - 6.5 kHz Max. Amplitude: 2 A	Information Unavailable
Arbin	PHPT-200A	0 - 5 V	0 - 200 A	External Module Required	2 kHz

All of the data listed is sourced from each manufacturer's website [73–76]. By examining the specifications of each product, a few key points can be observed:

- The sampling rate of each unit varies considerably
- EIS testing is not a commonly offered featured
- The voltage and current capabilities of some of the testers are less than required for characterization tests

A conclusion can be drawn that none of the products listed in Table 3.1 offer users an integrated solution that can characterize a cell as well as perform EIS testing over a wide range of frequencies. While the Gamry Reference 3000 can be utilized for EIS testing, it is not an ideal choice to run characterization tests such as drive cycle profiles or an HPPC test. The Digatron MCT-ME is able to perform characterization tests but requires a separate module to run EIS tests which offers a limited frequency range and amplitude that diminish the practicality of this test. Similarly, the Arbin PHPT-200A is sufficient for characterization tests, but it requires third party hardware to allow for EIS testing. Therefore, a test system that provides voltage and current capabilities that are sufficient for characterization tests, as well as the ability to perform EIS testing, would give users more flexibility in terms of testing methodologies and research areas to explore.

3.2 Hardware Components

The BCT is an integrated test platform that combines different hardware modules which are designed for specific test criteria. The unit's form factor and hardware components are showcased in Figure 3.1. It is comprised of three different module types and a [personal computer \(PC\)](#) that is used to command the software required to operate the unit as well as view results. The design and development of the unit is an ongoing collaborative effort between D&V Electronics and the Centre for Mechatronics and Hybrid Technologies (CMHT) at McMaster University. The ultimate goal of the unit is to offer a unique, integrated test solution that will allow users to utilize a number of test methodologies while reducing the cost and time involved in testing. Each module is designed for a specific test category, and an overview of each one will be provided in the coming sections.

3.2.1 High Frequency Signal Module

The high frequency module provides the capability to perform EIS testing over a range of frequencies, up to 50 kHz. This module is one of the two elements that are involved heavily in this research, and it is used to collect impedance data on a lithium-ion cell. It samples data at 200 kHz which helps to provide reliable high frequency data without the risk of aliasing. In order to expand the practicality of EIS testing, the module is able to simulate customizable waveforms that are generated through third party software. This way, users are able to tailor waveforms to their specific needs and are not limited to certain formulas or signals.



Figure 3.1: D&V Electronics' BCT-150 battery cell tester [77]

3.2.2 Cyclor Module (High Power)

The high power module is used to supply the tester with currents used to cycle the battery during various tests, such as running drive cycle profiles. An important aspect of drive cycle simulations is heavy acceleration and braking, which translate to large current draws and charge currents. Therefore, this is something that the high power module must be able to replicate. It is also necessary to deliver high current pulses to the tester, such as the ones used in HPPC testing. As such, the module is designed to deliver up to 100 A of current and more than one module can be combined to test multiple cells simultaneously. This is the second module that is used throughout this research, to characterize the performance of a lithium-ion cell.

3.2.3 Coulombic Efficiency Module (High Precision)

The high precision module is designed to address tests and data collection that require measurements with a high degree of accuracy. One example of such a test is coulombic efficiency, which is the ratio between total charge extracted and added to a battery during a full cycle. This ratio can see very small variations even after the cell is subjected to hundreds or thousands of cycles and thus, to reliably measure the coulombic efficiency, the high precision module is designed to measure current with an accuracy of up to ten parts per million (0.001 %).

Table 3.2: A summary of the specifications for each module used in the BCT-150 battery test system

	High Power	High Frequency	High Precision
Voltage Range	1 - 6 V	1 - 6 V	1 - 6 V
Maximum Current	100 A	5 A	2 A
Current Range	5 A / 25 A / 100 A	5 A	2 A / 5 A
Bandwidth	-	0 - 50 kHz	-

3.2.4 Advantages of Hardware Integration

A summary of the specifications for each module is presented in Table 3.2 [77]. When compared to the Cadex and Gamry units that are listed in Table 3.1, it is evident that the BCT provides a more complete test system as it allows users to perform characterization tests in addition to EIS tests. This is due to the fact that the Cadex unit does not offer EIS capabilities and the Gamry unit does not provide a voltage and current range that is sufficient for characterization tests. Furthermore, the BCT offers an advantage over the Digatron and Arbin systems because it offers EIS capabilities, which the aforementioned testers do not as standalone products. The Digatron system requires additional hardware to perform EIS tests, and in addition to this, the frequency range and current amplitude offered by the BCT allow for a broader range of testing. At the same time, the Arbin system requires the purchase of a third-party unit to perform EIS tests. This ultimately requires support and training from multiple vendors, and additional software refinement to allow users to use the modules together, both at an additional cost. The BCT is superior in this regard because all of the modules are designed and built in-house. As a result, users

are able to convey all of their training and support concerns to a single party, and the tester software is optimized to work seamlessly with all of the modules. Therefore, there is no need for the user to learn and operate multiple systems to perform EIS testing; instead, they have access to all of the BCT modules which are combined in a single entity.

The primary advantage of the BCT is the integration of the three different modules, which gives users greater autonomy to conduct different tests consecutively and collect data more frequently. For example, one of the biggest drawbacks of having separate units to cycle the battery and then perform EIS testing is having to repeatedly disconnect the cell and reconnect it to each device. This adds unnecessary time to testing and requires constant user intervention, which occupies valuable resources that can be spent on other research activities (e.g. data analysis or modelling work). By being able to automatically switch between modules, the BCT allows users to collect EIS data while operating the battery under various conditions and loads. The same holds true for coulombic efficiency testing. Ultimately, this reduces the costs and time involved in battery testing and provides the potential to collect data more extensively.

3.3 Tester Software

The software application used to operate the BCT is the main point of interaction between the user and the test hardware. As such, it is important that the application is user-friendly and can handle all of the functional requirements that the hardware dictates. During the course of this research, iterative updates and improvements were made to the application to ensure that the tester performs as expected and maintains its safety critical features.

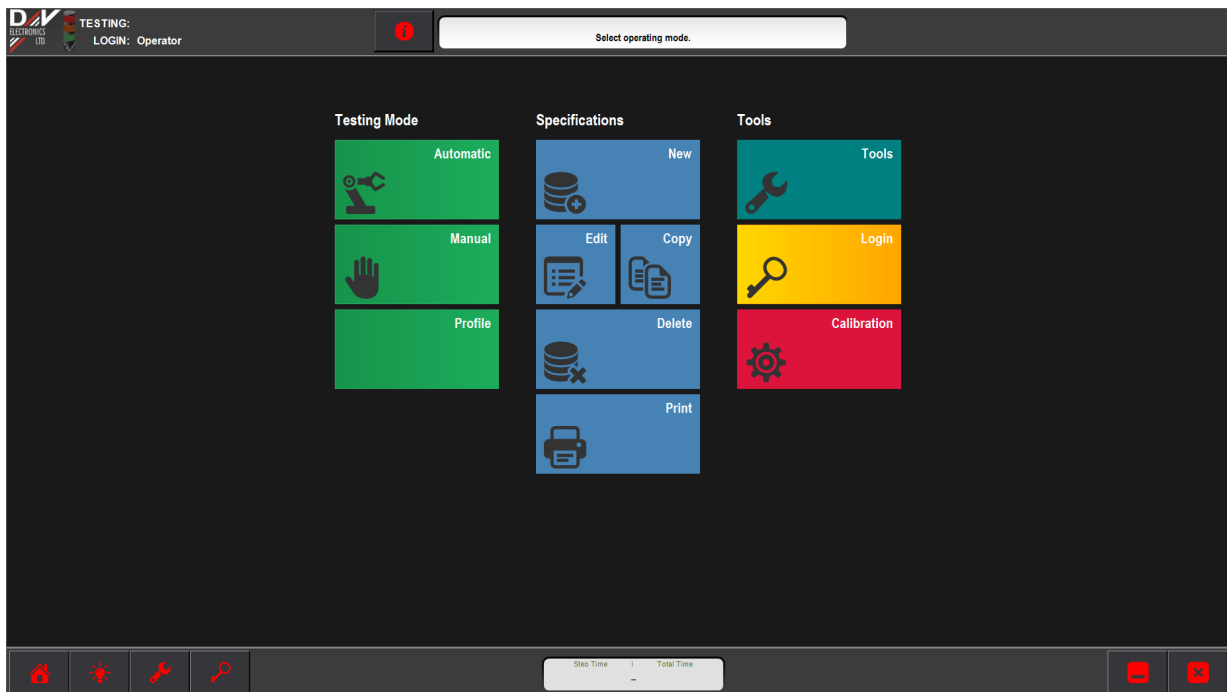


Figure 3.2: The main screen of the BCT test application

Examples of these changes include: bug fixes, code refactoring and user interface updates.

The main functions of the software are listed below:

- Provide an avenue for users to edit test procedures that is intuitive and easy to operate
- Present information regarding the current status of a test that is running, as well as real-time measurements from the [device under test \(DUT\)](#)
- Collect and store test data in a manner that is easily accessible to the user
- Allow users to view and analyze the stored data

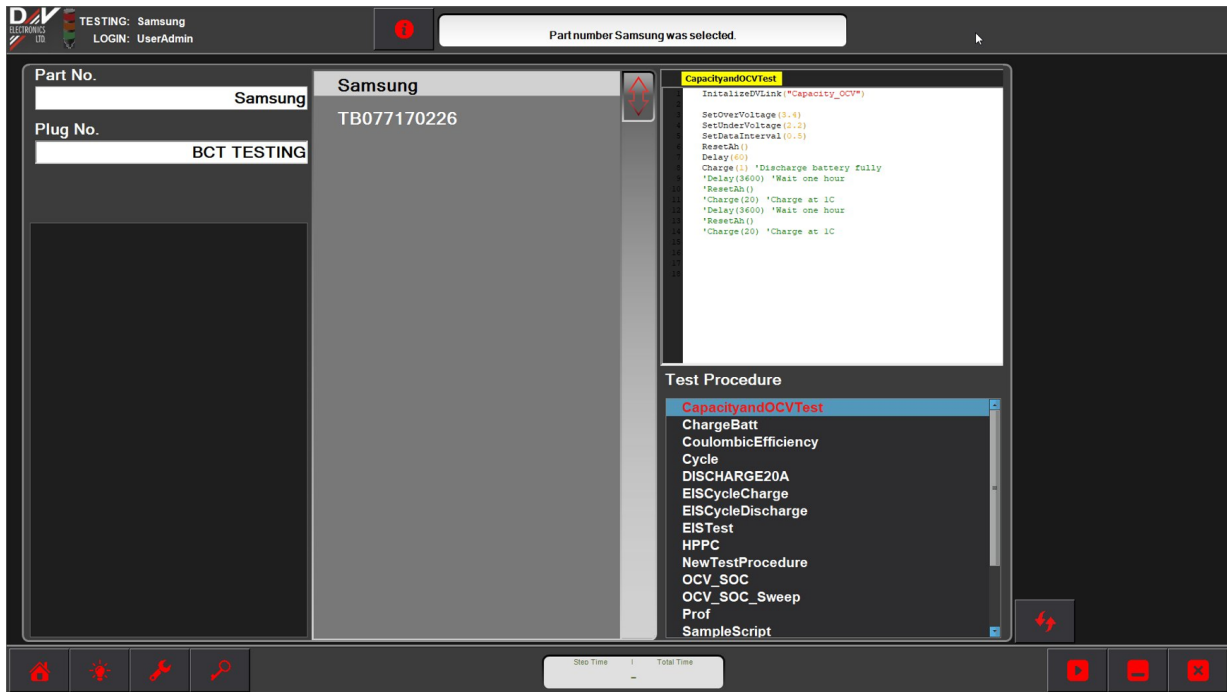


Figure 3.3: The BCT test application provides a list of available devices and test scripts to the user

Figure 3.2 showcases the main screen of the application used to operate the tester. This application is used to view the progress of a test and readings from the DUT, as well as interact with secondary applications for tasks such as editing test scripts and updating the specification profiles of different devices. When the user is ready to conduct a test, they are presented with a list of available device specifications and test scripts, as demonstrated in Figure 3.3. The device specifications and test scripts are user editable and will be discussed in more depth in Section 3.4. After the user starts a test, the application transitions to a screen that provides progress status and readings throughout the duration of the test, as shown in Figure 3.4. From this screen, the user is able to view information such as current and voltage measurements, in addition to readings that are user configurable. This screen

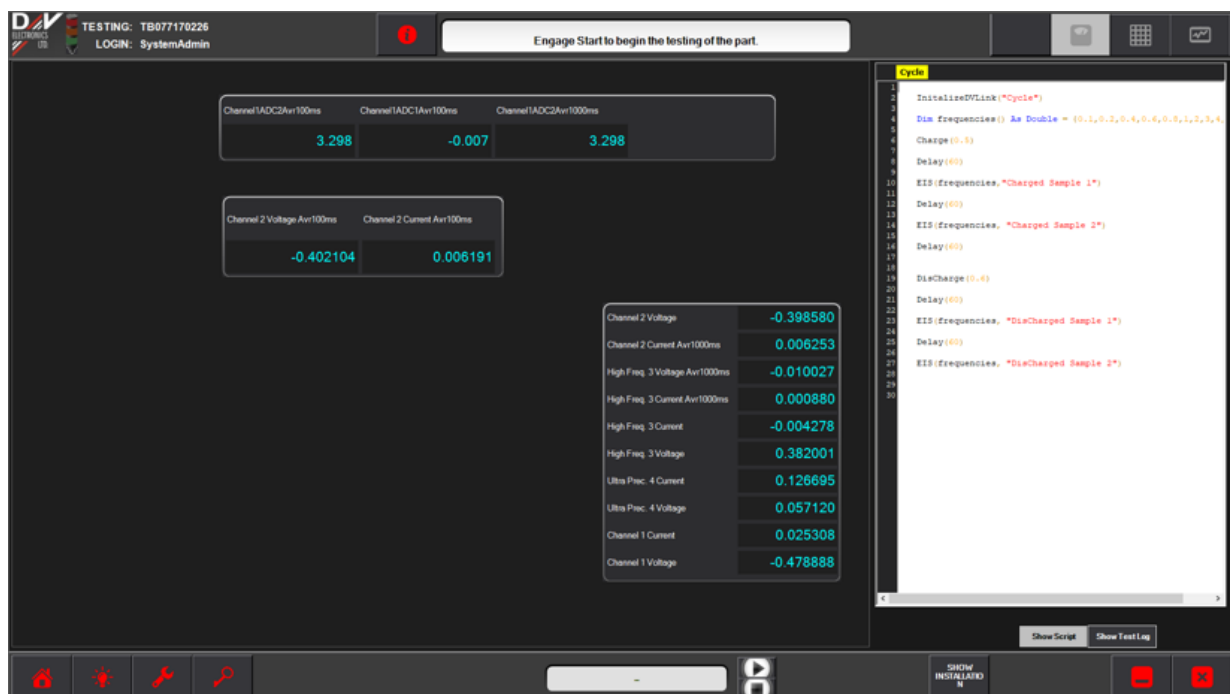


Figure 3.4: During a test, the BCT test application provides realtime measurements and information regarding test progress

also provides the following information regarding the progress of the test:

- Elapsed time since the beginning of the test
- The current step in the test procedure, which is highlighted in the test script
- The time stamp of the current step in the test procedure. For example, if the current step is a 30 minute delay, the user would be able to determine how much time remained until the delay finished and the test script continued to the next step

The main application also provides customizable tools and settings that the user can choose from based on their testing needs. Through these options, the user can configure additional peripherals such as a [temperature monitoring unit \(TMU\)](#). Due to the level of configuration available, accessibility is limited based on the login credentials used. Changes that are more complex are reserved for users with higher authorization (e.g. service engineers) to prevent any potential damage to the equipment and harm to the user.

3.4 Testing Sequence

To safely operate the BCT, there are various setup tasks involved to limit the potential risk of user harm or damage to the equipment. Performing a test generally involves the following steps:

1. Creating a specification profile for the DUT
2. Preparing a script for the specific test procedure desired, if one does not already exist

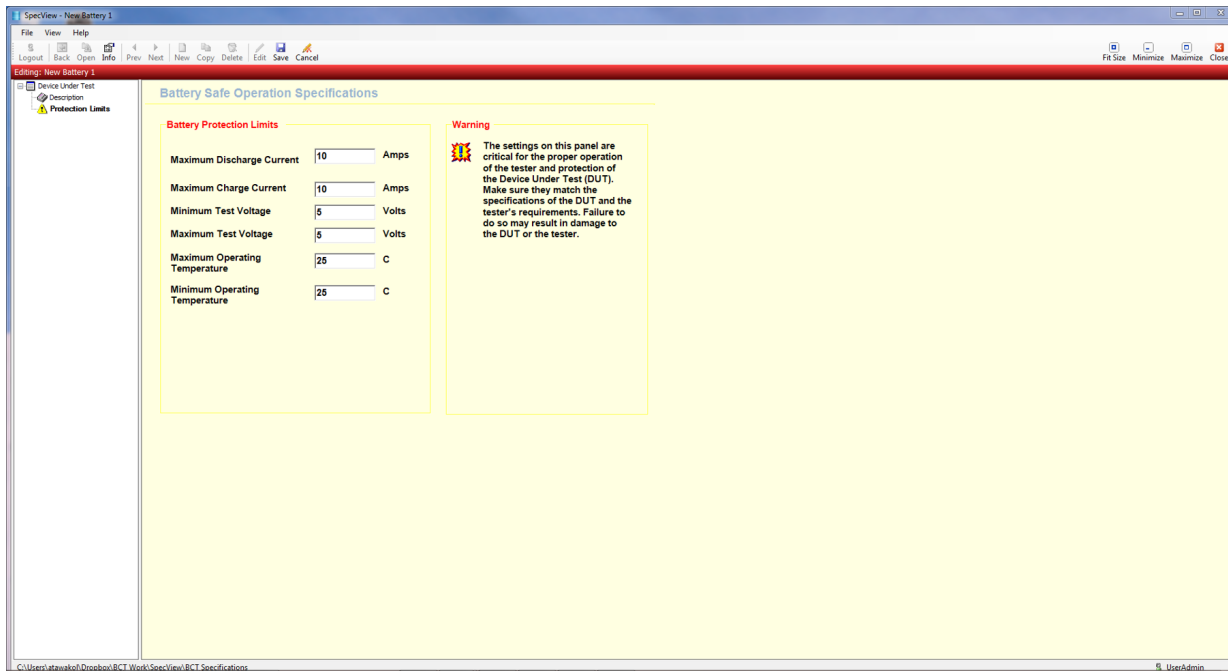


Figure 3.5: An example battery specification profile used during testing

3. Accessing the results for analysis and post-processing

The specification profile is necessary to assign hardware protection limits which the unit abides by during the course of any test. It also contains information that makes the DUT easier to identify in the database of available devices, by including the following properties:

- Rated voltage and capacity of the battery
- The serial number of the device
- The battery chemistry and manufacturer

An example of such a profile is presented in Figure 3.5. These protection limits ensure that during the testing, the battery does not operate outside the safety specifications that

the user provides. The example profile in Figure 3.5 lists a maximum allowable current of 10 A; if the user were to mistakenly command anything above 10 A in a test script, the test would automatically terminate to ensure that no damage occurs to the test equipment or DUT, and to eliminate the risk of user injury.

The next step that is required to run a test is creating a script which defines the procedure that the user wishes to apply. The script typically encompasses the following items:

- Initializing a link to the tester database so that test data can be logged
- Any current and voltage limits that the test should operate within
- The data interval desired for logging measurements
- The test sequence required

An example test script is presented in Appendix A. To make the script preparation process more intuitive for the user, the software makes use of a custom script editor, which is shown in Figure 3.6. Through this software, users can edit scripts with the aid of an auto-suggestion feature that helps users complete commands that are required. To ensure that the script is complete and will not interrupt a test prematurely, the software builds and compiles the script to search for any errors, such as syntax mistakes.

The final step in testing using the BCT is viewing data for analysis and post-processing. The software used to access these results is shown in Figure 3.7. Through this application, users can view results for an entire test as well as individual elements from each test. For

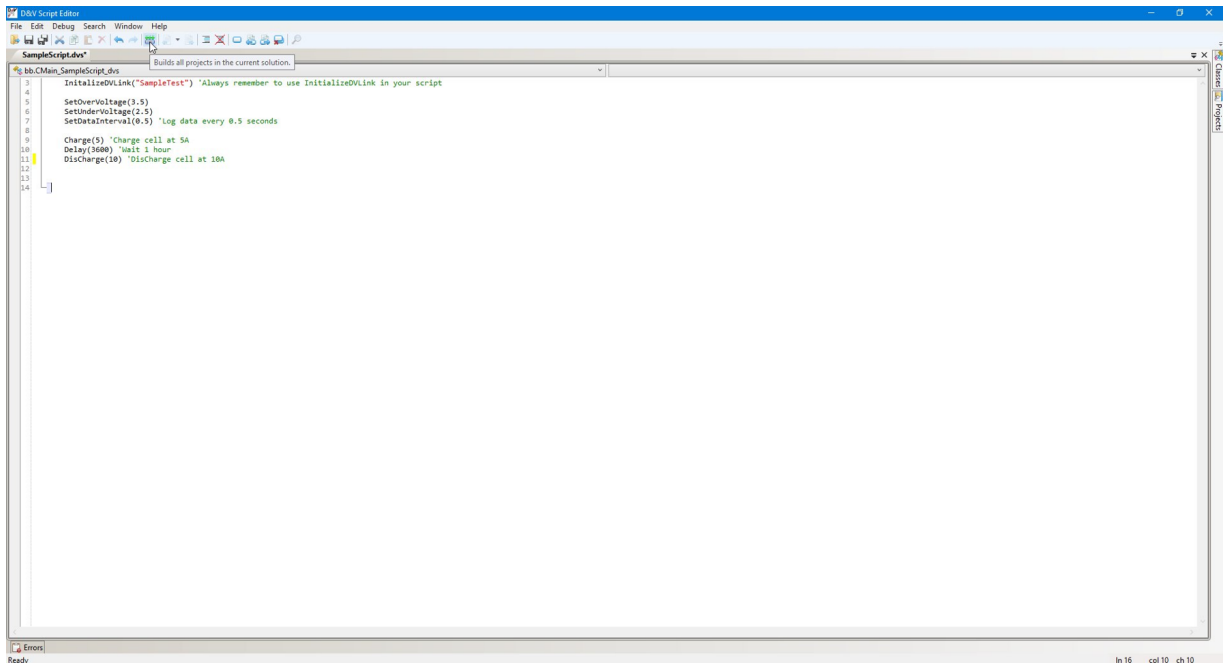


Figure 3.6: The custom script editor used as part of the BCT software

example, if a user was running drive cycle profiles and recharging the cell in between, they could view the measured voltage for the entire duration of the test, or for specific drive cycles/charge points. Users are able to view the data in a manner that they deem to be most suitable to their results, such as line plots or bar graphs. They are also able to overlay different measurements on the same plot, as demonstrated in Figure 3.7. The application also offers the option to export the data so that it can be further analyzed using third-party software such as MATLAB or EXCEL.

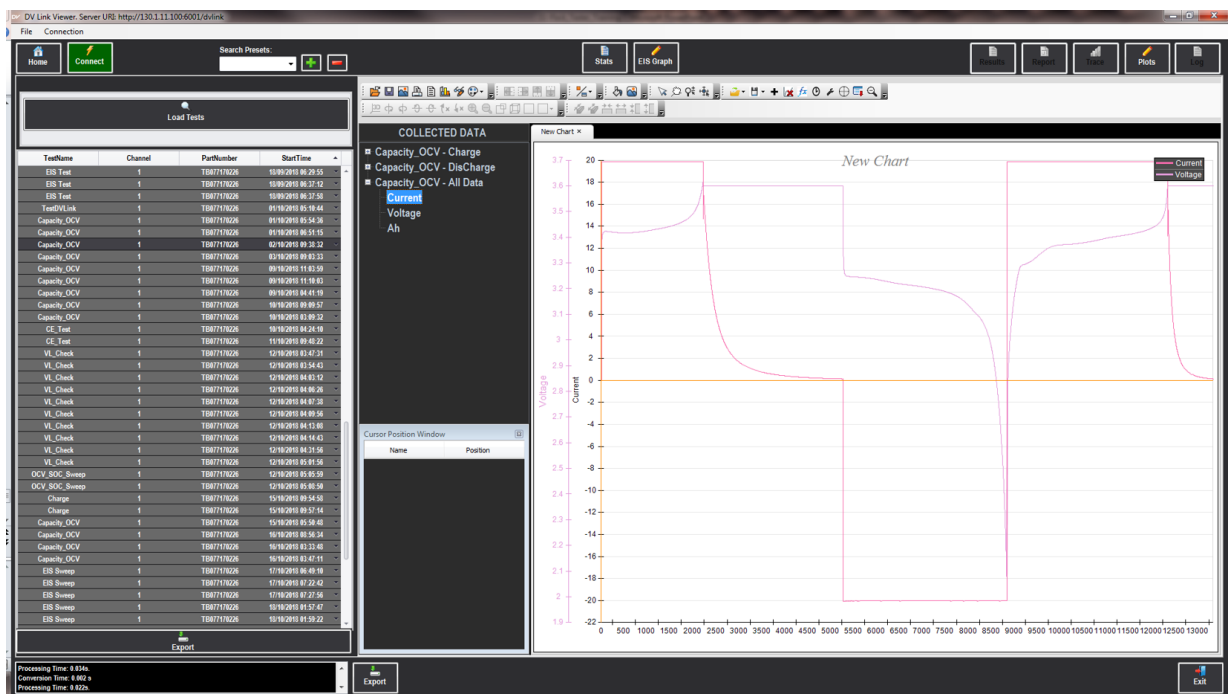


Figure 3.7: The BCT application used to view results

3.5 Experimental Setup

The test environment used to perform the required characterization tests is comprised of the following components:

- D&V battery test system (BCT Unit)
- The PC used to operate the BCT unit
- Environmental chamber
- Temperature monitoring unit (TMU)

A visual representation of the setup, as well as the connections between each component, is presented in Figure 3.8. The lithium-ion cell selected for testing, as well as the environmental chamber used, are covered in Section 3.5.1. A closer look at the cell fixture and physical connections is presented in Section 3.5.2. Lastly, Section 3.5.3 will provide details on how the components are connected to allow for remote access which streamlines test procedures and improves testing efficiency.

3.5.1 Description of Apparatus

The lithium-ion cell chosen for testing is a Samsung INR21700-50E, shown in Figure 3.9. The *INR* in the name refers to the chemistry of the cell which is lithium manganese nickel. This combination of different materials is advantageous for the following reasons [78]:

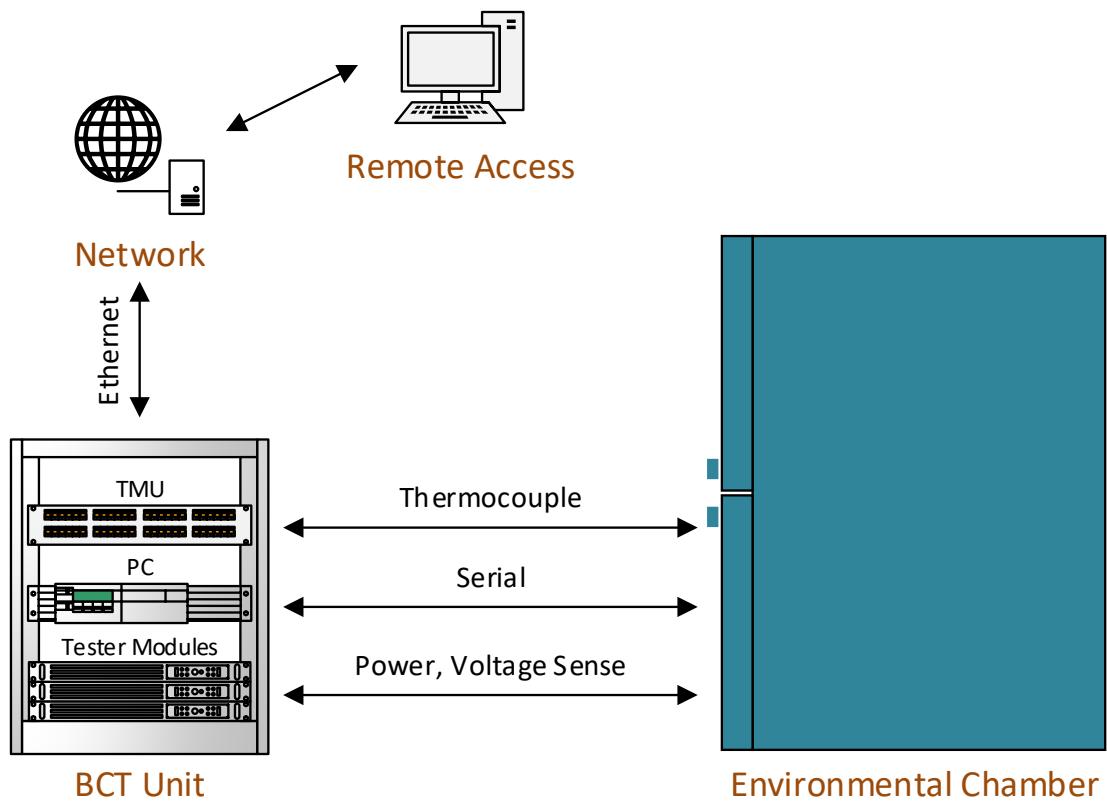


Figure 3.8: An overview of the test environment and the appropriate connections between each component



Figure 3.9: Samsung INR21700-50E Lithium-Ion Cell

- Manganese allows the cell to discharge at high current rates while maintaining a low temperature.
- Nickel is a material that provides a high specific energy.
- The chemistry is stable and does not require the use of protective circuits.

Another portion of the cell name is *21700* which refers to the dimensions of the cell (21 mm diameter and 70 mm length). A different cell type that is commonly used is 18650 cells (18 mm diameter and 65 mm length). 21700 cells are advantageous compared to 18650 cells due to an increased cell volume and an overall improvement in capacity storage [79]. This results in an increased amount of energy stored in a battery pack while reducing the number of cells required, therefore reducing the total weight of the pack. A summary of important parameters for the cell under study is provided in Table 3.3 [80]. The Samsung INR21700-50E is a high capacity, low resistance cell that is capable of providing high discharge currents; the aforementioned characteristics make it an ideal choice for research

Table 3.3: Samsung INR21700-50E Lithium-Ion Cell Specifications

Item	Specification
Capacity (Minimum / Typical)	4753 mA h / 4900 mA h (1C)
Nominal Voltage	3.6 V
Maximum Charging Voltage	4.2 V
Discharge Cut-off Voltage	2.5 V
Maximum Charge Current	4900 mA
Maximum Discharge Current	9800 mA (continuous) 14 700 mA (noncontinuous)
Cycles to 80% Capacity	500 (100 % DOD, 25 °C)
Weight	69 g
Operating Temperature	Charge: 0 to 45 °C Discharge: -20 to 60 °C



Figure 3.10: Envirotronics SH16 Temperature/Humidity System

involving EV applications.

To characterize the cell across a range of temperatures, it is necessary to use an environmental chamber to control the conditions for each test. An Envirotronics SH16 Temperature/Humidity system, shown in Figure 3.10, was used for this research. A summary of the relevant specifications for this system is provided in Table 3.4 [81].

While the primary function of using an environmental chamber during this research was to control temperature, it is also a crucial safety mechanism that plays a key role in protecting the cell, the user and the test equipment. A major concern that is present when testing lithium-ion batteries is the release of explosive gas generated by the electrolyte. If this concern is not addressed, flammable gases can reach an explosive level and be ignited by a battery fire or any electrical equipment present. Therefore, to mitigate this risk, the

Table 3.4: Envirotronics SH16 Temperature/Humidity System Specifications

Item	Specification
Minimum Temperature	-30 °C
Maximum Temperature	177 °C
Size	16 ft ³
Cooling Performance (25 °C to -30 °C)	32 minutes

environmental chamber is equipped with the following features:

- Gas sensing - there are sensors present to detect any explosive gas or carbon dioxide (CO_2), which can immediately stop any active equipment in the event of a fire or the presence of explosive gas.
- Fire suppression - an automated fire extinguishing system is used to flood the chamber in an attempt to put out a fire, and it also directly notifies the local fire department in such an event.
- Explosion venting - there are holes at the top of the chamber lined with stainless steel and plugged with foam. In the event of an explosion, this provides an outlet and prevents the chamber door from being blown open.

These measures help maintain the safety of the users, the equipment and the surrounding area. They also act as a redundancy to the setup of the cell being tested. In the event of the user incorrectly assessing the safety limitations of the cell being used, the safety

measures in the environmental chamber will help limit, or eliminate completely, the risk of a fire or explosion.

3.5.2 Cell Fixture and Connections

An important consideration of battery testing is user and equipment safety. Due to the nature of the tests being performed, which could include high voltage and current applications, the risk of serious injury is present if the necessary measures are not taken. Specifically, the following potential hazards must be accounted for:

- Cell voltage exceeding the rated value - if the cell voltage is not monitored or protected, damage can occur to the cell and could potentially result in the release of gas and/or a fire.
- Excessive cell heating - an internal failure or an excessively high current could also result in damage to the cell as well as the release of gas and/or a fire.
- Terminal shorting - some scenarios, including poorly secured cabling or exposed conductors, can result in high fault currents, damage to the cell and a potential fire occurring.

Therefore, an appropriate cell fixture must be built to address these hazards and ensure that any potential safety risks are mitigated. The cell fixture design, as well as the physical connections to the cell, are presented in Figure 3.11. The following elements are incorporated in the fixture to make it as safe and dependable as possible:

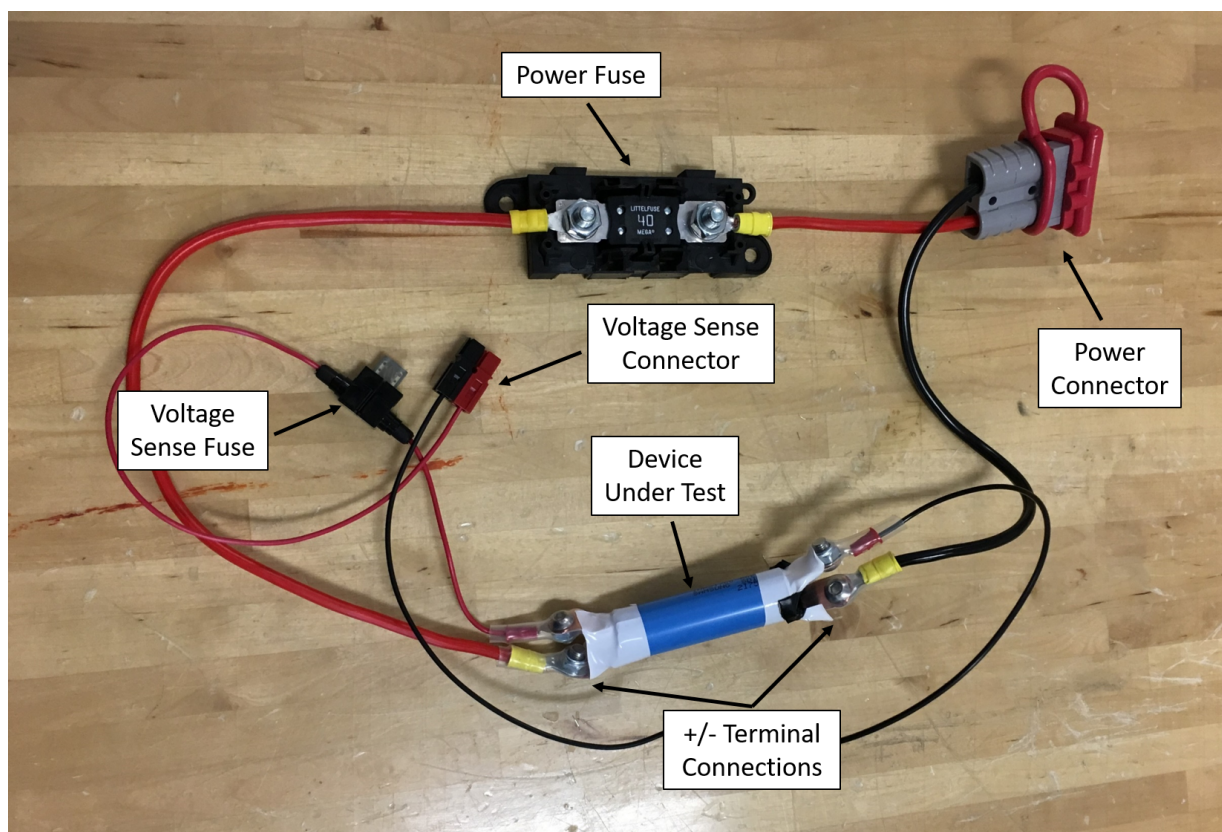
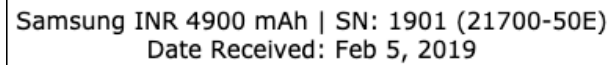


Figure 3.11: Cell fixture used during testing



Samsung INR 4900 mAh | SN: 1901 (21700-50E)
Date Received: Feb 5, 2019

Figure 3.12: An example of a cell label with identifying information, used for traceability in the test environment

- Reliable power connections and cabling - to prevent accidental damage to the cell, these are chosen based on the maximum current used for testing. In the event that the commanded current exceeds this value, this ensures that the wiring and connections are not damaged.
- A power fuse to ensure that, should the commanded current exceed the maximum value used for testing, no damage occurs to the cell.
- Voltage sensing at the cell terminals to measure voltage during the test, with an accompanying fuse. In order to directly connect the voltage sensor to the terminals, copper tabs are welded to the cell plates.
- A cell label with important identifying information (such as the serial number and chemistry type) so that the cell is easily distinguishable for other users. This is important to allow the cell to be easily traceable and for its identification and entry into a database containing protection limits for other available test devices. This label is not visible in Figure 3.11 due to the position of the cell. However, an example label is depicted in Figure 3.12.

The cell fixture and terminals are also covered with insulating material to prevent the cell from shorting and to guard against moisture inside the environmental chamber. Once the physical connections to the cell are complete, it is installed in the environmental

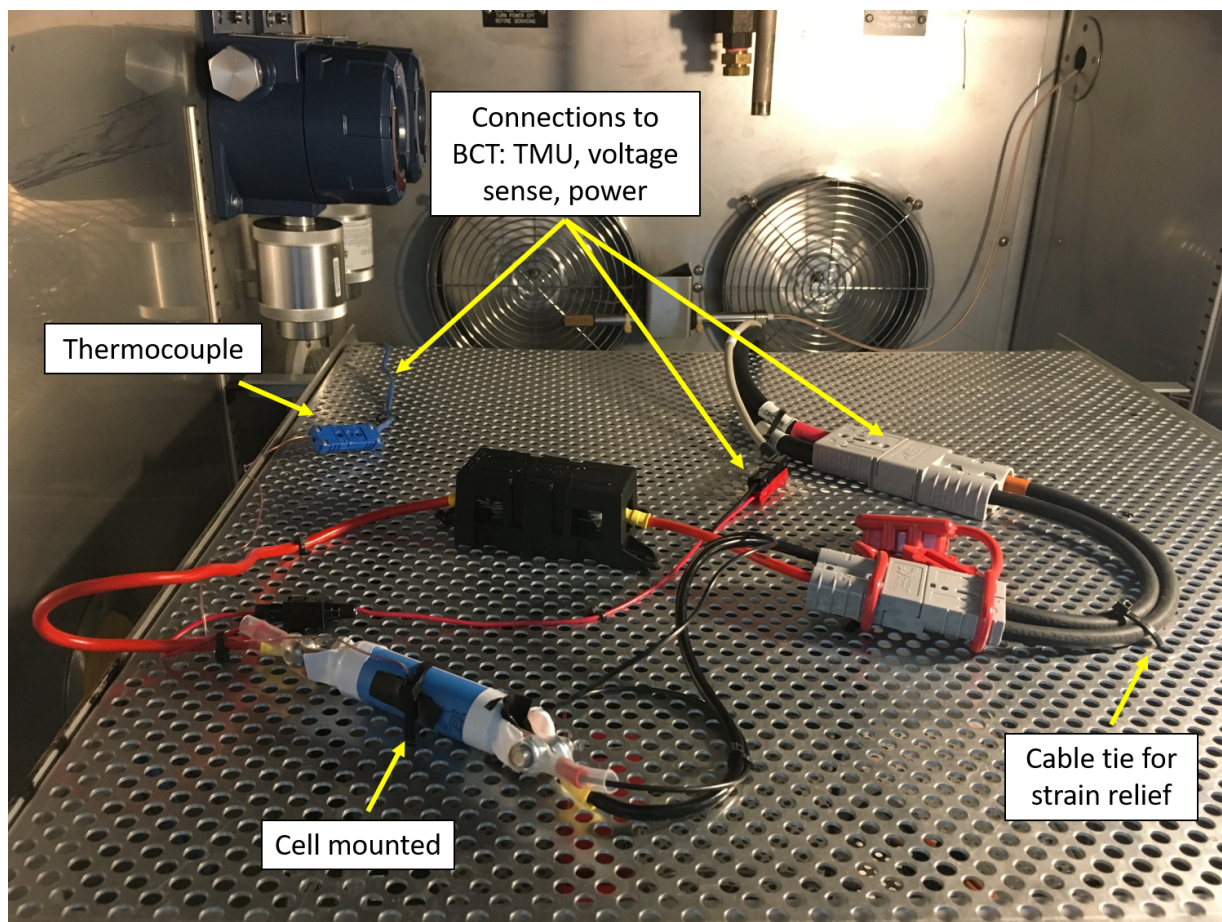


Figure 3.13: Installation of cell fixture and cabling inside environmental chamber

chamber as shown in Figure 3.13. The thermocouple is attached to the cell and connected to the TMU to monitor the surface temperature of the cell during testing. It is important to note the cable ties used to secure wiring inside the chamber, to provide strain relief and prevent a short from occurring if the cables are pulled from outside the chamber. The cell is also directly mounted to the surface of the thermal chamber; unlike prismatic and pouch cells, cylindrical cells do not pose a risk of expanding and thus do not require external clamping.

3.5.3 Remote Testing

The PC used to control the BCT is connected to the internet via an ethernet cable that links it to the local network in the lab. This allows users to remotely access the BCT from any location with a working internet connection. By doing so, they are able to utilize the full functionality of the unit to carry out tasks such as:

- Monitor important characteristics and measurements for the DUT at any time (e.g. voltage, temperature, etc.).
- Track the progress of the test currently running (e.g. total run time, current test step, etc.).
- Stop a test, make changes and run it again, or choose a different test to run.
- View data collected from previous tests as well as the current test.

This arrangement is crucial because it allows the user to continue testing and make changes as required without having to be physically situated in the lab which, ultimately

reduces the time, cost and energy involved in testing. By being able to access the tester at any time and from any convenient location, the user can adjust test procedures whenever it is necessary. For example, if a user notices an error in a test procedure in the evening on Friday, they can quickly make the necessary fixes remotely and restart the test. Conversely, if this option was not available, they would have to visit the lab to access the BCT and achieve the same outcome, or wait until Monday morning, which would waste more than two full days of valuable testing time. Furthermore, by viewing test results and live battery measurements, the user can determine if there are any imminent hazards and remotely stop the test immediately to prevent any damage to the unit, the DUT and the test environment. Lastly, the user can remotely access real-time results and stored data from previous tests which frees up time spent travelling to and from the testing lab. This also allows for easier collaboration between multiple users who are involved in testing (e.g. an industry researcher and a university researcher working on the same project from different locations).

Another aspect that is essential to the setup is the serial connection between the PC and the environmental chamber. This allows the user to communicate remotely with the chamber, which streamlines its use with the BCT seamlessly. Various serial commands that would commonly be used in a typical test procedure are listed in Table 3.5 [82]. The first major advantage of this setup is reducing the time, effort and cost involved in testing across a broad range of temperatures. For example, a user could perform a test at very low temperatures which requires the cell to be periodically charged. In order to avoid damaging the cell and aging it excessively, it is necessary to charge it at room temperature. Therefore, this example test procedure would be performed as follows:

Table 3.5: A list of relevant serial commands that can be used to communicate between the BCT and environmental chamber

Command	Description
emergency stop	Shut the chamber off in the event of an emergency.
set event <i>event_num</i>	Set a specified event to a specified state. An example of this would be controlling the circulators (event) to turn them on or off (state).
read event <i>event_num</i>	Read the current state of a specified event ("ON" or "OFF").
set setpoint <i>channel = value</i>	Set the temperature setpoint for a specified channel.
read setpoint <i>channel</i>	Read the current setpoint for a specified channel.
read pv <i>channel</i>	Read the present value of a specified channel.
read deviation <i>channel</i>	Read the deviation between the setpoint and present value for a specified channel.

1. The test starts with a fully charged battery.
2. The temperature of the chamber is set to the desired value (e.g. -10°C).
3. Testing is performed, which drains the battery to 0 % SOC.
4. The temperature of the chamber is set to room temperature (25°C) to charge the battery.
5. The battery is charged to 100 % SOC.
6. Steps 2 through 5 are repeated until the test procedure is complete.

Being able to control the temperature of the chamber as part of the test procedure makes the test much more efficient and reduces the amount of input required from the user, which frees up their time for other tasks. Specifically, without this feature, steps four and five from above would have to be supplemented as follows:

1. A delay is added to the test procedure once the battery is drained, until the user is able to return to the lab and manually adjust the temperature of the chamber.
2. Once the user is free and able to access the lab, they adjust the temperature of the chamber and must then wait for the temperature of the battery to rise before continuing the test.
3. Once the battery is fully charged, steps 1 and 2 are repeated for the desired testing temperature.

It is evident that the steps above add unnecessary time to the test and needlessly require input from the user. Furthermore, it is hard to predict exact test times and plan them so that the temperature changes occur at times when the user is available in the lab. For example, if a test procedure requires a change in temperature at 10:30 PM, the user would not be able to continue the test until the next morning when they are able to manually adjust the temperature setting for the chamber. This wastes valuable time which could instead be utilized to continue the test. Therefore, having a serial connection between the BCT and the environmental chamber allows the user to include temperature control as part of their test procedure, which ultimately reduces the time involved and user input required.

3.6 Summary

This chapter was dedicated to covering the BCT-150 battery test system that is used as part of this research to test and characterize a lithium-ion cell. An overview of existing industry systems was provided, which showcased how their offerings can be expanded to provide a more complete testing solution. The hardware specifications of the BCT were presented, which demonstrated the advantages it provided over existing systems with respect to testing capabilities. Furthermore, it was shown that the integration of the different modules that comprise the BCT can reduce the time and costs involved in testing, and allow users to collect more in-depth results for EIS and coulombic efficiency tests. Additionally, the software components involved in operating the tester were covered, as well as the sequence of events that are used to conduct testing. An overview of the test setup was provided,

including the equipment used and the relevant connections that are required. The safety mechanisms that are necessary to make the testing as safe and reliable as possible were explained as well. Finally, there were key aspects of the setup explained that highlighted the effectiveness of remote testing.

Chapter 4

Battery Testing and Characterization Using D&V Battery Testing System

A number of characterization tests used in industry and academic research were introduced in Section 2.5. Each test can help identify specific information regarding the behaviour of a cell, and will be used to develop and validate the impedance model studied in this research. This chapter will provide a detailed look at the procedures used for the tests, and results for each one will be analyzed. The following temperatures were chosen for the tests: 40 °C, 25 °C, 10 °C, 0 °C and –10 °C. This decision was based on the limitations of the cell, as well as various examples in literature that demonstrated that this variation sufficiently covered the temperature range of a lithium-ion cell in automotive applications [29, 33, 83].

Figure 4.1 provides an overview of the test sequence, the temperatures for each test as well as the specific purpose for each test. For the remainder of this thesis, the following abbreviations will be used when describing test procedures: **constant current (CC)** and **constant voltage (CV)**. A summary of the cell protection limits used during the characterization tests is listed in Table 4.1. Each test procedure will be covered in more detail in the

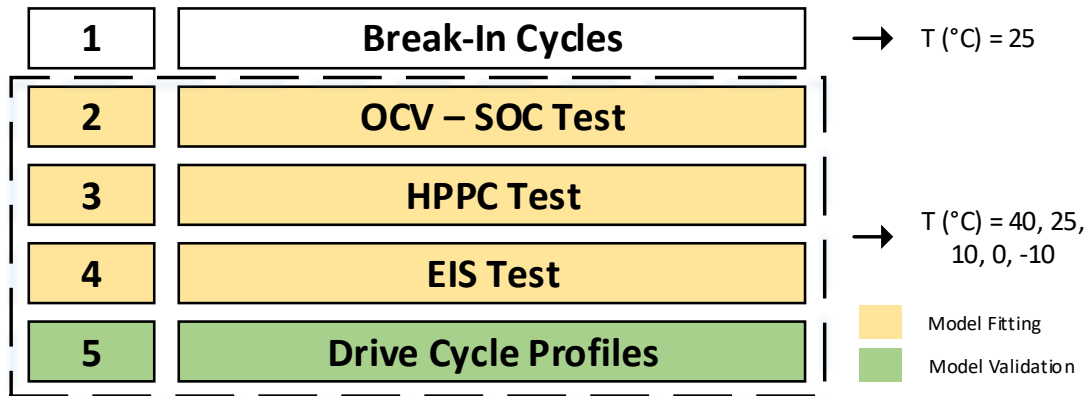


Figure 4.1: An overview of the tests used to characterize a lithium ion cell

Table 4.1: Hardware protection limits used during characterization tests

Specification	Hardware Protection Limit			
Voltage [V]	Maximum	4.25	Minimum	2.45
Current [A]	Maximum Charge	5	Maximum Discharge	15
Charge Temperature [°C]	Maximum	45	Minimum	-25
Discharge Temperature [°C]	Maximum	45	Minimum	-25

coming sections. However, the applied drive cycle profiles will be discussed in Section 5.4 as part of the impedance model validation.

4.1 Break-in Cycles

A series of ten break-in cycles was performed at room temperature (25 °C) before characterizing the battery. The procedure for these cycles is summarized below:

1. The temperature of the chamber is set to 25 °C.
2. When the surface temperature of the cell has reached a value of $25\text{ °C} \pm 2$ degrees, proceed to step 3.
3. Charge the cell at 0.5C (2450 mA) CC until the upper voltage limit, then switch to CV with a cut-off current of 0.02C (98 mA).
4. 15 minute delay.
5. Discharge the cell at 0.5C (2450 mA) CC until the lower voltage limit specified.
6. 15 minute delay.
7. Repeat steps 3-6 for a total of 10 cycles.

A visual representation of one break-in cycle is given in Figure 4.2, which shows the applied current and measured voltage during each portion of the cycle. The applied current for the entire series of break-in cycles, as well as the measured voltage of the cell, are presented in Figures 4.3 and 4.4, respectively.

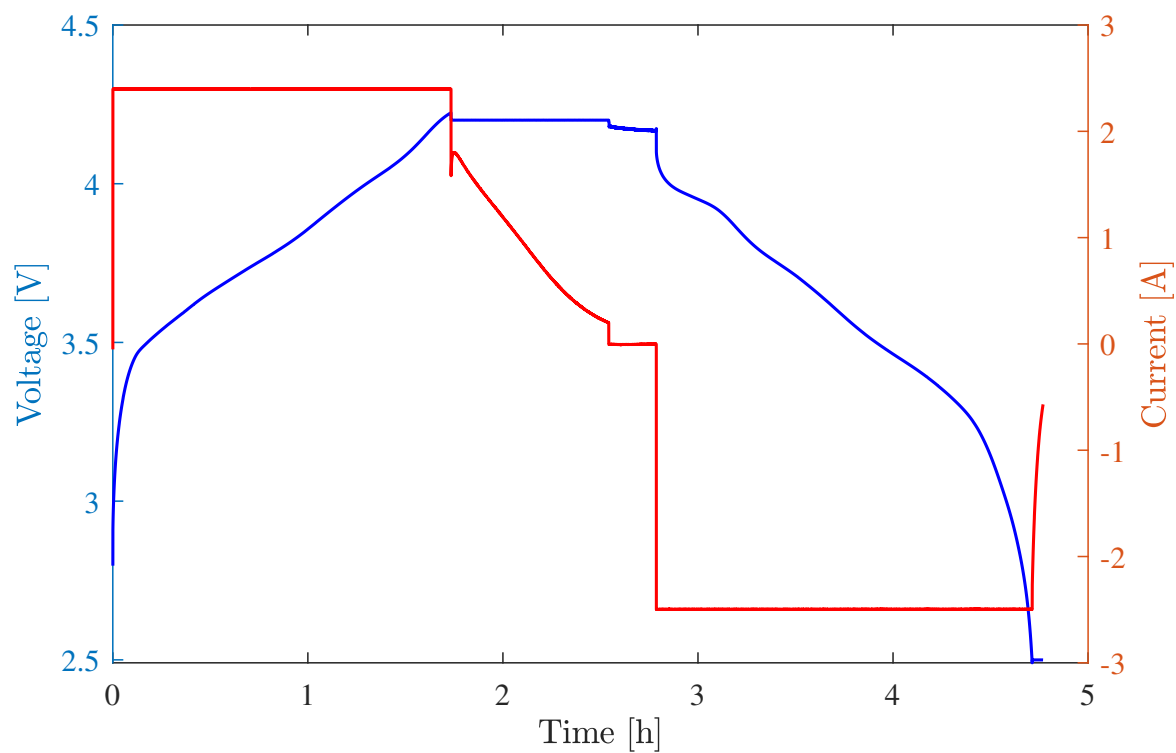


Figure 4.2: Applied current and measured voltage of the cell during a single break-in cycle

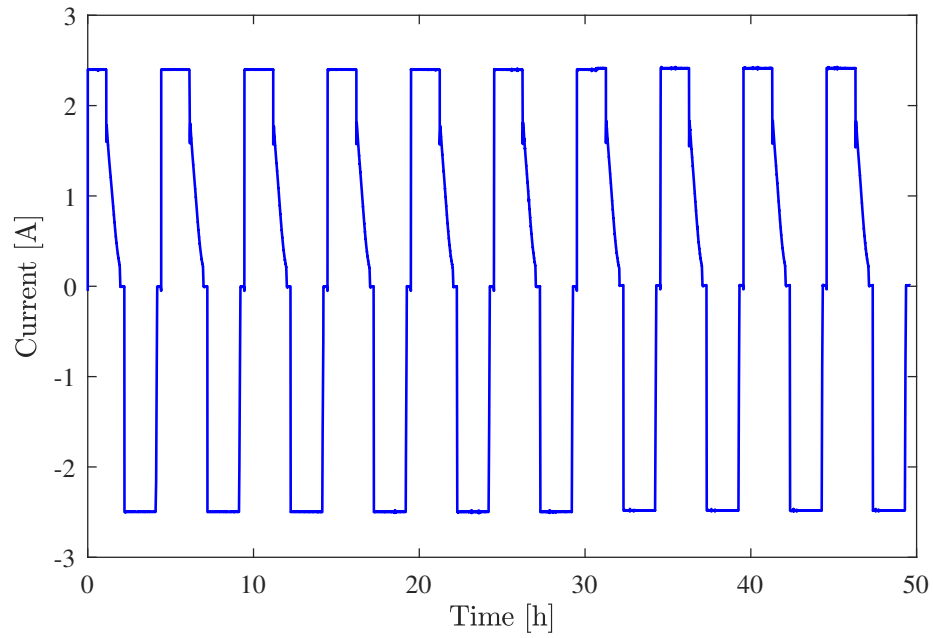
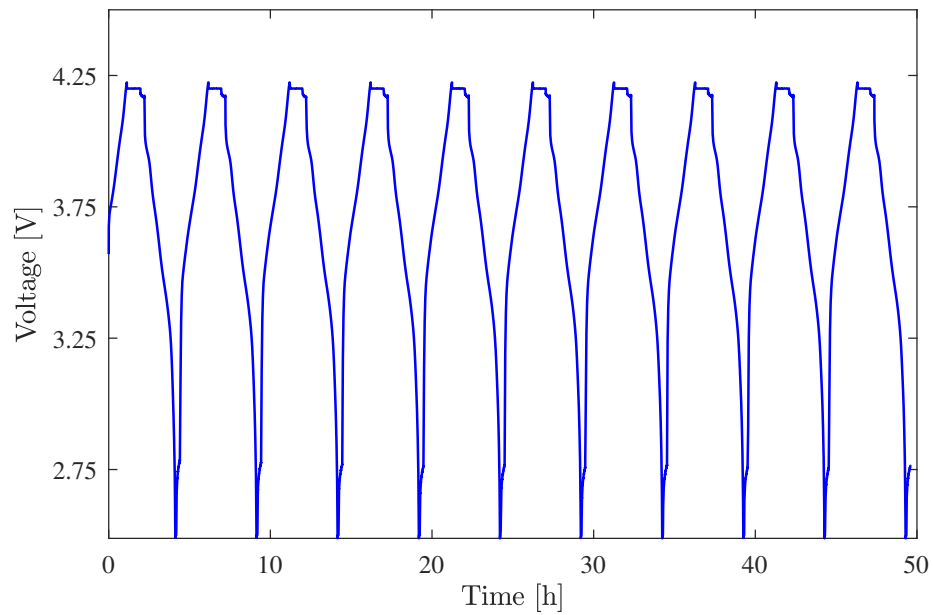


Figure 4.3: Applied current profile for break-in cycles

Figure 4.4: Measured voltage during break-in cycles ($T = 25\text{ }^{\circ}\text{C}$)

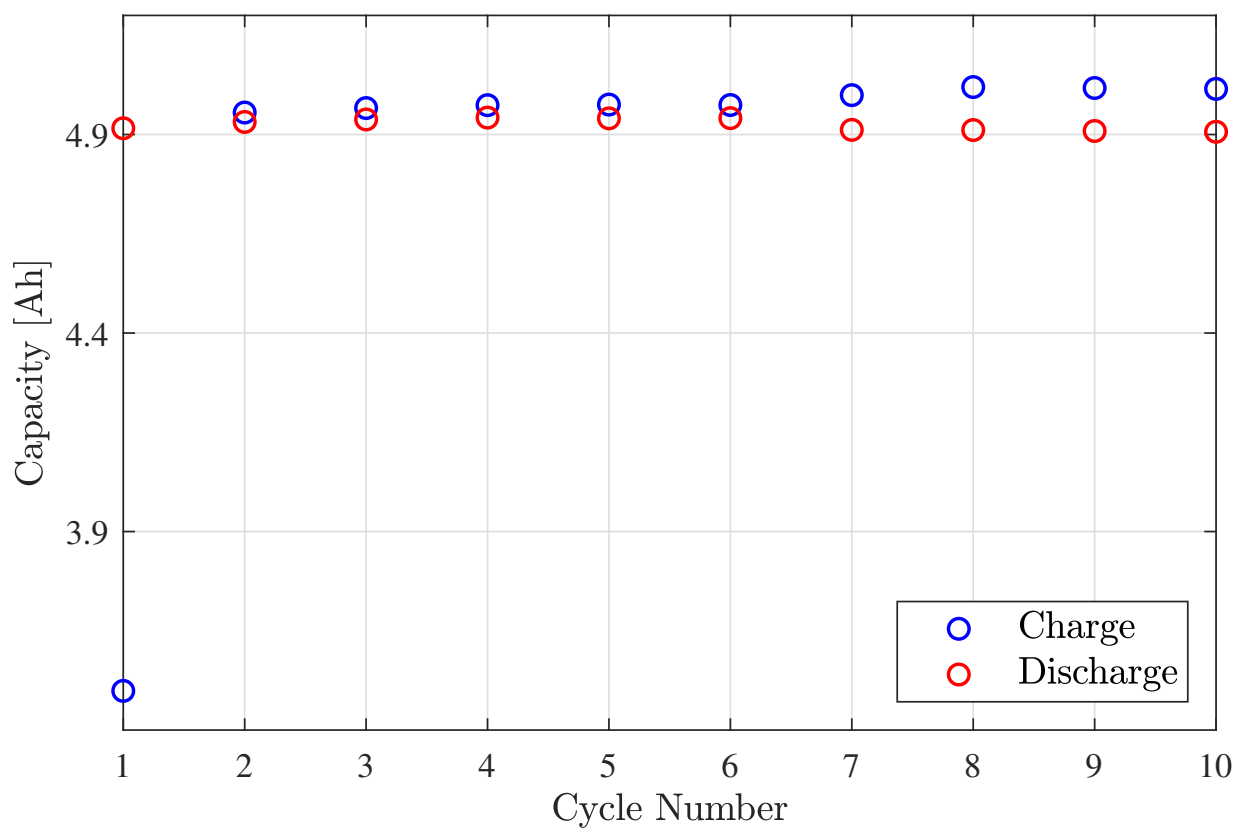


Figure 4.5: Charging and discharging capacity of the cell during the course of break-in cycling ($T = 25^{\circ}\text{C}$)

The effect of the break-in cycles on the capacity of the cell is demonstrated in Figure 4.5. The capacity for the first charge cycle is much lower compared to the remaining cycles due to the shipping condition of the cell, where it is partially charged. Furthermore, it can be noted that after the first cycle, the charge capacity is consistently higher than the discharge capacity. The reasoning behind this difference is the coulombic efficiency of the cell, which is the ratio between the two capacities as described in Equation (4.1):

$$CE = \frac{Q_{Discharge}}{Q_{Charge}} \cdot 100 \% \quad (4.1)$$

For a fresh cell, this ratio is very high, but typically does not reach 100 %. In this case, the coulombic efficiency of the cell is approximately 98 %, hence the slight difference between the discharge and charge capacities. Furthermore, the CV portion of the charge cycle slowly decreases the applied current to a specified point, as shown in Figure 4.2. This allows additional energy to be cycled into the cell, which contributes to the difference between the charge and discharge capacities. Ten break-in cycles was considered sufficient as they caused the capacity of the cell to reach a stable value, as highlighted in Figure 4.5, with a change of less than 0.05 % between three consecutive cycles.

4.2 OCV - SOC Test

An OCV-SOC test is used to characterize the OCV of the cell as a function of SOC. It is also performed at each individual temperature chosen for testing, to capture the dependence of OCV on temperature. This test is performed at a very low C-rate (C/20) in order to

minimize the cell dynamics and reduce the effects of the internal resistance of the cell, so that the terminal voltage of the cell can be considered an approximation of the OCV. The procedure for this test is summarized below:

1. The temperature of the chamber is set to 25 °C.
2. When the surface temperature of the cell has reached a value of 25 °C \pm 2 degrees, proceed to step 3.
3. Charge the cell to 100% SOC at 0.5C (2450 mA) CC until the upper voltage limit specified, then switch to CV with a cut-off current of 0.02C (98 mA).
4. 1 hour delay to allow the cell to relax.
5. The temperature of the chamber is set to the desired value (i.e. the temperature required for characterization).
6. When the surface temperature of the cell has reached a value that is within 2 degrees of the desired temperature, proceed to step 7.
7. Discharge the cell at C/20 (245 mA) CC.
8. 1 hour delay to allow the cell to relax.
9. Charge the cell at C/20 (245 mA) CC.
10. Repeat steps 4-9 as required.

The procedure for a C/20 discharge and charge is visualized in Figures 4.6 and 4.7, respectively. Several studies in literature have demonstrated that a period of one hour is

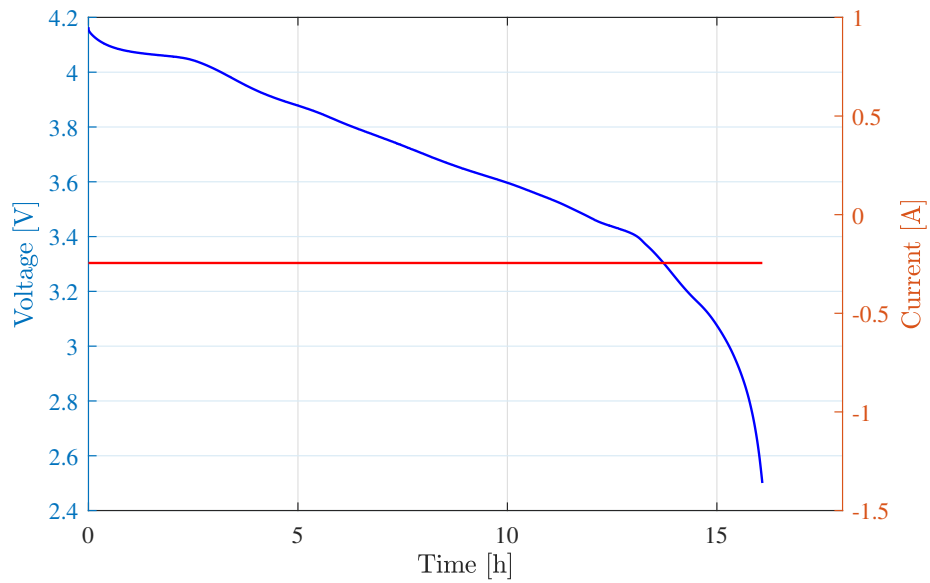


Figure 4.6: Applied current and measured voltage during a C/20 discharge ($T = 25\text{ }^{\circ}\text{C}$)

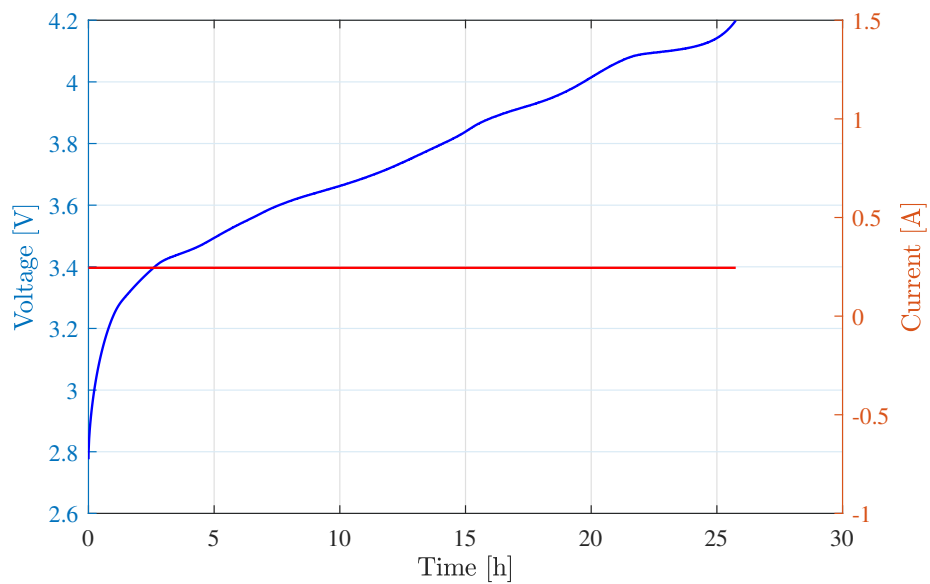


Figure 4.7: Applied current and measured voltage during a C/20 charge ($T = 25\text{ }^{\circ}\text{C}$)

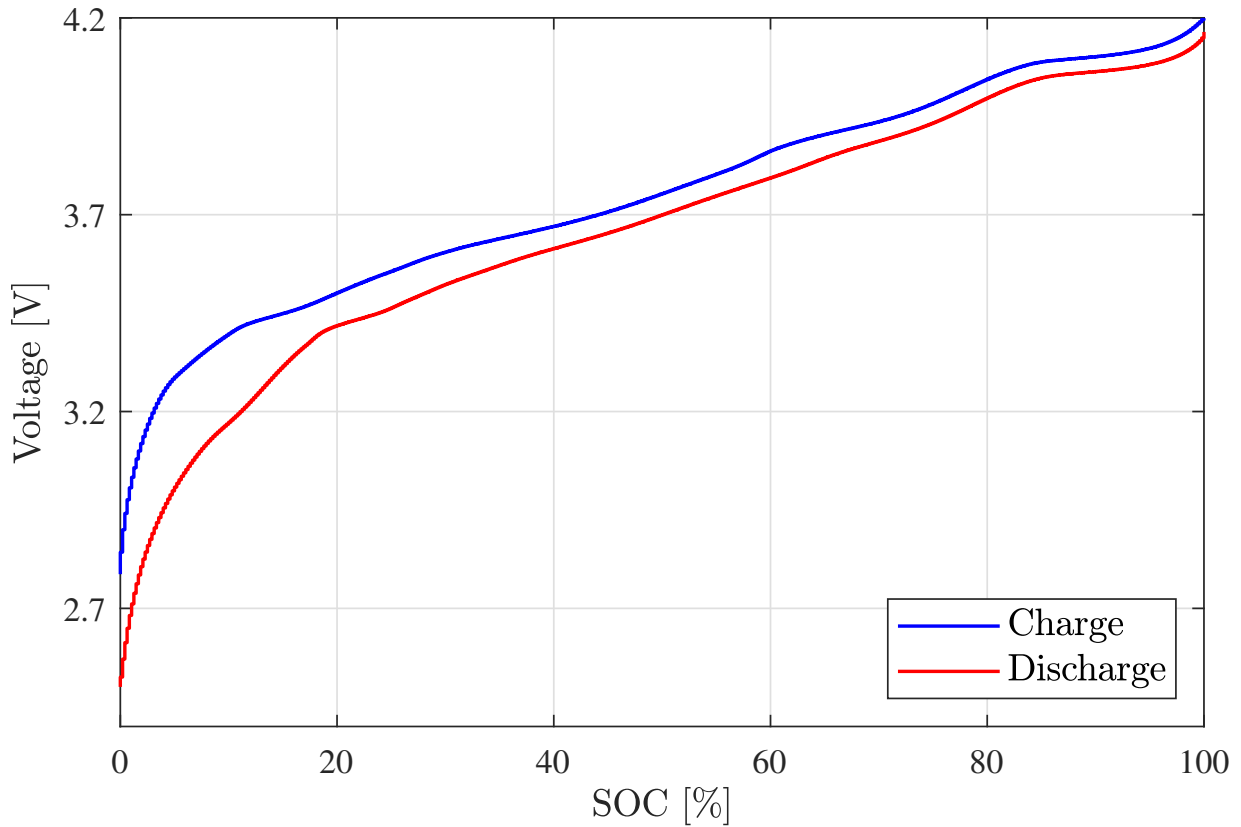


Figure 4.8: Hysteresis effect observed between charge and discharge curves during an OCV-SOC test ($T = 25\text{ }^{\circ}\text{C}$)

sufficient to allow the cell to relax and the OCV to reach a stable value, therefore it was considered appropriate for these characterization tests [29, 33, 53].

Figure 4.8 presents the OCV-SOC relationship recorded for the cell at $25\text{ }^{\circ}\text{C}$. A lag between the charge and discharge curves is observed, which can be attributed to hysteresis in the cell as well as ohmic resistance effects [61]. It has been shown in literature that, to account for these differences, taking the average of the discharge and charge curves can yield the true OCV-SOC relationship of the cell [24, 53, 61]. Therefore, the discharge

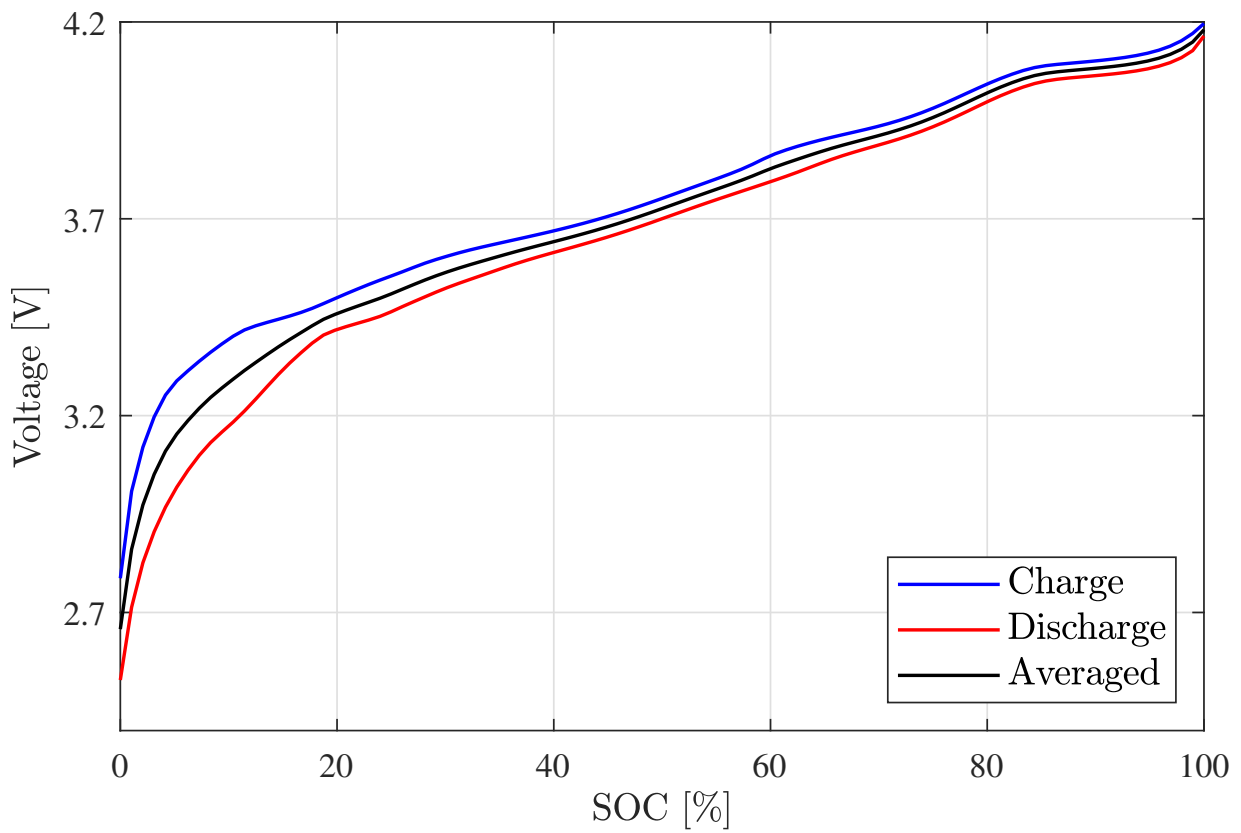


Figure 4.9: Resampled discharge and charge OCV-SOC curve with averaged curve ($T = 25^{\circ}\text{C}$)

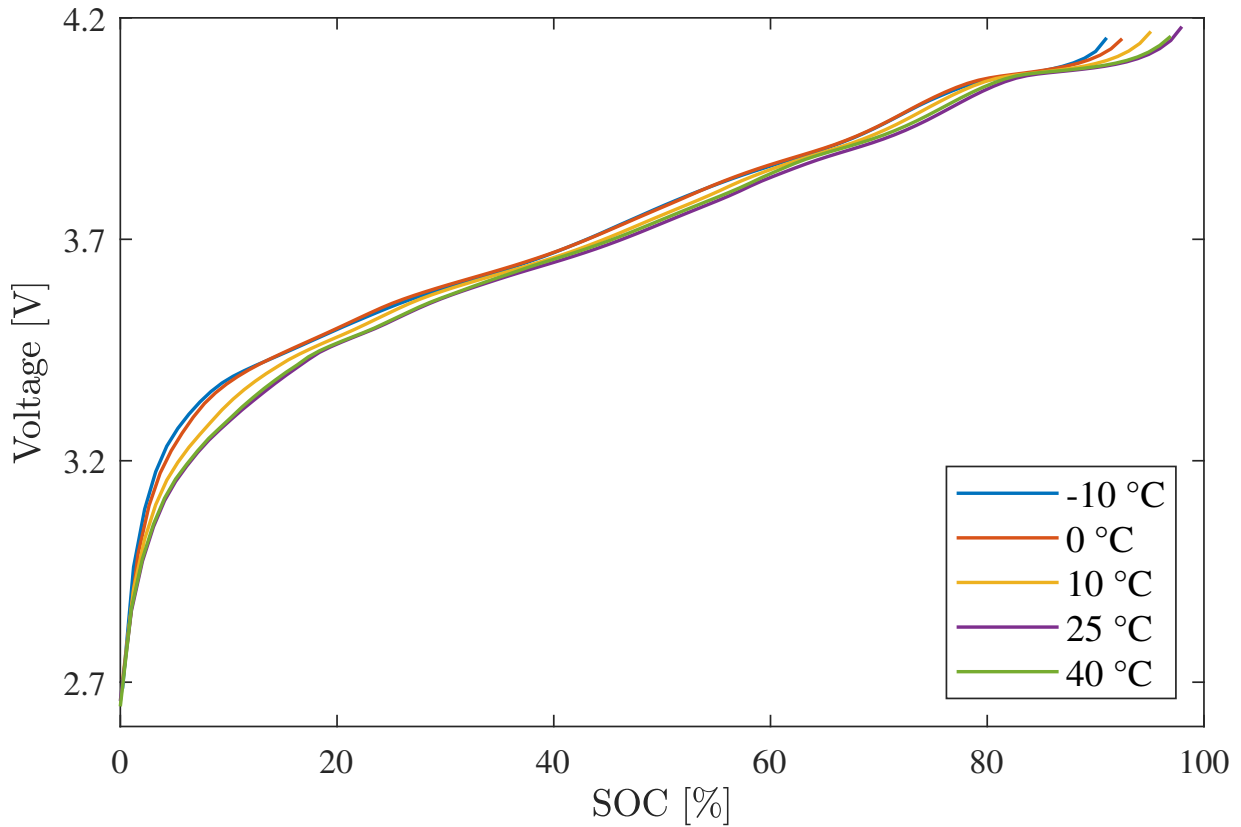


Figure 4.10: OCV-SOC relationship across a range of temperatures

and charge curves were resampled and averaged to obtain a single OCV-SOC relationship curve, as shown in Figure 4.9. This adjustment was repeated for all of the temperatures used to characterize the cell.

The results of the OCV-SOC test are presented in Figure 4.10 and demonstrate a clear dependence on the operating temperature of the cell. This dependency is particularly notable at temperatures below 25 °C where it is observed that the OCV of the cell is reduced. These results emphasize the need for this test, to increase the accuracy of the impedance model by accounting for the OCV as a function of temperature. The data from

Table 4.2: Summary of parameters used for HPPC test

Discharge Pulses [C]	Charge Pulses [C]	SOC Range [%]
0.5	0.25	
1	0.5	
2	0.75	100, 95, 90, 80 ... 30, 25, 20 ... 0
3	1	

this test will be stored as a look-up table that will be implemented as part of the impedance model validation, which will be discussed further in Chapter 5.

4.3 HPPC Test

An HPPC test is used to obtain the internal resistance of the cell, which is an important parameter that helps to identify its dynamic behaviour. This test was performed for an entire SOC range (100% - 0%) using different C-rates, to characterize the cell over a wide span of operating conditions. Table 4.2 provides a summary of the operating parameters used to conduct the HPPC test. The procedure for this test is summarized below:

1. The temperature of the chamber is set to 25 °C.
2. When the surface temperature of the cell has reached a value of 25 °C \pm 2 degrees, proceed to step 3.
3. Charge the cell to 100% SOC at 0.5C (2450 mA) CC until the upper voltage limit specified, then switch to CV with a cut-off current of 0.02C (98 mA).

4. The temperature of the chamber is set to the desired value (i.e. the temperature required for characterization).
5. When the surface temperature of the cell has reached a value that is within 2 degrees of the desired temperature, proceed to step 6.
6. 1 hour delay to allow the cell to relax.
7. Apply discharge pulse for 10 seconds. The accumulated discharge from this step is recorded.
8. Return the cell to the correct SOC level by charging at 0.3C (1470 mA) CC to counter the discharge recorded in step 7.
9. Apply charge pulse for 10 seconds. The accumulated charge from this step is recorded.
10. Return the cell to the correct SOC level by discharging at 0.3C (1470 mA) CC to counter the charge recorded in step 9.
11. 10 minute delay.
12. Repeat steps 7-11 for a total of 4 pulse sets (as listed in Table 4.2).
13. Discharge the cell to the next SOC level at 0.3C (1470 mA) CC. The increments for discharging above 90 %, between 90 % and 30 %, and below 30 % SOC are described in Table 4.2.
14. Repeat steps 6-13 for the entire SOC range of the test.
15. Repeat steps 1-14 for all of the temperatures used to characterize the cell.

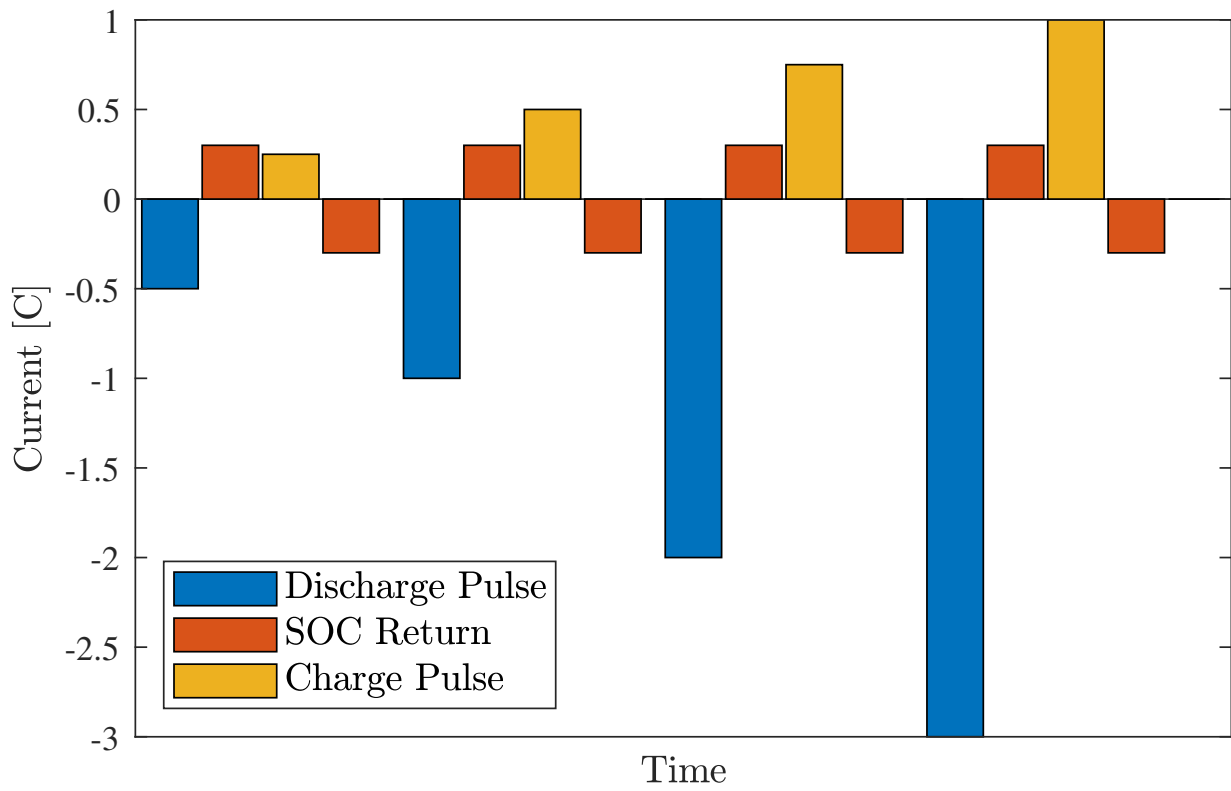


Figure 4.11: Pulse profile applied to cell during HPPC test

The pulse profile applied to the cell is visualized in Figure 4.11 which shows the magnitude of each pulse, the SOC correction after each pulse and the delay between each set of pulses. The applied current profile for an entire HPPC test, as well as the measured voltage response of the cell, are shown in Figures 4.12 and 4.13, respectively. A closer look at a single set of pulses, as well as the measured voltage response of the cell, is provided in Figure 4.14. The internal resistance of the cell is calculated in the manner described in Section 2.5.4.

The dependence of the cell's internal resistance on SOC is demonstrated in Figure 4.15. This characteristic is relatively consistent between 20% and 90% SOC, with a slight increase right before and after this range. Furthermore, the internal resistance shows a significant increase at SOC values below 20%. While the resistance values themselves differ, this trend is consistent for all of the temperatures presented. This data is also visualized in Figure 4.16, which shows the dependence of the cell's internal resistance on SOC across all of the temperatures used for characterization. It can be seen that the characteristic described earlier remains fairly unchanged for all temperatures. However, it can be noted that at lower temperatures, especially -10°C , the increase in resistance below 20% SOC is much higher. This observation at lower temperatures is also demonstrated in Figure 4.17, which shows the internal resistance normalized to 25°C . It can be seen here how the resistance increases as the temperature of the cell is lowered, which occurs at all SOC levels. It is also observed that at lower temperatures, the resistance increases at a higher rate, as previously demonstrated in Figures 4.15 and 4.16.

The nonlinear response of the cell with respect to internal resistance is also highlighted when looking at the measured data for different pulse current values. This characteristic is

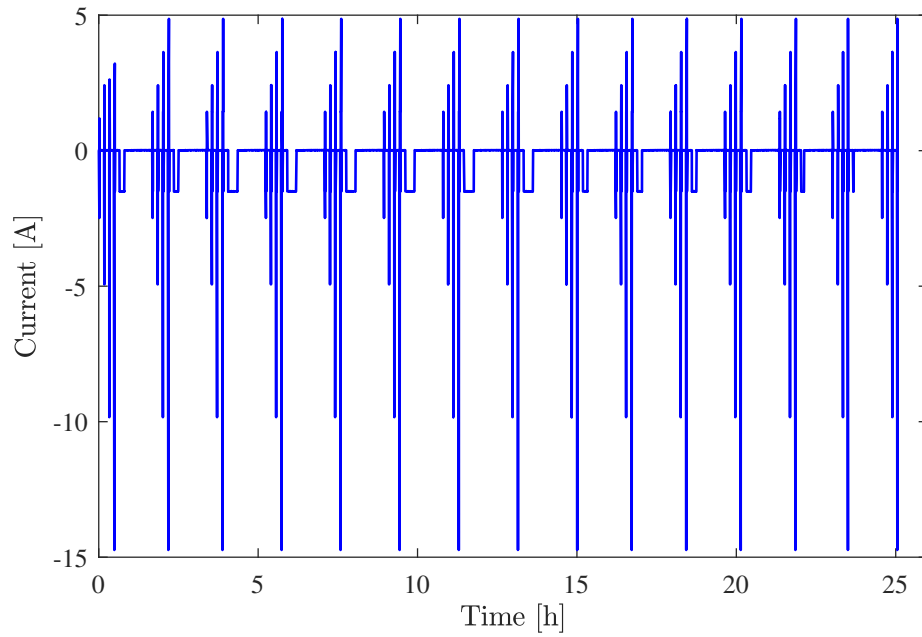


Figure 4.12: Applied current during entire duration of HPPC test ($T = 25\text{ }^{\circ}\text{C}$)

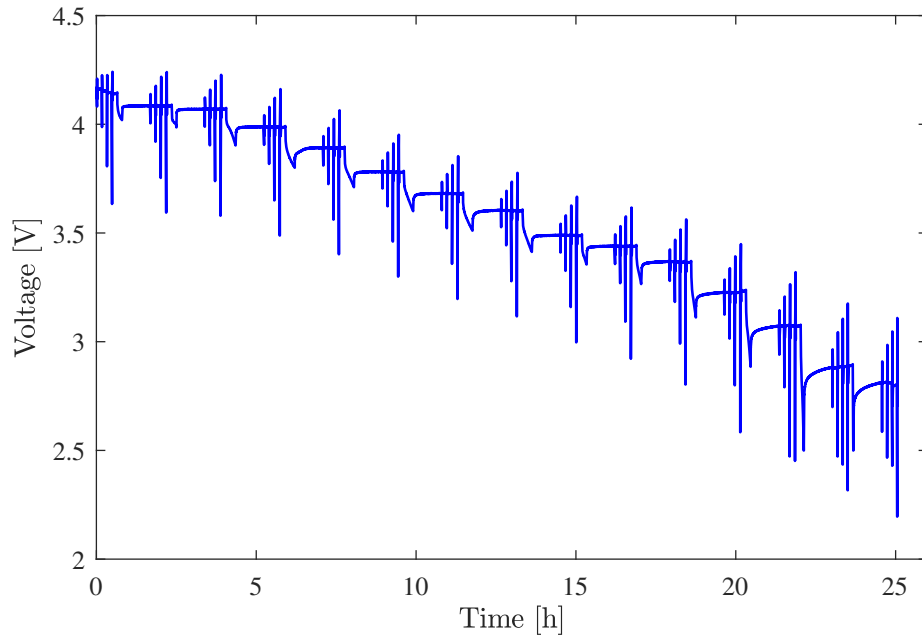


Figure 4.13: Measured voltage response of the cell during entire duration of HPPC test ($T = 25\text{ }^{\circ}\text{C}$)

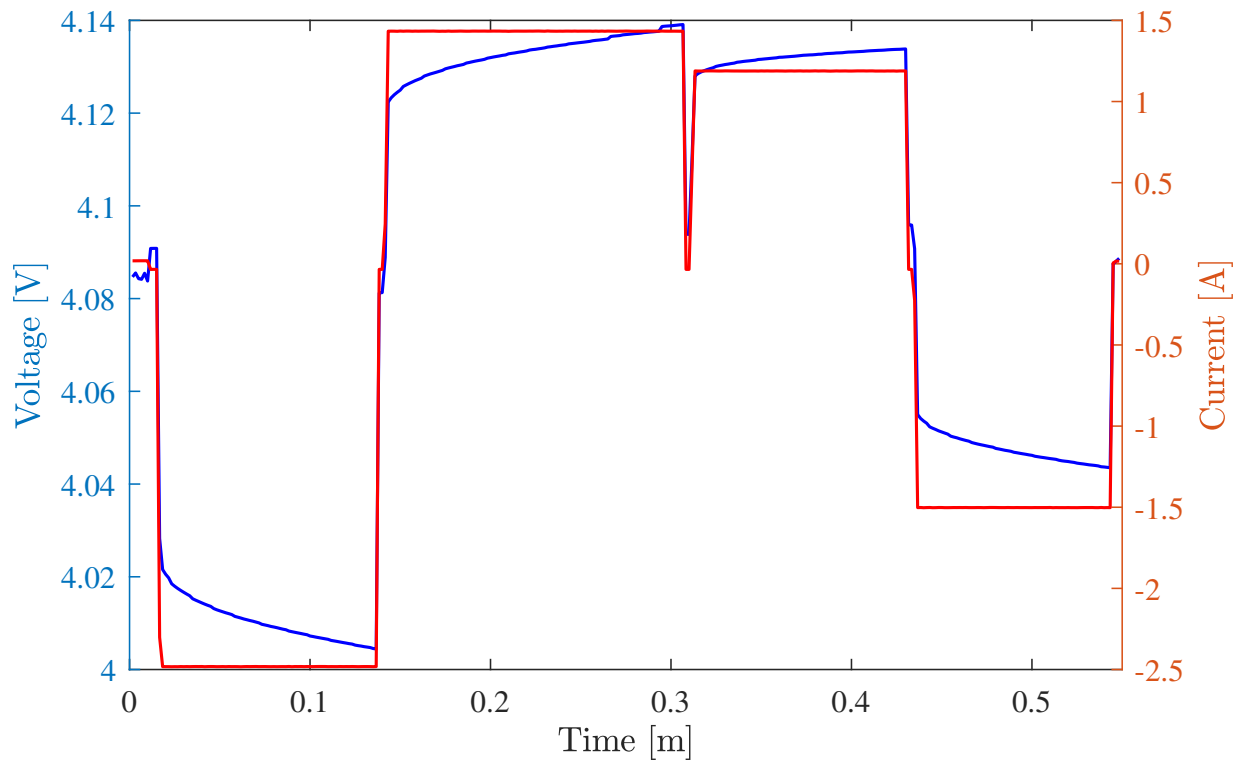


Figure 4.14: Applied current pulses and measured voltage response of the cell ($T = 25\text{ }^{\circ}\text{C}$, 90% SOC)

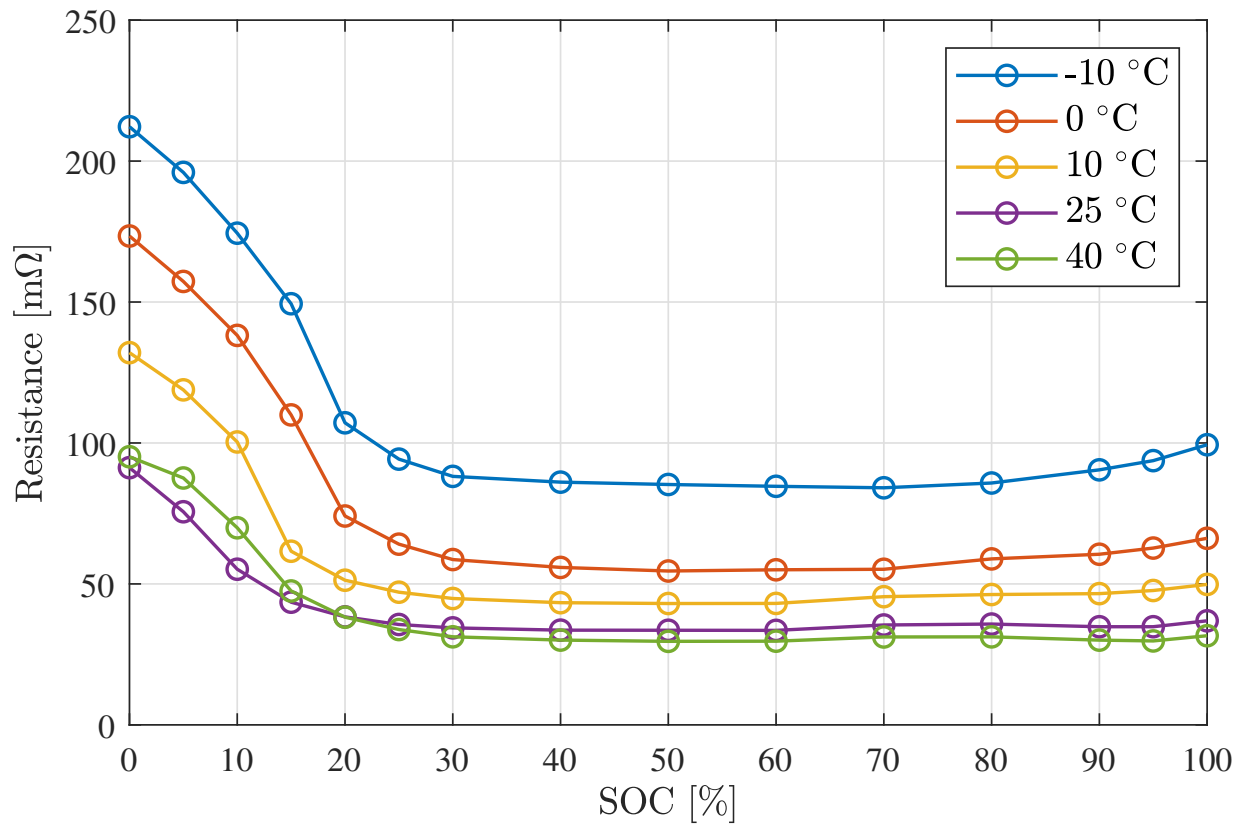


Figure 4.15: Internal resistance of the cell at different SOC values (measured for 0.5C discharging current)

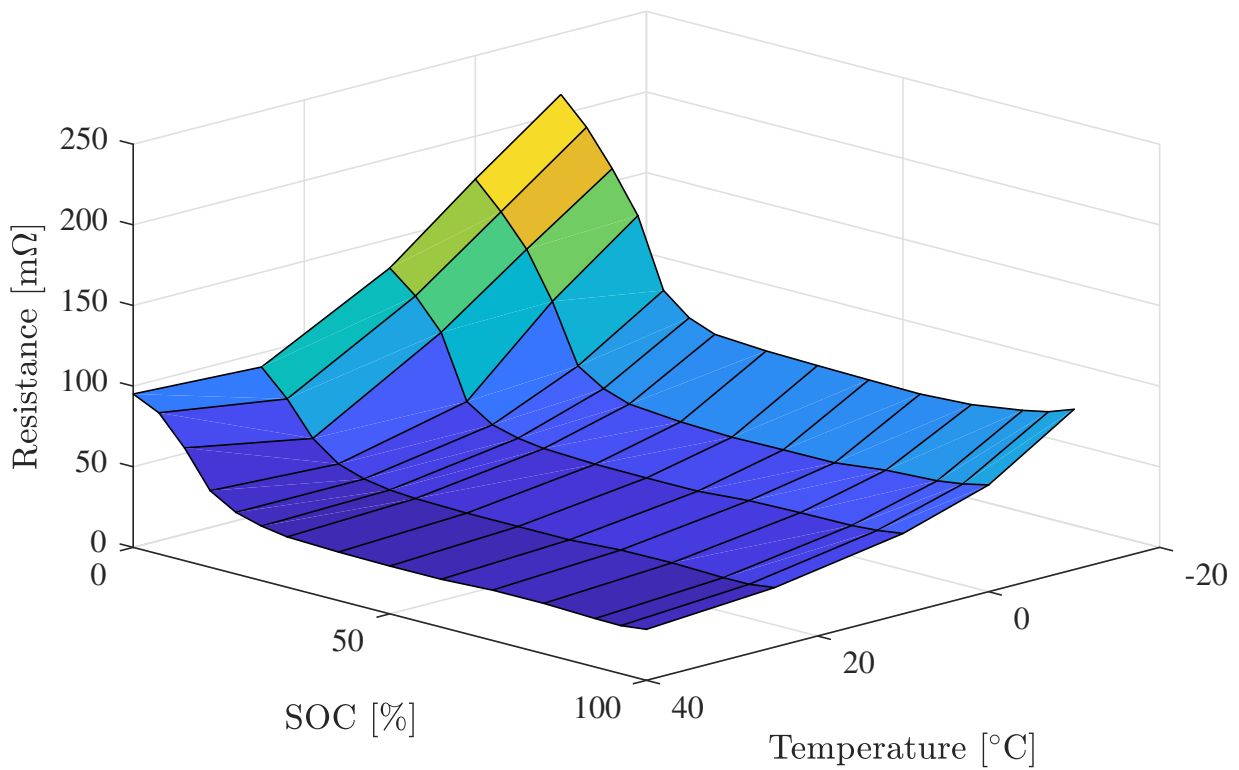


Figure 4.16: Internal resistance of the cell across all SOC values and temperatures (measured for 0.5C discharging current)

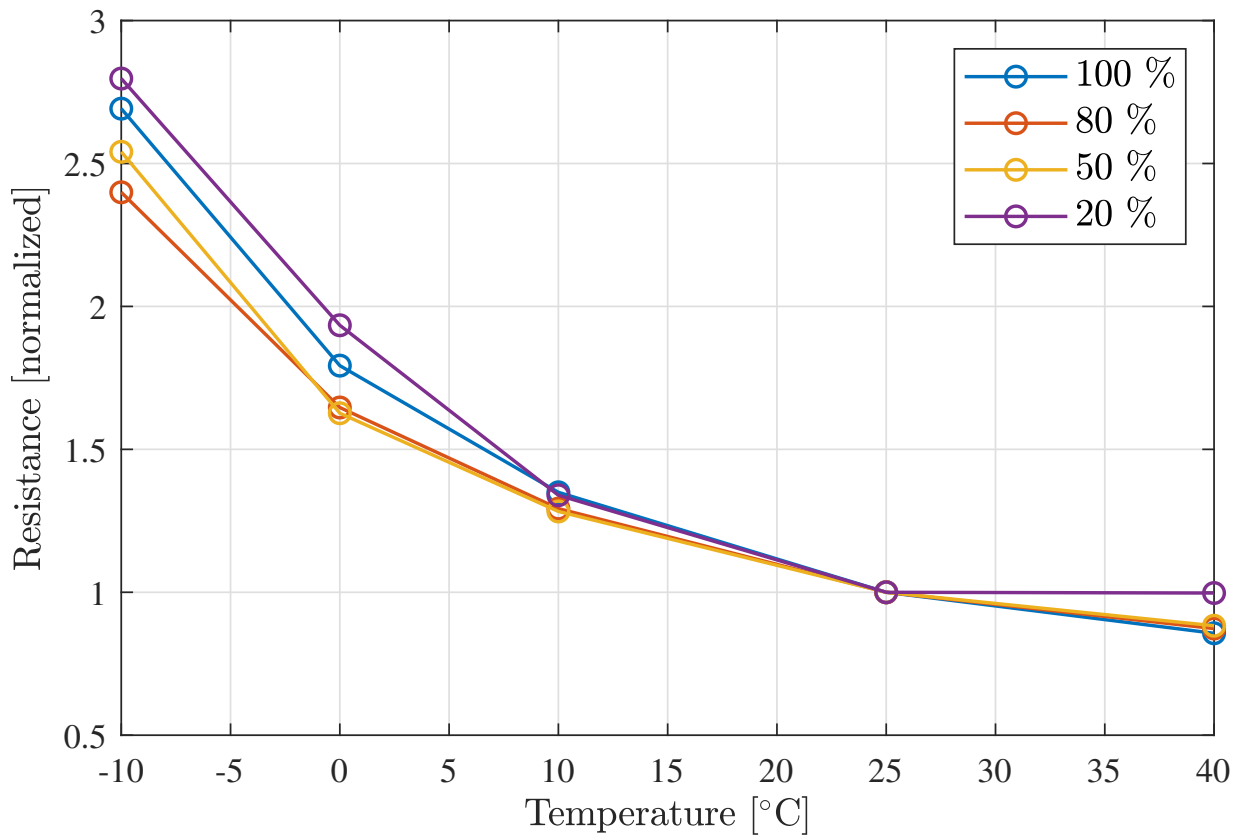


Figure 4.17: Normalized resistance versus temperature (measured for 0.5C discharging current)

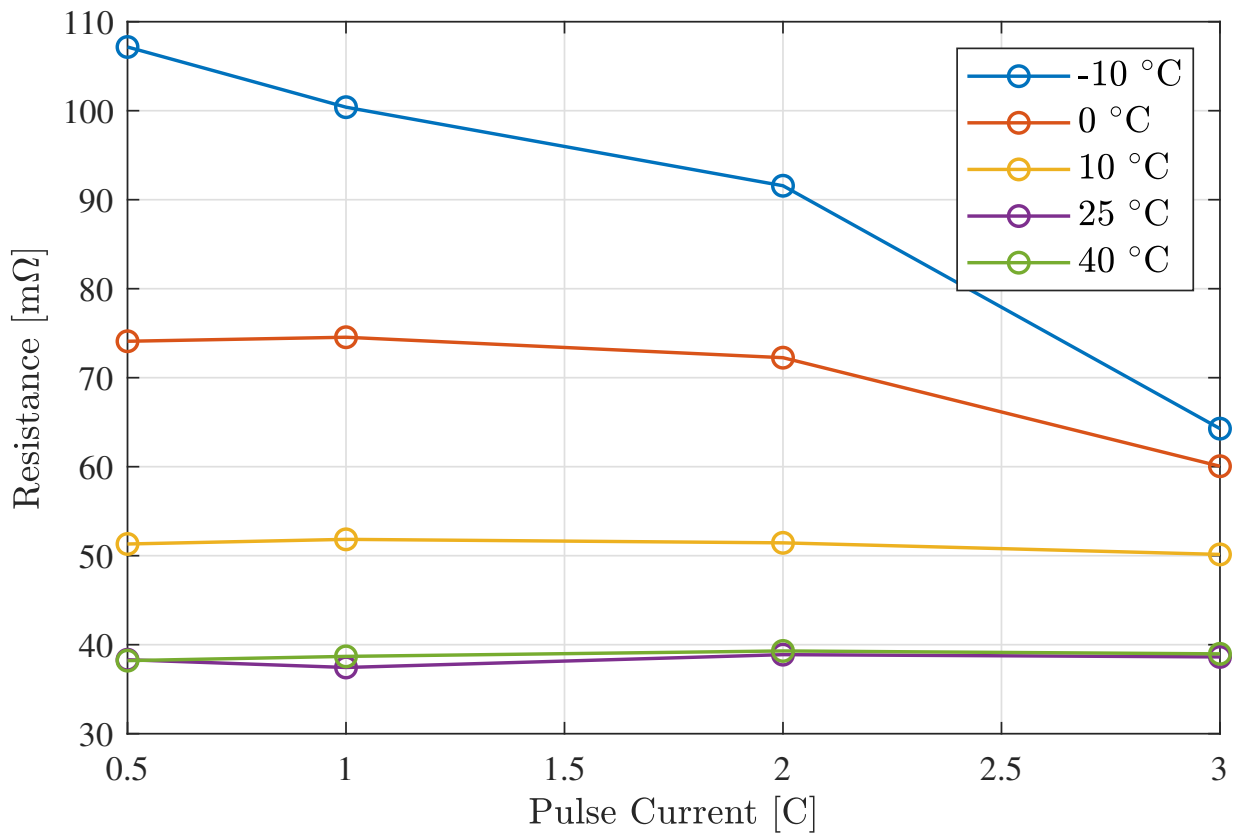


Figure 4.18: Internal resistance of the cell at different pulse current values (20% SOC)

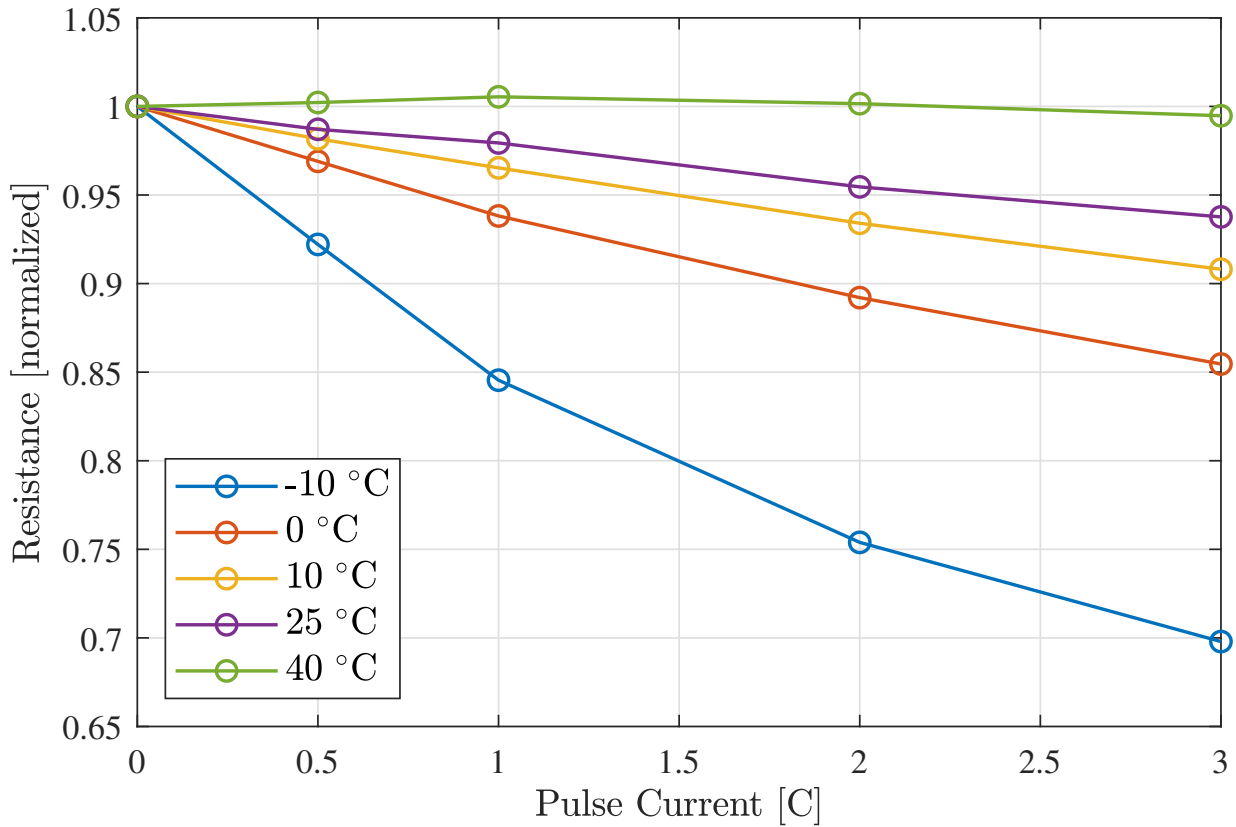


Figure 4.19: Normalized resistance versus pulse current between 80 % and 70 % SOC

illustrated in Figure 4.18, which shows how the internal resistance is not consistent across all of the pulse currents at lower temperatures, particularly -10°C . To better illustrate this characteristic, the measured resistance is normalized and extrapolated to OC current, as presented in Figure 4.19. It is observed that the internal resistance of the cell decreases at greater pulse currents, and this relationship gradually becomes more nonlinear as the temperature of the cell is lowered. This characteristic is prominent at -10°C where it is obvious that the resistance decreases at a much higher rate compared to 0°C and above. This nonlinear dependence on current can be interpreted using the Butler-Volmer equation

Table 4.3: Summary of parameters used for EIS test

Temperature [°C]	Frequency Range	Points Per Decade	Current Amplitude [A]
40, 25, 10, 0	30 kHz - 1 mHz	10 (above 1 Hz) 5 (below 1 Hz)	0.1
-10	30 kHz - 100 μ Hz	10 (above 1 Hz) 5 (below 1 Hz)	0.1

and will be covered in greater detail as part of the model parameterization in Chapter 5.

The results from the HPPC test demonstrate the clear dependence of the cell's internal resistance on various operating conditions. Namely, the cell's dynamic behaviour is not consistent at different current values, particularly at lower temperatures. Therefore, this characteristic is a crucial component of the impedance model that is studied during this research. Having an accurate representation of this parameter for all current values, across all SOC values and at all temperatures, will help increase the accuracy of the model.

4.4 EIS Test

EIS testing was used to characterize the impedance of the cell across a wide array of operating conditions. Similar to the HPPC test, this test was carried out at the entire SOC range (100% - 0%) at each temperature. It was performed in galvanostatic mode without DC bias current.

The parameters used for the EIS test are given in Table 4.3. The frequency points are distributed using a logarithmic scale, and the number of points below 1 Hz was reduced

to minimize the total test time without compromising the quality of the impedance plots. To better capture the diffusion of the cell at $-10\text{ }^{\circ}\text{C}$, the frequency range was extended to $100\text{ }\mu\text{Hz}$. The current amplitude for the applied signal was selected after considering the following criteria:

- It must be small enough to capture the response of the cell in a linear state. If the system is nonlinear, then the response of the cell will contain harmonics of the applied frequency [28]. It is suggested in literature that the current amplitude should not be larger than 5% of the standard charge current specified by the cell manufacturer [84].
- It must be as small as possible to reduce the amount of cycling that the cell undergoes during testing. For example, a $100\text{ }\mu\text{Hz}$ applied signal will have a half period of roughly 1.4 hours. At an amplitude of 0.5 A this would amount to 0.7 A h being cycled into the cell, which translates approximately to a 14% SOC swing. Therefore, it is important to keep the applied signal small to prevent the cell from aging excessively during testing.

In order to identify the most suitable amplitude, a simple EIS test (10 kHz - 10 mHz, 10 points per decade) was performed at various current amplitudes between 0.9 A and 0.01 A. Some of the results from this test are presented in Figure 4.20. It was found that an amplitude as low as 0.1 A provided a sufficient impedance spectrum. Below 0.1 A the measured data is poor, as seen in Figure 4.20. This can be attributed to a voltage measurement with an insufficient accuracy which results in a ratio of noise to signal that is too large. Therefore, 0.1 A was selected as an appropriate amplitude to be used for

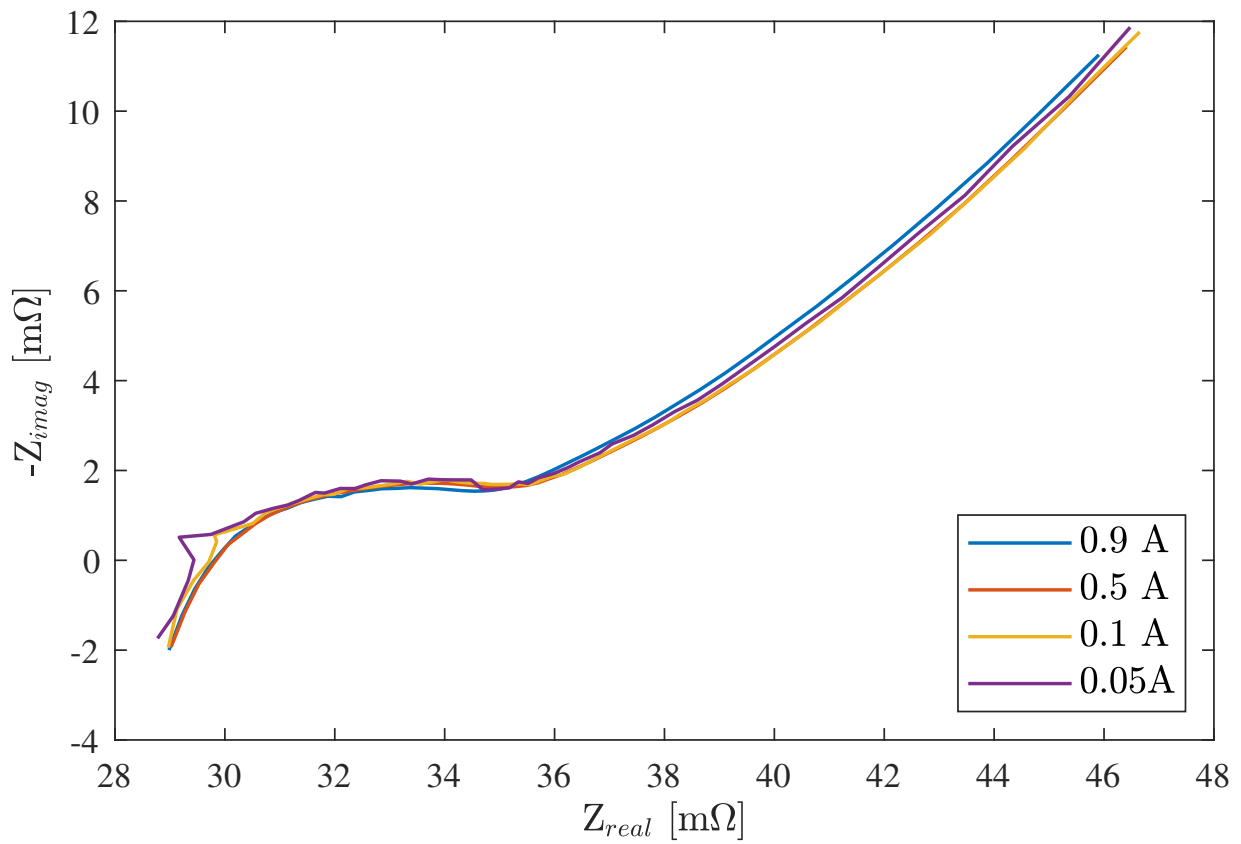
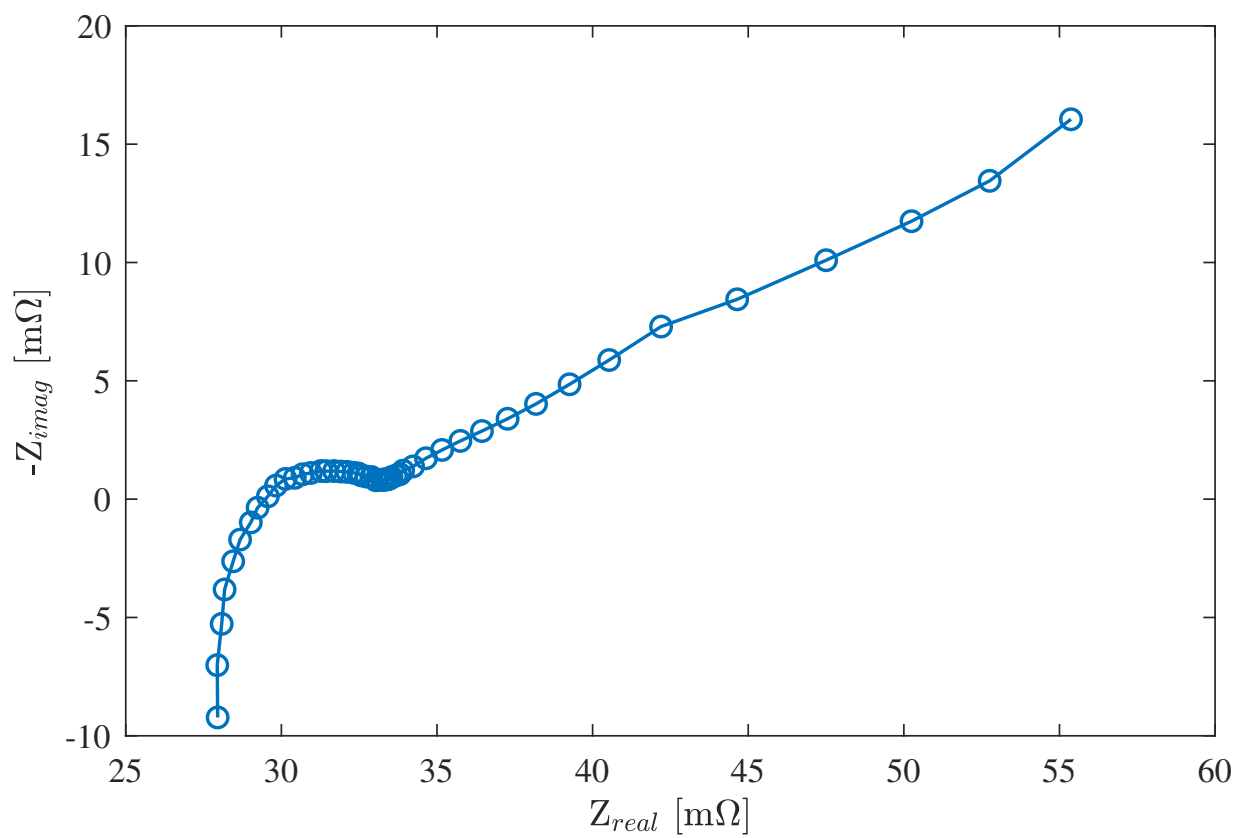


Figure 4.20: Results of simple EIS measurement sweep to determine appropriate current amplitude ($T = 25^\circ\text{C}$)

impedance characterization. This was the smallest amplitude that gave a small noise to signal ratio while retaining the cell in a piecewise linear region.

The procedure for this test is summarized below:

1. The temperature of the chamber is set to 25 °C.
2. When the surface temperature of the cell has reached a value of 25 °C \pm 2 degrees, proceed to step 3.
3. Charge the cell to 100 % SOC at 0.5C (2450 mA) CC until the upper voltage limit specified, then switch to CV with a cut-off current of 0.02C (98 mA).
4. The temperature of the chamber is set to the desired value (i.e. the temperature required for characterization).
5. When the surface temperature of the cell has reached a value that is within 2 degrees of the desired temperature, proceed to step 6.
6. 1 hour delay to allow the cell to relax.
7. Perform EIS test using the parameters listed in Table 4.3.
8. 10 minute delay.
9. Discharge the cell to the next SOC level at 0.3C (1470 mA) CC.
10. Repeat steps 6-9 for the entire SOC range of the test.
11. Repeat steps 1-10 for all of the temperatures used to characterize the cell.

Figure 4.21: Impedance spectrum of cell ($T = 25\text{ }^{\circ}\text{C}$, 95% SOC)

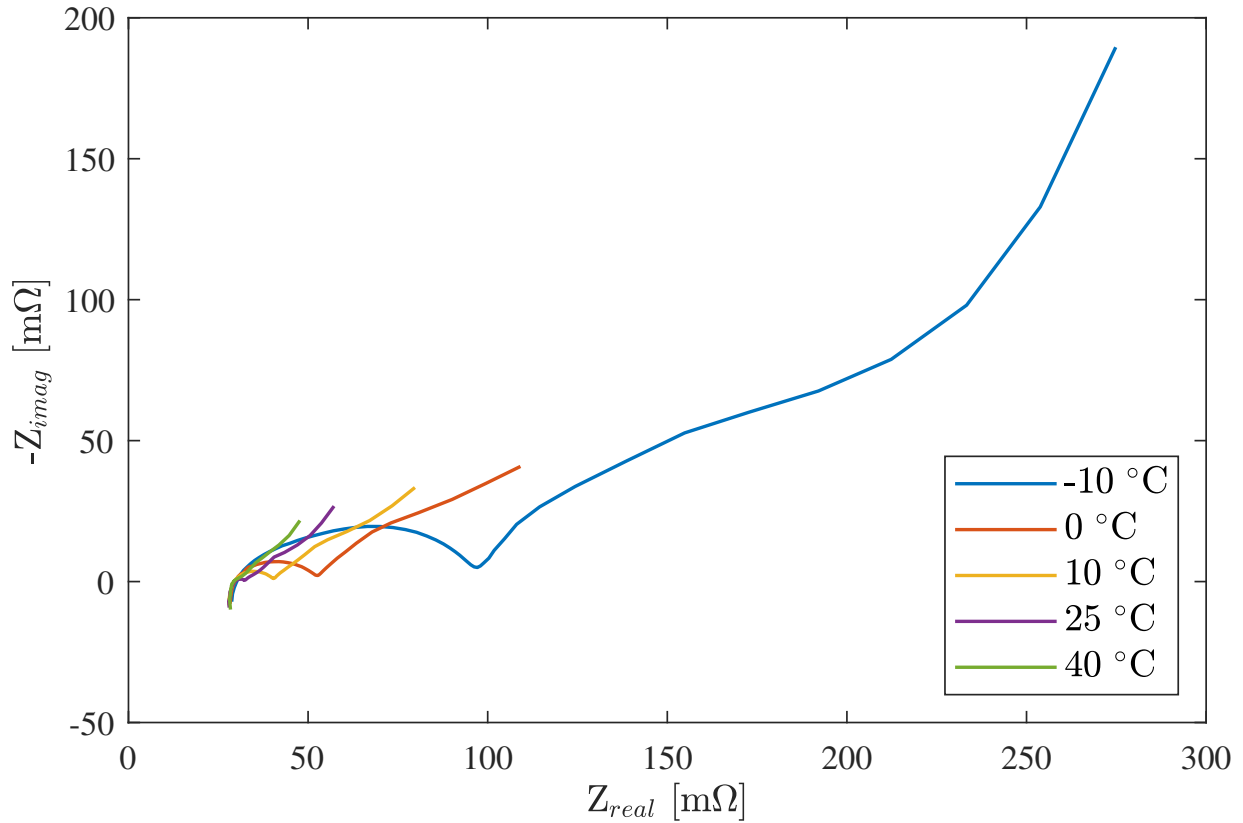


Figure 4.22: Dependence of cell's impedance spectra on operating temperature (measured at 60% SOC)

The impedance spectrum of the cell, measured at 25 °C and 95% SOC, is presented in Figure 4.21. The dependence of the cell's impedance on temperature is illustrated in Figure 4.22. Figure 4.23 provides a closer look at the high frequency region of the plot, where changes are more easily observed. At lower temperatures the intercept with the real axis shifts to the right, indicating an increase in the ohmic resistance of the cell, which is consistent with the results of the HPPC test. Furthermore, the charge transfer process of the cell is highly dependent on the operating temperature of the cell, as a result of slower reactions inside the cell. This is highlighted by the clear growth in the shape of

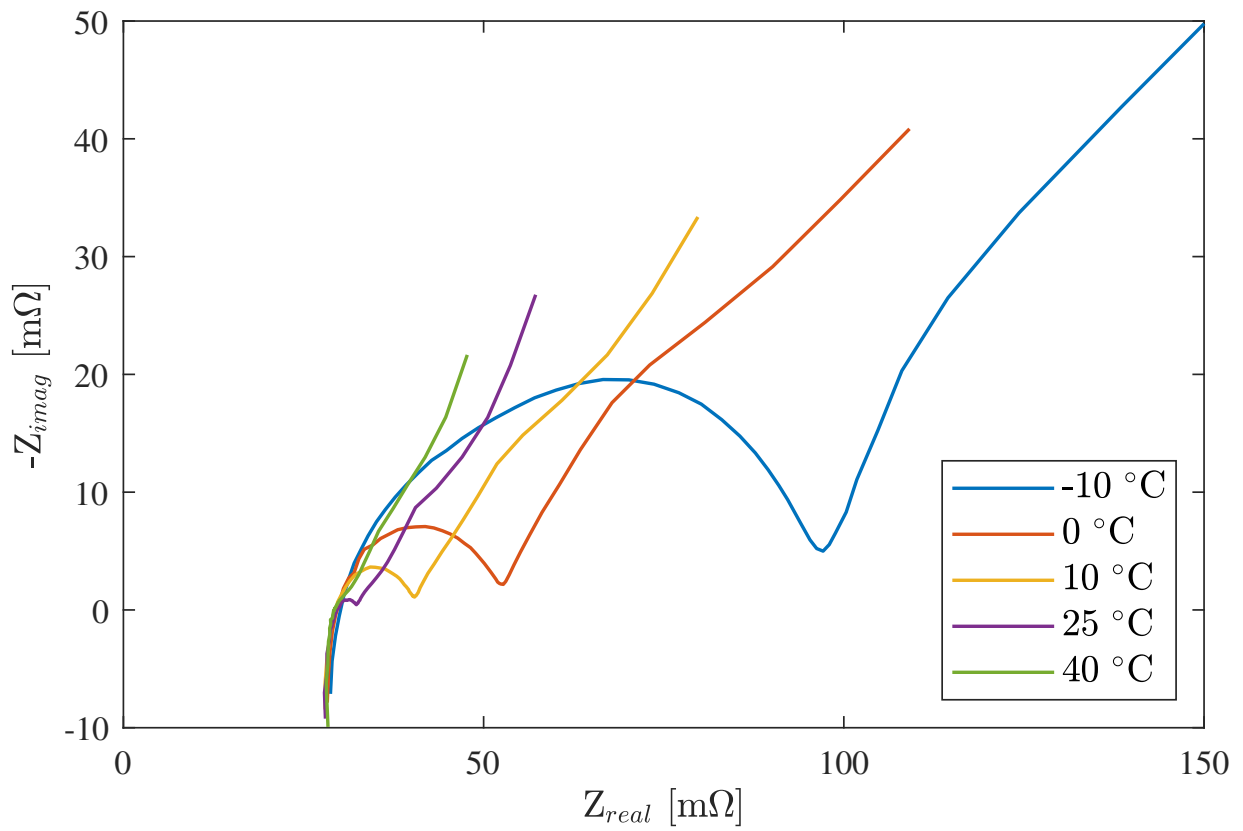


Figure 4.23: A magnified view of impedance spectra across a range of temperatures (measured at 60% SOC)

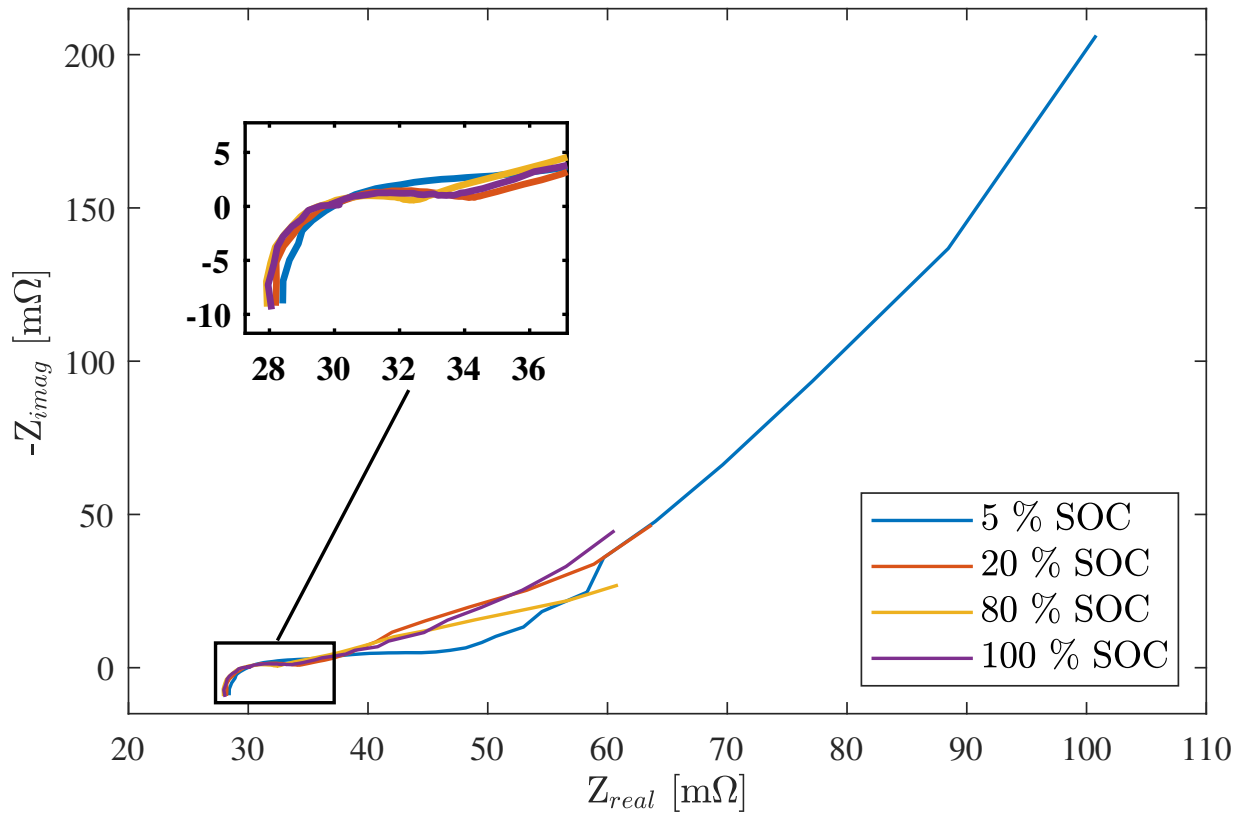


Figure 4.24: Impedance spectra at various SOC levels ($T = 25\text{ }^{\circ}\text{C}$)

the spectrum as the temperature is lowered, as demonstrated in Figure 4.23. Finally, the diffusion inside the cell is also influenced by temperature, as illustrated by the growth in the Warburg tail at lower temperatures.

The dependence of the cell impedance on SOC is illustrated in Figure 4.24. It can be seen that the shape of the plot remains fairly unchanged as the SOC level is varied. The most notable change that is observed is a growth in the Warburg tail at very low SOC levels. It can be concluded that for this cell, the charge transfer process is fairly independent of SOC, while the diffusion process is affected at very low SOC levels. However, at lower

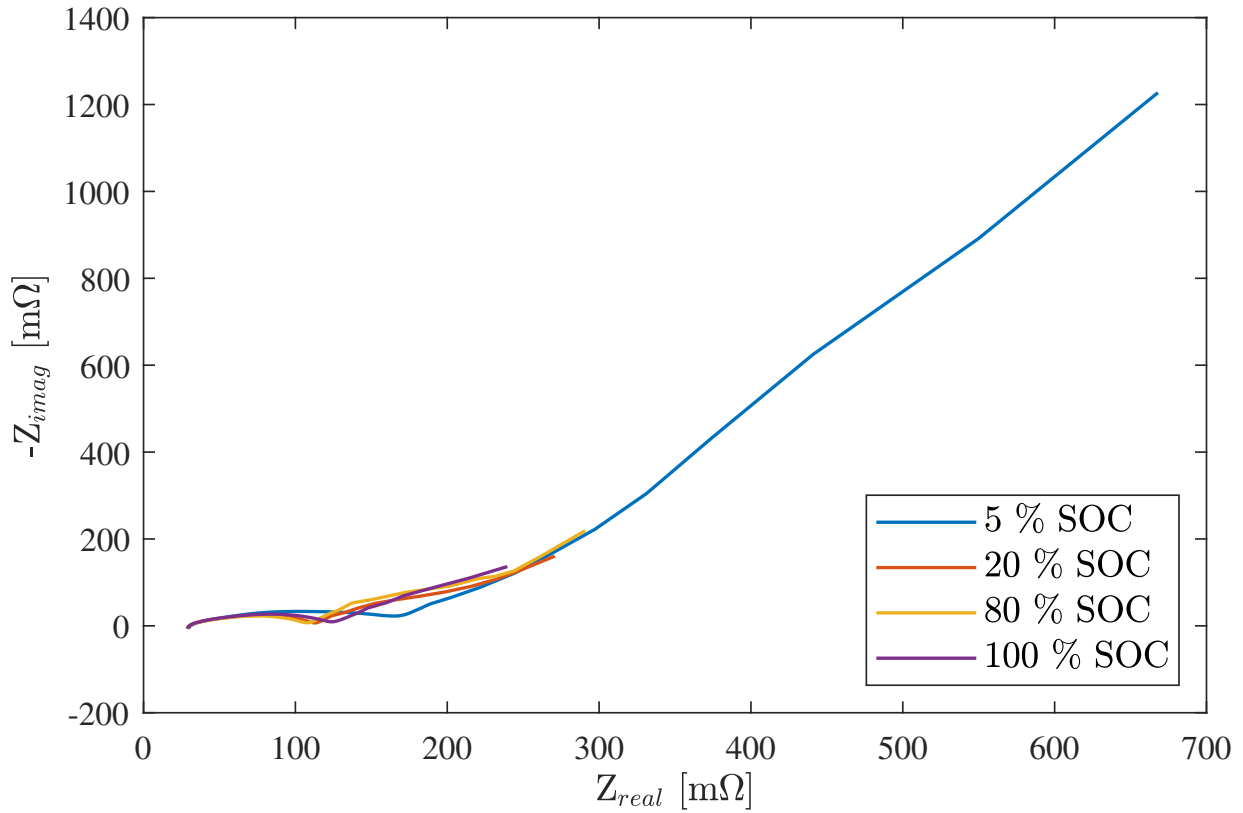


Figure 4.25: Impedance spectra at various SOC levels ($T = -10^\circ\text{C}$)

temperatures, a change in the semicircle region of the plot is observed. This change is slightly noticeable in the impedance spectra provided in Figure 4.25. To observe the growth in the spectra more clearly, a closer look is required at the semicircle region. It can be seen in Figure 4.26 that there is a significant growth in the semicircle region at -10°C , particularly at lower SOC levels. Therefore, the charge transfer process of this cell demonstrates a higher dependence on SOC level at lower temperatures, which was not observed at temperatures above 0°C .

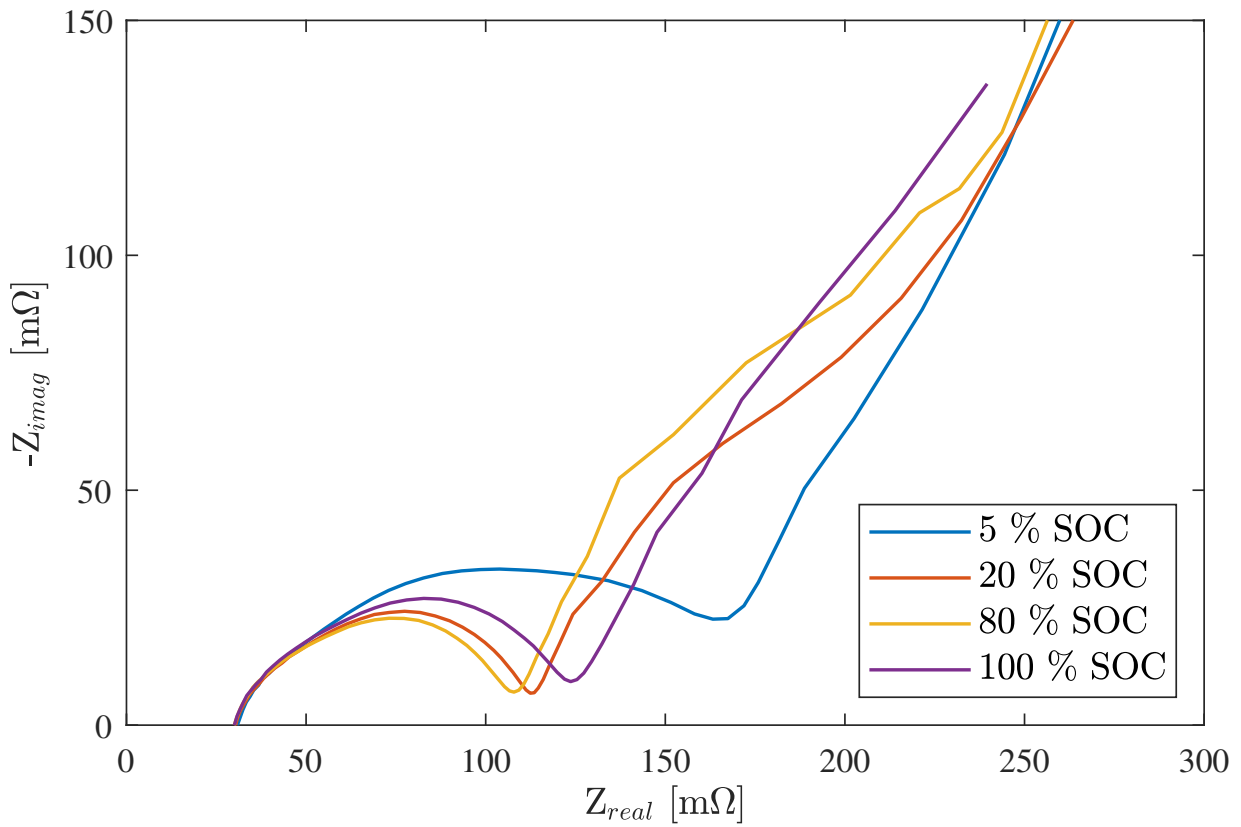


Figure 4.26: A magnified view of impedance spectra at various SOC levels ($T = -10^\circ\text{C}$)

4.5 Summary

This chapter covered the procedures involved in characterizing the cell across a wide range of operating conditions. Various characterization tests were considered, focusing on the following performance metrics of the cell: OCV, internal resistance and dynamic behaviour, as well as the impedance of the cell. The dependence of each characteristic on the various operating conditions used was analyzed. This analysis demonstrated how the performance of the cell varied at different temperatures, SOC levels and current amplitudes. The results from these characterization tests will be used in the next chapter to model the performance of the cell and refine the accuracy of the model.

Chapter 5

Impedance Modelling

Battery modelling plays an important role in understanding how batteries behave and how they will perform in specific applications. These models aim to demonstrate the dynamics of a battery, how it responds to various inputs as well as how its performance is affected under different operating conditions. There are many modelling options and techniques that are used in different studies; some of the most commonly used methods have been covered in Section 2.4.

In this research, equivalent circuit modelling is used to fit EIS data and validate the time domain performance of the lithium-ion cell under study. Figure 5.1 illustrates the process followed to collect data and the role it plays in building the model. The characterization tests that were presented in Chapter 4 are used to fit the model and optimize its parameters. A series of drive cycle tests were performed to validate the performance of the model and the parametrization method used. The results of the model fitting and the performance validation will be analyzed to draw conclusions on the model being studied and derive potential areas of refinement.

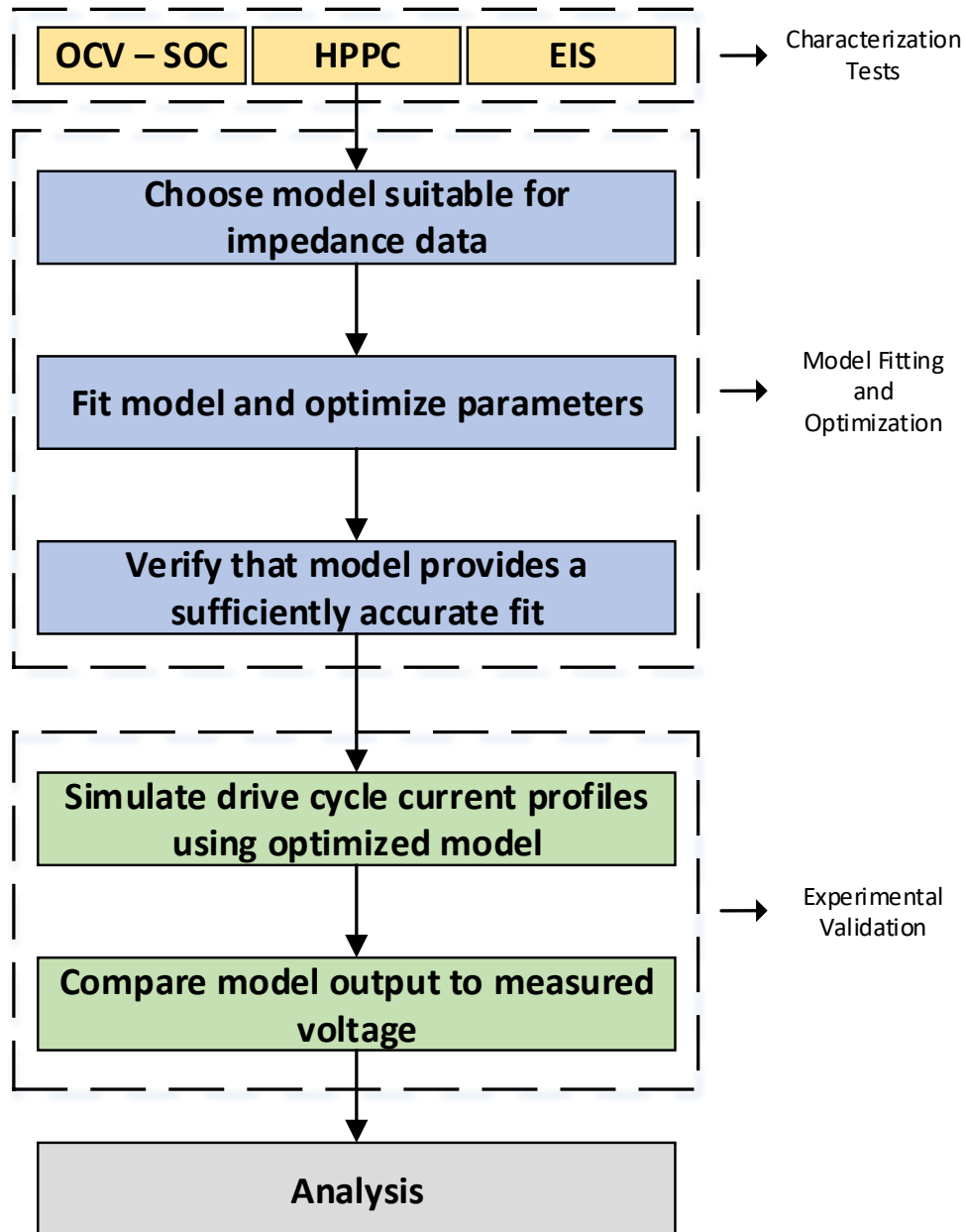


Figure 5.1: An overview of the battery modelling approach used in this research

This chapter will present an example equivalent circuit impedance model that has been previously studied in literature. It will discuss the shortcomings of this model and how they can be addressed using the time domain representation of [constant phase elements \(CPEs\)](#). The model will be fit to the impedance data collected and presented in Chapter 4. Furthermore, an improved model is proposed and will also be fit to the measured impedance data. The results will then be compared to determine if the proposed model provides an improved fit and can more accurately replicate the impedance characteristics of the cell. Finally, the experimental validation will be covered and drive cycle tests that were performed using the cell will be simulated using both models. This will help determine whether the proposed model is able to better capture the performance of the cell and if it provides any benefits to the model that was previously studied.

5.1 Battery Model Structure

In order to model a battery and fit it to EIS measurements, it is important to take into account behaviour that occurs at higher frequencies. Kollmeyer *et al.* studied an equivalent circuit model that utilizes various elements to capture the dynamic effects of a battery at different frequency ranges [83]. The $L - R - RC - RC - Z_{Wb}$ model that they studied, shown in Figure 5.2, is comprised of the following elements [83]:

- An inductor, L , to capture impedance behaviour at frequencies higher than 1 kHz.
- A resistance, R , to represent the ohmic resistance of the battery.

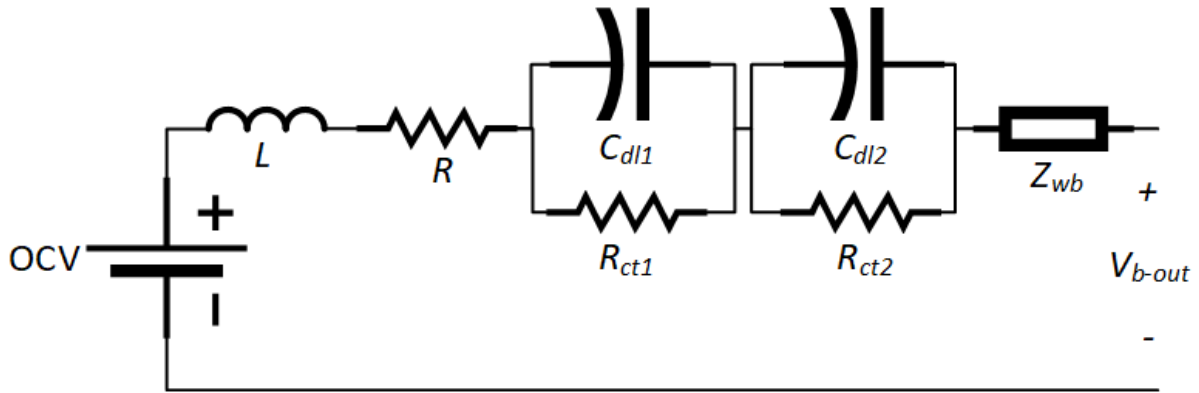


Figure 5.2: Example equivalent circuit model used for EIS fitting [83]

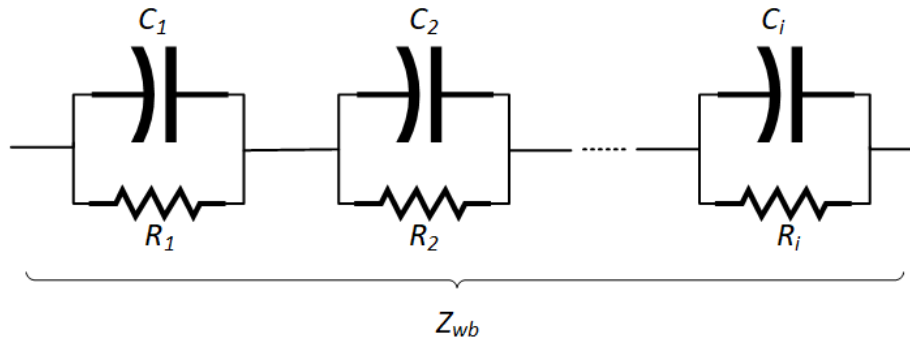


Figure 5.3: Representation of Warburg element using a series of RC-circuit pairs

- Two RC-circuit pairs, each consisting of charge transfer resistance (R_{ct}) and double layer capacitance (C_{dl}), to model frequencies between 1 Hz and 1 kHz.
- A Warburg element, Z_{wb} , to capture battery dynamics with large time constants. It has been shown in literature that a Warburg element can be used to model diffusion inside a battery [85] and that the element can be represented in the time domain using RC-circuit pairs [86], similar to Figure 5.3.

A sample fit using this model is shown in Figure 5.4 and it highlights two issues that can

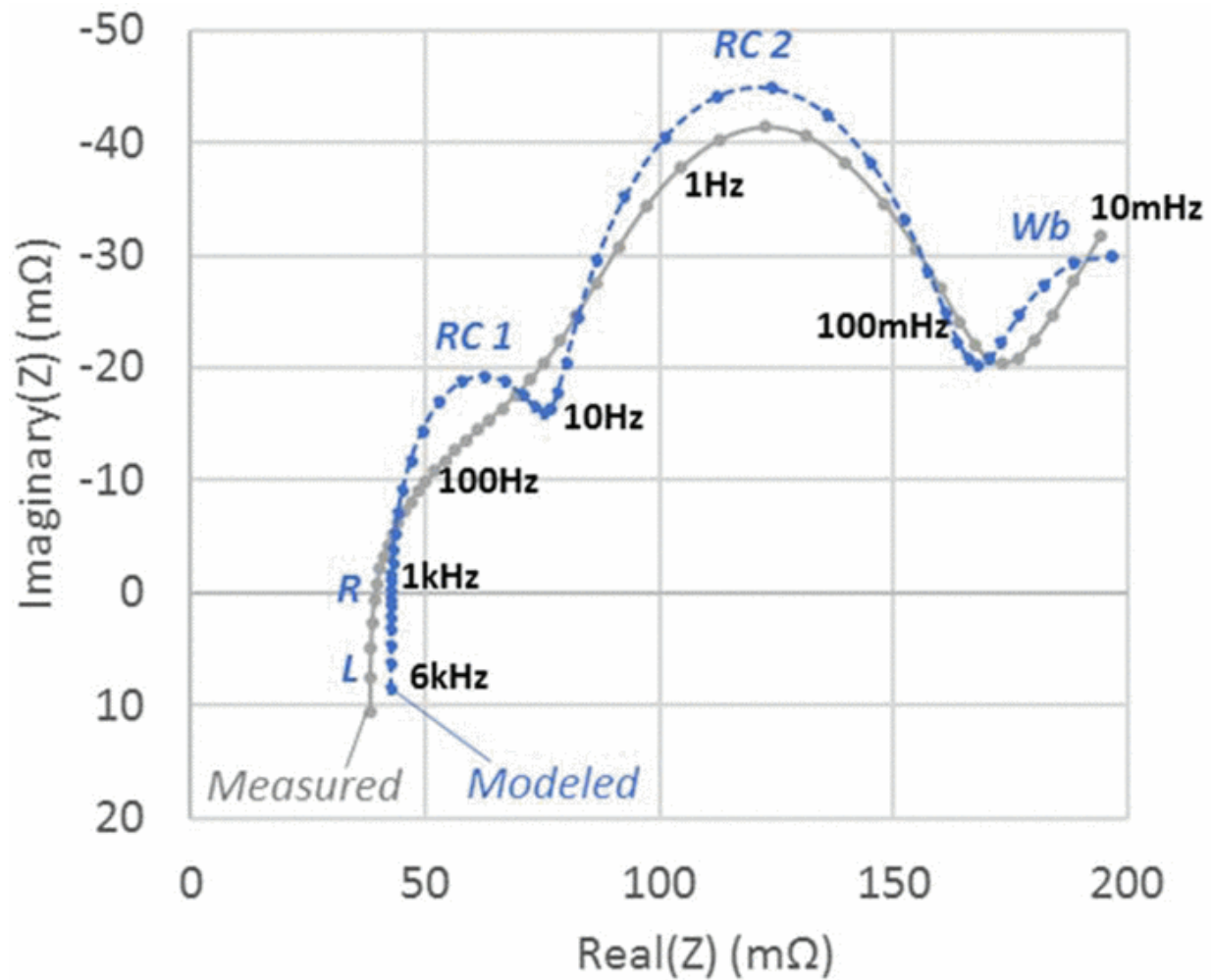


Figure 5.4: Example model fit to EIS measurement at -10°C and 80% SOC [83]

be addressed to provide a more accurate fit. Firstly, the model fails to accurately capture the battery's dynamics between 1 kHz and 100 mHz, as the modelled results produce two semi-circular diffusion regions that fail to emulate the measured data correctly [83]. One technique discussed in literature to address diffusion behaviour in this mid-frequency range is the use of fractional-order models [87]. Fractional-order capacitive elements, also known as CPEs, have a constant-phase angle and can capture the semi-ellipse shape that occurs during diffusion [87].

Therefore, to address this issue, a modified equivalent circuit model is proposed, that will utilize a ZARC element in place of the current RC-pairs. A ZARC element is comprised of a parallel connection between a CPE and resistance [88]. While this configuration provides a reliable method of fitting impedance data in the frequency domain, it is necessary to be able to represent it in the time domain to validate the model using drive cycle data [89–91]. However, transferring a ZARC to the time domain is challenging and requires approximation using linear elements. Buller demonstrated that it is possible to approximate a ZARC element using only resistive (R) and capacitive (C) elements [40]. His work concluded that a series of 5 RC-pairs provided the most accurate representation of the ZARC element, as shown in Figure 5.5, which was also validated in several research studies [88, 89].

There are various examples in literature that suggest using two ZARC elements allows for more robustness to uncertainty [53, 87, 89, 90]. However, to reduce the number of parameters and computational effort required to optimize the model, a single ZARC element is used. This decision is also supported by the fact that the measured impedance spectra for the cell being studied showed only one semi-circular diffusion region, and that the tail

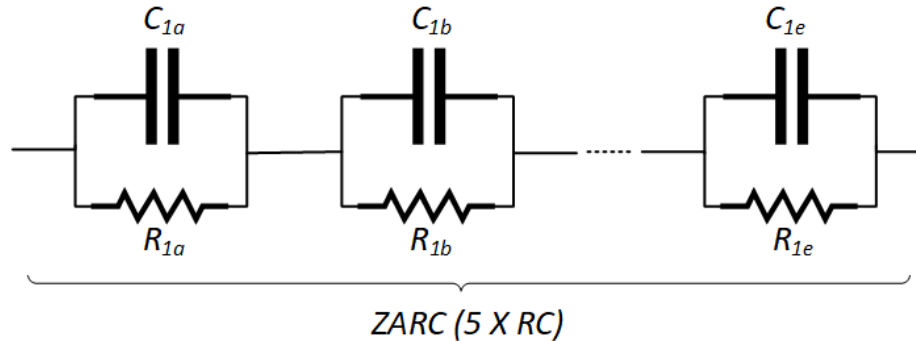


Figure 5.5: Time domain representation of ZARC element

of the spectra is being modelled using a Warburg element. With these conclusions, the proposed $L - R - ZARC - Z_{Wb}$ model is shown in Figure 5.6. Throughout the remainder of this thesis, the example model studied by Kollmeyer *et al.* will be referred to as *the example model* or *the 2RC model* or the *the $L - R - RC - RC - Z_{wb}$ model* [83]. Similarly, the suggested model will be referred to as *the proposed model* or *the ZARC model* or the *$L - R - ZARC - Z_{wb}$ model*.

Another area that the example model does not represent well is the fitting of the tail portion of the impedance spectra. It can be seen in Figure 5.4 that the modelled data does not follow the measured data at the end and instead starts to bend at a right angle. It has been suggested in literature that one way of addressing this issue is to collect EIS measurements at low frequencies to provide more data points for fitting, particularly at lower temperatures. In the work presented by Kollmeyer *et al.*, EIS testing was performed down to 10 mHz [83]. Therefore, to potentially improve the fitting in this region, EIS characterization tests were performed down to 1 mHz at 0°C and above, and down to 100 μ Hz at -10°C, as presented in Chapter 4.

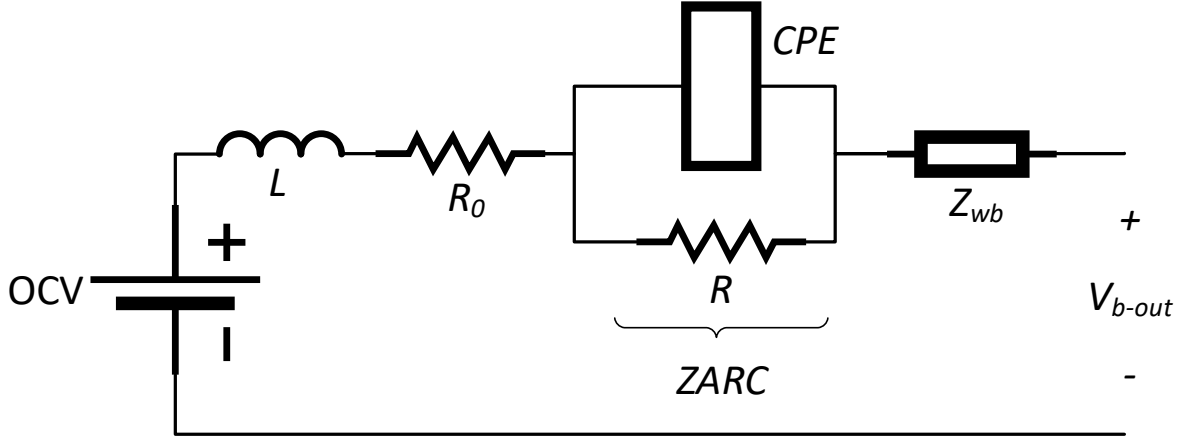


Figure 5.6: Proposed equivalent circuit model for EIS fitting, utilizing a constant phase element

5.2 Model Parameterization

The impedance of the proposed model introduced in Section 5.1 consists of a total of 14 parameters that require optimization:

- L
- R
- Five resistors $R_{ZARC_a} \dots R_{ZARC_e}$ and five corresponding capacitances $C_{ZARC_a} \dots C_{ZARC_e}$ to represent the ZARC element
- R_{wb} and C_{wb} to represent the Warburg element

The Warburg impedance can be approximated mathematically to reduce the number of parameters required to represent it in the time domain. The impedance is defined as

follows [85, 86]:

$$Z_{wb} = \frac{c}{\sqrt{j\omega D}} \cdot \tanh\left(\frac{l}{\sqrt{D}}\right) \cdot \sqrt{j\omega} \quad (5.1)$$

where:

ω = angular frequency

D = diffusion coefficient

l = diffusion length

c = additional constant

It is then transformed to the time domain as follows [83, 92]:

$$R_i = \omega_i \cdot \frac{cl}{D} = \omega_i \cdot R_{wb} \quad (5.2)$$

$$C_i = \frac{l}{2c} = C_{wb} \quad (5.3)$$

$$\tau_i = R_i \cdot C_i = \omega_i R_{wb} C_{wb} \quad (5.4)$$

$$\omega_i = \frac{8}{(2i - 1)^2 \cdot \pi^2} \quad (5.5)$$

where:

i = number of RC-circuits in series

R_i = resistance of the i^{th} RC pair

C_i = capacitance of the i^{th} RC pair

τ_i = time constant of the i^{th} RC pair

ω_i = scaling factor of the i^{th} RC pair

This simplified time domain representation of the Warburg element is depicted in Figure 5.3. For the example model, as well as the proposed model, $i = 5$ was considered a sufficient number of circuits to approximate the Warburg element [83]. The impedance of the inductor and resistance, respectively, are:

$$Z_L = j\omega L \quad (5.6)$$

$$Z_R = R \quad (5.7)$$

Finally, the impedance for each RC-pair representing the ZARC element is given by:

$$Z_{ZARCi} = \frac{R_i \times X_{Ci}}{R_i + X_{Ci}} \quad (5.8)$$

where:

i = each respective RC pair

$$X_{Ci} = \frac{1}{j\omega C}$$

$$j\omega = 2\pi f$$

Therefore, utilizing Equations (5.2) to (5.8), the total impedance of the proposed model is given by:

$$Z_{L-R-ZARC-Zwb} = Z_L + Z_R + Z_{ZARC a \dots ZARC e} + Z_{wb} \quad (5.9)$$

Similarly, the impedance of the example model is given by [83]:

$$Z_{L-R-RC-RC-Zwb} = Z_L + Z_R + Z_{RC} + Z_{RC} + Z_{wb} \quad (5.10)$$

Table 5.1: Summary of optimization algorithm options used to parametrize model in MATLAB

Option	Description	Value
<i>MaxFunEvals</i>	Maximum number of function evaluations allowed.	1000
<i>MaxIterations</i>	Maximum number of iterations allowed.	500
<i>FunctionTolerance</i>	Termination tolerance on the function value.	1×10^{-10}

To parametrize the models using the measured EIS data, an objective function and an optimization algorithm are required. In this case, the objective function chosen to be minimized is the error between the model output and the measured impedance data. The non-linear least squares method is a common optimization algorithm used to fit impedance data, which is implemented in this work using an available MATLAB function [93]. A summary of the options chosen for the optimization algorithm is presented in Table 5.1. The optimized parameters will be implemented with each model and used in Section 5.4 to validate their performance.

5.3 Impedance Spectra Fitting Results

The optimized Warburg resistance (R_{wb}) values obtained during the fitting of the $L - R - RC - RC - Z_{wb}$ model demonstrate that the model fit is poor at low SOC levels, particular at 15% SOC and below. This observation is highlighted in Figure 5.7 which presents the R_{wb} values obtained at every SOC level at 25 °C. The upper bound set for R_{wb} during the optimization process is 4 Ω; therefore, when the optimization algorithm repeatedly arrives at this limit while searching for the most suitable values, it indicates that the model cannot

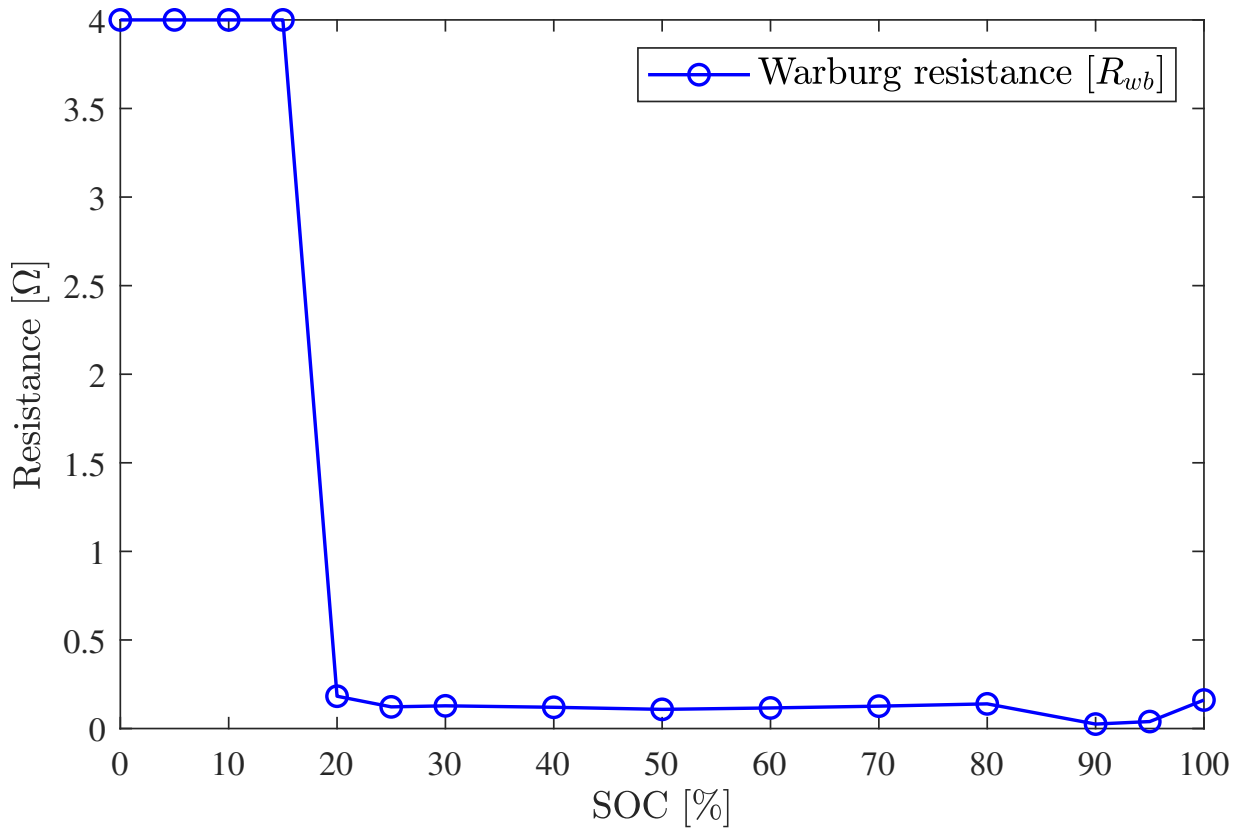


Figure 5.7: Optimized R_{wb} values for $L - R - RC - RC - Z_{wb}$ model at 25°C

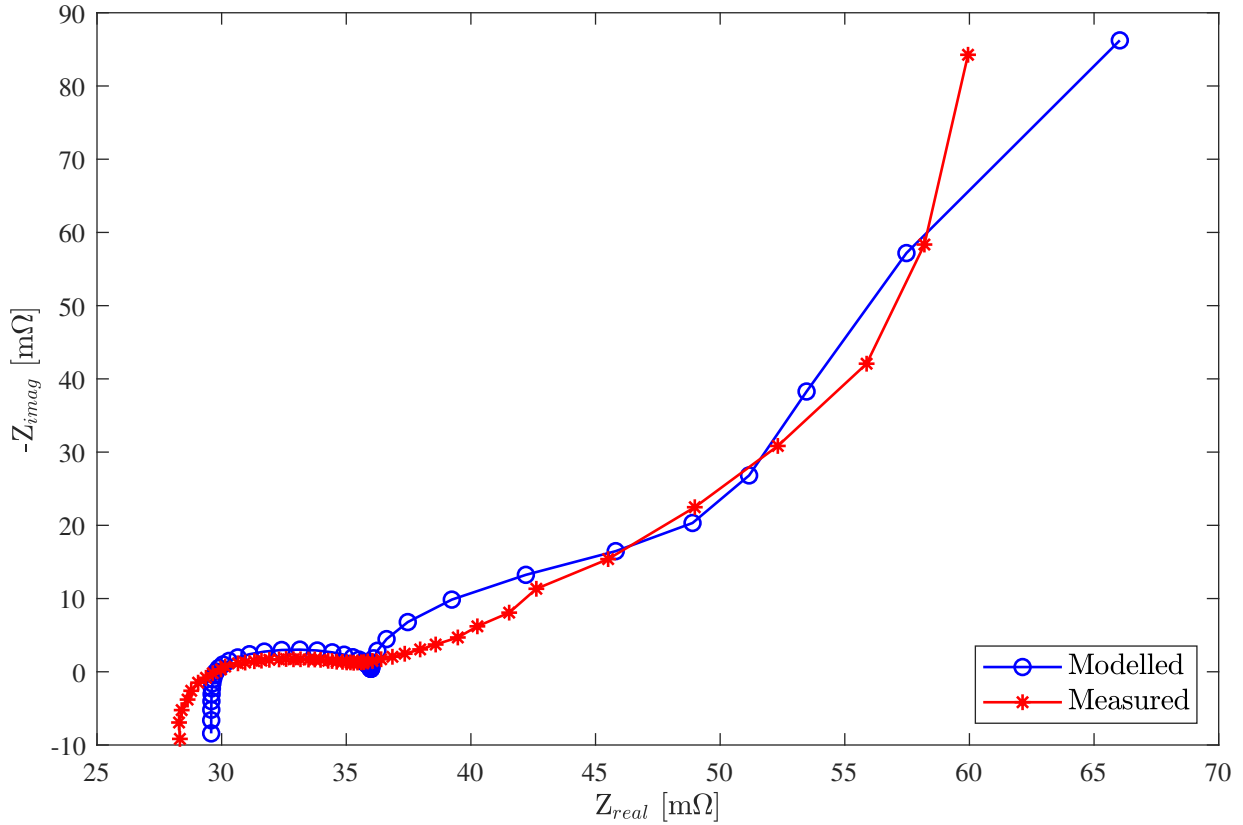


Figure 5.8: Fitting of $L - R - RC - RC - Z_{wb}$ model to impedance data measured at 15% SOC ($T = 25\text{ }^{\circ}\text{C}$)

accurately fit the measured impedance of the cell. It can be seen in Figure 5.7 that the resistance values are consistent at 20% SOC and above (with an average of approximately 115 mΩ), but they drastically increase below that and repeatedly reach 4 Ω. An example of this poor fitting is presented in Figure 5.8, where it is evident the model does not correctly represent the measured data. Specifically, the failure of the model to correctly estimate the Warburg element resistance translates to a poor fitting of the tail region of the plot. The optimized model parameters for each temperature and SOC level are presented in Appendix B. The poor fitting of the measured data at low SOC levels was also evident

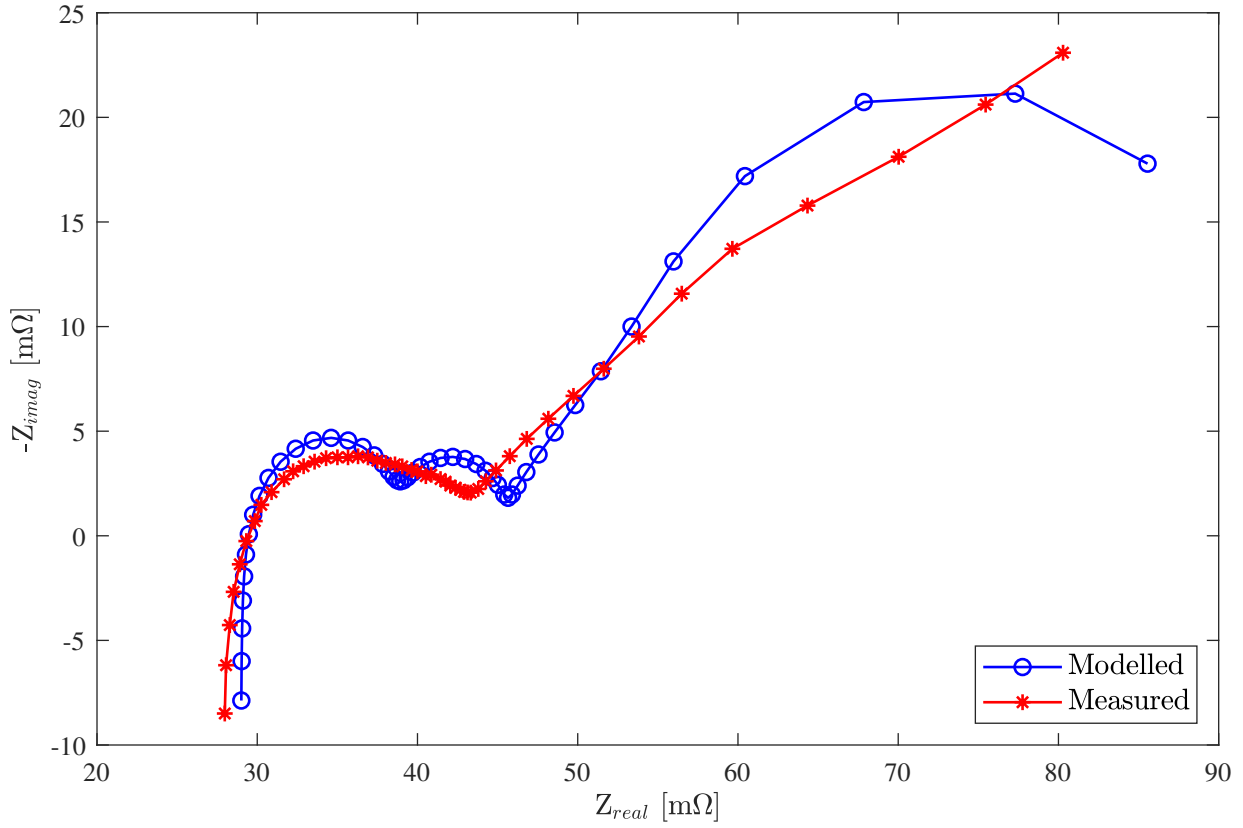


Figure 5.9: Fitting of $L - R - RC - RC - Z_{wb}$ model to impedance data measured at 95% SOC ($T = 10^\circ\text{C}$)

at other temperatures. As such, these model parameters were discarded and were not considered during the validation of the model in Section 5.4.

When fit to the measured impedance data, the $L - R - RC - RC - Z_{wb}$ model's performance was consistent with the results presented by Kollmeyer *et al.* [83]. An example of this is presented in Figure 5.9 which depicts the poor fitting of the model to impedance data measured at 10°C and 95% SOC. It can be observed that the high frequency region is not captured well by the model, which produces two semi-circular regions and does not

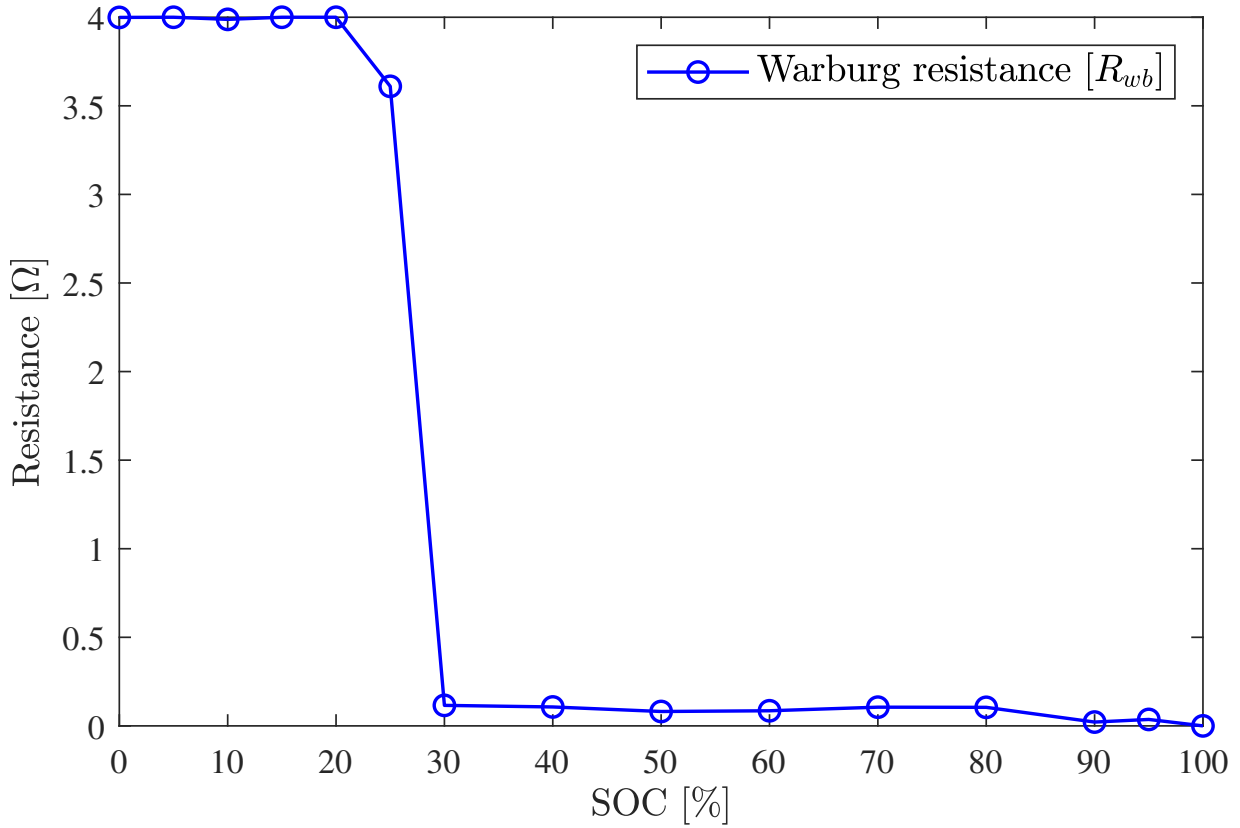


Figure 5.10: Optimized R_{wb} values for $L-R-ZARC-Z_{wb}$ model at 40°C

align with the shape of the measured data. Furthermore, the tail region of the modelled data does not follow the same slope or pattern as the measured data. In addition to this, the modelled Warburg tail bends at a right angle at very low frequencies, which was also an issue highlighted by Kollmeyer *et al.* as shown in Figure 5.4 [83].

Similar to the example model, the $L-R-ZARC-Z_{wb}$ model demonstrated a poor fit to the measured data at low SOC levels. This is once again highlighted by the optimized R_{wb} values presented in Figure 5.10. The values at 30% SOC and above are fairly consistent, whereas below that they approach or reach the upper bound limit of $4\ \Omega$ used while fitting

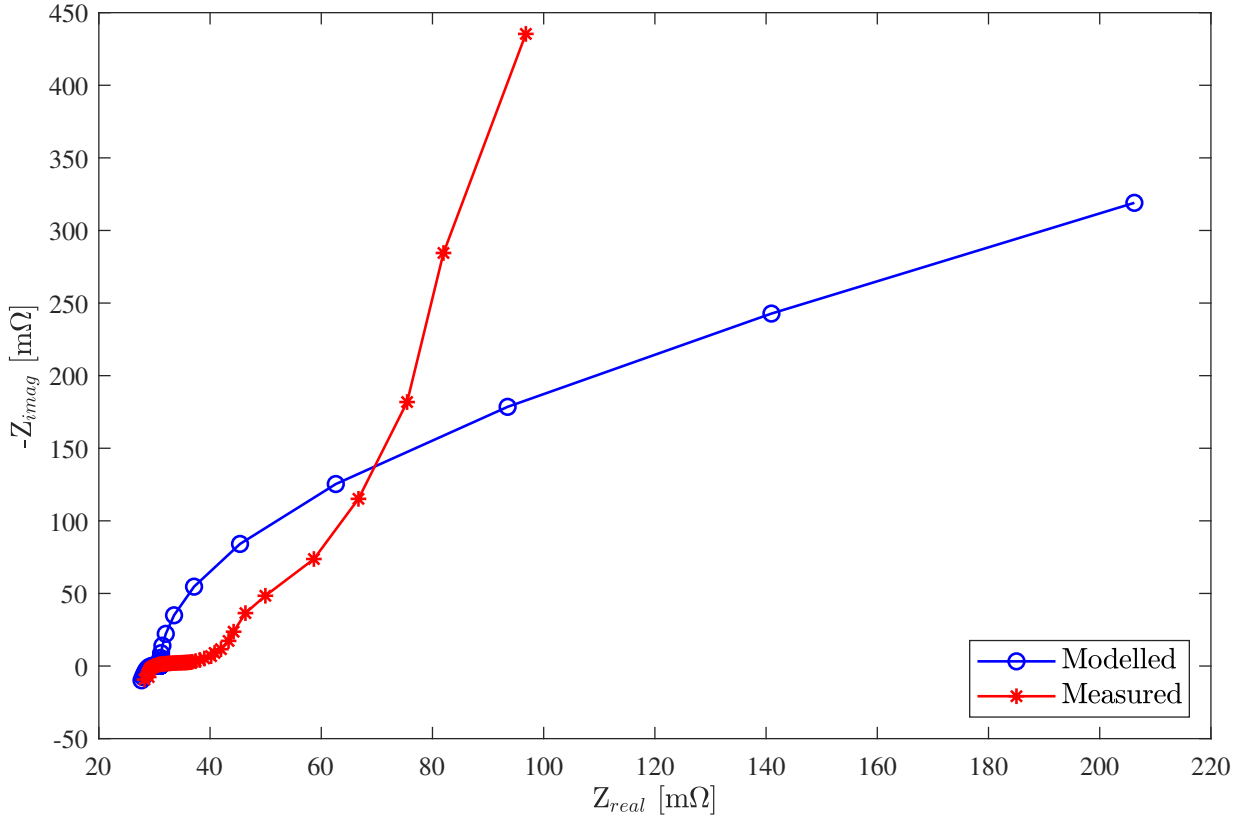


Figure 5.11: Fitting of $L - R - ZARC - Z_{wb}$ model to impedance data measured at 10% SOC ($T = 40^\circ\text{C}$)

the model to the measured data. An example of this poor fitting is presented in Figure 5.8 where it is evident that the modelled Warburg tail fails to accurately represent the measured data. The optimized model parameters for each temperature and SOC level are presented in Appendix C. This poor fitting at low SOC levels was also seen at other temperatures; consequently, these model parameters were discarded and were not considered during the validation of the model in Section 5.4.

The results achieved with the optimized $L - R - ZARC - Z_{wb}$ model show a strong

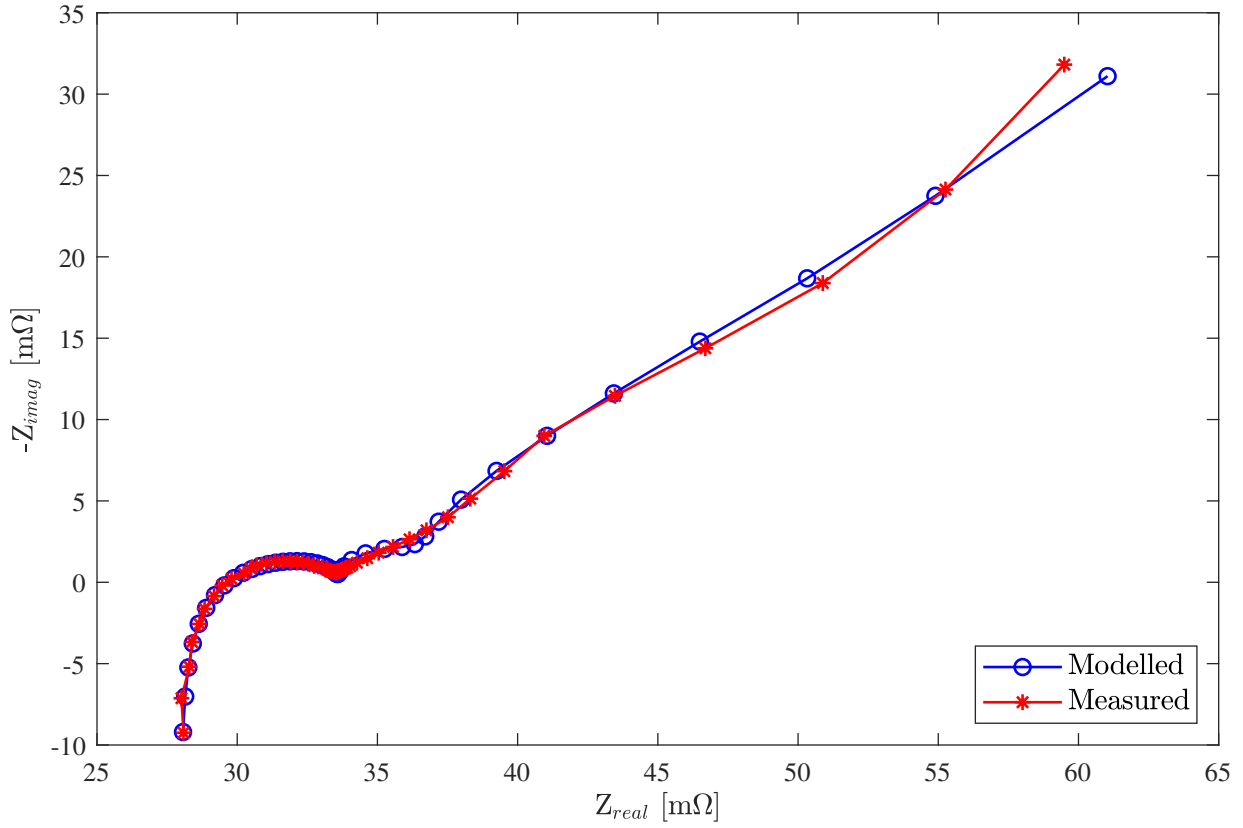


Figure 5.12: Fitting of $L - R - ZARC - Z_{wb}$ model to impedance data measured at 25% SOC ($T = 25^\circ\text{C}$)

performance across a wide range of SOC levels at all of the temperatures used for impedance measurements. Figures 5.12 to 5.14 showcase the performance of the model at multiple temperatures and SOC levels. The use of the ZARC element demonstrates that the model can capture the mid-frequency semi-circle portion of the measured impedance data with a high degree of accuracy. Whereas the example model produced *two* semi-circular patterns, as shown in Figure 5.9, the proposed model is able to mitigate this issue and reproduce the shape of this region precisely.

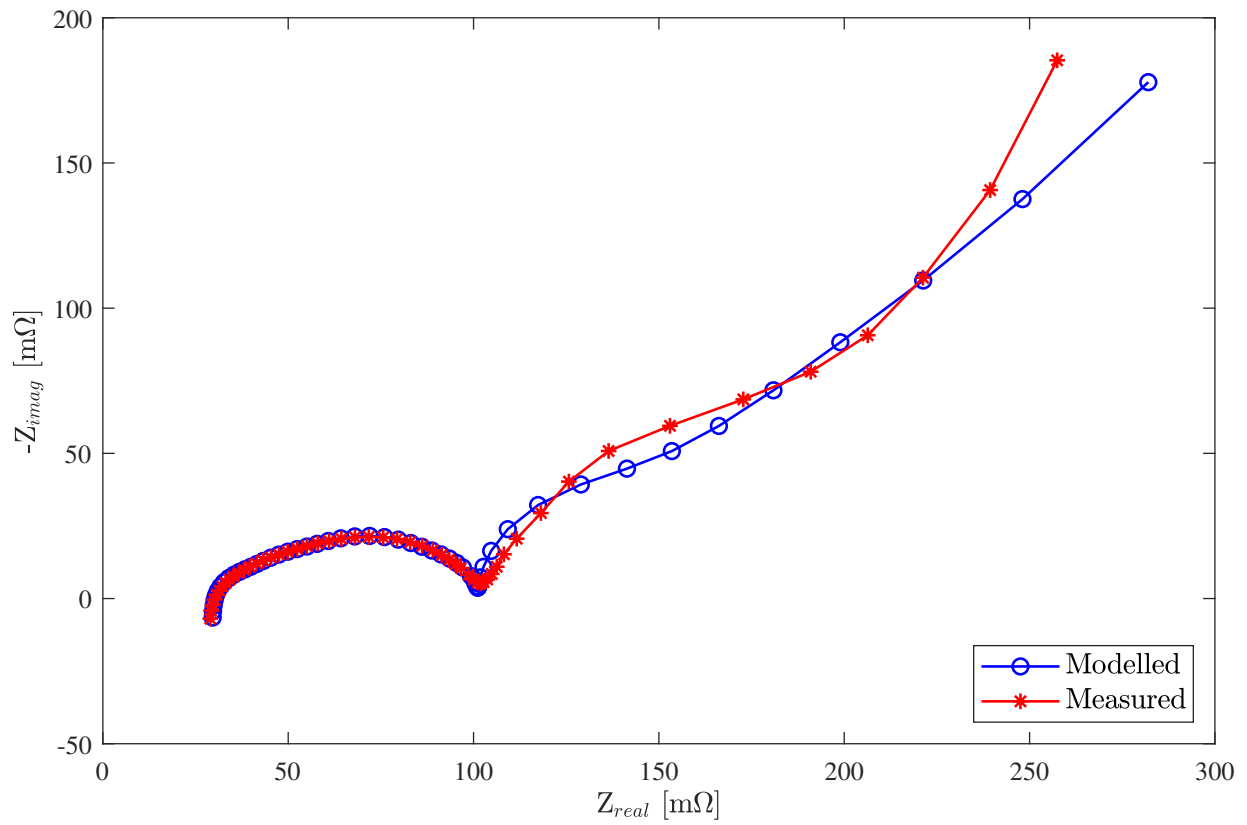


Figure 5.13: Fitting of $L - R - ZARC - Z_{wb}$ model to impedance data measured at 50% SOC ($T = -10^{\circ}\text{C}$)

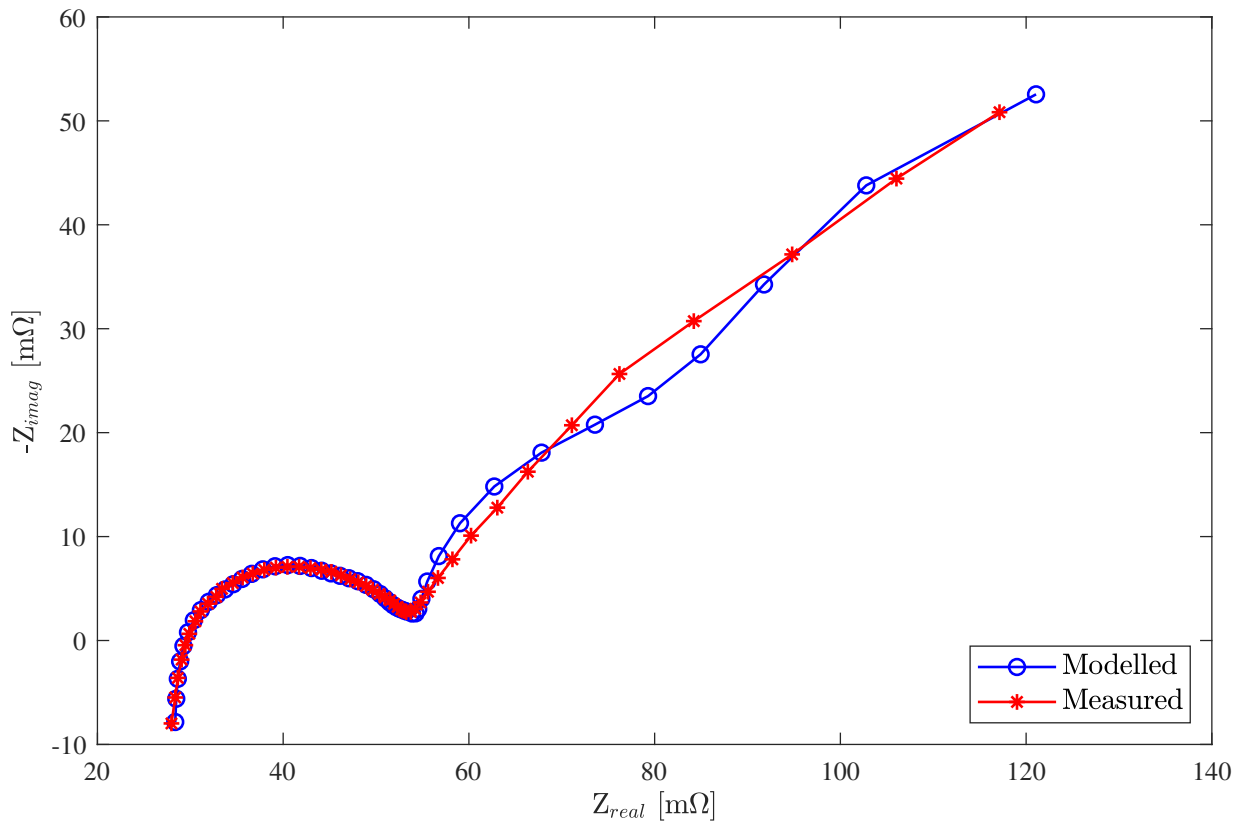


Figure 5.14: Fitting of $L - R - ZARC - Z_{wb}$ model to impedance data measured at 80% SOC ($T = 0^\circ\text{C}$)

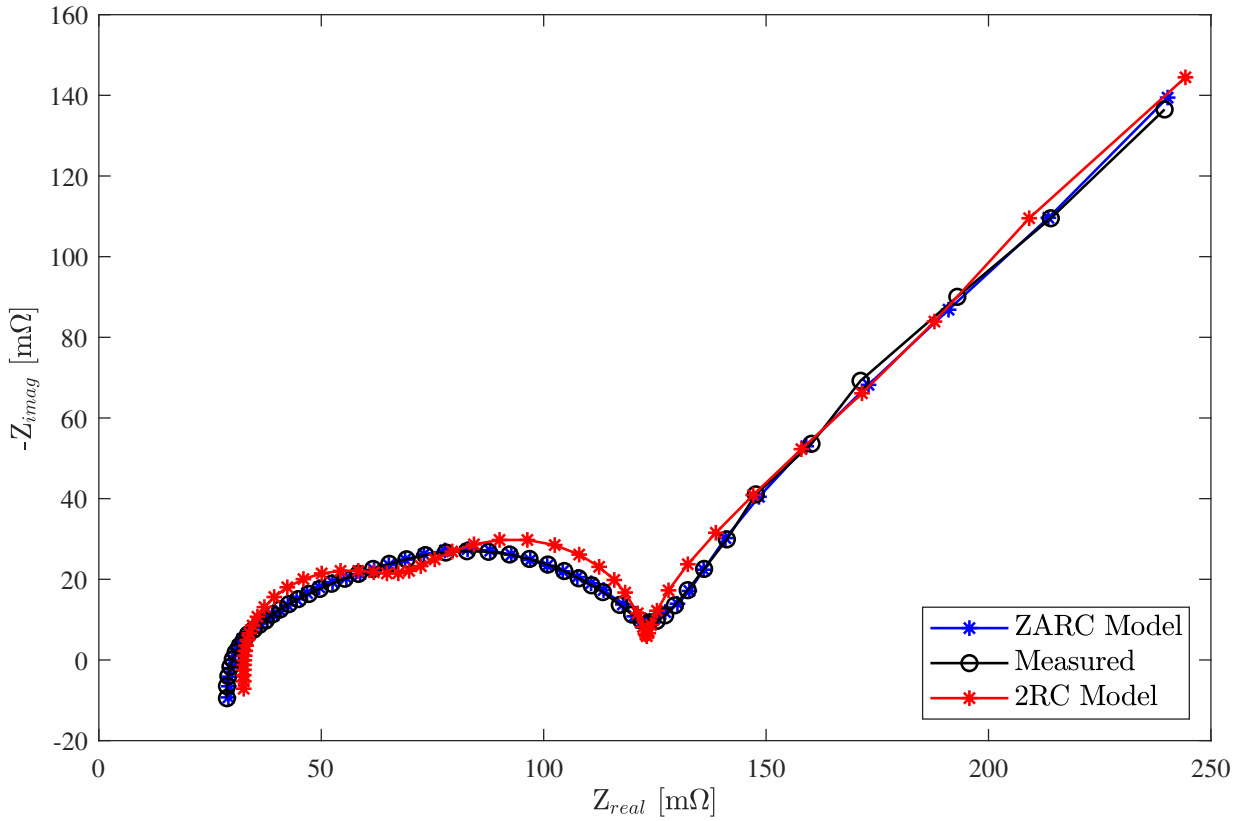


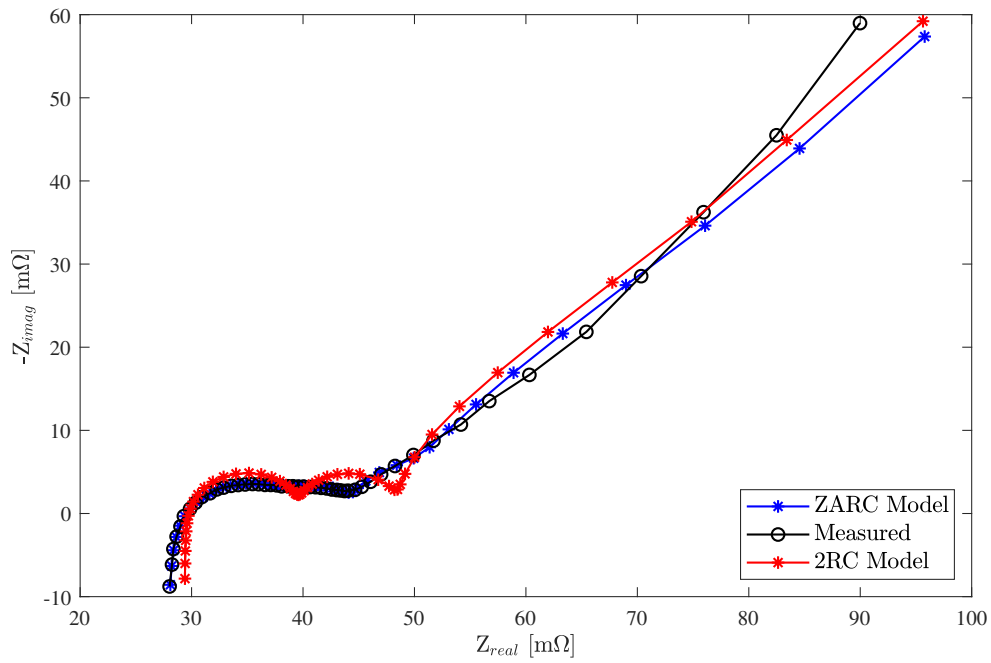
Figure 5.15: Fitting of example and proposed models to impedance data measured at 100 % SOC ($T = -10^{\circ}\text{C}$)

In order to compare the change in performance between the example model presented by Kollmeyer *et al.* and the proposed model, it is useful to examine the results of both models together to highlight any significant improvements [83]. One such example is provided in Figure 5.15 where it is evident that the proposed $L - R - ZARC - Z_{wb}$ model provides a much more precise fit to the measured data, especially in the mid-frequency semi-circle region. In addition to this, the proposed model is able to better capture the Warburg tail region of the measured data. While the improvement in this area is less prominent, it can be observed that the proposed model can capture the slope, pattern and spacing of the tail

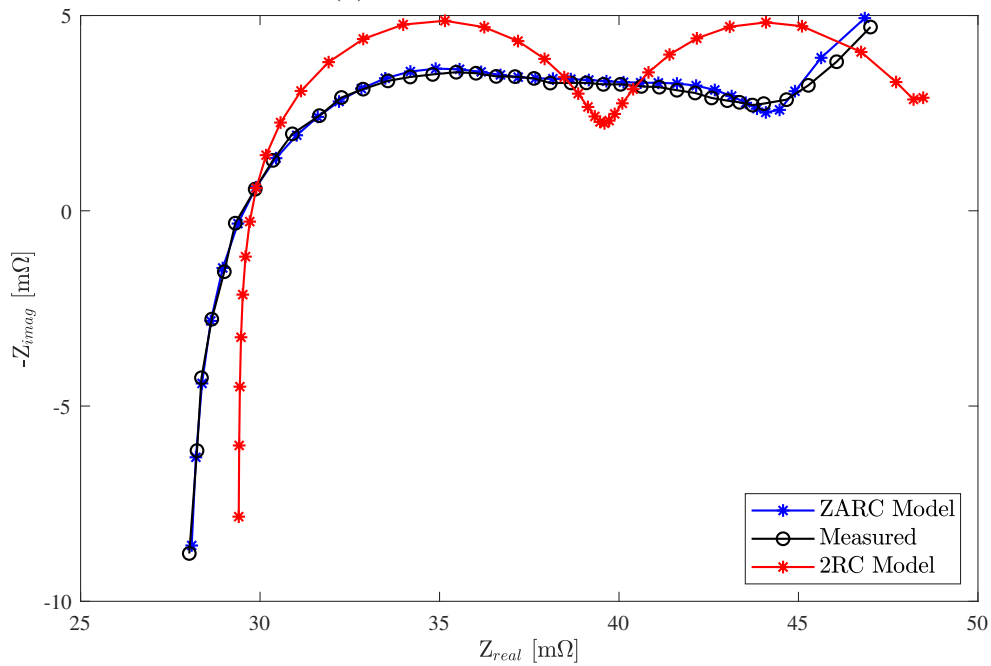
region more accurately.

In some cases, the proposed model provides a better overall fit to the measured data without a significant improvement in the Warburg tail fitting. One example of this scenario is provided in Figure 5.16. A closer look at the high and mid-frequency region of the plot shows a major improvement in the semi-circle fitting, as demonstrated in Figure 5.16b. However, as can be seen in Figure 5.16a, the Warburg tail fitting with the proposed model is relatively the same as the example model. Although the Warburg tail obtained with the proposed model initially improves the slope and alignment relative to the example model, it ultimately diverts in the same manner; thus, there is not any meaningful improvement offered in this regard. Another example of the improved performance provided by the proposed model is provided in Figure 5.17. It can be seen once again that the ZARC model is able to precisely capture the semi-circle region of the plot, as shown in Figure 5.17b. The Warburg tail fitting is also improved with the proposed model, although it still does not exactly replicate the shape of the measured data. As seen in Figure 5.17a, relative to the example model, the proposed model does follow the slope and pattern of the measured data more closely and overall provides a more accurate fit.

While a visual representation of the modelling results provides an idea of the improvement offered by the proposed $L - R - ZARC - Z_{wb}$ model, it is also worth examining a more tangible comparison such as the calculated error between the measured data and the model output. The **root mean square error (RMSE)** formula used to calculate the error

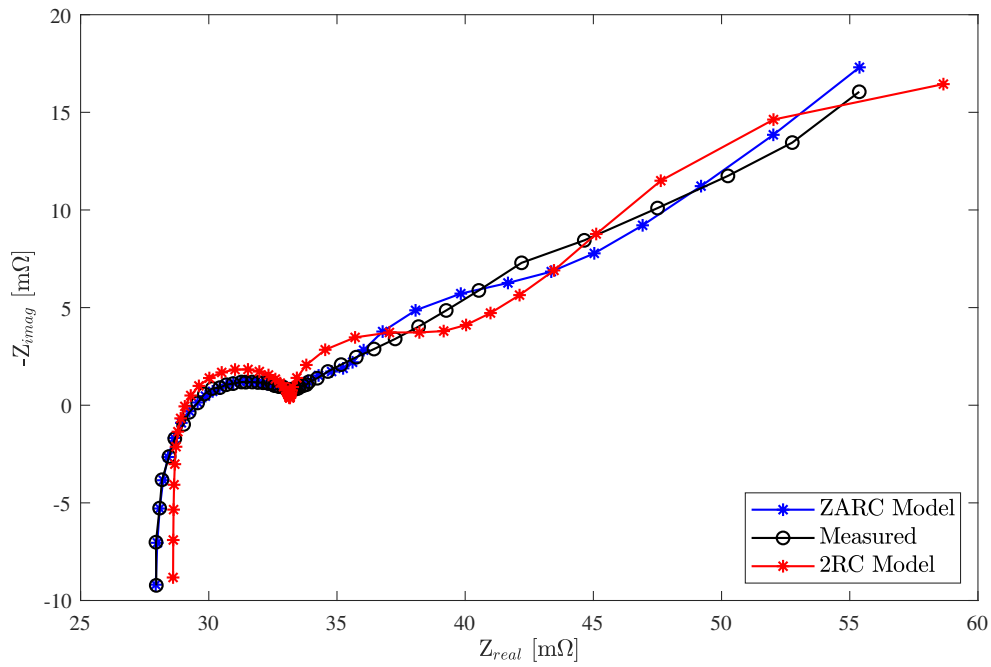


(a) Entire frequency range

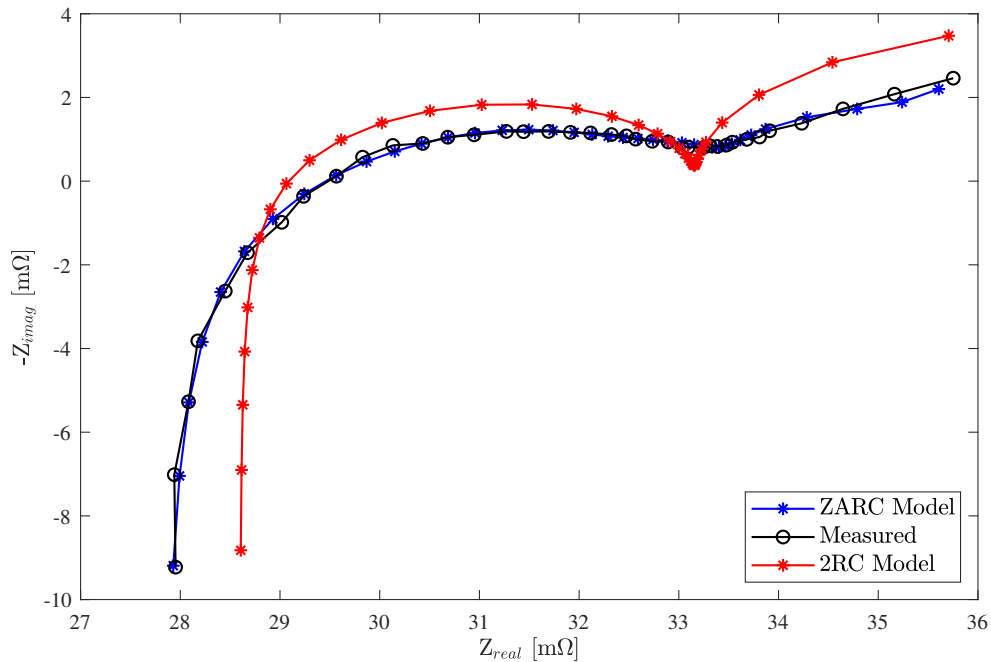


(b) Magnified view of high and mid-frequency impedance points, focusing on semi-circle region

Figure 5.16: Comparing fit of example and proposed models to impedance data measured at 100 % SOC ($T = 10\text{ }^{\circ}\text{C}$)



(a) Entire frequency range



(b) Magnified view of high and mid-frequency impedance points, focusing on semi-circle region

Figure 5.17: Comparing fit of example and proposed models to impedance data measured at 95 % SOC ($T = 25\text{ }^{\circ}\text{C}$)

produced by each model is given in Equation (5.11) below:

$$RMSE = \sqrt{\frac{1}{n} \sum_{i=1}^n (Z_{measured} - Z_{modelled})^2} \quad (5.11)$$

where:

$Z_{measured}$ = measured impedance at given frequency point

$Z_{modelled}$ = model output at given frequency point

n = total number of frequency points

This equation is used to calculate the error for the real (Z_{real}) and imaginary (Z_{imag}) impedance values separately. A graphical representation of the real and imaginary impedance RMSE values for both models is presented in Figure 5.18. These graphs provide the cumulative error for all of the SOC levels at each temperature. For example, to obtain the *total* real impedance RMSE at 25 °C, the error is calculated for each individual SOC level using Equation (5.11) and all of the values are summed. As indicated by Figure 5.18, both models performed best between 0 °C and 25 °C, while producing the largest error at -10 °C. The $L - R - RC - RC - Z_{wb}$ model's best performance was with data measured at 25 °C, registering real and imaginary impedance RMSE values of 27.4 mΩ and 20 mΩ, respectively. Conversely, the $L - R - ZARC - Z_{wb}$ model's best performance was with data measured at 10 °C, with real and imaginary impedance RMSE values of 16.5 mΩ and 11.4 mΩ, respectively.

A quick glance at Figure 5.18 indicates that fitting the measured impedance data using the proposed model generally provides an improvement over the example model. With the

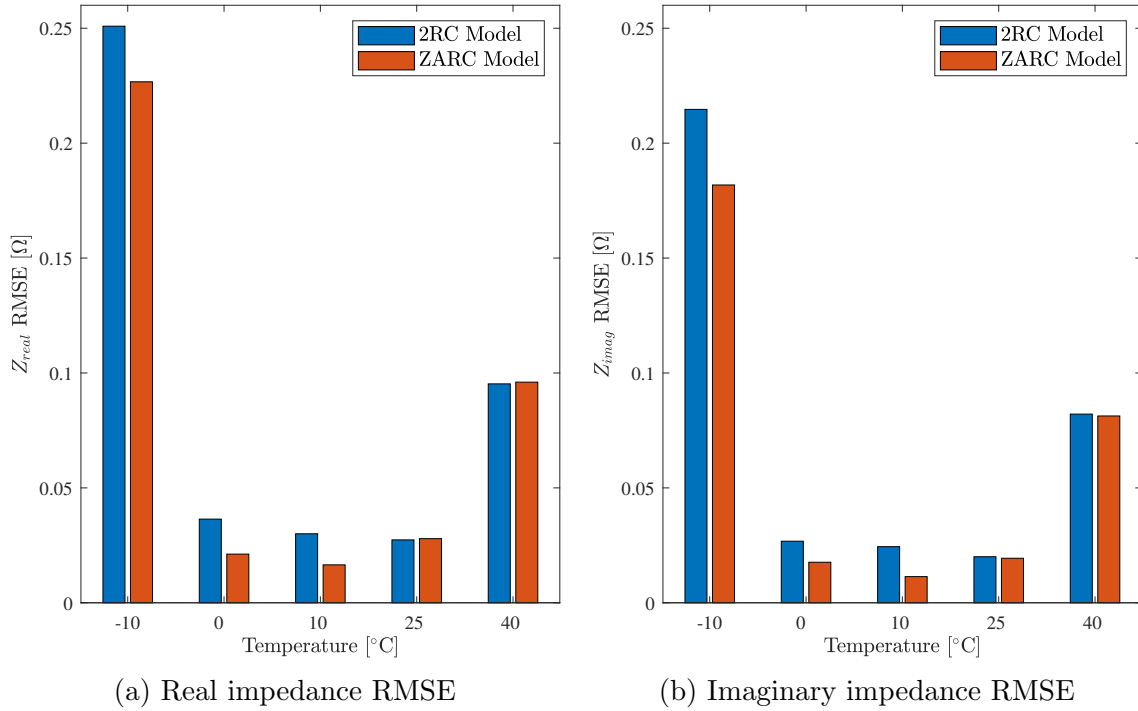


Figure 5.18: Real and imaginary impedance RMSE for example (2RC) and proposed (ZARC) models

exception of 25 °C and 40 °C, it is evident that the use of the ZARC element has reduced the total RMSE between the modelled and measured data, when compared to the example model. To gain a more insightful look at this difference, the percentage change in model error is calculated using Equation (5.12):

$$\text{Percent Change (\%)} = \left(\frac{RMSE_{proposed} - RMSE_{example}}{RMSE_{example}} \right) \times 100 \quad (5.12)$$

where:

Table 5.2: Average percentage change in RMSE between example (2RC) and proposed (ZARC) models

Temperature [°C]	Z_{real} RMSE Average Change [%]	Z_{imag} RMSE Average Change [%]
-10	-33.42	-30.99
0	-49.83	-41.06
10	-51.48	-54.27
25	0.3399	0.2637
40	0.0866	0.0040

$RMSE_{proposed}$ = Calculated RMSE for the ZARC model

$RMSE_{example}$ = Calculated RMSE for the 2RC model

Equation (5.12) is used to calculate the change in error at every SOC level for all temperatures. The average percentage change between the example model and proposed model RMSE values is given in Table 5.2. As demonstrated by these values, the use of the ZARC element is able to significantly improve the fitting results when compared with the example model, particularly at 10 °C and below. At 25 °C and above, the average RMSE change between the two models is negligible. This is also validated by the total errors for each model as previously highlighted in Figure 5.18, demonstrating that the performance of both models is comparable at 25 °C and 40 °C.

Another important consideration when comparing the performance of both models is the computational effort and time required to optimize them. If an improvement in performance and accuracy comes at the expense of heavy computational requirements, it may be deemed disadvantageous or impractical in certain applications. The total computation time recorded when fitting the measured impedance data, using both models, is presented

Table 5.3: Total computation time required to parameterize original ($2RC$) and proposed ($ZARC$) models

Temperature [°C]	Example Model Computation Time [s]	Proposed Model Computation Time [s]
-10	1.9944	2.3656
0	1.1721	1.7974
10	1.2873	1.6950
25	1.1051	1.4437
40	0.9207	1.2516

in Table 5.3. It can be noted that there is an increase in the computation time required to optimize the proposed model relative to the example model, at all temperatures. However, given the increase in the number of parameters that the proposed model utilizes, this is to be expected. The example model ($L-R-RC-RC-Z_{wb}$) consists of 8 parameters whereas the proposed model ($L-R-ZARC-Z_{wb}$) consists of 14 parameters. Given this context, the increase in computation time is deemed acceptable based on the reduced model error that is presented in Table 5.2 and Figure 5.18. The largest increase in computation time is roughly 0.63 s to optimize the proposed model at 0 °C, which resulted in a decrease of 33.42 % and 30.99 % in the real and imaginary impedance RMSE values, respectively. As such, the increase in computational time required to optimize the proposed model is offset by the reduction of the modelling error achieved and the ability of the model to fit the measured data more precisely.

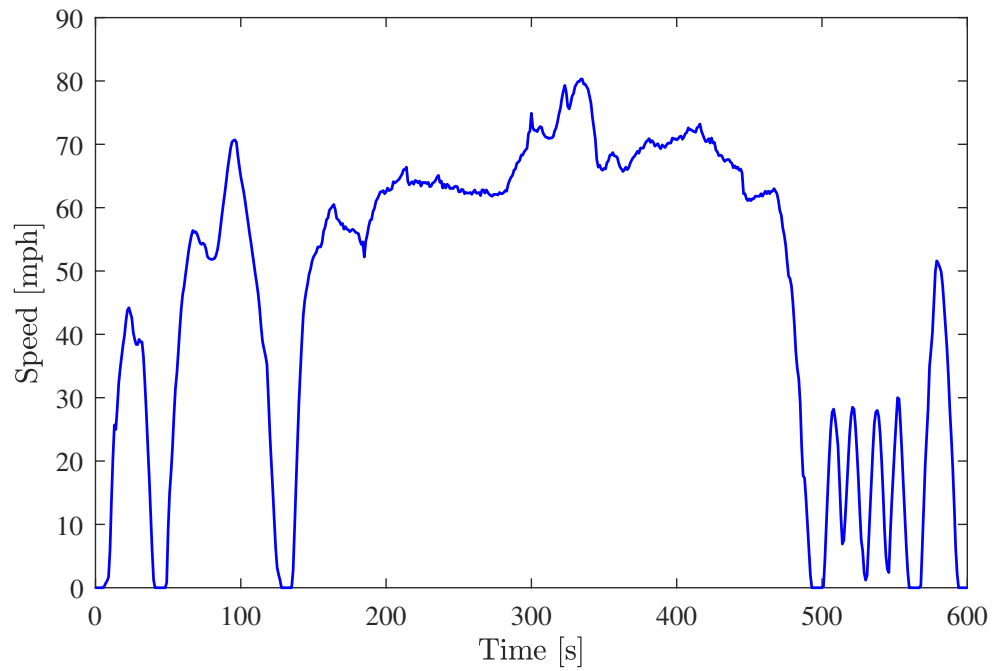
Table 5.4: Characteristics summary of drive cycles used for experimental validation [72]

Drive Cycle	Total Time [s]	Distance [miles / km]	Average Speed [mph / kph]
HWFET	765	10.26 / 16.51	48.3 / 77.73
LA92	1435	9.82 / 15.80	24.61 / 39.61
UDDS	1369	7.45 / 11.99	19.59 / 31.53
US06	596	8.01 / 12.89	48.37 / 77.84

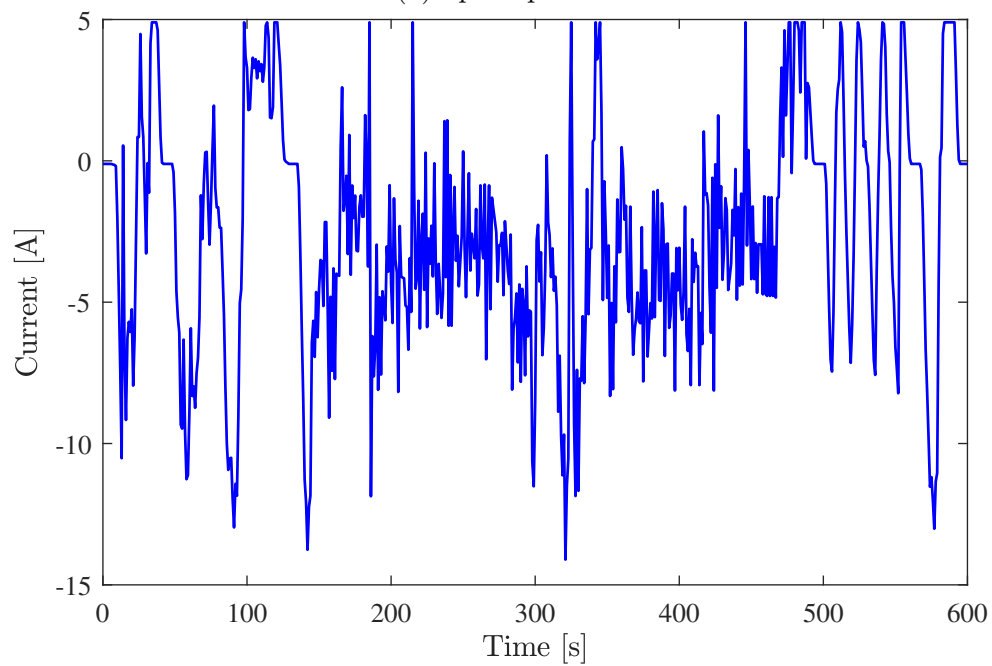
5.4 Experimental Validation

To validate and compare the performance of both models, a series of drive cycle profiles were performed at all of the temperatures used to collect impedance data (-10°C , 0°C , 10°C , 25°C and 40°C). The profiles chosen are some of the common drive cycles used by the United States [Environmental Protection Agency \(EPA\)](#) for vehicle emissions and fuel economy testing [72]. These cycles were used for experimental validation because they have unique characteristics and will challenge the models in various ways. A summary of the characteristics for the drive cycles used is provided in Table 5.4.

The current profiles corresponding to each drive cycle are calculated for a Fiat 500e electric vehicle battery pack and scaled for a single Samsung INR21700-50E cell [94]. The speed profile and corresponding current profile for the US06 drive cycle are presented in Figure 5.19. The data for the remaining drive cycles is presented in Appendix D. In some instances, the current profiles generated for the drive cycles have peak currents that are larger than the cell specifications defined in Table 3.3. In such cases, the currents are capped to avoid going above the safety limitations specified and damaging the cell. An example of this adjustment is provided in Figure 5.20.



(a) Speed profile



(b) Current profile

Figure 5.19: US06 drive cycle profile data

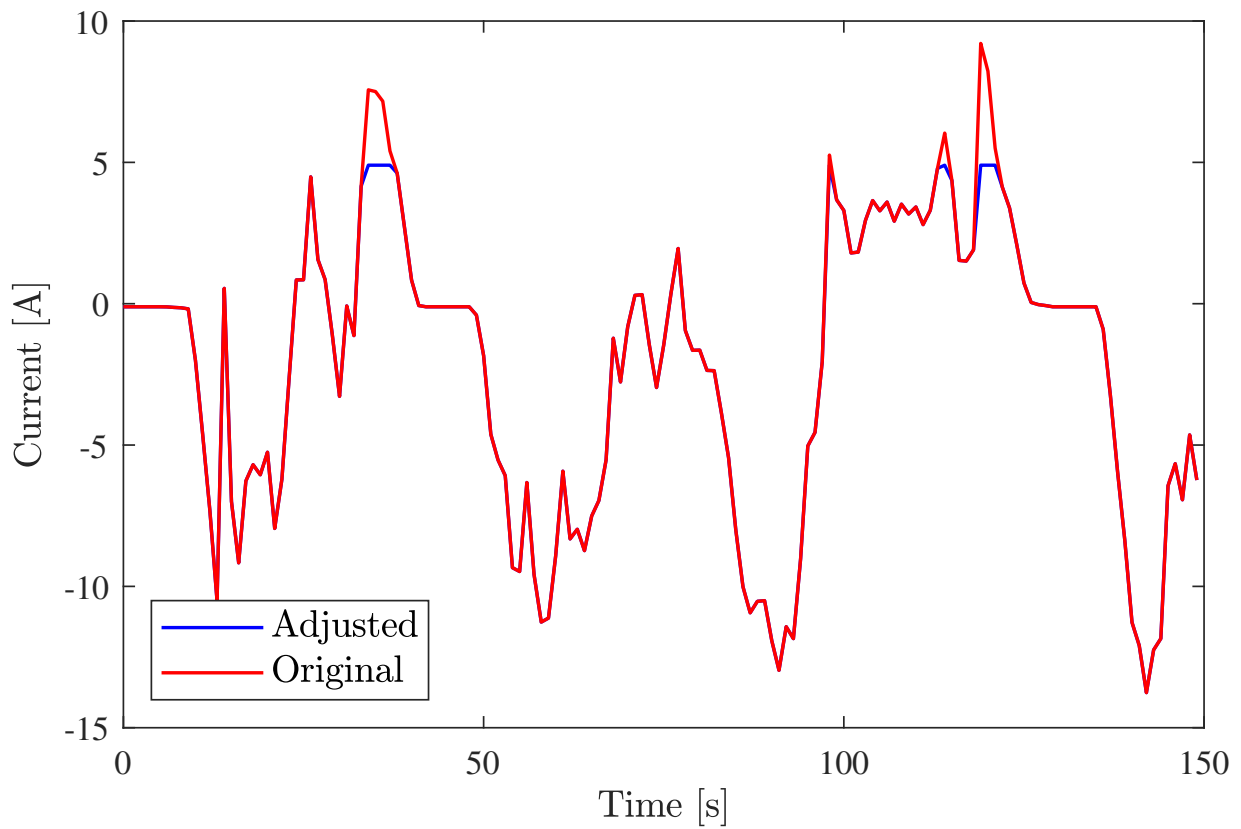


Figure 5.20: Example of adjustment applied to US06 current profile to avoid peak currents that are above the safety specifications of the cell

In order to run the drive cycle current profiles across a range of operating conditions, it is necessary to determine the discharge capacity of the cell at each individual temperature. This discharge capacity is then used as the stopping condition for the current profiles i.e. the profiles would run repeatedly until a specific capacity was discharged from the cell. The procedure to run a drive cycle current profile is described below:

1. The temperature of the chamber is set to 25 °C.
2. When the surface temperature of the cell has reached a value of 25 °C \pm 2 degrees, proceed to step 3.
3. Charge the cell to 100% SOC at 0.5C (2450 mA) CC until the upper voltage limit specified, then switch to CV with a cut-off current of 0.02C (98 mA).
4. The temperature of the chamber is set to the desired value (i.e. the temperature required for validation).
5. When the surface temperature of the cell has reached a value that is within 2 degrees of the desired temperature, proceed to step 6.
6. Discharge the cell at 1C (4900 mA) CC until the lower voltage limit specified.
7. Repeat steps 1-5.
8. When the surface temperature of the cell has reached a value that is within 2 degrees of the desired temperature, proceed to step 9.
9. Apply drive cycle current profile until capacity recorded in step 6 is discharged from the cell.

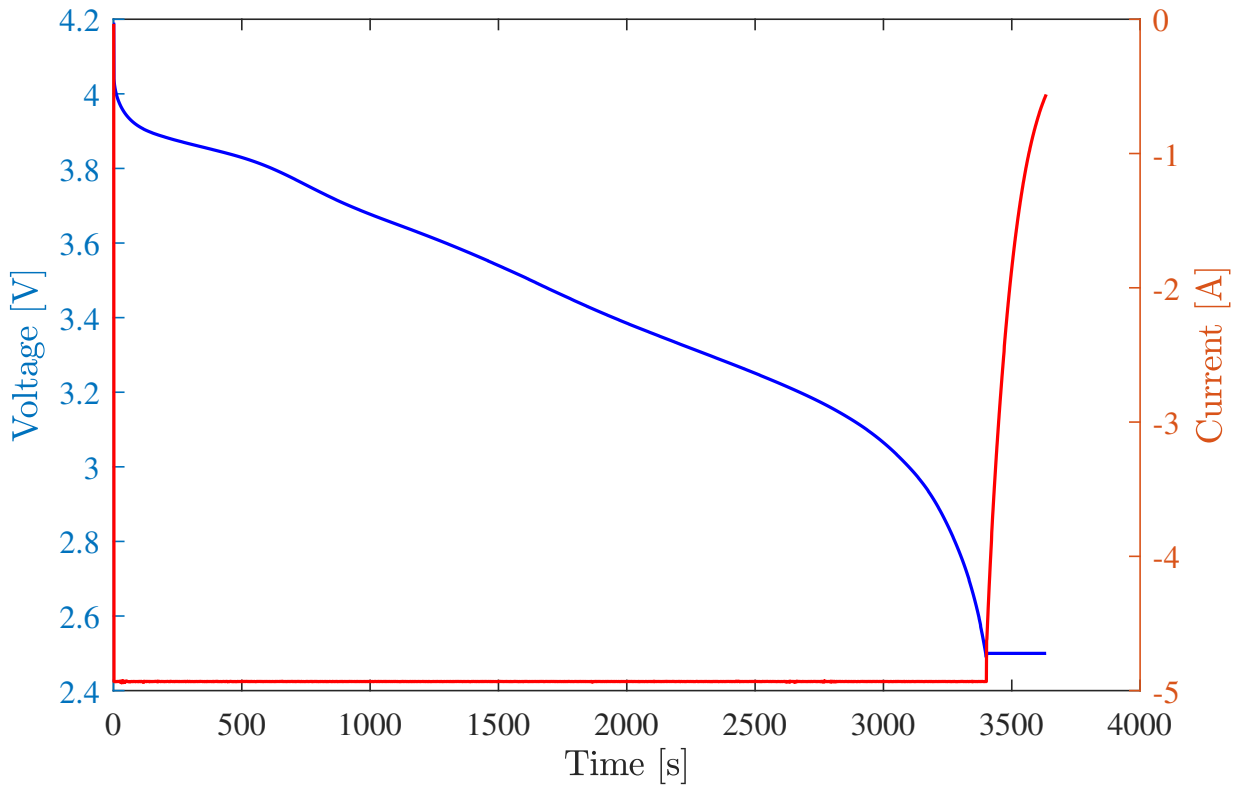


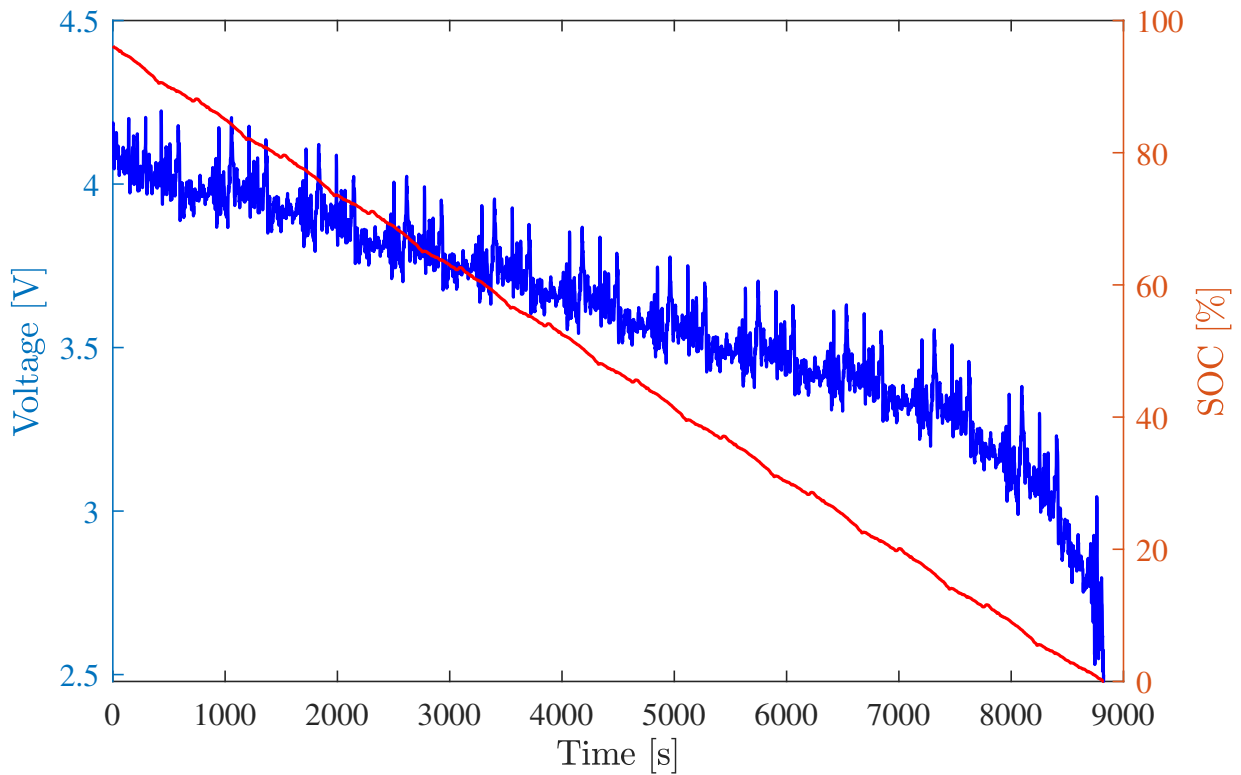
Figure 5.21: Example of procedure used to determine drive cycle stopping condition ($T = 25\text{ }^{\circ}\text{C}$)

10. Repeat steps 7-9 for all of the drive cycles used for experimental validation.
11. Repeat steps 1-10 for all of the temperatures used for experimental validation.

A visual representation of step 6 from the aforementioned procedure is presented in Figure 5.21. The recorded capacities that were discharged from the cell at each temperature are shown in Table 5.5. These values were used as the stopping conditions for the drive cycle current profiles. Figure 5.22 depicts the measured voltage of the cell to an applied drive cycle current profile, as described in step 9 of the aforementioned test procedure.

Table 5.5: Discharge capacity used for drive cycle profiles at each temperature

Temperature [°C]	Discharged Capacity [A h]
40	4.8698
25	4.8487
10	4.7584
0	4.6513
-10	4.6386

Figure 5.22: Measured voltage during HWFET drive cycle current profile ($T = 25\text{ }^{\circ}\text{C}$)

The model validation process is comprised of different components that are gathered throughout the course of this research. The measured current, temperature of the cell and SOC level of the cell are used as the inputs for the model. The OCV, capacitive and resistive properties of the cell were determined at a range of temperatures, current points and SOC levels through the characterization tests performed in Chapter 4. These values are linearly interpolated to cover the entire duration of each drive cycle profile used. The optimized model parameters are obtained through fitting the measured impedance data as described in Section 5.3. All of these elements function concurrently to simulate the voltage of the cell using the applied current profiles. The results will be discussed in Section 5.4.1.

5.4.1 Drive Cycle Simulation Results

There are two metrics considered in this research to compare the results between the measured experimental data and the simulated voltage obtained during model validation: RMSE and average voltage error. These values are calculated using Equations (5.13) and (5.14) below:

$$\text{RMSE (V)} = \sqrt{\frac{1}{n} \sum_{i=1}^n (V_{modelled} - V_{measured})^2} \quad (5.13)$$

$$\text{Average Error (V)} = \frac{1}{n} \sum_{i=1}^n (V_{modelled} - V_{measured}) \quad (5.14)$$

where:

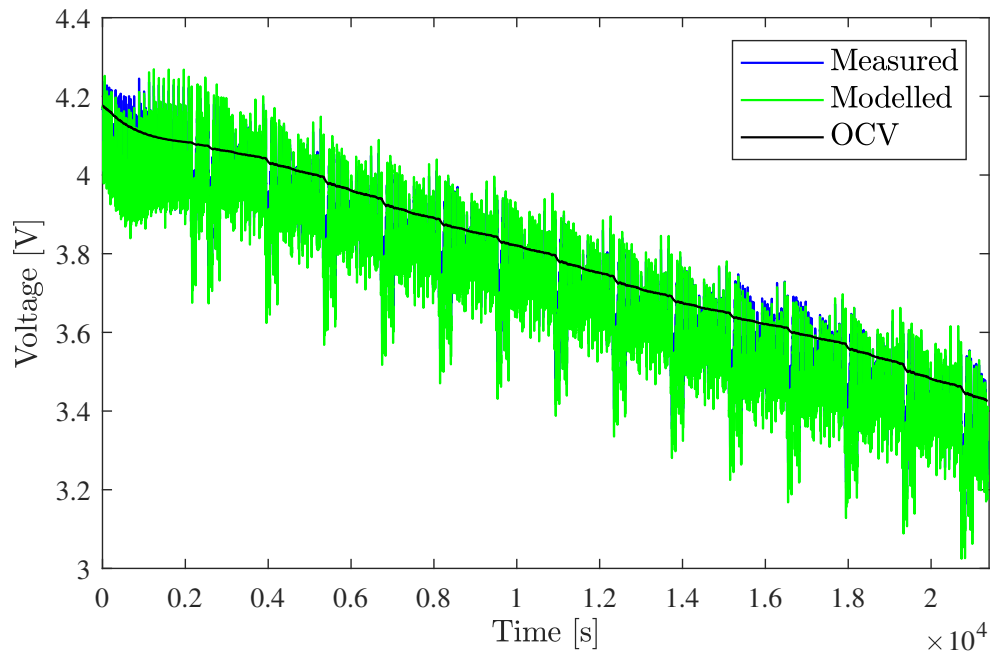
$V_{modelled}$ = model predicted voltage

$V_{measured}$ = experimentally measured voltage

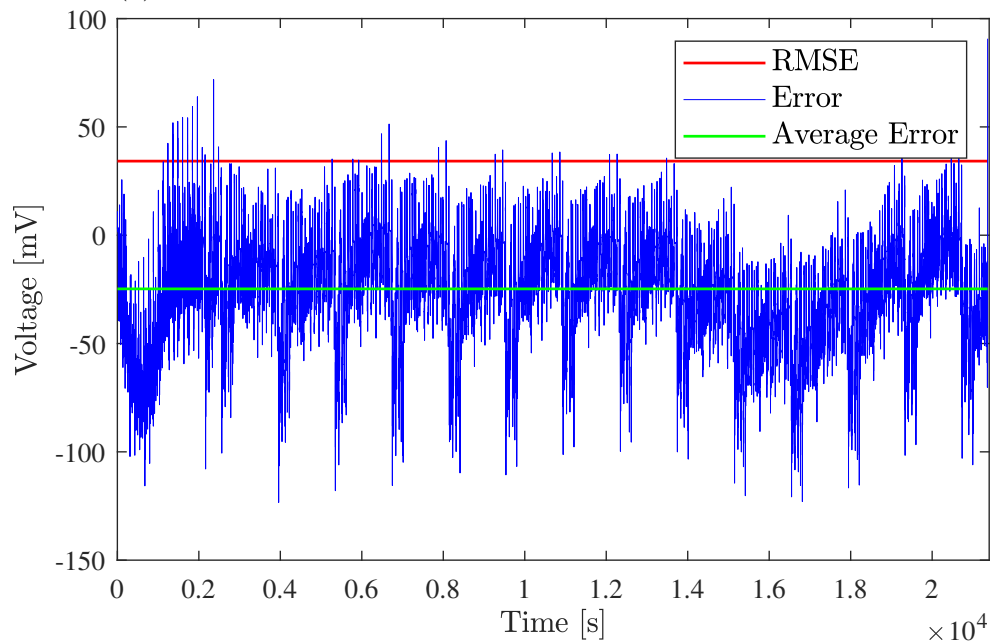
n = total number of simulation points

The experimental validation of both models demonstrated that they perform well with drive cycles that have little resistive voltage drop and that do not stress the cell excessively. In this case, the UDDS and LA92 drive cycles have the lowest power characteristics and thus produced the smallest error. Figures 5.23 and 5.24 provide an example of these simulations for the example and proposed models, respectively. Conversely, the HWFET and US06 drive cycles have higher peak and average power characteristics and therefore they place a lot more stress on the cell during test. This observation was consistent with the results obtained using both models, which registered a larger error when attempting to simulate these drive cycles. Figures 5.25 and 5.26 provide an example of these simulations for the example and proposed models, respectively.

When comparing the results in Figure 5.23 through 5.26, it is evident that the voltage error increases greatly between drive cycles with low power characteristics and those that place more stress on the cell. The example model is able to achieve 34.21 mV RMSE and -24.77 mV average error with the UDDS drive cycle. However, the error for the same model when simulating the HWFET cycle is 147.55 mV RMSE and -139.65 mV average error. Similarly, the proposed model produces 29.47 mV RMSE and -24.89 mV average error with the UDDS drive cycle. When simulating the US06 drive cycle, the same model produces 181.82 mV RMSE and -153.32 mV average error. This is a clear demonstration that neither model can accurately replicate the cell's performance when it is subjected to

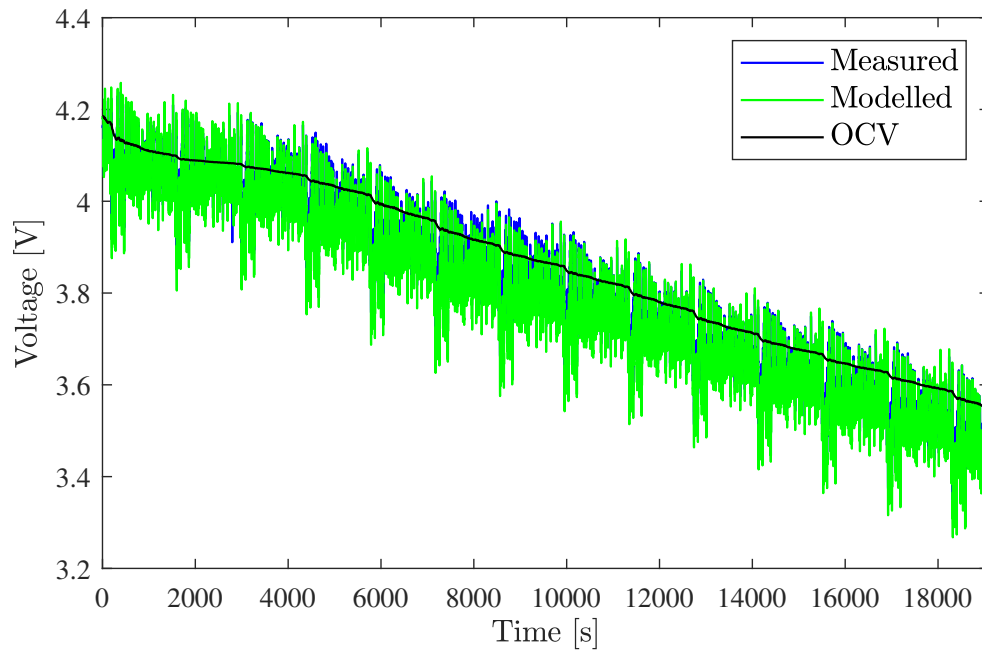


(a) Model predicted versus experimentally measured voltage

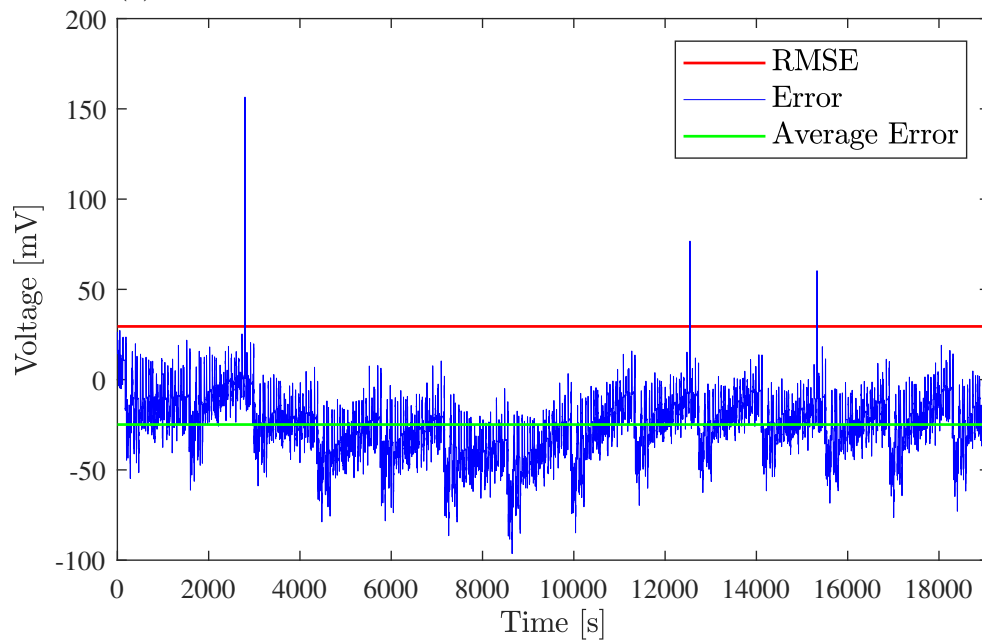


(b) Voltage error

Figure 5.23: Experimental validation of UDDS drive cycle with $L - R - RC - RC - Z_{wb}$ model ($T = 10^\circ\text{C}$)

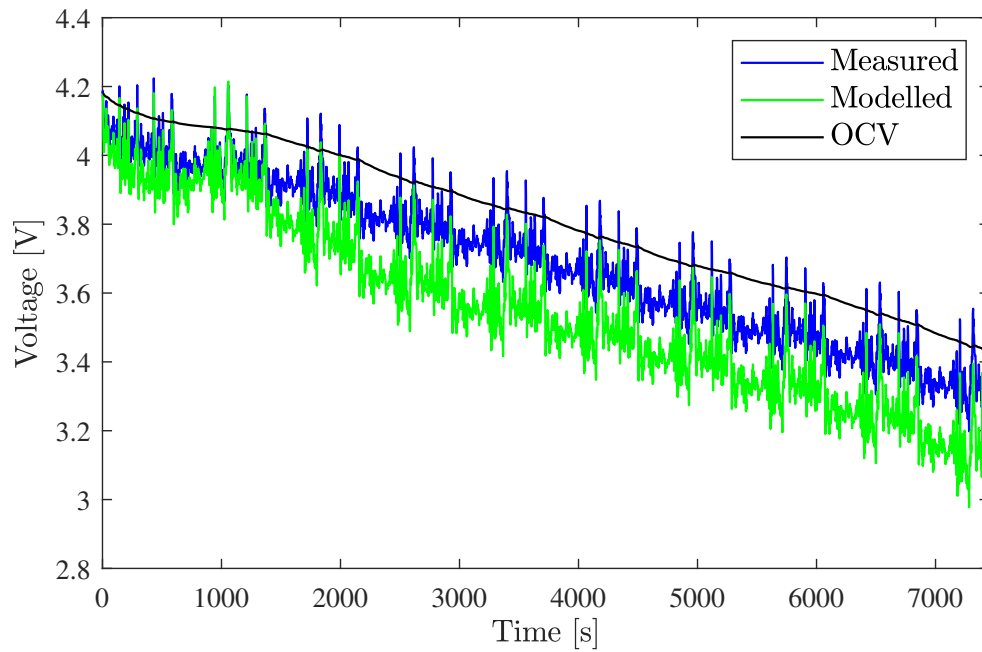


(a) Model predicted versus experimentally measured voltage

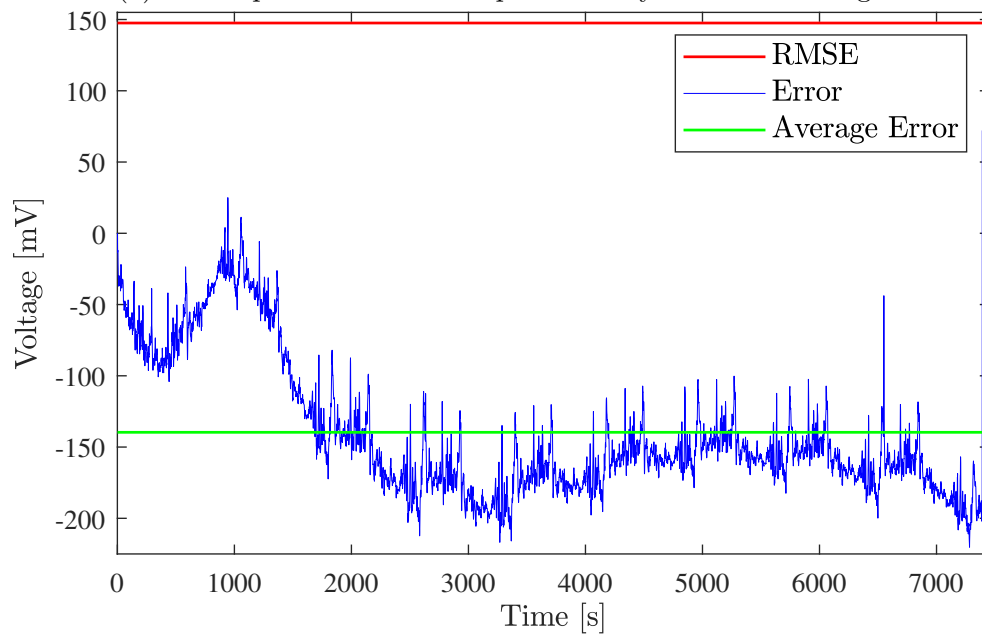


(b) Voltage error

Figure 5.24: Experimental validation of UDDS drive cycle with $L - R - ZARC - Z_{wb}$ model ($T = 40^\circ\text{C}$)

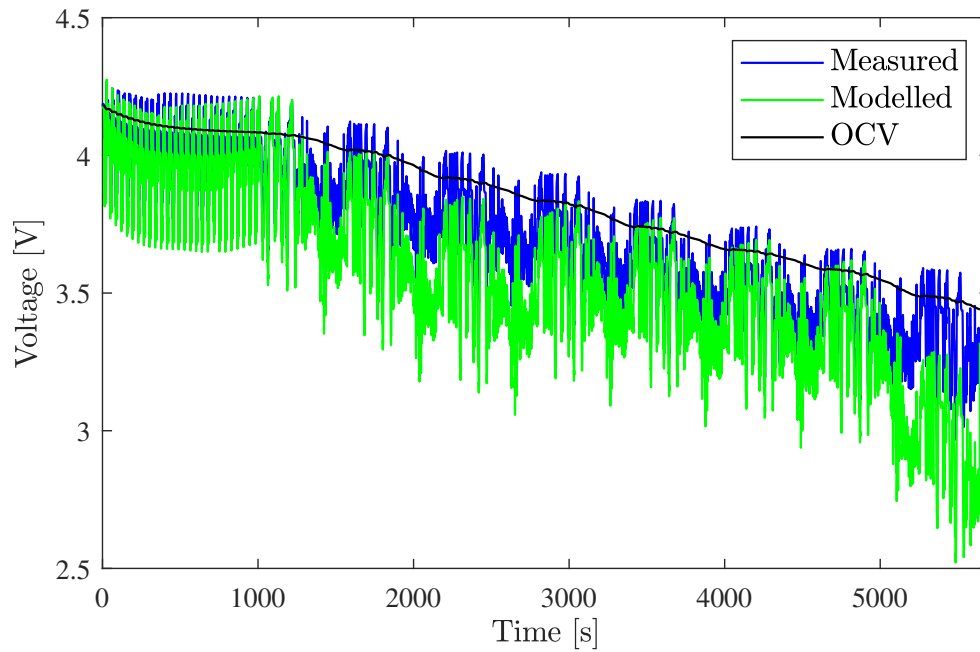


(a) Model predicted versus experimentally measured voltage

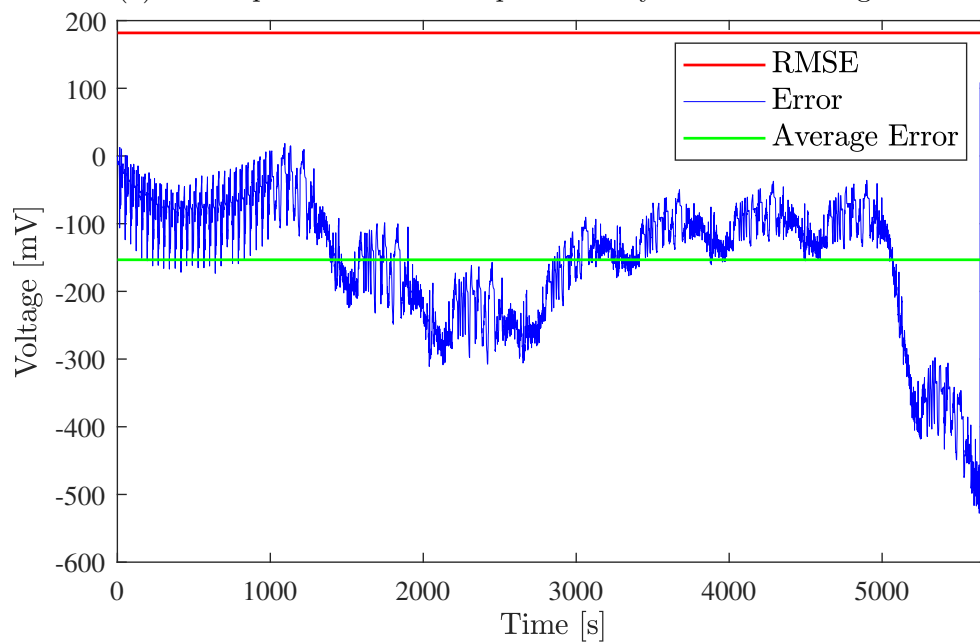


(b) Voltage error

Figure 5.25: Experimental validation of HWFET drive cycle with $L - R - RC - RC - Z_{wb}$ model ($T = 25^\circ\text{C}$)



(a) Model predicted versus experimentally measured voltage



(b) Voltage error

Figure 5.26: Experimental validation of US06 drive cycle with $L-R-ZARC-Z_{wb}$ model ($T = 25\text{ }^{\circ}\text{C}$)

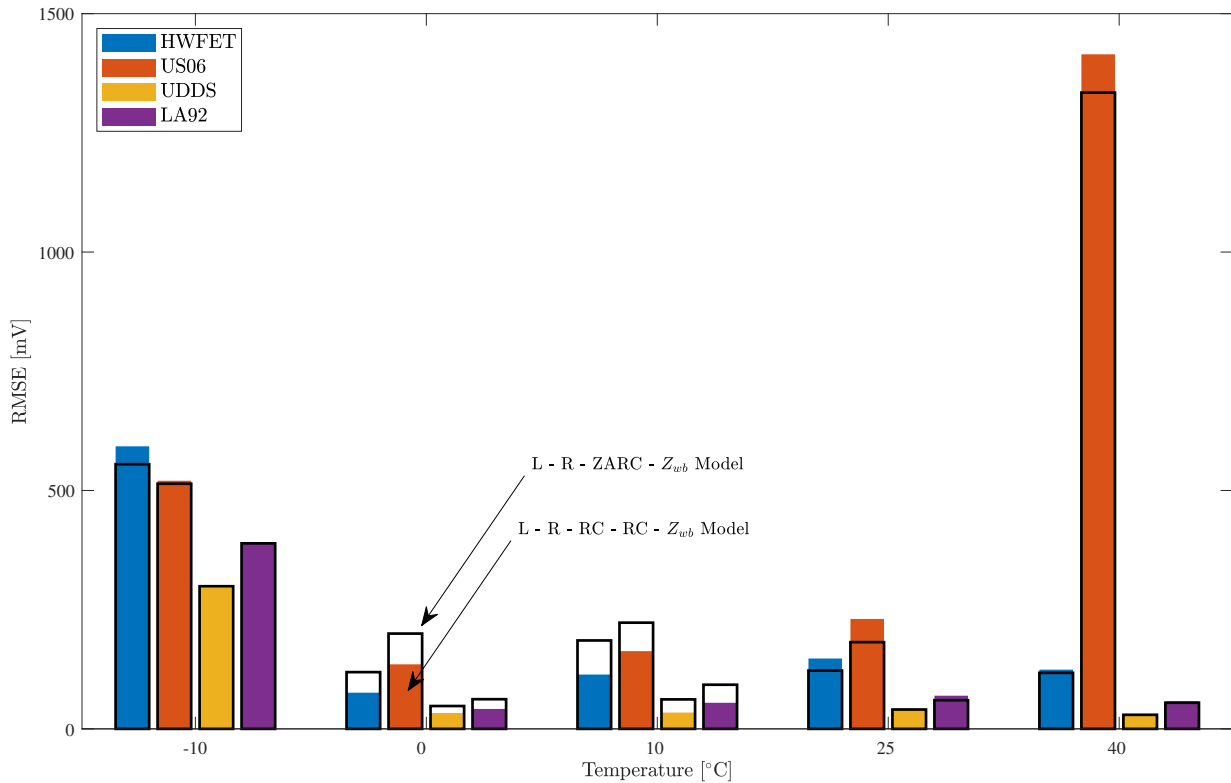


Figure 5.27: Voltage RMSE between model predicted and experimentally measured voltage for all drive cycles

aggressive drive cycles that are challenging to model.

Figure 5.27 presents the recorded RMSE for both models when simulating drive cycles at every temperature. In this figure, the solid colour bars represent the $L-R-RC-RC-Z_{wb}$ model, and the unshaded bars with the black outline represent the $L-R-ZARC-Z_{wb}$ model. The first observation that can be made is that both models fail to accurately capture the cell's performance at -10°C , where both models registered significant error during every drive cycle simulation. The smallest RMSE value recorded at this temperature was 296.22 mV when simulating the UDDS drive cycle using the example model. Beyond

this, the remaining RMSE values are larger, going up to 595.55 mV when simulating the HWFET drive cycle using the proposed model. In general, this inaccuracy is too large, particularly in safety critical applications such as an EV BMS where a 0.5 V offset could lead to catastrophic error. As such, the error is deemed unacceptable and it can be concluded that the models cannot precisely replicate the behaviour of the cell at -10°C .

Another observation that can be made from Figure 5.27 is that, across all temperatures, both models recorded a lower error for the less dynamic drive cycles that are relatively easier to model (UDDS and LA92). This is consistent with the results presented earlier that highlight the poor performance of both models when simulating the HWFET and US06 drive cycles. This trend for the $L - R - RC - RC - Z_{wb}$ model is also consistent with the findings presented by Kollmeyer *et al.* in their research [83]. Furthermore, the parameterization results from Section 5.3 demonstrated that the worst performance for both models occurred at -10°C and 40°C . This is generally reflected in the experimental validation of the models as they both performed relatively poorly at these temperatures.

There are two conclusions that can be drawn from the simulation results obtained using both models. Firstly, the performance of both models indicates that they do not accurately capture the behaviour of the cell when subjected to real-world driving scenarios. The lowest RMSE recorded by the $L - R - RC - RC - Z_{wb}$ model was 31.25 mV when simulating the UDDS drive cycle at 40°C . In addition to this, the lowest value recorded by the $L - R - ZARC - Z_{wb}$ model was 29.47 mV for the UDDS drive cycle at 40°C . These values are still relatively too large and not favourable in BMS applications; as indicated in literature, an ideal error value for such scenarios would be smaller than 10 mV or even as high as 20 mV [53, 89, 90]. Furthermore, comparing the results between both models

demonstrates that there is significant difference in their performance and that there is no concrete evidence to indicate that one model is more accurate than the other when simulating the cell's behaviour. For example, as seen in Figure 5.27, the performance for both models is comparable at -10°C and 40°C , with the exception of two specific cases. More so, the proposed model is able to reduce the simulation RMSE at 25°C but in fact produces a larger error at 0°C and 10°C . Therefore, while the performance of both models is inadequate for the purpose of simulating the cell's behaviour, there is no clear indication that the proposed model provides any improvement to the example model studied by Kollmeyer *et al.* [83].

5.5 Analysis of Low Frequency Impedance Data

One of the shortcomings of the example model identified in Section 5.1 is the poor fitting of the Warburg tail region, as demonstrated in Figure 5.4. To address this issue, EIS data collected during this research was performed down to 1 mHz at 0°C and above, and down to 100 μHz at -10°C . This was done to provide more data points in this low frequency range as input to the model in hopes of improving the accuracy of the fitting. To determine whether using low frequency impedance points was advantageous, this section will examine how the use of different frequency ranges will affect the parametrization process discussed in Section 5.3 as well as the experimental validation discussed in Section 5.4.

The parameterization process for the proposed model is repeated using the impedance data collected at 25°C while terminating the frequency range at the following values: 1 mHz, 25 mHz, 63 mHz and 100 mHz. For example, the model is fit to the impedance

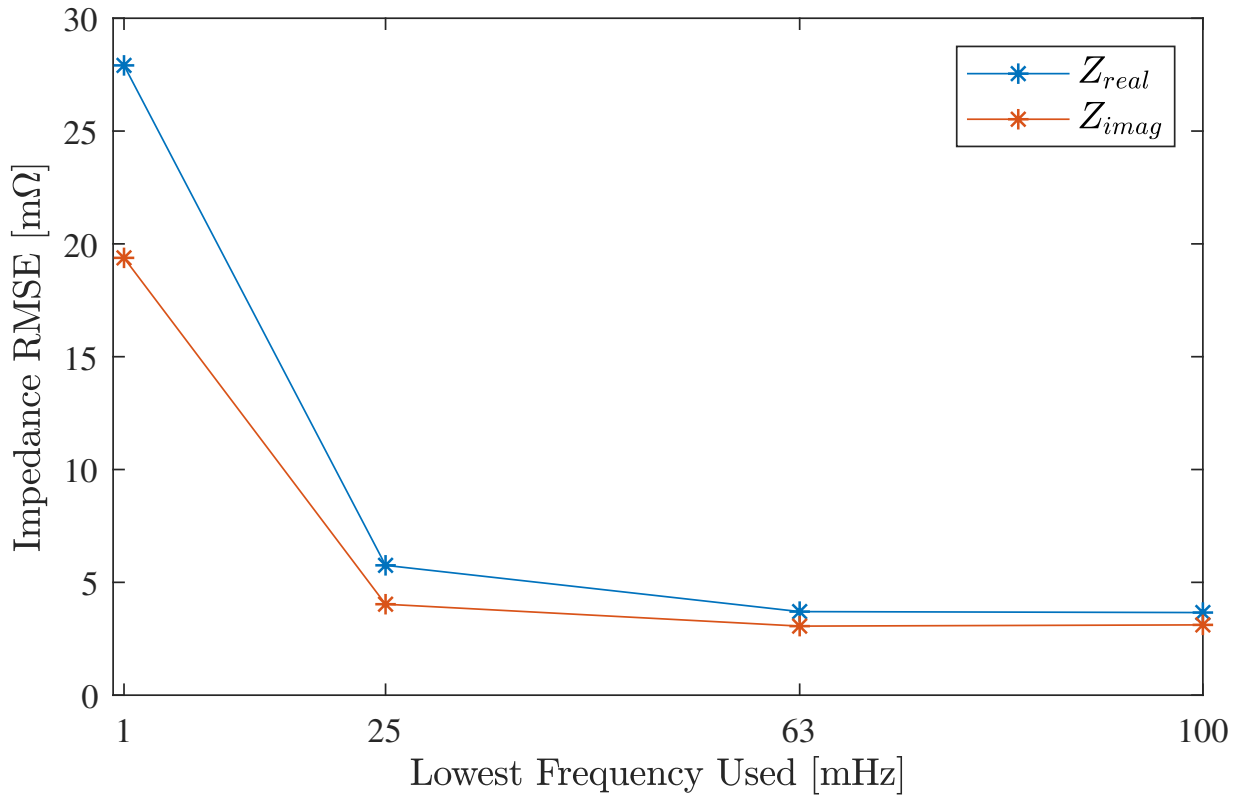


Figure 5.28: Real and imaginary impedance RMSE for ZARC model at different stopping frequencies ($T = 25\text{ }^{\circ}\text{C}$)

data collected all the way down to 100 mHz, and then again down to 63 mHz, and so on. The real and imaginary impedance RMSE values for each of these scenarios are calculated using Equation (5.11). Figure 5.28 provides a visual representation of the total error (across all SOC levels) when using these varying frequency ranges. It can be immediately observed from this plot that terminating the frequency range at 25 mHz or higher reduces the modelling error to a stable value of approximately 5 mΩ.

It is also worth taking a look at an example plot from each frequency range to visually compare the fitting in each scenario, as demonstrated in Figure 5.29. The first observation

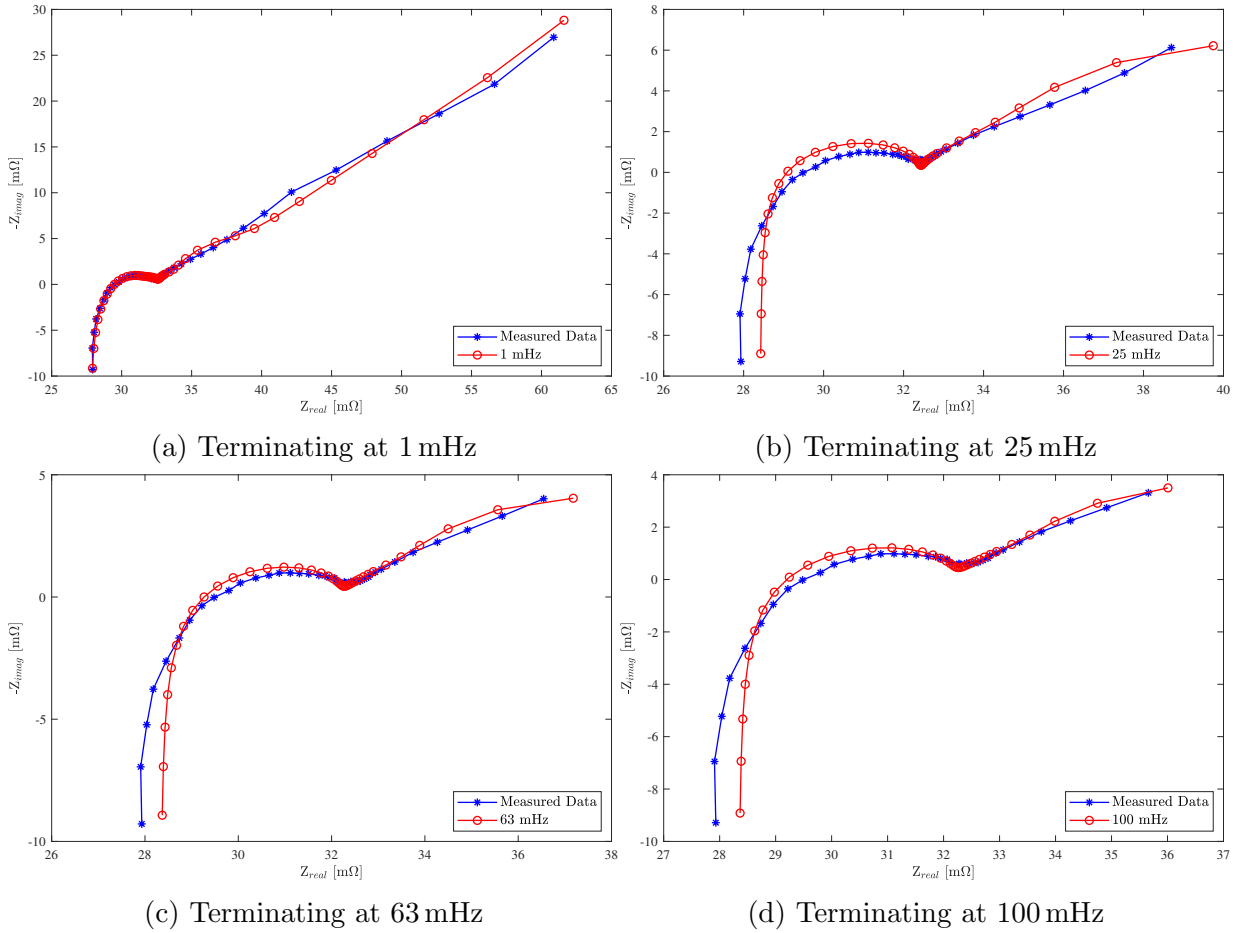


Figure 5.29: Modelling impedance data with $L - R - ZARC - Z_{wb}$ model using different frequency ranges ($T = 25^\circ\text{C}$, 80% SOC)

that can be made is that at 25 mHz and above, the Warburg tail region of the modelled data continues to bend at a right angle (Figures 5.29b through 5.29d). This trend is consistent with the original findings related to the example model studied by Kollmeyer *et al.* [83]. Furthermore, for these scenarios, the fitting of the mid-frequency semi-circle region is slightly deteriorated when compared to the example in Figure 5.29a. However, based on the reduction in total modelling error that is presented in Figure 5.28, the model fitting

Table 5.6: Time constant values for Warburg element when modelling with different stopping frequencies

SOC [%]	1 mHz [s]	25 mHz [s]	63 mHz [s]	100 mHz [s]
100	6.581E+02	8.734E+00	1.218E+01	1.486E+01
95	1.245E+03	6.062E+00	1.721E+00	1.829E+00
90	1.041E+02	6.238E+00	2.391E+00	1.890E+00
80	9.664E+02	9.215E+00	3.479E+00	2.636E+00
70	1.108E+03	8.691E+00	3.429E+00	2.442E+00
60	2.885E+02	9.327E+00	3.308E+00	2.100E+00
50	3.141E+02	9.674E+00	3.259E+00	2.129E+00
40	2.992E+02	9.495E+00	2.903E+00	1.496E+00
30	3.519E+02	9.583E+00	3.384E+00	1.069E+00
25	6.963E+02	1.009E+01	2.101E+00	1.326E+00
20	5.331E+03	2.418E+01	1.129E+01	1.347E+01
15	3.532E+04	1.042E+01	1.731E+00	4.753E+01
10	2.456E+04	2.562E+01	1.048E+01	7.583E+00
5	1.284E+04	2.538E+01	5.234E+00	5.438E+00
0	8.031E+03	2.816E+01	1.498E+01	2.586E+00

at these frequency ranges is deemed acceptable and can be considered sufficient for the purpose of capturing the cell's impedance behaviour.

Another worthwhile observation that can be made from this exercise is the change in the Warburg element time constant as the frequency range used for modelling varies. The calculated Warburg time constant for each frequency range is presented in Table 5.6. Additionally, the average time constant for each stopping frequency is listed in Table 5.7. These results highlight a significant decrease in the time constant when modelling down to 25 mHz or higher. The average time constant when modelling down to 1 mHz is close to two hours, whereas at 25 mHz and above it is no larger than 14 seconds. The long Warburg element time constant needed to model the data down to 1 mHz immediately brings to light

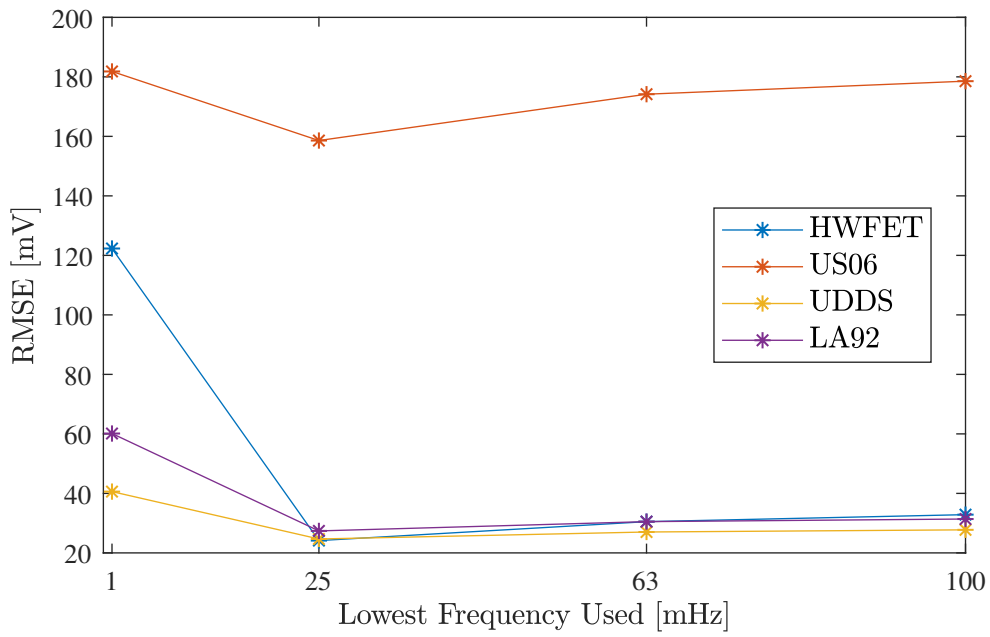
Table 5.7: Average Warburg element time constant values across all SOC levels for different stopping frequencies ($T = 25\text{ }^{\circ}\text{C}$)

1 mHz [s]	25 mHz [s]	63 mHz [s]	100 mHz [s]
6.141E+03	1.339E+01	5.458E+00	7.226E+00

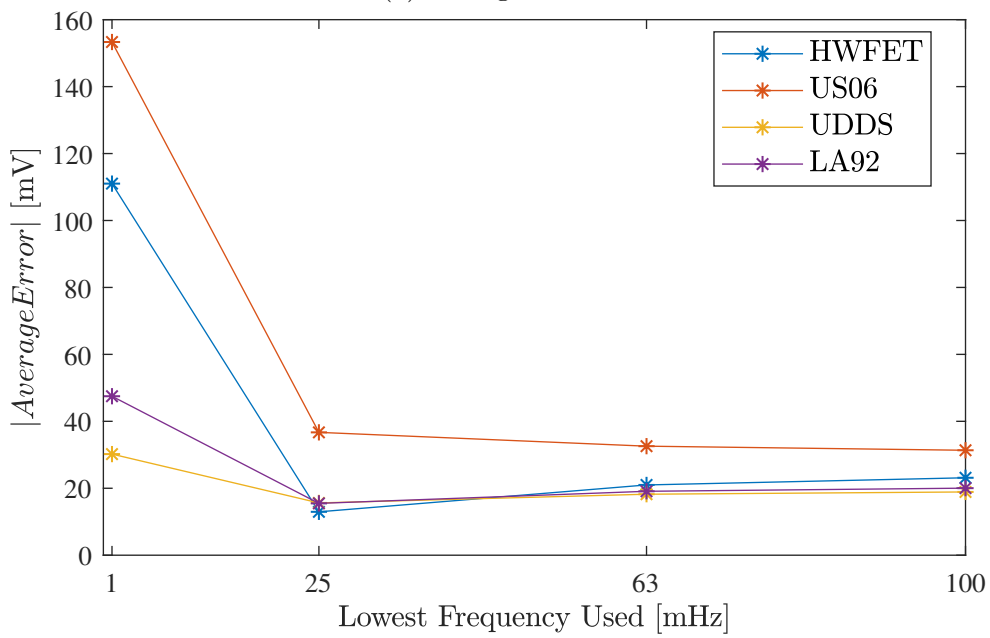
a potential issue with the impedance data that is being used to fit the models.

The choice to use a frequency as low as 1 mHz was originally intended to provide the model with more data to fit and improve the accuracy of the fitting. However, this time constant value indicates that the model is treating the cell as a very large capacitor which ultimately means that it is not properly capturing the dynamic behaviour of the cell. This issue may be the underlying cause that is increasing the voltage offset when simulating the experimental data and skewing the results by producing a large error. Furthermore, using a very low frequency for EIS testing could prove to be more detrimental to the model fitting than originally anticipated. A signal with a frequency of 1 mHz translates to a period of roughly 0.28 hours. This means that, with a current amplitude of 0.1 A, there is approximately 28 mA of charge being cycled in and out of the cell, resulting in an SOC swing of roughly 0.6%. This change could be influencing the EIS results which are supposed to determine the response of the cell to a very small variation.

To further examine the effect of this change in the Warburg element time constant, the experimental validation is repeated using the model parameters from each frequency range. The RMSE and average error values in each case are presented in Figure 5.30. It can be observed that the smaller Warburg element time constant has a significant impact on the experimental validation of the model as there is an error reduction in nearly every



(a) Voltage RMSE



(b) Average voltage error

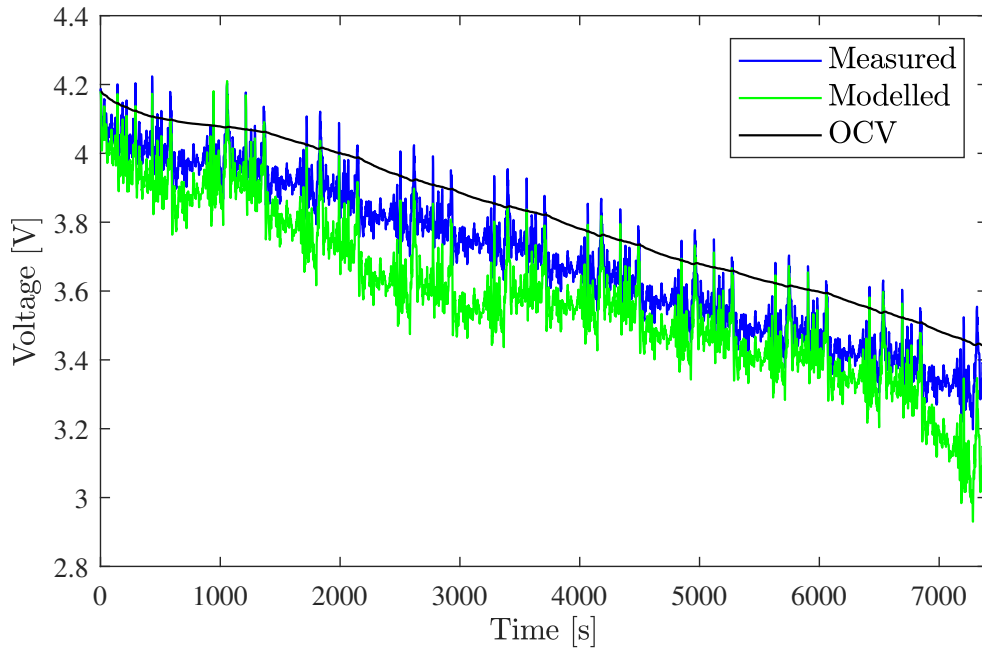
Figure 5.30: Comparing error values from model validation using different stopping frequencies ($T = 25\text{ }^\circ\text{C}$)

scenario recorded. With respect to the drive cycles that do not place a lot of stress on the cell (UDDS and LA92), the error reduction is not as prominent as the error was initially relatively low. However, with the exception of the RMSE for the US06 drive cycle, there is significant improvement in the error values for the HWFET and US06 drive cycles.

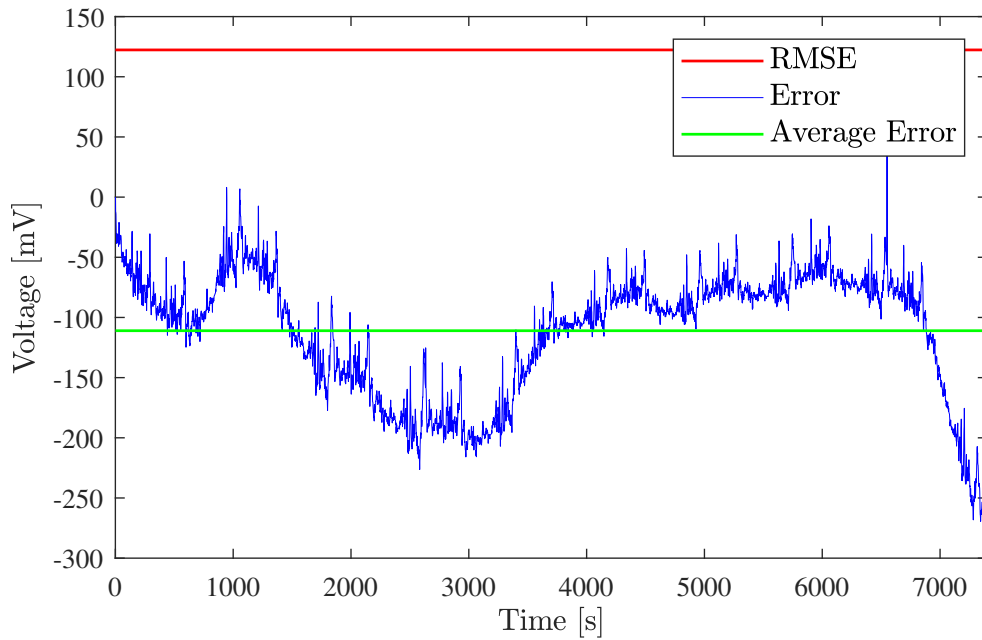
Figure 5.31 presents the experimental validation of the HWFET drive cycle after fitting the model down to 1 mHz. Fitting the model down to 25 mHz reduces the RMSE and average error by as much as 80% and 88%, respectively. When fitting the model to data at this frequency range, the $L - R - ZARC - Z_{wb}$ model is now able to simulate the HWFET drive cycle with an RMSE of 24.14 mV and an average error of 12.96 mV. This improvement is highlighted by the results presented in Figure 5.32. Additionally, the average error for the US06 drive cycle is also reduced by as much as 80%. While these values can still be improved further, this adjustment in the Warburg element time constant brings the modelling error much closer to an acceptable value.

5.6 Summary

This chapter focused on the impedance modelling of the cell being studied and the approach involved in choosing a model, optimizing it and validating its performance. An example model from literature was introduced and its shortcomings were assessed to derive potential areas of improvement. From there a different model was proposed that utilized the time domain representation of a CPE to improve upon the accuracy of the example model. Each element that the proposed model is comprised of was discussed to indicate its role in modelling the measured impedance data. Furthermore, the rationale behind low frequency

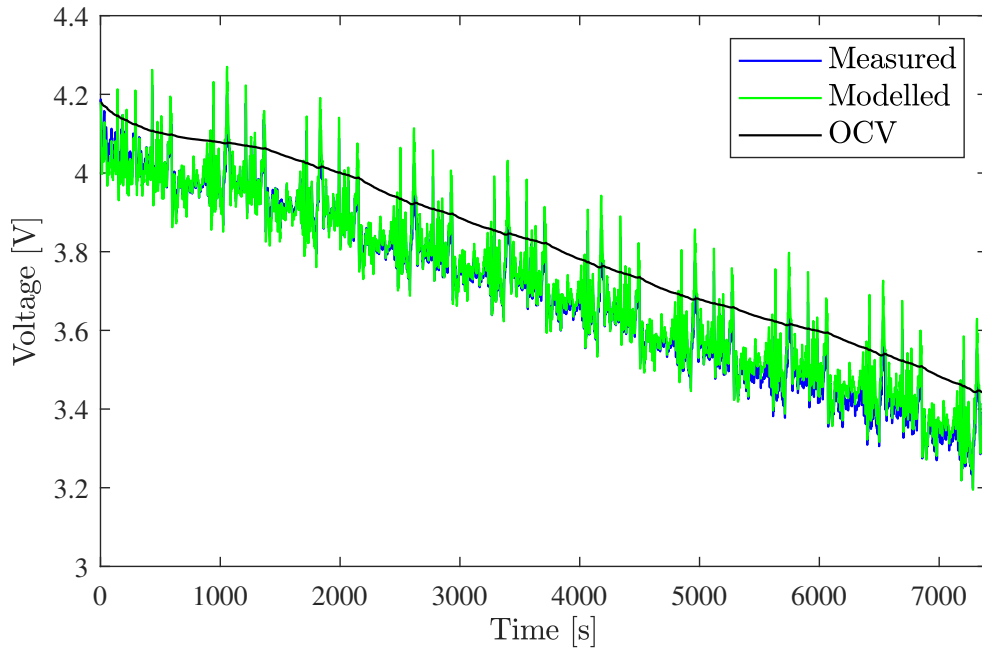


(a) Model predicted versus experimentally measured voltage

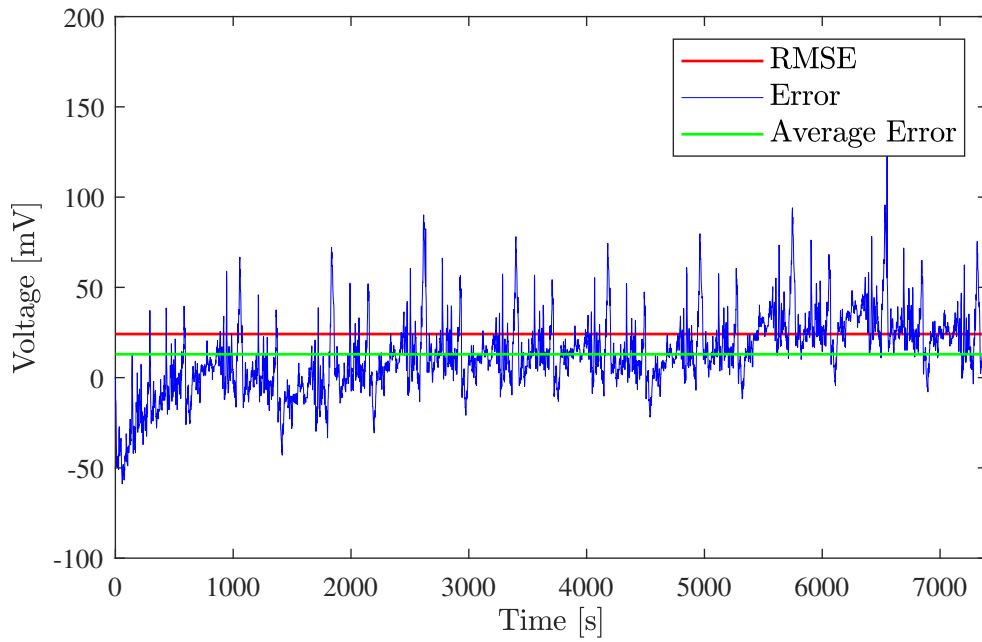


(b) Voltage error

Figure 5.31: Experimental validation of HWFET drive cycle with $L - R - ZARC - Z_{wb}$ model after fitting down to 1 mHz ($T = 25\text{ }^\circ\text{C}$)



(a) Model predicted versus experimentally measured voltage



(b) Voltage error

Figure 5.32: Experimental validation of HWFET drive cycle with $L - R - ZARC - Z_{wb}$ model after fitting down to 25 mHz ($T = 25\text{ }^{\circ}\text{C}$)

EIS testing was explained as well as its role in improving the proposed model's accuracy. The procedure to fit and optimize the models using MATLAB was also explained.

The results of the impedance spectra fitting were able to demonstrate a strong improvement by the proposed model relative to the example model. It was shown that the use of the ZARC element greatly improved the fitting of the mid-frequency semi-circle region of the impedance data. This improvement was consistent across a range of SOC levels and temperatures. Additionally, the calculated impedance RMSE and average impedance error values indicated that the proposed model provided a significant increase in fitting accuracy at 10°C, 0°C and -10°C. The performance of the two models at 25°C and 40°C was comparable, with a negligible difference in their impedance RMSE and average impedance error values. It was also shown that this improvement in performance was achieved with a very minor increase in computation time, despite the need to optimize 6 additional parameters, demonstrating the benefit of using the proposed model to fit the impedance data.

The procedure required to experimentally validate the performance of both models using drive cycle profiles was described. These results indicated that both models performed relatively well with drive cycles that have low power characteristics and that do not stress the cell excessively. However, with more challenging drive cycles that have higher power characteristics, both models produced more error. Furthermore, it was shown that both models performed poorly and were not able to capture the performance of the cell at -10°C. While in some cases the models were able to simulate the voltage of the cell with a relatively low voltage RMSE and average voltage error, it was ultimately concluded that their overall performance was not accurate enough for a safety critical application such

as a BMS. There was also no concrete evidence found in the results to suggest that the proposed model was able to capture the dynamic behaviour of the cell more accurately, or vice versa.

The final section of this chapter analyzed the use of low frequency impedance data in the model fitting approach by revisiting the modelling process at 25 °C. It was shown that using a frequency range with a stopping frequency higher than 1 mHz (such as 25 mHz) greatly reduced the impedance RMSE without comprising the fitting of the impedance plots. This analysis also showcased a very large reduction in the Warburg element time constant. This led to the conclusion that using a frequency as low as 1 mHz is not necessary and that it actually deteriorated the performance of the model. This change in the Warburg element time constant was also validated experimentally which also demonstrated an improvement in the model performance. It was shown that, by modelling down to 25 mHz, there was an improvement in the voltage RMSE and average voltage error by 80 % and 88 %, respectively.

Chapter 6

Conclusions and Future Work

The search for clean transportation and renewable energy sources is a fundamental challenge that is a major driving force behind the need for electrified transportation today. A crucial aspect of transportation electrification is using batteries to store energy and improving their performance and range to match traditional technologies that are already available. The main motivation behind this research and the work presented in this thesis is to help advance the study of battery technology and strive towards a more sustainable future.

A key area of battery research is testing and characterizing different systems which involves precise and highly specialized equipment. As battery systems grow in complexity, testing them and improving their performance requires more resources and higher costs. Therefore, battery testing equipment is a critical consideration for any stakeholders involved in battery research. Furthermore, battery modelling is an essential asset for researchers as it can help them simulate a battery's behaviour across a wide range of conditions. This approach can ultimately give critical insight about a battery and help improve

its performance while reducing the cost and time involved in conducting research.

This research and thesis is comprised of two concurrent segments: the development and testing of an integrated battery cell testing unit, as well as collecting data to analyze and characterize the impedance of a cell. The objective of this thesis is to provide a comprehensive study of a battery's performance under a wide range of operating conditions while showcasing the importance and benefits of using an integrated testing unit. The contributions of this research work are summarized as follows:

1. The joint development of a state of the art, integrated testing unit that provides a wide range of processes aimed at streamlining and improving battery test procedures. As part of this work, the usability and functionality of this tester was refined through software development. Furthermore, the tester was fully integrated into a research lab in order to validate its operation and safety controls. This involved incorporating the tester with a TMU, an environmental chamber and safety mechanisms in the lab such as fire suppression. By validating the tester's operation and making it available in the lab it is now able to serve many other researches in this area who have the need for elaborate and extended battery testing procedures. As part of this thesis, the benefits of the integrated tester were highlighted, as well as the advantages it offers relative to existing industry battery test solutions.
2. Thorough testing and characterization of a lithium-ion cell with specifications comparable to cells used in industry applications such as HEV and EV battery packs. This testing was carried out at a wide range of temperatures (40 °C to -10 °C) to cover the general operating limits of a cell used in electrified transportation appli-

cations. It was also done at a full SOC range (100% to 0%) to cover the entire span of the cell's performance capabilities. These tests focused on crucial aspects of the cell's performance to capture OCV-SOC, resistive and capacitive, as well as impedance characteristics. This extensive testing provides a detailed understanding of how the cell's performance is influenced by different operating conditions and why it is important to capture these characteristics when modelling the behaviour of the cell. The full characterization data can now be made available for other researchers that may utilize it, who do not have access to similar apparatus or the funding and resources required to extensively test a cell for their research needs. Additionally, this thesis provided a detailed test procedure description and setup that can serve as a reference for other researchers.

3. The proposal of an equivalent circuit model that can accurately capture the impedance behaviour of lithium-ion cell across a wide range of operating conditions. The results produced by this model demonstrated that the use of a ZARC element can greatly improve the mid-frequency fitting of impedance data relative to a conventionally used modelling approach. This was highlighted by a reduction in impedance RMSE of up to 54% without requiring a considerable increase in computational effort. This research also demonstrated the importance of choosing the right modelling approach for specific applications, as the accurate impedance fitting did not translate to acceptable results when experimentally validating the model using temporal data.
4. A study and analysis of low frequency EIS data and the effect it has on model fitting as well as experimental validation. This research was able to demonstrate

that using a frequency as low as 1 mHz is not required to improve the accuracy of an impedance model. Furthermore it was shown that a stopping frequency of 25 mHz or higher could reduce the real and imaginary impedance RMSE values without compromising the overall fit of the model to the measured data. This improvement was also noted during experimental validation which showed that using 25 mHz as a stopping frequency reduced the voltage RMSE and average voltage error by as much as 80 % and 88 %, respectively. This observation can ultimately benefit many researchers who utilize these results as it will reduce the amount of time required for EIS testing (by avoiding very low frequencies) while also eliminating the need for specialized and potentially expensive equipment to run EIS tests at very low frequencies.

6.1 Future Work

There are various potential areas of development that could help refine the results of this research work, pertaining to both the modelling approach as well as the collection of characterization data. These improvements are suggested for any researchers who wish to utilize this work in the future and may benefit from the additional research considerations:

1. Extending the range of operating temperatures at which the cell is tested and characterized. In this research, the following temperatures are used: 40 °C, 25 °C, 10 °C, 0 °C and -10 °C. Collecting data at more frequent temperature intervals (e.g. 5 °C increments) could make the model more robust and better capture the cell's perfor-

mance over the entire temperature range.

2. Considering battery aging when collecting characterization data and choosing inputs for a battery model. As part of this research, the cell is tested extensively and constantly subjected to temperature variations, current variations as well as SOC swings. All of these factors could increase the effects of aging on the cell, and addressing them could translate to further improvement in the model accuracy.
3. Incorporating a thermal model for estimating the internal temperature of the battery. During the course of characterizing the cell and collecting experimental validation data, the temperature of the cell can experience temperature fluctuations which could impact modelling results. For example, there is considerable battery heating that occurs when running drive cycles with large power characteristics. This can result in additional error by creating a lag between the measured temperature of the cell, which is inputted to the model, and the actual internal temperature of the cell.
4. Collecting more characterization data sets for the cell, repeating it several times using different cells and if possible more than one test device. Due to time constraints and the availability of lab resources, it was only possible to test a single cell using the battery tester under development. It would be beneficial to have multiple cells tested to demonstrate that the results are consistent and identify any points of variation that could be present. Furthermore, the tester used to collect the characterization data was still under development at the time of testing and undergoing continuous refinement. It would be worthwhile to run the same characterization tests under the same operating conditions while using a different tester, if possible. This

can increase confidence that the characterization data is consistent and accurate.

References

- [1] Larry Fromm, “Why an Internal Combustion Engine?” <http://achatespower.com/why-internal-combustion-engine/>, April 2015.
- [2] energysage, “Tesla Model S and Model X charging: everything you need to know,” <https://www.energysage.com/electric-vehicles/charging-your-ev/charging-a-tesla/>, January 2019.
- [3] Chris Dinesen Rogers, “The Effects of Carbon Dioxide on Air Pollution,” <https://sciencing.com/list-5921485-effects-carbon-dioxide-air-pollution.html>, Jan. 2018.
- [4] Environment and Climate Change Canada, “Air pollution: drivers and impacts,” <http://www.ec.gc.ca/indicateurs-indicators/default.asp?lang=en&n=D189C09D-1>, Aug. 2017.
- [5] ———, “Canadian Environmental Sustainability Indicators: Greenhouse gas emissions,” <https://www.canada.ca/content/dam/eccc/documents/pdf/cesindicators/greenhouse-gas-emissions/greenhouse-gas-emissions-en.pdf>, 2018.
- [6] United States Environmental Protection Agency, “Global Greenhouse Gas Emissions Data,” <https://www.epa.gov/ghgemissions/global-greenhouse-gas-emissions-data>, Apr. 2017, last accessed: January 24th, 2019.
- [7] National Aeronautics and Space Administration, “Climate change: How do we know?” <https://climate.nasa.gov/evidence/>, Dec. 2018.
- [8] CBC News Interactives, “How a 2 C temperature increase could change the planet,” <https://www.cbc.ca/news2/interactives/2degrees/>.
- [9] K. G. Høyer, “The history of alternative fuels in transportation: The case of electric and hybrid cars,” *Utilities Policy*, vol. 16, no. 2, pp. 63 –

- 71, 2008, sustainable Energy and Transportation Systems. [Online]. Available: <http://www.sciencedirect.com/science/article/pii/S0957178707000768>
- [10] R. Farrell, “Gustave trouve pioneers electric transport in 1881,” <https://www.upsbatterycenter.com/blog/gustave-trouve-electric-tricycle/>, June 2018.
- [11] E. H. Wakefield, *History of the electric automobile: hybrid electric vehicles*. 400 Commonwealth Dr., Wallendale PA USA: Society of Automotive Engineers, 1998.
- [12] Nissan Canada. [Online]. Available: <https://www.nissan.ca/en>
- [13] Honda Canada. [Online]. Available: <https://www.honda.ca/>
- [14] M. Farag, “Lithium-ion batteries: Modelling and state of charge estimation,” Master’s thesis, McMaster University, <http://hdl.handle.net/11375/15253>, October 2013.
- [15] S. J. Moura, J. B. Siegel, D. J. Siegel, H. K. Fathy, and A. G. Stefanopoulou, “Education on vehicle electrification: Battery systems, fuel cells, and hydrogen,” in *2010 IEEE Vehicle Power and Propulsion Conference*, Sep. 2010, pp. 1–6.
- [16] V. Pop, H. J. Bergveld, D. Danilov, P. P. L. Regtien, and P. H. L. Notten, *Battery Management Systems*, 1st ed., ser. Philips Research Book Series. Springer Netherlands, 2008, vol. 9.
- [17] J. Chiasson and B. Vairamohan, “Estimating the state of charge of a battery,” *IEEE Transactions on Control Systems Technology*, vol. 13, no. 3, pp. 465–470, May 2005.
- [18] Y. Tian, D. Li, J. Tian, and B. Xia, “A comparative study of state-of-charge estimation algorithms for lithium-ion batteries in wireless charging electric vehicles,” in *2016 IEEE PELS Workshop on Emerging Technologies: Wireless Power Transfer (WoW)*, Oct 2016, pp. 186–190.
- [19] A. Vasebi, S. Bathaee, and M. Partovibakhsh, “Predicting state of charge of lead-acid batteries for hybrid electric vehicles by extended kalman filter,” *Energy Conversion and Management*, vol. 49, no. 1, pp. 75 – 82, 2008. [Online]. Available: <http://www.sciencedirect.com/science/article/pii/S0196890407001550>
- [20] R. Babazadeh and A. G. Khiabani, “Nonlinear observer design for rc battery model for estimating state of charge state of health based on state-dependent riccati equation,” in *2018 IEEE Electrical Power and Energy Conference (EPEC)*, Oct 2018, pp. 1–5.

- [21] N. Fouquet, C. Doulet, C. Nouillant, G. Dauphin-Tanguy, and B. Ould-Bouamama, "Model based pem fuel cell state-of-health monitoring via ac impedance measurements," *Journal of Power Sources*, vol. 159, no. 2, pp. 905 – 913, 2006. [Online]. Available: <http://www.sciencedirect.com/science/article/pii/S0378775305015946>
- [22] V. Sangwan, A. Sharma, R. Kumar, and A. K. Rathore, "Estimation of optimal li-ion battery parameters considering c-rate, soc and temperature," in *2016 7th India International Conference on Power Electronics (IICPE)*, Nov 2016, pp. 1–6.
- [23] Electropaedia, "Battery Performance Characteristics," <https://www.mpoweruk.com/performance.htm>, 2005.
- [24] R. Ahmed, "Modeling and state of charge estimation of electric vehicle batteries," Ph.D. dissertation, McMaster University, <http://hdl.handle.net/11375/16436>, 2014.
- [25] M. E. V. Team, "A guide to understanding battery specifications," Massachusetts Institute of Technology, http://web.mit.edu/evt/summary_battery_specifications.pdf, Tech. Rep., December 2008.
- [26] T. Guena and P. Leblanc, "How depth of discharge affects the cycle life of lithium-metal-polymer batteries," in *INTELEC 06 - Twenty-Eighth International Telecommunications Energy Conference*, Sep. 2006, pp. 1–8.
- [27] energymag, "Depth of discharge," <https://energymag.net/dod-depth-of-discharge/>, October 2012.
- [28] Gamry Instruments. Basics of electrochemical impedance spectroscopy. [Online]. Available: <https://www.gamry.com/application-notes/EIS/basics-of-electrochemical-impedance-spectroscopy/>
- [29] D. Andre, M. Meiler, K. Steiner, C. Wimmer, T. Soczka-Guth, and D. Sauer, "Characterization of high-power lithium-ion batteries by electrochemical impedance spectroscopy. i. experimental investigation," *Journal of Power Sources*, vol. 196, no. 12, pp. 5334 – 5341, 2011, selected papers presented at the 12th Ulm ElectroChemical Talks (UECT):2015 Technologies on Batteries and Fuel Cells. [Online]. Available: <http://www.sciencedirect.com/science/article/pii/S0378775311000681>
- [30] S. Alavi, C. Birkl, and D. Howey, "Time-domain fitting of battery electrochemical impedance models," *Journal of Power Sources*, vol. 288, pp. 345 – 352, 2015. [Online]. Available: <http://www.sciencedirect.com/science/article/pii/S0378775315007569>

- [31] J. P. Christophersen, "Battery state-of-health assessment using a near real-time impedance measurement technique under no-load and load conditions," Ph.D. dissertation, Montana State University, <https://scholarworks.montana.edu/xmlui/handle/1/1077>, 2011.
- [32] J. P. Christophersen, J. Morrison, W. Morrison, and C. Motloch, "Rapid impedance spectrum measurements for state-of-health assessment of energy storage devices," *SAE Int. J. Passeng. Cars - Electron. Electr. Syst.*, vol. 5, pp. 246–256, 04 2012. [Online]. Available: <https://doi.org/10.4271/2012-01-0657>
- [33] D.-I. Stroe, M. Swierczynski, A.-I. Stroe, and S. Knudsen Kær, "Generalized characterization methodology for performance modelling of lithium-ion batteries," *Batteries*, vol. 2, no. 4, 2016. [Online]. Available: <https://www.mdpi.com/2313-0105/2/4/37>
- [34] Min Chen and G. A. Rincon-Mora, "Accurate electrical battery model capable of predicting runtime and i-v performance," *IEEE Transactions on Energy Conversion*, vol. 21, no. 2, pp. 504–511, June 2006.
- [35] D. Fregosi, S. Bhattacharya, and S. Atcitty, "Empirical battery model characterizing a utility-scale carbon-enhanced vrla battery," in *2011 IEEE Energy Conversion Congress and Exposition*, Sep. 2011, pp. 3541–3548.
- [36] X. Hu, S. Li, and H. Peng, "A comparative study of equivalent circuit models for li-ion batteries," *Journal of Power Sources*, vol. 198, pp. 359 – 367, 2012. [Online]. Available: <http://www.sciencedirect.com/science/article/pii/S0378775311019628>
- [37] K. A. Smith, C. D. Rahn, and C. Wang, "Model-based electrochemical estimation of lithium-ion batteries," in *2008 IEEE International Conference on Control Applications*, Sep. 2008, pp. 714–719.
- [38] S. Li and B. Ke, "Study of battery modeling using mathematical and circuit oriented approaches," in *2011 IEEE Power and Energy Society General Meeting*, July 2011, pp. 1–8.
- [39] C. M. Shepherd, "Design of primary and secondary cells: Li . an equation describing battery discharge," *Journal of The Electrochemical Society*, vol. 112, no. 7, pp. 657–664, 1965. [Online]. Available: <http://jes.ecsdl.org/content/112/7/657.abstract>

- [40] S. Buller, *Impedance Based Simulation Models for Energy Storage Devices in Advanced Automotive Power Systems*, ser. Aachener Beiträge des ISEA. Shaker, 2003. [Online]. Available: <https://books.google.ca/books?id=2Q-mAAAACAAJ>
- [41] G. L. Plett, “Extended kalman filtering for battery management systems of lipb-based hev battery packs: Part 1. background,” *Journal of Power Sources*, vol. 134, no. 2, pp. 252 – 261, 2004. [Online]. Available: <http://www.sciencedirect.com/science/article/pii/S0378775304003593>
- [42] R. L. H. II, “An aging model for lithium-ion cells,” Ph.D. dissertation, University of Akron, Electrical Engineering, http://rave.ohiolink.edu/etdc/view?acc_num=akron1226887071, 2008.
- [43] D. W. Dees, V. S. Battaglia, and A. Bélanger, “Electrochemical modeling of lithium polymer batteries,” *Journal of Power Sources*, vol. 110, no. 2, pp. 310 – 320, 2002. [Online]. Available: <http://www.sciencedirect.com/science/article/pii/S0378775302001933>
- [44] M. Doyle, T. F. Fuller, and J. Newman, “Modeling of galvanostatic charge and discharge of the lithium/polymer/insertion cell,” *Journal of The Electrochemical Society*, vol. 140, no. 6, pp. 1526–1533, 1993. [Online]. Available: <http://jes.ecsdl.org/content/140/6/1526.abstract>
- [45] T. F. Fuller, M. Doyle, and J. Newman, “Simulation and optimization of the dual lithium ion insertion cell,” *Journal of The Electrochemical Society*, vol. 141, no. 1, pp. 1–10, 1994. [Online]. Available: <http://jes.ecsdl.org/content/141/1/1.abstract>
- [46] A. V. Randall, R. D. Perkins, X. Zhang, and G. L. Plett, “Controls oriented reduced order modeling of solid-electrolyte interphase layer growth,” *Journal of Power Sources*, vol. 209, pp. 282 – 288, 2012. [Online]. Available: <http://www.sciencedirect.com/science/article/pii/S0378775312005368>
- [47] K. A. Smith, C. D. Rahn, and C. Wang, “Model-based electrochemical estimation and constraint management for pulse operation of lithium ion batteries,” *IEEE Transactions on Control Systems Technology*, vol. 18, no. 3, pp. 654–663, May 2010.
- [48] J. L. Lee, A. Chemistruck, and G. L. Plett, “One-dimensional physics-based reduced-order model of lithium-ion dynamics,” *Journal of Power Sources*, vol. 220, pp. 430 – 448, 2012. [Online]. Available: <http://www.sciencedirect.com/science/article/pii/S0378775312012104>

- [49] G. Ilis, H. Demir, M. Akbaş, and M. Mobedi, “Recent developments on heat pump systems in electric vehicle and a suggestion,” in *Heated Powered Cycles*, Nottingham, United Kingdom, 06 2016.
- [50] N. Lin, S. Ci, and H. Li, “An enhanced circuit-based battery model with considerations of temperature effect,” in *2014 IEEE Energy Conversion Congress and Exposition (ECCE)*, Sep. 2014, pp. 3985–3989.
- [51] Guangming Liu, L. Lu, Hong Fu, Jianfeng Hua, J. Li, M. Ouyang, Yanjing Wang, Shan Xue, and Ping Chen, “A comparative study of equivalent circuit models and enhanced equivalent circuit models of lithium-ion batteries with different model structures,” in *2014 IEEE Conference and Expo Transportation Electrification Asia-Pacific (ITEC Asia-Pacific)*, Aug 2014, pp. 1–6.
- [52] M. Bahramipناه, D. Torregrossa, R. Cherkaoui, and M. Paolone, “Enhanced electrical model of lithium-based batteries accounting the charge redistribution effect,” in *2014 Power Systems Computation Conference*, Aug 2014, pp. 1–8.
- [53] D. Stroe, “Lifetime models for lithium-ion batteries used in virtual power plant applications,” Ph.D. dissertation, Aalborg University, <https://vbn.aau.dk/en/publications/lifetime-models-for-lithium-ion-batteries-used-in-virtual-power-p>, November 2014.
- [54] F. Saidani, F. X. Hutter, R.-G. Scurtu, W. Braunwarth, and J. N. Burghartz, “Lithium-ion battery models: a comparative study and a model-based powerline communication,” *Advances in Radio Science*, vol. 15, pp. 83–91, 2017. [Online]. Available: <https://www.adv-radio-sci.net/15/83/2017/>
- [55] D. Gallo, C. Landi, M. Luiso, A. Rosano, M. Landi, and V. Paciello, “Testing protocols for battery characterization,” in *2014 IEEE International Instrumentation and Measurement Technology Conference (I2MTC) Proceedings*, May 2014, pp. 374–379.
- [56] W. Jacobi and G. Eichinger, “Lithium rechargeable batteries for portable telecommunication appliances-basic concepts and recent developments,” in *TELESCON 2000. Third International Telecommunications Energy Special Conference (IEEE Cat. No.00EX424)*, May 2000, pp. 123–127.
- [57] Lijun Gao, Shengyi Liu, and R. A. Dougal, “Dynamic lithium-ion battery model for system simulation,” *IEEE Transactions on Components and Packaging Technologies*, vol. 25, no. 3, pp. 495–505, Sep. 2002.

- [58] M. Ecker, J. B. Gerschler, J. Vogel, S. Käbitz, F. Hust, P. Dechent, and D. U. Sauer, "Development of a lifetime prediction model for lithium-ion batteries based on extended accelerated aging test data," *Journal of Power Sources*, vol. 215, pp. 248 – 257, 2012. [Online]. Available: <http://www.sciencedirect.com/science/article/pii/S0378775312008671>
- [59] S. Grolleau, A. Delaille, H. Gualous, P. Gyan, R. Revel, J. Bernard, E. Redondo-Iglesias, and J. Peter, "Calendar aging of commercial graphite/lifepo4 cell – predicting capacity fade under time dependent storage conditions," *Journal of Power Sources*, vol. 255, pp. 450 – 458, 2014. [Online]. Available: <http://www.sciencedirect.com/science/article/pii/S0378775313019411>
- [60] M. Świerczyński, D. I. Stroe, A. Stan, R. Teodorescu, and D. U. Sauer, "Selection and performance-degradation modeling of $\text{limo}_2/\text{li}_4\text{ti}_5\text{o}_{12}$ and lifepo₄/c battery cells as suitable energy storage systems for grid integration with wind power plants: An example for the primary frequency regulation service," *IEEE Transactions on Sustainable Energy*, vol. 5, no. 1, pp. 90–101, Jan 2014.
- [61] F. Zheng, Y. Xing, J. Jiang, B. Sun, J. Kim, and M. Pecht, "Influence of different open circuit voltage tests on state of charge online estimation for lithium-ion batteries," *Applied Energy*, vol. 183, pp. 513 – 525, 2016. [Online]. Available: <http://www.sciencedirect.com/science/article/pii/S0306261916313125>
- [62] S. Schwunk, N. Armbruster, S. Straub, J. Kehl, and M. Vetter, "Particle filter for state of charge and state of health estimation for lithium–iron phosphate batteries," *Journal of Power Sources*, vol. 239, pp. 705 – 710, 2013. [Online]. Available: <http://www.sciencedirect.com/science/article/pii/S037877531201614X>
- [63] Y. Xing, W. He, M. Pecht, and K. L. Tsui, "State of charge estimation of lithium-ion batteries using the open-circuit voltage at various ambient temperatures," *Applied Energy*, vol. 113, pp. 106 – 115, 2014. [Online]. Available: <http://www.sciencedirect.com/science/article/pii/S0306261913005746>
- [64] H. He, X. Zhang, R. Xiong, Y. Xu, and H. Guo, "Online model-based estimation of state-of-charge and open-circuit voltage of lithium-ion batteries in electric vehicles," *Energy*, vol. 39, no. 1, pp. 310 – 318, 2012, sustainable Energy and Environmental Protection 2010. [Online]. Available: <http://www.sciencedirect.com/science/article/pii/S036054421200014X>

- [65] G. Dong, J. Wei, C. Zhang, and Z. Chen, "Online state of charge estimation and open circuit voltage hysteresis modeling of lifepo4 battery using invariant imbedding method," *Applied Energy*, vol. 162, pp. 163 – 171, 2016. [Online]. Available: <http://www.sciencedirect.com/science/article/pii/S0306261915013197>
- [66] M. A. Roscher, O. S. Bohlen, and D. U. Sauer, "Reliable state estimation of multicell lithium-ion battery systems," *IEEE Transactions on Energy Conversion*, vol. 26, no. 3, pp. 737–743, Sep. 2011.
- [67] D. Stroe, M. Świerczyński, A. Stan, R. Teodorescu, and S. J. Andreasen, "Experimental investigation on the internal resistance of lithium iron phosphate battery cells during calendar ageing," in *IECON 2013 - 39th Annual Conference of the IEEE Industrial Electronics Society*, Nov 2013, pp. 6734–6739.
- [68] W. Waag, S. Käbitz, and D. U. Sauer, "Experimental investigation of the lithium-ion battery impedance characteristic at various conditions and aging states and its influence on the application," *Applied Energy*, vol. 102, pp. 885 – 897, 2013, special Issue on Advances in sustainable biofuel production and use - XIX International Symposium on Alcohol Fuels - ISAF. [Online]. Available: <http://www.sciencedirect.com/science/article/pii/S030626191200671X>
- [69] R. Zhang, B. Xia, B. Li, L. Cao, Y. Lai, W. Zheng, H. Wang, W. Wang, and M. Wang, "A study on the open circuit voltage and state of charge characterization of high capacity lithium-ion battery under different temperature," *Energies*, vol. 11, no. 9, 2018. [Online]. Available: <https://www.mdpi.com/1996-1073/11/9/2408>
- [70] I. 12405, "Electrically propelled road vehicles – test specification for lithium-ion traction battery packs and systems – part 1: High-power applications," International Organization for Standardization (ISO), Geneva, Switzerland, Standard 12405-1:2011, 2011.
- [71] S. Thanagasundram, R. Arunachala, K. Makinejad, T. Teutsch, and A. Jossen, "A cell level model for battery simulation," in *European Electric Vehicle Congress*, Brussels, Belgium, 11 2012.
- [72] United States Environmental Protection Agency, "Vehicle and fuel emissions testing. dynamometer drive schedules." <https://www.epa.gov/vehicle-and-fuel-emissions-testing/dynamometer-drive-schedules>, last accessed: June 24th, 2019.

-
- [73] Cadex Electronics Ltd., “C8000 Battery Testing System. Affordable Lab-Grade Accuracy and Power.” <https://www.cadex.com/en/products/c8000-battery-testing-system>.
- [74] Gamry Instruments, “Reference 3000,” <https://www.gamry.com/potentiostats/reference-3000/>.
- [75] Digatron — power electronics, “MCT-ME,” <https://www.digatron.com/en-us/Products/Laboratory/Cycler/Cell-Tester/MCT-ME-en-US>.
- [76] Arbin Instruments, “Battery: Cell Testing,” <https://www.arbin.com/products/battery-test-equipment/cell-testing/>.
- [77] D&V Electronics Ltd., “BCT-150 Battery Cell Tester — Performance and Endurance Testing,” <https://www.dvelectronics.com/products/battery-test-systems/bct-150/>, 130 Zenway Boulevard, Woodbridge, Ontario Canada L4H 2Y7.
- [78] B. University, “Bu-205: Types of lithium-ion,” https://batteryuniversity.com/learn/article/types_of_lithium_ion.
- [79] CleanTechnica, “Tesla model 3 battery pack & battery cell teardown highlights performance improvements,” <https://cleantechnica.com/2019/01/28/tesla-model-3-battery-pack-cell-teardown-highlights-performance-improvements/>, 1 2019.
- [80] Samsung SDI, “INR21700-50E Specification of Product,” <https://batteryservice.bg/wp-content/uploads/2018/12/INR21700-50E.pdf>, 12 2017.
- [81] Envirotronics, “S & SH Series Standard Temperature and Temperature/Humidity Systems,” <https://www.atecorp.com/getattachment/products/envirotronics/st8/envirotronics-st8-series-datasheet.pdf?lang=en-us&ext=.pdf>, 3881 N. Greenbrooke S.E., Grand Rapids, MI 49512, 2 2002.
- [82] Envirotronics, “Instrument Manual Systems Plus Programmer/Controller,” <http://weiss-na.com/wp-content/uploads/sysplsman.pdf>, 3881 N. Greenbrooke S.E., Grand Rapids, MI 49512, 12 1997.
- [83] P. Kollmeyer, A. Hackl, and A. Emadi, “Li-ion battery model performance for automotive drive cycles with current pulse and eis parameterization,” in *2017 IEEE Transportation Electrification Conference and Expo (ITEC)*, June 2017, pp. 486–492.

- [84] Gamry Instruments. EIS: Potentiostatic or Galvanostatic Mode? [Online]. Available: <https://www.gamry.com/application-notes/EIS/eis-potentiostatic-galvanostatic-mode/>
- [85] E. Barsoukov and J. R. Macdonald, *Impedance Spectroscopy: Theory, Experiment, and Applications*, 2nd ed. Hoboken, New Jersey: Wiley, 2005.
- [86] B. Schweighofer, H. Wegleiter, M. Recheis, and P. Fulmek, "Fast and accurate battery model applicable for ev and hev simulation," *Conference Record - IEEE Instrumentation and Measurement Technology Conference*, 05 2012.
- [87] C. Zou, L. Zhang, X. Hu, Z. Wang, T. Wik, and M. Pecht, "A review of fractional-order techniques applied to lithium-ion batteries, lead-acid batteries, and supercapacitors," *Journal of Power Sources*, vol. 390, pp. 286 – 296, 2018. [Online]. Available: <http://www.sciencedirect.com/science/article/pii/S0378775318303768>
- [88] W. Waag, S. Käbitz, and D. U. Sauer, "Application-specific parameterization of reduced order equivalent circuit battery models for improved accuracy at dynamic load," *Measurement*, vol. 46, no. 10, pp. 4085 – 4093, 2013. [Online]. Available: <http://www.sciencedirect.com/science/article/pii/S0263224113003242>
- [89] D. Andre, M. Meiler, K. Steiner, H. Walz, T. Soczka-Guth, and D. Sauer, "Characterization of high-power lithium-ion batteries by electrochemical impedance spectroscopy. ii: Modelling," *Journal of Power Sources*, vol. 196, no. 12, pp. 5349 – 5356, 2011, selected papers presented at the 12th Ulm ElectroChemical Talks (UECT):2015 Technologies on Batteries and Fuel Cells. [Online]. Available: <http://www.sciencedirect.com/science/article/pii/S0378775310012942>
- [90] S. Skoog and S. David, "Parameterization of linear equivalent circuit models over wide temperature and soc spans for automotive lithium-ion cells using electrochemical impedance spectroscopy," *Journal of Energy Storage*, vol. 14, pp. 39 – 48, 2017. [Online]. Available: <http://www.sciencedirect.com/science/article/pii/S2352152X16301906>
- [91] J. Shim and K. Striebel, "Characterization of high-power lithium-ion cells during constant current cycling: Part i. cycle performance and electrochemical diagnostics," *Journal of Power Sources*, vol. 122, pp. 188–194, 07 2003.
- [92] P. Mauracher and E. Karden, "Dynamic modelling of lead/acid batteries using impedance spectroscopy for parameter identification," *Journal of Power Sources*,

- vol. 67, no. 1, pp. 69 – 84, 1997, proceedings of the Fifth European Lead Battery Conference. [Online]. Available: <http://www.sciencedirect.com/science/article/pii/S0378775397024981>
- [93] Solve nonlinear least-squares (nonlinear data-fitting) problems - matlab lsqnonlin. [Online]. Available: <https://www.mathworks.com/help/optim/ug/lsqnonlin.html>
- [94] P. J. Kollmeyer, “Electromechanical modeling and analysis of a corbin sparrow electric vehicle using on the road data,” Master’s thesis, University of Wisconsin-Madison, 2012.

APPENDICES

Appendix A

Sample Test Script for BCT-150 Unit

```
'Always remember to use InitializeDVLink in your script  
InitializeDVLink("SampleTest")
```

```
'Setting a soft limit for the maximum voltage for the duration of this test  
SetChargeVoltage(3.5)
```

```
'Setting a soft limit for the minimum voltage for the duration of this test  
SetDisChargeVoltage(2.5)
```

```
'Log data every 0.5 seconds  
SetDataInterval(0.5)
```

```
Charge(35) 'Charge cell at 35A
```

```
Wait(3600) 'Wait 1 hour
```

```
DisCharge(10) 'Discharge cell at 10A
```

Appendix B

Solutions for $L - R - RC - RC - Z_{wb}$ model fitting

This appendix contains tables that list the optimized $L - R - RC - RC - Z_{wb}$ model parameters at each temperature and SOC level. Rows highlighted in red indicate SOC levels where the model fitting was deemed inaccurate, as demonstrated in Section 5.3. As such, this data was not considered during the model validation process presented in Section 5.4. Measured impedance data at 40 °C and 100 % SOC is not available.

Table B.1: Solution values for $L - R - RC - RC - Z_{wb}$ model at -10°C

SOC [%]	L [H]	R [Ω]	R_{wb} [Ω]	C_{wb} [F]	R_1 [Ω]	C_1 [F]	R_2 [Ω]	C_2 [F]
100	5.21E-07	3.26E-02	4.56E-01	1.61E+03	3.61E-02	9.35E-02	5.44E-02	9.11E-01
95	1.58E-07	3.92E-02	5.45E-01	1.44E+04	6.82E-02	6.84E+02	7.39E-02	2.52E-01
90	4.52E-07	3.24E-02	1.70E-01	2.16E+03	3.30E-02	9.69E-02	5.07E-02	8.65E-01
80	2.09E-07	3.81E-02	8.23E-01	8.45E+03	6.49E-02	2.61E-01	5.75E-02	7.42E+02
70	2.08E-07	3.83E-02	9.14E-01	8.66E+03	6.49E-02	2.69E-01	6.24E-02	7.19E+02
60	2.62E-07	3.71E-02	6.55E-01	9.35E+03	5.67E-02	2.52E-01	5.13E-02	6.58E+02
50	2.36E-07	3.76E-02	7.35E-01	9.97E+03	5.99E-02	2.52E-01	4.51E-02	7.97E+02
40	2.56E-07	3.72E-02	5.49E-01	9.36E+03	5.77E-02	2.53E-01	4.48E-02	7.39E+02
30	3.88E-07	3.38E-02	7.03E-01	6.94E+03	3.94E-02	1.36E-01	3.93E-02	2.00E+00
25	4.17E-07	3.37E-02	7.67E-01	6.89E+03	3.85E-02	1.39E-01	3.57E-02	2.36E+00
20	2.17E-07	3.87E-02	7.38E-01	1.15E+04	6.86E-02	2.85E-01	5.32E-02	6.75E+02
15	3.44E-07	3.49E-02	4.00E+00	6.76E+03	5.46E-02	1.61E+00	4.31E-02	1.32E-01
10	3.48E-07	3.45E-02	4.00E+00	3.47E+03	3.96E-02	1.23E-01	6.10E-02	1.24E+00
5	3.56E-07	3.40E-02	4.00E+00	1.84E+03	3.70E-02	1.16E-01	6.42E-02	1.04E+00
0	3.75E-07	3.36E-02	4.00E+00	1.74E+03	3.53E-02	1.15E-01	6.13E-02	1.04E+00

Table B.2: Solution values for $L - R - RC - RC - Z_{wb}$ model at 0°C

SOC [%]	L [H]	R [Ω]	R_{wb} [Ω]	C_{wb} [F]	R_1 [Ω]	C_1 [F]	R_2 [Ω]	C_2 [F]
100	5.87E-07	3.06E-02	2.38E-01	1.71E+03	1.81E-02	1.40E-01	1.92E-02	6.86E+00
95	6.03E-07	3.02E-02	8.04E-02	1.40E+03	1.75E-02	1.26E-01	1.45E-02	4.63E+00
90	6.27E-07	2.99E-02	7.40E-02	1.27E+03	1.23E-02	3.20E+00	1.63E-02	1.17E-01
80	6.53E-07	2.96E-02	1.18E-01	1.45E+03	1.50E-02	1.11E-01	1.05E-02	2.51E+00
70	6.73E-07	2.95E-02	1.18E-01	1.35E+03	1.41E-02	1.04E-01	1.03E-02	1.89E+00
60	6.66E-07	2.95E-02	9.06E-02	1.53E+03	1.39E-02	1.04E-01	1.03E-02	1.71E+00
50	6.76E-07	2.95E-02	9.89E-02	1.87E+03	1.40E-02	1.04E-01	1.06E-02	1.65E+00
40	6.50E-07	2.97E-02	9.90E-02	1.93E+03	1.03E-02	2.14E+00	1.48E-02	1.11E-01
30	6.58E-07	2.98E-02	9.60E-02	1.86E+03	1.14E-02	2.12E+00	1.51E-02	1.12E-01
25	6.07E-07	3.03E-02	1.22E-01	2.17E+03	1.75E-02	1.33E-01	1.14E-02	4.15E+00
20	6.19E-07	3.03E-02	1.09E-01	1.87E+03	1.36E-02	3.47E+00	1.71E-02	1.30E-01
15	5.99E-07	3.06E-02	2.21E-01	2.16E+03	1.84E-02	1.40E-01	1.63E-02	4.68E+00
10	5.72E-07	3.10E-02	3.73E-01	1.58E+03	2.30E-02	4.75E+00	2.02E-02	1.51E-01
5	5.37E-07	3.17E-02	5.54E-01	1.07E+03	2.33E-02	1.70E-01	3.67E-02	5.99E+00
0	5.27E-07	3.18E-02	7.38E-01	1.15E+03	4.35E-02	6.07E+00	2.40E-02	1.66E-01

Table B.3: Solution values for $L - R - RC - RC - Z_{wb}$ model at 10 °C

SOC [%]	L [H]	R [Ω]	R_{wb} [Ω]	C_{wb} [F]	R_1 [Ω]	C_1 [F]	R_2 [Ω]	C_2 [F]
100	6.89E-07	2.94E-02	2.21E-01	2.79E+03	1.02E-02	1.76E-01	8.92E-03	1.40E+01
95	7.02E-07	2.90E-02	5.15E-02	2.06E+03	9.88E-03	1.43E-01	6.77E-03	7.54E+00
90	7.18E-07	2.88E-02	4.85E-02	1.75E+03	9.36E-03	1.34E-01	5.85E-03	5.26E+00
80	6.70E-07	2.94E-02	1.01E-01	2.75E+03	7.14E-03	2.49E+02	1.07E-02	1.89E-01
70	6.78E-07	2.93E-02	8.95E-02	2.53E+03	1.05E-02	1.76E-01	6.22E-03	2.39E+02
60	6.78E-07	2.93E-02	8.38E-02	3.06E+03	5.80E-03	2.54E+02	1.05E-02	1.72E-01
50	6.81E-07	2.92E-02	8.98E-02	3.42E+03	1.05E-02	1.70E-01	5.13E-03	1.95E+02
40	6.70E-07	2.94E-02	1.73E-01	5.64E+03	1.08E-02	1.82E-01	7.12E-03	2.36E+02
30	6.70E-07	2.95E-02	1.32E-01	3.85E+03	1.12E-02	1.88E-01	5.45E-03	1.10E+02
25	7.02E-07	2.91E-02	9.84E-02	3.08E+03	1.01E-02	1.48E-01	5.85E-03	6.89E+00
20	7.04E-07	2.92E-02	1.71E-01	3.02E+03	1.02E-02	1.50E-01	6.95E-03	6.23E+00
15	6.87E-07	2.93E-02	3.16E-01	2.23E+03	1.03E-02	1.53E-01	8.48E-03	4.52E+00
10	5.04E-07	3.31E-02	4.00E+00	4.65E+03	1.97E-02	8.61E-01	2.71E-02	2.37E+02
5	5.79E-07	3.12E-02	2.69E+00	3.01E+03	3.34E-02	1.46E+01	1.65E-02	2.94E-01
0	5.61E-07	3.15E-02	4.00E+00	2.80E+03	1.74E-02	3.22E-01	4.04E-02	1.48E+01

Table B.4: Solution values for $L - R - RC - RC - Z_{wb}$ model at 25 °C

SOC [%]	L [H]	R [Ω]	R_{wb} [Ω]	C_{wb} [F]	R_1 [Ω]	C_1 [F]	R_2 [Ω]	C_2 [F]
100	7.63E-07	2.87E-02	1.61E-01	4.26E+03	4.16E-03	4.07E-01	3.37E-03	6.35E+01
95	7.52E-07	2.86E-02	3.94E-02	5.48E+03	4.57E-03	3.35E-01	5.22E-03	2.09E+02
90	7.38E-07	2.87E-02	2.52E-02	1.88E+03	2.38E-03	5.65E-01	2.42E-03	9.78E-01
80	7.63E-07	2.84E-02	1.39E-01	6.60E+03	4.06E-03	2.78E-01	6.15E-03	2.11E+02
70	7.68E-07	2.85E-02	1.26E-01	6.62E+03	6.40E-03	2.49E+02	3.98E-03	2.71E-01
60	7.74E-07	2.84E-02	1.16E-01	6.55E+03	3.94E-03	2.33E-01	4.53E-03	2.00E+02
50	7.75E-07	2.84E-02	1.08E-01	6.51E+03	3.96E-03	2.14E+02	3.92E-03	2.37E-01
40	7.76E-07	2.84E-02	1.20E-01	7.24E+03	4.05E-03	2.08E+02	4.11E-03	2.37E-01
30	7.68E-07	2.86E-02	1.28E-01	6.06E+03	3.18E-03	1.45E+02	4.33E-03	2.41E-01
25	7.65E-07	2.86E-02	1.22E-01	5.45E+03	3.15E-03	1.20E+02	4.59E-03	2.61E-01
20	7.56E-07	2.88E-02	1.82E-01	4.35E+03	2.33E-03	6.39E+01	4.76E-03	2.83E-01
15	7.10E-07	2.96E-02	4.00E+00	8.88E+03	6.42E-03	5.68E-01	1.55E-02	7.99E+02
10	6.80E-07	3.02E-02	4.00E+00	6.10E+03	1.45E-02	5.18E+02	7.98E-03	8.15E-01
5	6.28E-07	3.12E-02	4.00E+00	3.19E+03	1.10E-02	1.61E+00	1.30E-02	1.46E+02
0	7.19E-07	2.94E-02	4.00E+00	2.01E+03	6.93E-03	2.83E-01	1.15E-02	7.64E+00

Table B.5: Solution values for $L - R - RC - RC - Z_{wb}$ model at 40 °C

SOC [%]	L [H]	R [Ω]	R_{wb} [Ω]	C_{wb} [F]	R_1 [Ω]	C_1 [F]	R_2 [Ω]	C_2 [F]
100	-	-	-	-	-	-	-	-
95	8.12E-07	2.84E-02	2.98E-02	8.20E+03	1.60E-03	1.11E+00	3.65E-03	3.08E+02
90	8.34E-07	2.83E-02	2.14E-02	5.34E+03	1.44E-03	8.35E-01	2.86E-03	2.01E+02
80	8.31E-07	2.82E-02	1.01E-01	7.24E+03	1.27E-03	5.43E-01	3.70E-03	1.82E+02
70	8.13E-07	2.84E-02	1.03E-01	7.47E+03	1.17E-03	8.48E-01	3.76E-03	1.82E+02
60	8.26E-07	2.83E-02	8.74E-02	8.04E+03	2.59E-03	1.83E+02	1.13E-03	6.56E-01
50	8.16E-07	2.84E-02	9.44E-02	7.77E+03	1.19E-03	5.57E-01	2.40E-03	1.76E+02
40	8.29E-07	2.85E-02	1.05E-01	7.21E+03	1.22E-03	7.73E-01	2.30E-03	2.01E+02
30	8.21E-07	2.85E-02	1.30E-01	6.57E+03	1.57E-03	5.99E-01	2.19E-03	1.38E+02
25	8.84E-07	2.88E-02	3.92E+00	1.15E+04	2.38E-03	7.93E-01	1.33E-02	8.20E+02
20	7.92E-07	2.92E-02	4.00E+00	7.71E+03	3.02E-03	1.27E+00	1.27E-02	7.44E+02
15	7.47E-07	2.94E-02	4.00E+00	4.93E+03	7.70E-03	4.37E+02	4.01E-03	1.30E+00
10	7.78E-07	2.86E-02	4.00E+00	1.42E+03	3.58E-04	1.67E+00	1.92E-03	4.74E-01
5	7.04E-07	2.66E-02	4.00E+00	9.51E+02	7.15E-06	3.92E-01	3.10E-05	6.81E-03
0	7.12E-07	2.29E-02	4.00E+00	8.62E+02	3.32E-03	3.01E-03	4.94E-05	4.75E-01

Appendix C

Solutions for $L - R - ZARC - Z_{wb}$ model fitting

This appendix contains tables that list the optimized $L - R - ZARC - Z_{wb}$ model parameters at each temperature and SOC level. Rows highlighted in red indicate SOC levels where the model fitting was deemed inaccurate, as demonstrated in Section 5.3. As such, this data was not considered during the model validation process presented in Section 5.4. Measured impedance data at 40 °C and 100% SOC is not available.

Table C.1: Solution values for $L - R - ZARC - Z_{wb}$ model at $-10\text{ }^\circ\text{C}$

SOC [%]	L [H]	R [Ω]	R_{wb} [Ω]	C_{wb} [F]	R_{ZARC_a} [Ω]	C_{ZARC_a} [F]	R_{ZARC_b} [Ω]
100	7.36E-07	2.89E-02	7.30E-01	2.37E+03	2.00E-02	6.27E+00	4.00E-02
95	6.53E-07	2.97E-02	5.76E-01	1.53E+04	2.74E-02	2.61E-01	3.99E-02
90	6.74E-07	2.95E-02	5.43E-01	3.18E+04	2.63E-02	2.49E-01	3.95E-02
80	6.83E-07	2.93E-02	8.39E-01	8.60E+03	5.34E-02	8.20E+02	3.53E-02
70	7.14E-07	2.91E-02	9.33E-01	8.85E+03	1.17E-02	2.15E+01	1.05E-02
60	6.96E-07	2.94E-02	6.65E-01	9.55E+03	4.67E-02	8.20E+02	2.86E-02
50	6.95E-07	2.95E-02	7.54E-01	1.02E+04	1.10E-02	6.05E-02	3.08E-02
40	7.05E-07	2.93E-02	5.68E-01	9.61E+03	1.10E-02	5.81E-02	2.00E-02
30	7.10E-07	2.92E-02	7.92E-01	8.40E+03	3.43E-02	6.79E-01	9.86E-03
25	7.24E-07	2.93E-02	8.16E-01	7.71E+03	3.18E-02	7.67E-01	1.90E-02
20	7.21E-07	2.94E-02	7.54E-01	1.19E+04	2.01E-02	2.13E-01	1.03E-02
15	6.67E-07	3.02E-02	4.00E+00	6.94E+03	2.17E-02	2.39E-01	1.23E-02
10	6.24E-07	3.06E-02	4.00E+00	3.47E+03	3.90E-02	1.20E+00	5.86E-03
5	6.39E-07	3.02E-02	4.00E+00	1.85E+03	1.35E-02	1.94E+00	4.18E-02
0	4.90E-07	3.22E-02	4.00E+00	1.57E+03	1.18E-02	9.17E+00	1.31E-02

SOC [%]	C_{ZARC_b} [F]	R_{ZARC_c} [Ω]	C_{ZARC_c} [F]	R_{ZARC_d} [Ω]	C_{ZARC_d} [F]	R_{ZARC_e} [Ω]	C_{ZARC_e} [F]
100	6.20E-01	1.10E-02	4.69E-02	2.21E-02	1.74E-01	1.03E-02	2.53E+02
95	1.02E+00	1.48E-02	5.64E-02	8.65E-03	7.92E+01	6.35E-02	8.20E+02
90	9.84E-01	1.02E-02	6.07E+01	8.85E-02	8.20E+02	1.38E-02	5.60E-02
80	9.07E-01	1.24E-02	5.75E-02	2.22E-02	2.46E-01	9.39E-03	3.12E+01
70	5.38E-02	3.72E-02	7.59E-01	2.07E-02	2.02E-01	5.82E-02	8.20E+02
60	1.21E+00	1.24E-02	5.95E-02	2.24E-02	2.69E-01	7.47E-03	7.80E+01
50	6.50E-01	1.59E-02	2.39E-01	1.41E-02	6.62E+00	4.22E-02	8.20E+02
40	2.38E-01	8.56E-03	2.84E+01	3.11E-02	8.80E-01	4.11E-02	8.20E+02
30	5.57E-02	1.17E-02	1.05E+01	1.85E-02	2.09E-01	2.75E-02	8.17E+02
25	2.19E-01	9.85E-03	5.71E-02	2.01E-02	7.27E+02	1.05E-02	1.55E+01
20	5.48E-02	4.92E-02	8.19E+02	1.54E-02	1.10E+01	3.81E-02	7.13E-01
15	5.68E-02	2.23E-02	6.87E+00	1.54E-02	6.27E+02	3.92E-02	7.60E-01
10	3.07E+01	2.81E-02	3.09E-01	1.69E-02	1.17E+01	1.56E-02	5.92E-02
5	2.45E+00	2.22E-02	2.81E-01	1.45E-02	1.75E+00	1.38E-02	5.59E-02
0	1.18E+01	4.40E-02	3.06E-01	1.27E-02	5.26E+00	9.46E-03	8.18E-02

Table C.2: Solution values for $L - R - ZARC - Z_{wb}$ model at 0°C

SOC [%]	L [H]	R [Ω]	R_{wb} [Ω]	C_{wb} [F]	R_{ZARC_a} [Ω]	C_{ZARC_a} [F]	R_{ZARC_b} [Ω]
100	7.65E-07	2.84E-02	3.97E-01	2.74E+03	9.74E-03	1.68E+01	8.30E-03
95	7.49E-07	2.84E-02	8.33E-02	2.79E+03	1.60E-02	8.20E+02	7.41E-03
90	7.56E-07	2.83E-02	6.95E-02	2.42E+03	6.91E-03	7.36E-02	1.49E-02
80	7.68E-07	2.82E-02	1.30E-01	2.12E+03	6.35E-03	7.42E-02	2.66E-03
70	7.84E-07	2.81E-02	1.21E-01	1.75E+03	5.44E-03	7.22E-02	9.27E-03
60	7.83E-07	2.80E-02	9.52E-02	2.46E+03	1.28E-02	8.20E+02	9.83E-03
50	7.99E-07	2.80E-02	1.19E-01	2.79E+03	4.82E-03	6.76E-02	9.44E-03
40	7.84E-07	2.81E-02	1.14E-01	2.73E+03	9.03E-03	8.62E-01	8.63E-03
30	7.91E-07	2.81E-02	1.06E-01	2.56E+03	3.70E-03	2.03E+01	8.44E-03
25	7.74E-07	2.83E-02	2.70E-01	4.67E+03	1.10E-02	5.39E+02	5.15E-03
20	7.72E-07	2.84E-02	1.39E-01	2.85E+03	1.01E-02	8.20E+02	5.79E-03
15	7.29E-07	2.90E-02	2.87E-01	2.76E+03	7.72E-03	4.17E-01	9.18E-03
10	7.38E-07	2.90E-02	3.81E-01	1.62E+03	6.12E-04	6.01E+00	7.82E-03
5	7.00E-07	2.95E-02	5.77E-01	1.11E+03	1.14E-03	2.75E+00	1.08E-02
0	7.67E-07	2.85E-02	6.97E-01	1.12E+03	3.87E-03	7.07E-02	1.18E-02

SOC [%]	C_{ZARC_b} [F]	R_{ZARC_c} [Ω]	C_{ZARC_c} [F]	R_{ZARC_d} [Ω]	C_{ZARC_d} [F]	R_{ZARC_e} [Ω]	C_{ZARC_e} [F]
100	3.40E+00	1.24E-02	2.91E+02	1.07E-02	2.88E-01	6.99E-03	6.94E-02
95	7.31E-02	9.35E-03	3.71E+00	5.67E-03	5.36E+01	1.16E-02	3.12E-01
90	8.20E+02	4.22E-03	4.46E+01	8.03E-03	2.98E+00	1.13E-02	2.90E-01
80	5.22E+01	1.06E-02	2.75E-01	6.72E-03	2.49E+00	1.20E-02	8.20E+02
70	8.20E+02	9.77E-03	2.32E-01	2.67E-03	2.96E+01	7.16E-03	1.53E+00
60	1.95E-01	4.64E-03	7.03E-02	2.64E-03	3.13E+01	8.02E-03	1.21E+00
50	2.02E-01	2.89E-03	2.37E+01	9.52E-03	8.20E+02	8.36E-03	1.06E+00
40	2.05E-01	3.67E-03	1.55E+01	8.78E-03	8.20E+02	4.70E-03	7.07E-02
30	1.31E+00	1.00E-02	2.22E-01	5.27E-03	7.00E-02	8.45E-03	8.20E+02
25	7.41E-02	5.15E-03	1.78E+01	9.87E-03	2.17E-01	9.64E-03	1.16E+00
20	7.38E-02	9.20E-03	1.82E+00	1.11E-02	2.46E-01	5.80E-03	2.09E+01
15	9.72E+00	8.10E-03	8.98E-02	7.11E-03	2.55E+02	8.47E-03	1.56E+00
10	8.14E-02	1.06E-02	1.89E+00	1.04E-02	3.71E-01	1.68E-02	1.26E+01
5	9.01E-02	1.29E-02	5.84E-01	2.59E-02	1.52E+01	1.28E-02	5.83E+00
0	5.58E+00	1.29E-02	5.72E-01	9.07E-03	1.58E-01	3.35E-02	1.22E+01

Table C.3: Solution values for $L - R - ZARC - Z_{wb}$ model at 10°C

SOC [%]	L [H]	R [Ω]	R_{wb} [Ω]	C_{wb} [F]	R_{ZARC_a} [Ω]	C_{ZARC_a} [F]	R_{ZARC_b} [Ω]
100	8.07E-07	2.79E-02	2.34E-01	3.05E+03	3.22E-03	3.26E+00	5.20E-03
95	7.99E-07	2.77E-02	5.34E-02	3.69E+03	4.88E-03	2.62E+00	3.36E-03
90	7.96E-07	2.78E-02	4.66E-02	3.17E+03	2.16E-03	1.13E+02	4.50E-03
80	7.99E-07	2.77E-02	2.88E-01	7.53E+03	3.14E-03	4.17E+00	3.82E-03
70	8.02E-07	2.77E-02	9.37E-02	2.90E+03	1.77E-03	1.12E+02	3.63E-03
60	7.94E-07	2.78E-02	8.86E-02	3.49E+03	3.46E-03	1.85E+00	4.91E-03
50	7.96E-07	2.78E-02	2.05E-01	7.13E+03	5.87E-03	2.97E-01	3.82E-03
40	7.85E-07	2.80E-02	1.76E-01	5.83E+03	4.44E-03	9.62E-02	1.56E-03
30	7.99E-07	2.79E-02	1.66E-01	4.65E+03	4.04E-03	3.31E-01	3.70E-03
25	7.81E-07	2.81E-02	1.82E-01	5.25E+03	2.08E-03	2.08E+01	2.72E-03
20	8.04E-07	2.79E-02	2.23E-01	3.82E+03	5.38E-03	2.25E-01	3.39E-03
15	7.76E-07	2.83E-02	2.72E+00	7.70E+03	6.88E-03	4.93E-01	6.52E-03
10	7.10E-07	2.92E-02	4.00E+00	4.76E+03	1.41E-03	8.64E+01	1.10E-02
5	7.43E-07	2.88E-02	4.00E+00	3.68E+03	1.62E-02	7.53E+00	8.11E-03
0	7.48E-07	2.88E-02	4.00E+00	2.95E+03	7.66E-03	9.88E-02	8.49E-03

SOC [%]	C_{ZARC_b} [F]	R_{ZARC_c} [Ω]	C_{ZARC_c} [F]	R_{ZARC_d} [Ω]	C_{ZARC_d} [F]	R_{ZARC_e} [Ω]	C_{ZARC_e} [F]
100	3.40E-01	6.28E-03	2.07E+02	4.09E-03	1.30E+01	4.03E-03	8.91E-02
95	9.06E-02	6.16E-03	2.42E-01	8.94E-03	8.20E+02	3.06E-03	6.30E+01
90	8.97E-02	8.73E-03	8.18E+02	5.80E-03	3.82E-01	3.71E-03	4.19E+00
80	8.99E-02	6.07E-03	3.01E-01	1.27E-02	8.20E+02	3.83E-03	1.89E+02
70	9.03E-02	3.23E-03	2.41E+00	5.45E-03	2.80E-01	7.10E-03	8.20E+02
60	3.05E-01	3.79E-03	9.46E-02	1.56E-03	9.78E+01	6.46E-03	8.20E+02
50	9.28E-02	2.84E-03	3.63E+00	2.28E-03	2.02E+02	7.65E-03	8.16E+02
40	4.50E+00	1.73E-03	1.60E+01	5.59E-03	3.91E-01	6.59E-03	3.86E+02
30	9.70E-02	2.15E-03	1.34E+01	4.48E-03	1.02E+00	5.38E-03	3.34E+02
25	3.86E+00	5.01E-03	9.84E-02	6.25E-03	3.75E+02	5.55E-03	4.75E-01
20	1.01E+01	2.85E-03	1.01E-01	4.75E-03	1.26E+00	4.72E-03	2.34E+02
15	5.36E+00	5.74E-03	1.36E+02	5.46E-03	9.45E-02	2.12E-02	8.20E+02
10	2.21E+01	9.93E-03	1.33E-01	2.32E-02	5.21E+02	8.21E-03	2.23E+00
5	9.44E-01	2.41E-02	5.76E+02	8.20E-03	1.04E-01	1.35E-02	6.54E+01
0	7.36E-01	1.40E-02	7.15E+00	1.98E-02	3.78E+02	1.86E-02	2.90E+01

Table C.4: Solution values for $L - R - ZARC - Z_{wb}$ model at 25 °C

SOC [%]	L [H]	R [Ω]	R_{wb} [Ω]	C_{wb} [F]	R_{ZARC_a} [Ω]	C_{ZARC_a} [F]	R_{ZARC_b} [Ω]
100	8.41E-07	2.79E-02	1.56E-01	4.21E+03	3.77E-04	5.61E+00	2.69E-03
95	8.12E-07	2.78E-02	9.60E-02	1.30E+04	2.54E-03	1.51E-01	2.13E-03
90	7.87E-07	2.80E-02	2.80E-02	3.71E+03	1.11E-03	3.10E-01	1.62E-03
80	8.15E-07	2.77E-02	1.40E-01	6.88E+03	1.26E-03	1.71E+02	1.52E-03
70	8.15E-07	2.80E-02	1.42E-01	7.79E+03	1.59E-03	2.14E+00	2.84E-03
60	7.62E-07	2.86E-02	6.74E-02	4.28E+03	1.01E-03	1.62E+00	1.01E-03
50	7.79E-07	2.86E-02	7.08E-02	4.44E+03	7.17E-04	9.34E-01	8.21E-04
40	7.76E-07	2.87E-02	6.74E-02	4.44E+03	1.05E-03	9.69E-01	8.15E-04
30	7.38E-07	2.89E-02	6.71E-02	5.24E+03	2.70E-05	4.71E-01	3.70E-04
25	8.20E-07	2.79E-02	1.25E-01	5.57E+03	2.22E-03	1.72E-01	4.35E-04
20	8.21E-07	2.80E-02	5.40E-01	9.86E+03	6.70E-03	8.20E+02	1.86E-03
15	8.12E-07	2.82E-02	4.00E+00	8.83E+03	2.13E-03	5.76E+00	2.63E-03
10	8.17E-07	2.82E-02	4.00E+00	6.14E+03	1.27E-02	8.20E+02	3.12E-03
5	8.72E-07	2.73E-02	4.00E+00	3.21E+03	3.34E-03	5.25E-02	4.09E-04
0	7.99E-07	2.85E-02	4.00E+00	2.01E+03	4.67E-04	3.08E+00	5.81E-03

SOC [%]	C_{ZARC_b} [F]	R_{ZARC_c} [Ω]	C_{ZARC_c} [F]	R_{ZARC_d} [Ω]	C_{ZARC_d} [F]	R_{ZARC_e} [Ω]	C_{ZARC_e} [F]
100	1.22E-01	2.95E-05	6.74E+01	2.43E-03	2.56E+00	2.99E-03	1.25E+02
95	1.48E+02	6.71E-03	8.20E+02	1.97E-03	1.09E+00	1.12E-03	1.34E+01
90	5.75E+00	3.72E-04	6.84E-01	2.20E-03	4.97E-01	3.78E-03	2.67E+02
80	1.50E-01	1.01E-03	8.53E+00	2.37E-03	4.36E-01	5.38E-03	4.81E+02
70	1.57E-01	2.18E-03	1.40E+02	1.65E-06	3.23E-02	5.71E-03	7.64E+02
60	1.61E+00	1.01E-03	1.26E+00	1.01E-03	1.63E+00	1.01E-03	2.10E+00
50	8.70E-01	1.73E-03	4.20E+00	1.33E-03	9.61E-01	4.14E-04	4.16E+00
40	9.10E-01	1.99E-03	3.39E+00	1.02E-03	9.51E-01	1.73E-04	3.20E+00
30	5.89E-02	2.40E-03	2.81E+00	9.05E-04	1.41E+00	2.40E-03	2.81E+00
25	5.95E-01	2.95E-03	1.92E+02	1.32E-03	1.06E+00	1.69E-03	3.06E+00
20	3.55E+00	1.75E-03	1.30E+02	2.54E-03	4.12E-01	1.72E-03	1.48E-01
15	6.91E-01	2.15E-03	1.10E+02	2.37E-03	1.51E-01	1.42E-02	8.20E+02
10	1.31E-01	2.93E-03	1.35E+02	3.36E-03	7.75E+00	3.21E-03	9.36E-01
5	6.05E+02	6.34E-03	5.61E-01	8.36E-03	1.15E+01	1.04E-02	3.71E+02
0	3.35E+01	6.00E-03	7.71E+00	3.85E-03	1.09E+00	3.56E-03	1.34E-01

Table C.5: Solution values for $L - R - ZARC - Z_{wb}$ model at 40°C

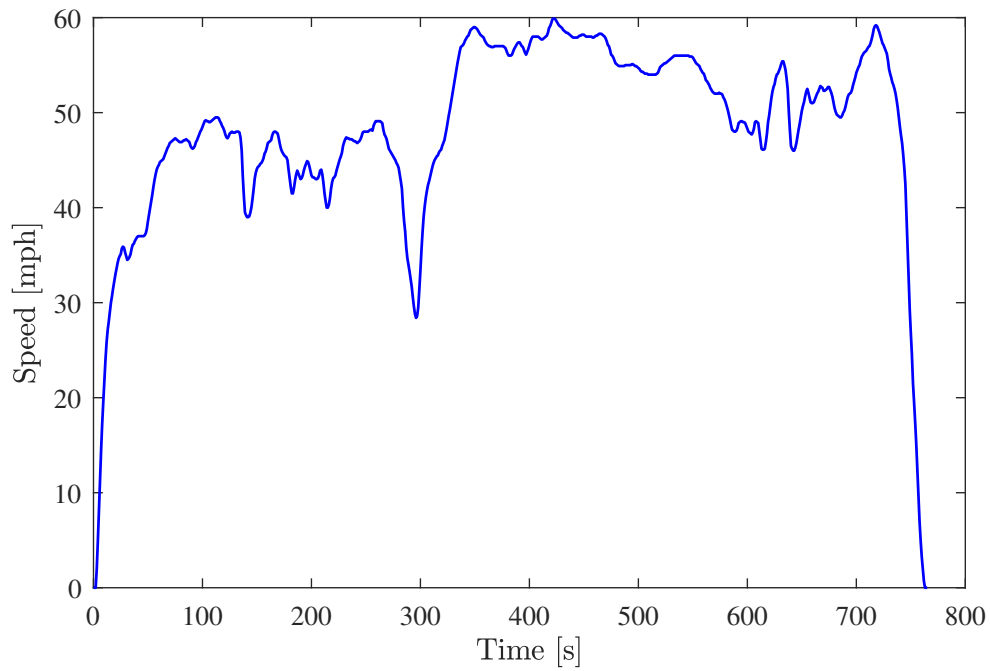
SOC [%]	L [H]	R [Ω]	R_{wb} [Ω]	C_{wb} [F]	R_{ZARC_a} [Ω]	C_{ZARC_a} [F]	R_{ZARC_b} [Ω]
100	-	-	-	-	-	-	-
95	8.42E-07	2.76E-02	3.64E-02	1.03E+04	5.23E-04	1.56E-02	1.11E-03
90	8.35E-07	2.80E-02	2.16E-02	3.88E+03	5.22E-04	3.97E+00	5.23E-04
80	8.29E-07	2.83E-02	1.05E-01	7.40E+03	6.82E-04	1.70E+00	6.69E-04
70	8.24E-07	2.83E-02	1.06E-01	7.73E+03	5.91E-04	3.95E-01	5.31E-04
60	8.36E-07	2.82E-02	8.53E-02	7.89E+03	9.39E-06	5.94E-03	7.90E-04
50	8.39E-07	2.76E-02	8.12E-02	6.55E+03	1.43E-05	1.17E+00	1.16E-03
40	8.71E-07	2.80E-02	1.07E-01	7.28E+03	7.15E-04	8.63E-01	4.29E-04
30	8.46E-07	2.78E-02	1.16E-01	6.04E+03	6.22E-04	3.96E-02	6.90E-04
25	9.12E-07	2.74E-02	3.61E+00	1.14E+04	1.11E-03	1.11E-04	1.54E-03
20	8.31E-07	2.73E-02	4.00E+00	7.71E+03	1.35E-03	1.82E-03	1.78E-03
15	7.97E-07	2.87E-02	4.00E+00	4.95E+03	1.58E-03	3.66E-01	6.62E-03
10	9.21E-07	2.57E-02	3.99E+00	1.42E+03	5.73E-04	5.02E-03	2.46E-03
5	7.03E-07	2.42E-02	4.00E+00	9.52E+02	6.30E-04	3.74E-04	7.29E-05
0	7.08E-07	2.46E-02	4.00E+00	8.51E+02	7.72E-04	4.30E-02	9.50E-05

SOC [%]	C_{ZARC_b} [F]	R_{ZARC_c} [Ω]	C_{ZARC_c} [F]	R_{ZARC_d} [Ω]	C_{ZARC_d} [F]	R_{ZARC_e} [Ω]	C_{ZARC_e} [F]
100	-	-	-	-	-	-	-
95	4.14E-01	1.26E-03	1.08E+02	6.13E-04	5.84E+00	3.66E-03	8.13E+02
90	2.71E-03	1.85E-05	9.29E+00	5.22E-04	2.99E+00	1.07E-03	1.01E+01
80	8.80E+01	2.31E-03	5.18E+02	6.80E-04	1.01E+00	6.21E-04	2.47E+02
70	1.16E+02	7.34E-04	2.88E+02	5.73E-04	3.24E+00	2.89E-03	5.70E+02
60	4.13E-01	1.12E-04	7.81E+02	4.71E-04	4.32E+00	2.40E-03	1.81E+02
50	1.43E-01	1.24E-03	1.40E+01	6.00E-04	9.70E-02	6.95E-06	8.21E+00
40	1.72E+01	2.19E-03	2.14E+02	7.38E-04	2.53E-01	2.31E-06	3.26E+02
30	4.22E+00	2.13E-06	1.22E+02	1.10E-03	4.35E-01	1.82E-03	1.47E+02
25	2.55E-01	1.22E-02	8.19E+02	1.25E-03	1.20E+02	5.81E-04	1.23E+01
20	4.14E-01	1.80E-03	1.36E+02	1.13E-03	6.71E+00	1.18E-02	8.20E+02
15	7.50E+02	1.71E-03	1.18E+02	1.63E-03	9.07E+00	1.23E-03	2.28E+00
10	3.41E-01	2.13E-04	8.78E-05	3.68E-04	1.24E-01	1.75E-03	4.50E-02
5	6.25E-03	4.37E-04	9.95E-04	4.84E-04	9.20E-04	9.00E-04	4.91E-04
0	3.75E-01	2.93E-04	2.25E-02	1.47E-04	7.98E-03	1.57E-04	2.60E-02

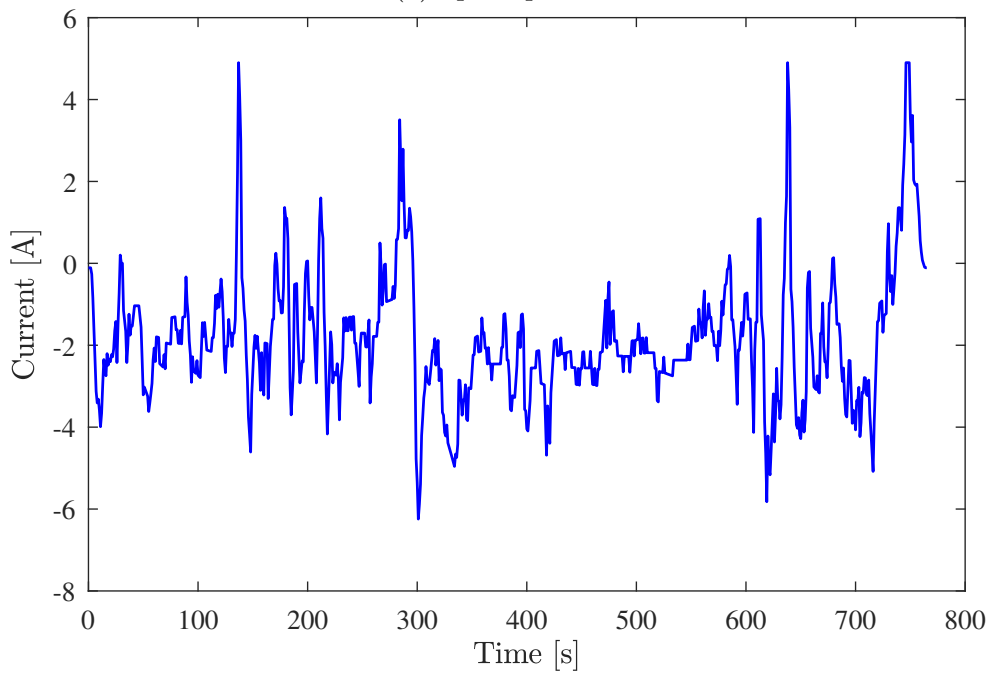
Appendix D

Drive Cycles Used for Experimental Validation of Model

The velocity and current profiles for the US06 drive cycle are presented in Section [5.4](#). This appendix contains the velocity and current profiles for the remaining drive cycles that are used for model validation: HWFET, LA92 and UDDS.

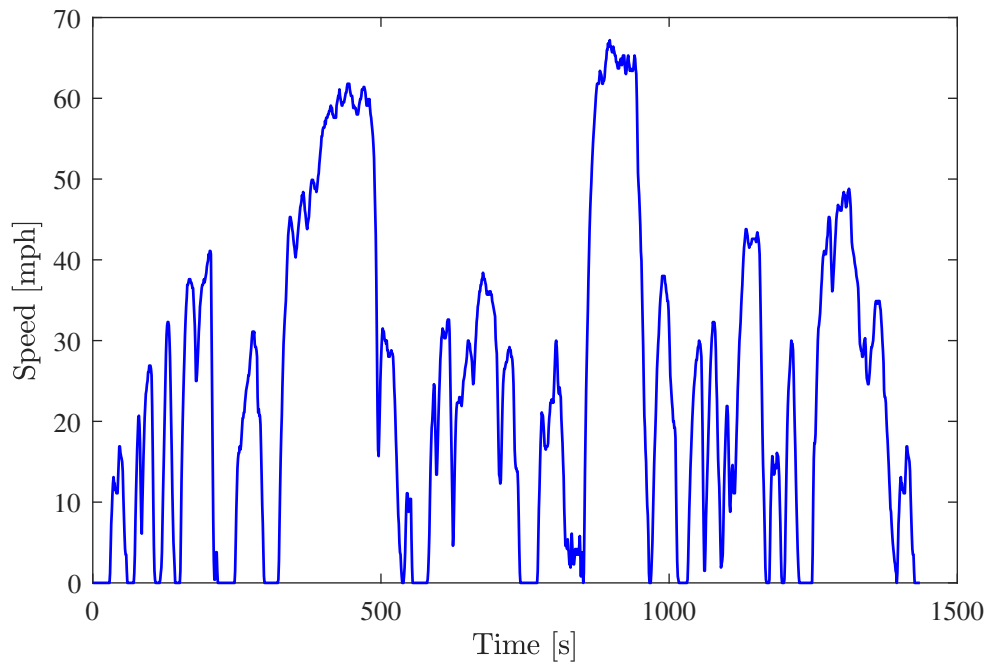


(a) Speed profile

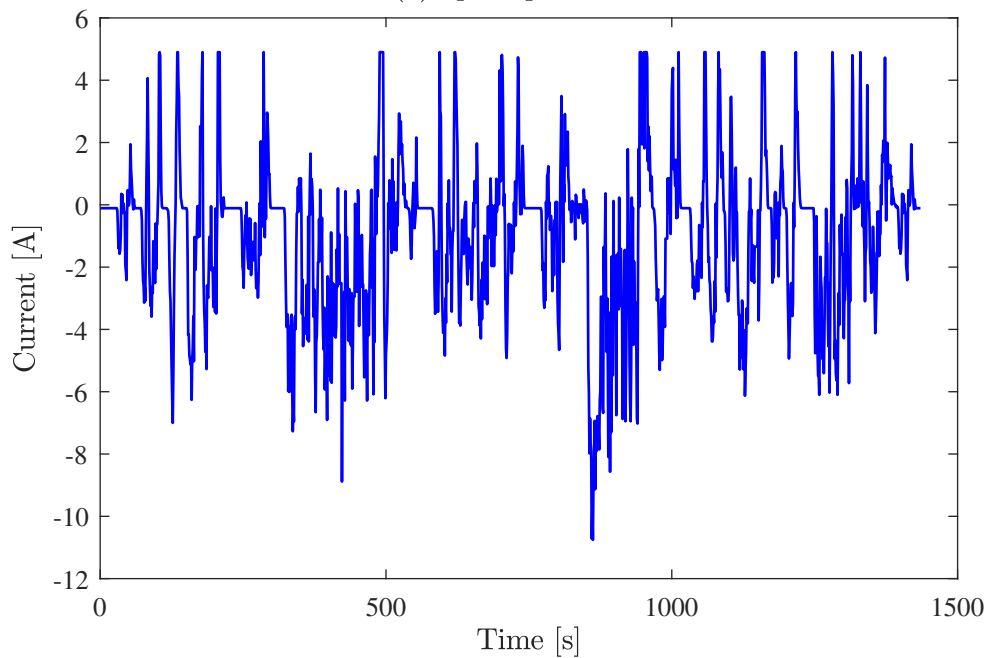


(b) Current profile

Figure D.1: HWFET drive cycle profile data

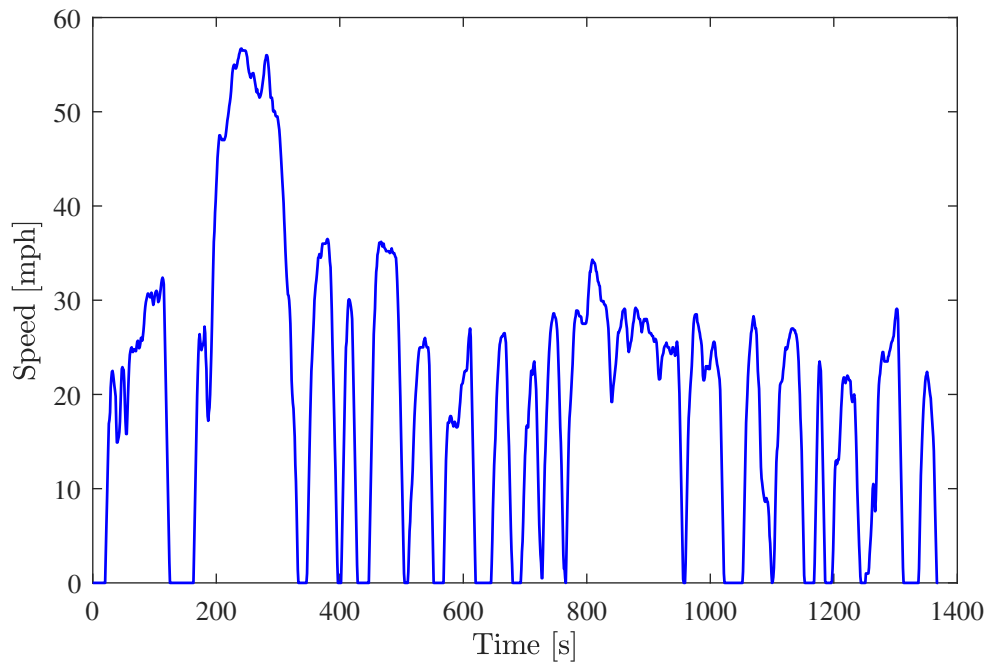


(a) Speed profile

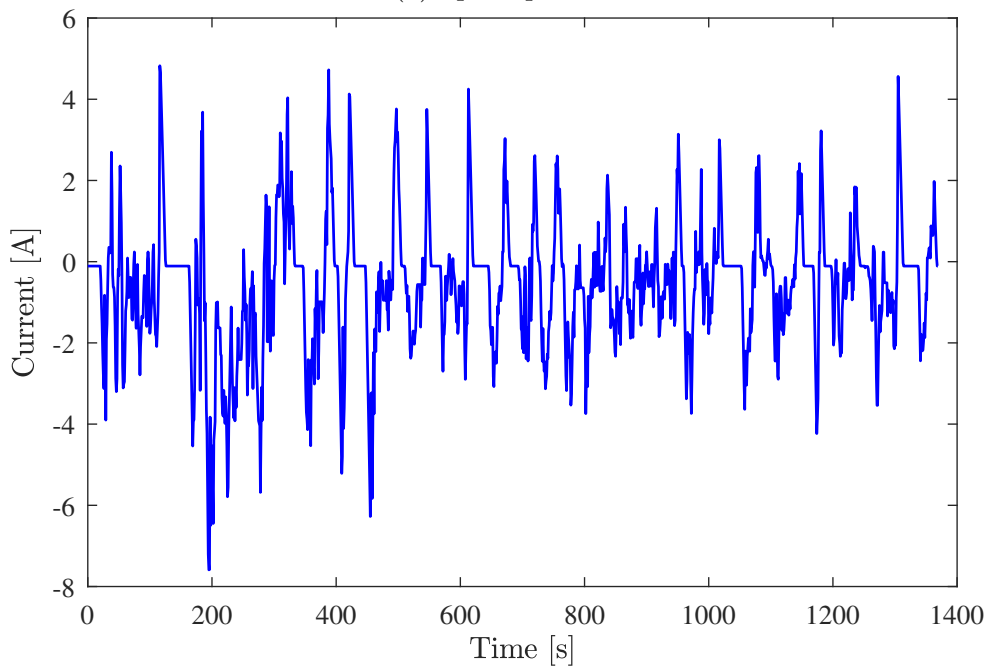


(b) Current profile

Figure D.2: LA92 drive cycle profile data



(a) Speed profile



(b) Current profile

Figure D.3: UDDS drive cycle profile data